Image Processing for Fluoroscopy Guided Atrial Fibrillation Ablation Procedures

Bildverarbeitung für fluoroskopiegestützte Ablationsbehandlungen von Vorhofflimmern

Der Technischen Fakultät der
Universität Erlangen-Nürnberg

zur Erlangung des Grades

DOKTOR-INGENIEUR

vorgelegt von

Alexander Benjamin Brost

Erlangen — 2012

Als Dissertation genehmigt von der
Technischen Fakultät der
Universität Erlangen-Nürnberg

Tag der Einreichung:	20.03.2012
Tag der Promotion:	07.05.2012
Dekanin:	Prof. Dr.-Ing. M. Merklein
Berichterstatter:	Prof. Dr.-Ing. J. Hornegger
	Prof. R. Bammer, Ph.D.

Abstract

Atrial fibrillation is a common heart arrhythmia and is associated with an increased risk of stroke. The current state-of-the-art treatment option is the minimally invasive catheter ablation. During such procedures, the four pulmonary veins attached to the left atrium are electrically isolated. New methods to guide these procedures are presented in this work.

Two methods for catheter reconstruction from two views are presented and evaluated. The first method focuses on the circumferential mapping catheter and the second on the cryo-balloon catheter. The result of the mapping catheter reconstruction is later used for the motion compensation methods.

As there is currently no planning support for single-shot-devices like the cryoballoon catheter, a planning tool is presented, the ***A****trial* ***Fi****brillation Ablation Planning* ***T****ool* (AFiT). AFiT provides direct visual feedback about the fit of a cyroballoon to the patient's anatomy. Another tool to provide intra-procedural support is the tracking of cyro-balloon catheters. Visual feedback about the position and dimensions of the balloon catheter can be superimposed onto live fluoroscopy.

In order to provide overlay images in sync with live fluoroscopic images, cardiac and respiratory motion must be taken into account. Therefore, several novel approaches for motion compensation are presented. The methods differ in their targeted application. A novel method, particularly designed for monoplane image acquisition, facilitates motion compensation by model-based 2-D/2-D registration. Another novel method focuses on simultaneous biplane image acquisition, requiring a 3-D catheter model of the circumferential mapping catheter. Motion compensation is then achieved by using a model-based 2-D/3-D registration to simultaneously acquired biplane images. As simultaneous biplane acquisition is rarely used in clinical practice, a new approach for a constrained model-based 2-D/3-D registration is presented to facilitate motion compensation using sequentially acquired biplane images. The search space of the registration is restricted to be parallel to the image plane. To further extend this approach, a novel method is proposed that involves a patient-specific motion model. A biplane training phase is used to generate this motion model, which is afterwards used to constrain the model-based registration. Overall, our motion compensation approaches achieve a tracking accuracy of less than 2.00 mm in 98.03 % of the frames.

As the circumferential mapping catheter needs to be moved during the procedure, a novel method to detect this motion is introduced. This approach requires the tracking of the mapping catheter and a virtual reference point on the coronary sinus catheter. As soon as the relative distance between circumferential mapping catheter and the reference point changes by more than 5 %, non-physiological motion can be considered. We also investigated an option to provide motion compensation when the circumferential mapping catheter is not available. We propose a novel method for compensation using the coronary sinus catheter that requires a training phase. Our method outperforms a similar method reported in literature. We can conclude that motion compensation using the coronary sinus catheter is possible, but it is not as accurate as it could be using the circumferential mapping catheter.

Kurzübersicht

Vorhofflimmern ist die häufigste Herzrhythmusstörung und wird mit einem erhöhten Schlaganfallrisiko in Verbindung gebracht. Die modernste Behandlungsmethode ist die minimal invasive Katheterablation. Bei einer solchen Prozedur werden die vier Pulmonalvenen vom linken Vorhof elektrisch abgetrennt. In der vorliegenden Arbeit werden neue Methoden zur Unterstützung dieser Behandlung vorgestellt.

Es werden zwei Methoden zur Katheterrekonstruktion aus zwei Ansichten präsentiert und ausgewertet. Die erste Methode ist für den zirkulären Mappingkatheter und die zweite für den Cryo-Ballon-Katheter konzipiert. Da es derzeit keine Planungsunterstützung für sogenannte *single-shot-devices* wie den Cryo-Ballon-Katheter gibt, wird ein Planungsprogramm speziell für derartige Katheter mit dem Namen ***A****trial* ***Fi****brillation Ablation Planning* ***T****ool* (AFiT) vorgestellt. Dieses Programm ermöglicht eine direkte Visualisierung der Passgenauigkeit des Cryo-Ballons hinsichtlich der Anatomie des Patienten. Ein weiteres Hilfsmittel zur Unterstützung der Operation stellt die Nachverfolgung des Cryo-Ballon-Katheters dar. Ein virtueller Katheters kann auf den Röntgenbildern angezeigt werden.

Um Überlagerungsbilder synchron mit den Röntgenbildern darzustellen, muss die Bewegung durch Herzschlag und Atmung berücksichtigt werden. Aus diesem Grund werden neue Ansätze zur Bewegungskompensation vorgestellt. Die Methoden unterscheiden sich hinsichtlich ihres Einsatzgebietes. Die erste Methode ist speziell für monoplane Bildakquisition ausgelegt und die eigentliche Bewegungskompensation wird mittels einer modell-basierten 2D-2D Registrierung erzielt. Die zweite Methode wurde für simultane biplane Bildaufnahmen entwickelt. Hierzu wird ein dreidimensionales Kathetermodell des zirkulären Mappingkatheters benötigt und die Bewegungskompensation wird anschließend durch eine 2D-3D Registrierung des Modells zu den simultanen biplanen Aufnahmen erreicht. Da solche Aufnahmen im klinischen Alltag selten sind, wird ein neuer Ansatz für eine eingeschränkte Bewegungskompensation vorgestellt. Dieser ermöglicht eine 2D-3D Registrierung des Kathetermodells zu reinen monoplanen Aufnahmen. Der Suchraum der Registrierung wird hier auf Richtungen parallel zur Bildebene eingeschränkt und der Ansatz danach um ein patienten-spezifisches Bewegungsmodell erweitert. Eine biplane Trainingsphase wird verwendet, um das Modell zu generieren, das anschließend bei der eingeschränkten Registrierung verwendet wird. Unsere vorgestellten Methoden erzielen eine Genauigkeit von weniger als 2,00 mm in 98,03 % unserer Bilddaten.

Da der zirkuläre Mappingkatheter während der Prozedur bewegt wird, wurde eine neue Methode entwickelt dies festzustellen. Sobald sich der Abstand des Mappingkatheters und einem virtuellen Referenzpunkt auf dem Koronar-Sinus-Katheter um mehr als 5 % verändert, kann von einer nicht-physiologischen Bewegung ausgegangen werden. Darüberhinaus stellen wir eine neue Methode zur Bewegungskompensation mittels Koronar-Sinus-Katheter vor, falls der zirkuläre Mappingkatheter nicht verfügbar ist. Unser Ansatz mit einer Trainingsphase erzielt bessere Ergebnisse als eine ähnliche Methode in der Literatur. Abschließend können wir feststellen, daß Bewegungskompensation mittels Koronar-Sinus-Katheter möglich ist, jedoch nicht so genau wie mit dem zirkulären Mappingkatheter.

Acknowledgments

When I started this thesis back in May 2009, not many people were working on electrophysiology procedures. Even from a medical point of view these procedures are quite new and not all answers have been found yet. Now that I am finishing this thesis the research focus has shifted towards electrophysiology procedures - and I am proud to be a part of that.

I deeply appreciate the support and encouragement by Prof. Dr.-Ing. Joachim Hornegger over the years and also the freedom he gave me for my work. His feedback made a significant contribution to my work and on the papers and some questions would have been left unanswered without his questioning. I have learned much more from him regarding scientific work than I could have ever expected. Whenever there were problems, Achim was within reach and provided options and solutions on all levels of my work.

I gratefully thank Dr. Norbert Strobel. He has been much more than a supervisor during the years of this thesis. He spent a lot of his time, including countless nights, in reviewing papers. The discussions we had were always encouraging and had a huge impact on the course of this work and on the project in general. I enjoyed our discussions very much and I am glad that I could work with Norbert.

I also would like to thank is Dr. Rui Liao. She has been very encouraging during the time of this work. Rui has been a great supervisor and host whenever I visited SCR in Princeton.

Special thanks go to Andreas Wimmer. I am deeply grateful that he allowed me to use his framework for the catheter segmentation used in this work. I also appreciate his feedback on the papers we were able to publish during the course of this thesis. Some parts of this work would not have been possible without Felix Bourier. He spent a lot of time explaining the medical detail and also collected a lot of data that has been very valuable for my work. I appreciated the good times we had at the EP lab in Regensburg as well as at some conferences.

I would like to thank Liron Yatziv and Hari Sundar for their help during some difficult programming tasks. It was a pleasure working with you, in Princeton, Forchheim, or any dark control room at some random hospital. I would like to thank Wen Wu and Terrence Chen for sharing the implementation of their catheter tracking and for the support of our papers. I also would like to thank Atilla Kiraly, Julien Barbot, Christophe Chefd'hotel, Frank Sauer and Dorin Comaniciu for their support, in particular during my visits at SCR. Thanks also go to my colleagues at Siemens in Forchheim. I appreciate it that I was considered as a colleague and not as some student. It was also a great experience to work in the innovations team and I enjoyed my time. In particular, I would like to thank Dr. Marcus Pfister, Andreas Meyer, Dr. Martin Ostermeier and Dr. Klaus Klingenbeck.

Thanks also go to the Siemens TestCenter in Forchheim. Those guys were always helpful when we - once again - broke the system.

I also owe a big *Thank You* to that person that provided the first sequences, Teri Moore. These sequences actually made it possible that we could start working on the first place. During the time I spent working on this thesis her feedback from physicians was very welcome and encouraging to go further down the road. I also appreciated the time she showed me the EP labs at Seattle and Stanford.

I would like to thank Dr. med. Klaus Kurzidim at the Klinik für Herzrhythmusstörungen at the Krankenhaus Barmherzige Brüder in Regensburg. He provided most of the data that was used in this thesis. I also would like to thank the clinical team in Regensburg, in particular Marion Lottner. They allowed me to watch some of the cases and also answered my questions regarding the medical background. Thanks also go to Prof. Dr. Hein Heidbüchel and Dr. Stijn de Buck at the University Hospital Gasthuisberg, University of Leuven, Belgium. It was a pleasure to work with those who already made a significant impact to electrophysiology procedures. I also would like to thank Dr. Amin Al-Ahmad who showed me his work with the current and next generation tools available.

My thanks go to Martin Koch, my roommate at the Lab and at Siemens. We spent a lot of time discussing issues, papers, posters and source code. I appreciate the amount of time he took to review the papers we were able to write during our time together. Thank You!

I would like to thank my students Andreas Kleinoeder, Carolin Jakob, Tanja Kurzendorfer, Sebastian Kaeppler, and Matthias Hoffmann. Their excellent work was more than helpful and we were also able to put some publications out. In particular, I would like to Andreas for the review of parts of this thesis.

I would like to say a special *Thank You* to my "review committee" Dr.-Ing. Anja Borsdorf and Dr.-Ing. Andreas Maier. All three provided very valuable feedback and criticism of the manuscripts I sent them. Even on a short notice, they came directly back with feedback which allowed me to updated this thesis in a much faster way than usual. Thanks also go to Jens Raab for his comments on this thesis and the great times in Erlangen, Forchheim, Princeton and wheresoever.

Special thanks go to all my colleagues at the Pattern Recognition Lab. I enjoyed the pleasant atmosphere at the lab, which was more shaped by friendship than by daily business. I also would like to thank the Medical Image Registration Group (MIRG) who had to endure some reviewing sessions with my papers, posters and talks.

Last but not least, I thank my mother Marianne and particularly my girlfriend Christa for the patience and mental support during the last years. I know that I sometimes spent more time working than I probably should have and I appreciated it that there were only rare complaints about that.

Erlangen, May 20, 2012 Alexander Brost

Because the people who are crazy enough to think they can change the world,
are the ones who do.

Think Different
Apple Inc.
1997

Contents

CHAPTER 1

Introduction

The heart is often considered as the engine of a living being. Its main task is to maintain the blood circulation, thus providing oxygen to all cells. If this organ is malfunctioning, serious complications may occur, even resulting in the death of a patient. With the development of modern angiography systems many of the diseases of the heart can be treated in a minimally invasive way. While clinical outcomes of minimally invasive procedures are often comparable to classical surgical treatment, these methods have the great advantage that the patient recovers much quicker from the procedure which increases patient comfort and reduces cost in patient care [Nitt 12, Suri 12].

In order to treat a patient minimally invasive, imaging technology needs to be applied. As the intervention is performed on a living heart, everything is in motion and cardiologists need a lot of experience. Image guidance can help to make such interventions safer and increase the operator's comfort [Lint 10]. Guidance, however, is very specific for the targeted application. This thesis is devoted to improved guidance for atrial fibrillation ablation procedures which is the most common arrhythmia of the heart. In this chapter, we will focus on the medical background of atrial fibrillation and described the current state-of-the-art treatment options.

1.1 The Human Heart

From a technical point of view, the human heart is a muscular pump with four main parts separated by valves, that deliver oxygenated blood to the body [Ecke 02]. The deoxygenated blood enters the heart in the right atrium via the inferior and superior vena cava and the coronary sinus vein. An overview of the anatomy of a human heart is given in Figure 1.1. The coronary sinus (CS) collects the blood from the coronary arteries that supply the heart with oxygenated blood. When the right atrium contracts and the right ventricle relaxes, the blood is pressed through the tricuspid valve into the right ventricle. The valves in the heart operate only by pressure differences. Small tendons known as the chordae tendineae and the papillary muscles prevent that the valves are pushed back into the atria. On expansion of the right atrium the tricuspid valve prevents blood from flowing back from the right ventricle to the right atrium. The right ventricle pushes the blood via the pulmonary artery into the lungs. The oxygenated blood comes back into the left atrium (LA) via four pulmonary veins (PVs). These are separated anatomy-wise into left and right as well as superior and inferior pulmonary veins.

In some cases, the anatomy of a patient may show a common ostium at which two PVs disembogue the left atrium [Zhen 10]. In rare cases, a fifth pulmonary vein can be observed. This so-called right middle pulmonary vein is usually much smaller than the other PVs [Cron 04]. The left atrium also has a small appendage, the left atrial appendage, which is not relevant for the blood flow in general, but becomes more important in the presence of arrhythmias, in particular with atrial fibrillation. On contraction of the left atrium and relaxation of the left ventricle, the blood is pressed through the mitral valve into the left ventricle. From the ventricle, the blood is pumped through the aortic valve into the aorta from which the oxygenated blood spreads to the whole body.

The blood flow described here holds for human beings after a certain period after their birth. The fetus receives oxygenated blood from its mother and via its inferior vena cava. The blood flows directly from the right atrium to the left atrium via the foramen ovale. This connection can be considered as a very simple valve that closes after birth, leaving the fossa ovalis as remnant.

The pumping action of the heart is controlled by electrical signals, initiated by the sinus node. From there electrical signals are emitted that lead to contractions of both atria. The electrical excitation is delayed on its way to the atrio-ventricular (AV) node as the conductivity is reduced. The transition from the AV node to the His-bundle is much faster and at the His-bundle the signals are split into a left and right branch. One branch is for the left ventricle and one is for the right ventricle. The signals are then passing through the Purkinje fibers on the endocardium of the heart. The endocardium is the inner tissue of the heart and the epicardium is the outer tissue. The myocardium denotes the heart muscle and the pericardium is a sack that contains the heart itself. The Purkinje fibers transport the excitation from the endocardium to the epicardium. The signals then cause the myocardium to contract almost instantly, resulting in the contraction of the ventricles.

The electrical signals can be measured as differences in electrical potentials using electrocardiograms (ECG). The one-channel ECG signal is probably the most commonly known way of measuring the heart activity. The visualization of this signal shows certain peaks or waves which are used to characterize the heart activity. The so-called P-wave indicates a contraction of the atria. The QRS-complex shows the contraction of the ventricles and the T-wave finally indicates the expansion of the ventricles. A visualization of such an ECG is given in Figure 1.2 [Will 07].

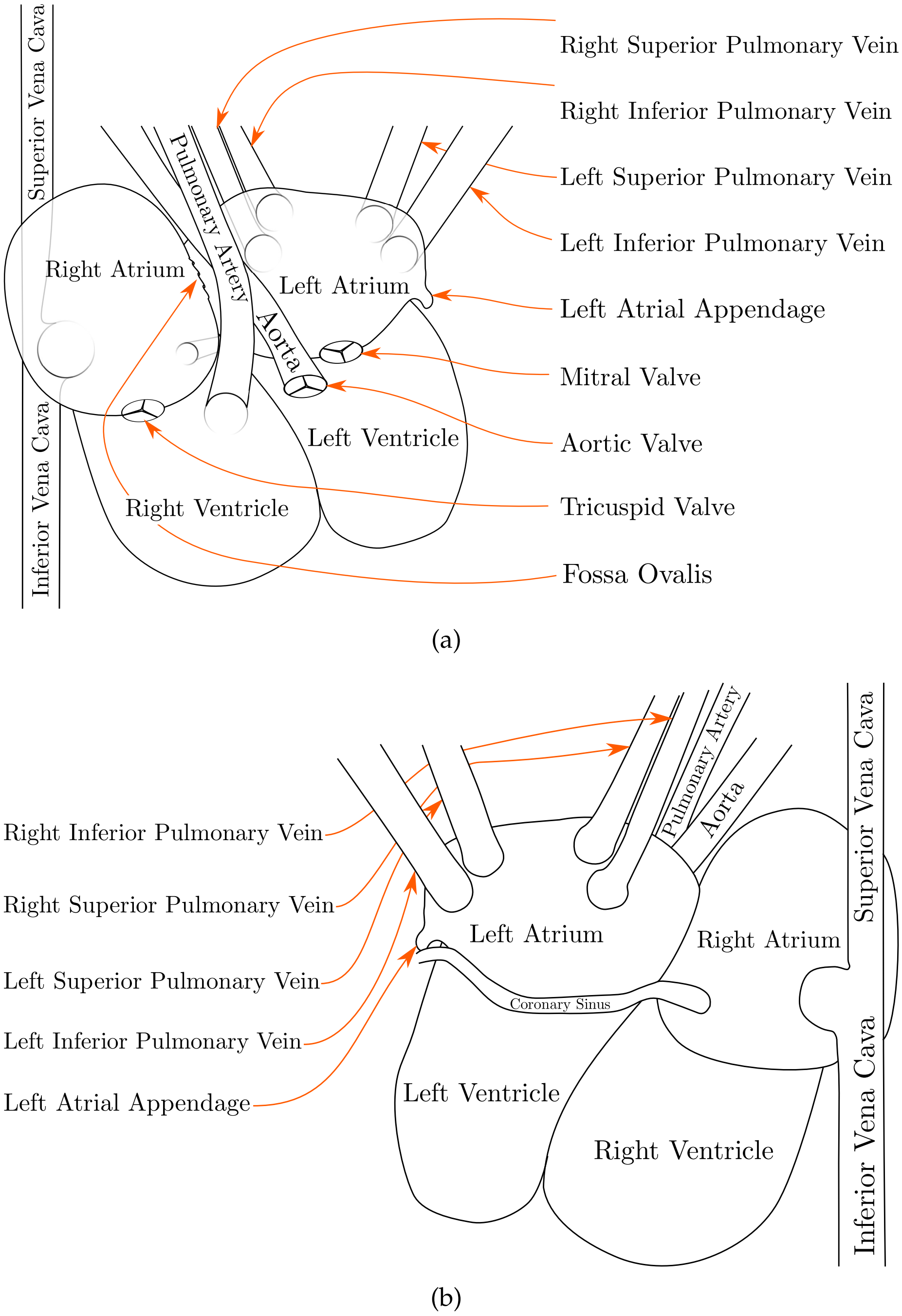

Figure 1.1: Anatomy of the human heart. (a) Anterior view of the heart. The two chambers and two atria are shown as well as the most import structures. (b) Posterior view of the heart. The coronary sinus vein is placed in the sulcus between the left atrium and the left ventricle [Stan 08].

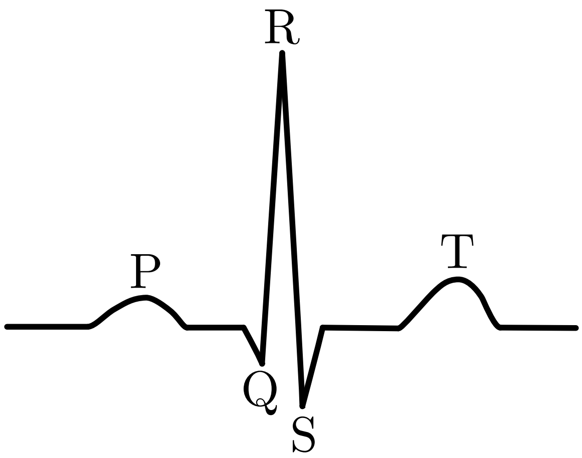

Figure 1.2: Simple illustration of an electrocardiogram (ECG). The P-wave indicates a contraction of the atria. The QRS-complex shows the contraction of the ventricles and the T-wave indicates the expansion of the ventricles.

The delay between P and S usually does not change, at least not in healthy hearts. An increasing heart beat leads to a shortened delay between the T and next upcoming P wave. Considering the sum of P-S periods over one day under normal conditions, the heart has a work day of about 8 hours [Ecke 02].

1.2 Cardiac Arrhythmias

In general, the heart is controlled by electrical signals. Distortions within the circuits of the heart lead to an abnormal heart rhythm. Cardiac arrhythmias are usually considered when patients present themselves in primary care with palpitations or concerns about skipped heart beats [Tayl 05]. Nevertheless, symptoms are difficult to determine and arrhythmias are also often detected in asymptomatic patients. Arrhythmias can be due to wide variety of factors, including stress, mental conditions, stimulants, depressants, prescription and illicit drugs, damage to myocardial cells as well as alterations in the conduction system, but not all of these factors require a hospitalization of the patient. One of the first decisions a physician is facing, is the question regarding the stability of the patient. Hemodynamically unstable patients require immediate care, whereas stable patients can undergo electrocardiographic or electrophysiology study to determine the arrhythmia.

ECG is probably the most frequently used diagnostic tool for cardiac patients [Will 07]. Various tests can be performed, including simple graded exercise testing, as well as long-term continuous monitoring over a period of 24 to 48 hours. Transesophageal echocardiography can be used to detect structural changes that may indicate an arrhythmia. An electrophysiologic examination may be the most powerful diagnostic tool, but it requires a catheterization of the patient. This might be the best option if a catheter ablation is already considered as the best way of treatment.

Common Cardiac Arrhythmias
Supraventricular Arrhythmias
Sinus Bradycardia
Sinus Pause / Sinus Arrests
Atrial Premature Beats
Supraventricular Tachyarrhythmias
Sinus Tachycardia
Atrial Tachycardia
Multifocal Atrial Tachycardia
AV Nodal Reentrant Tachycardias
AV Reciprocating Tachycardias
Atrial Fibrillation
Atrial Flutter
Other Atrioventricular Conduction Abnormalities
1st-degree AV Block
2nd-degree AV Block, Mobitz Type I
2nd-degree AV Block, Mobitz Type II
3nd-degree AV block
Ventricular Arrhythmias
Ventricular Premature Beats
Ventricular Tachycardia
Ventricular Fibrillation

Table 1.1: Types of common cardiac arrhythmias according to medical literature [Tayl 05].

Arrhythmias are classified by different means, but unfortunately there is no unique classification in medical literature. One example of a possible classification is given in Table 1.1. In general, arrhythmias can be separated into three types: tachycardia, bradycardia, and flutter/fibrillation. Tachycardia is considered when the heart beat is faster than 100 beats-per-minute (bpm), whereas bradycardia describes an unusual slow heart beat of less than 60 bpm. Flutter and fibrillation are used to describe irregular heart beats, also described as chaotic [Tayl 05]. The classification is also performed depending on the part of the heart that is affected. From a very simple point of view, this includes the atria and the ventricles. The diagnosis which arrhythmia a patient is suffering from, depends on the physician and his evaluation of the ECG. The medical application that is targeted here is the minimally invasive treatment of atrial fibrillation. It is one of the major health problems, and it is the most common sustained arrhythmia [Sart 08].

1.3 Atrial Fibrillation

The first reports of *Atrial Fibrillation* can already be found prior to World War I. At that time, it was known as *Auricular Fibrillation*. In 1913 H. W. Allen published an article titled ‘Auricular Fibrillation’ in the *California State Journal of Medicine*

Risk Groups for AFib	
Age	Percentage
40 - 49	< 0.5 %
50 - 59	1.5 %
70 - 79	9.9 %
80 - 89	23.5 %

Table 1.2: Risk for occurrence of atrial fibrillation depending on age, as reported in [Camm 10, Mill 05a].

[Alle 13]. At that time, atrial fibrillation (AFib) was diagnosed by using electrocardiographic records that showed atrial impulses discharged at rates of 300 to 500 per minute [Alle 13]. Today, different types of AFib are known and have to be considered for the differential, but the diagnosis is still based on electrocardiograms. AFib is considered, if the ECG shows impulses discharged at rates of 350 to 600 per minute [Calk 07, Deis 06, Lip 95]. The use of a long-term 12-lead ECG is recommended as atrial fibrillation progresses from short and rare episodes to longer and more frequent attacks [Camm 10]. Clinically, the following six types of AFib need to be distinguished [Camm 10]:

- **Silent:** Without diagnosis. The patient may not know of an underlying condition.
- **First Diagnosed:** Patient presents first episodes of AFib.
- **Paroxysmal:** Self-terminating within 48 hours. May continue up to 7 days.
- **Persistent:** Episodes last longer than 7 days or require termination by cardioversion.
- **Long-Standing:** Duration of more than one year before treatment has begun.
- **Permanent:** Arrhythmia is accepted by the patient and physician and no further treatment is pursued.

Atrial fibrillation is a disease that affects the left atrium (LA) which is responsible to transfer the blood from the lungs to the left ventricle [Murg 02]. About 2 % of the general population suffer from AFib [Camm 10], but it affects an increasing percentage of elder people [Dela 07, Gaur 03, Mill 05a]. The risk for occurrence of atrial fibrillation increases for people older than 80 up to 23.5 %, see Table 1.2.

The cause for AFib is not clearly known. The most popular hypotheses in medical literature are the focal model and the multiple wavelet model. The focal model assumes a triggering point or firing focus is causing the electrical signals that lead to fibrillation. The multiple wavelet model assumes depolarization waves are propagating through the atrium. Although the hypotheses about the reasons for AFib are different, the treatment is usually independent of the underlying theory.

Even though atrial fibrillation itself is not a critical disease, strokes are reported to be due to AFib in 31 % of the cases [Klee 11]. The main reasons for the increased risk that an ischemic stroke emerges from cardiac emboli is due to the irregular heart rhythm and the left atrial appendage. During the regular heart rhythm the blood is pushed from the LA into the ventricle such that almost no blood remains in the left atrium. During episodes of fibrillation, a blood pool remains in the LA and forms blood clots. The main region for such clots is assumed to be the left atrial appendage [Tamu 10, Wolf 91].

Studies have investigated the effectiveness and costs of stroke treatment. The results showed that about 30 % of the patients suffering from a stroke will die within the first year [Hank 99]. In addition to that, the life time cost for a stroke patient is about $ 140,000.00 [Mill 05b, Mill 05a] and healthcare system in various countries are under pressure to either reduce costs [Back 04, Ghat 04, Saka 09] or patients are not able to afford the required treatment [Khea 03, Tayl 96].

The prospects for recovery after a stroke are in general worse for patients that suffer from AFib [Mill 05a]. These facts make it absolutely necessary to treat the underlying cause. As AFib is the main risk factor of strokes for these patients, the treatment should focus on the arrhythmia [Calk 07, Camm 10, Gage 01]. To avoid blood clotting, pharmacotherapy and closing devices are also considered as treatment options.

1.4 Treatment Options for Atrial Fibrillation

In the presence of an arrhythmia, a first step is to check for reversible causes, such as medication or ingestions [Tayl 05]. Changing or discontinuing medication or the use of substances such as caffeine may already eliminate the arrhythmia. Pharmacotherapy is considered next, and different classes of drugs are available. For complex arrhythmias this is sometimes difficult [Alle 13, Calk 07, Capp 05, Wazn 05]. In addition to that, the effectiveness of the medication plays also an important role and may be only short compared to pulmonary vein isolation [Marc 09]. Pharmacotherapy is not a curative solution and means life-long medication for the patient. In the next step, cardioversion may be an option. This low-energy defibrillation is heavily discussed in medical literature [Ante 09, Wyse 09]. Cardioversion is mostly considered for hemodynamically unstable patients.

A curative approach is the percutaneous catheterization to ablate tissue that is assumed to cause irregular electrical signals [Calk 07, Camm 10, Hais 94]. Catheter ablation itself can be subdivided into smaller groups depending on the devices used to perform the ablation procedure. The first group consists of standard ablation catheters and although these catheters are the standard way of treatment, recent research also focuses on further improvements. Examples are the combination of mapping and ablation catheter [Arru 07] or the integration of the contact force at the catheter tip [Koch 11, Shah 06, Shah 10, Shah 11a, Shah 11b]. Besides ablation, another option is to freeze the tissue. This can be achieved by using cyroablation tip catheters [Mont 05b, Mont 05a, Silv 10].

The second group of catheters comprises so-called *single-shot-devices*. Such devices try to isolate a pulmonary vein by a single application. Standard ablation catheters require creation of multiple lesions, whereas a single-shot-device may be equipped with more than one ablation electrode. Examples are the pulmonary

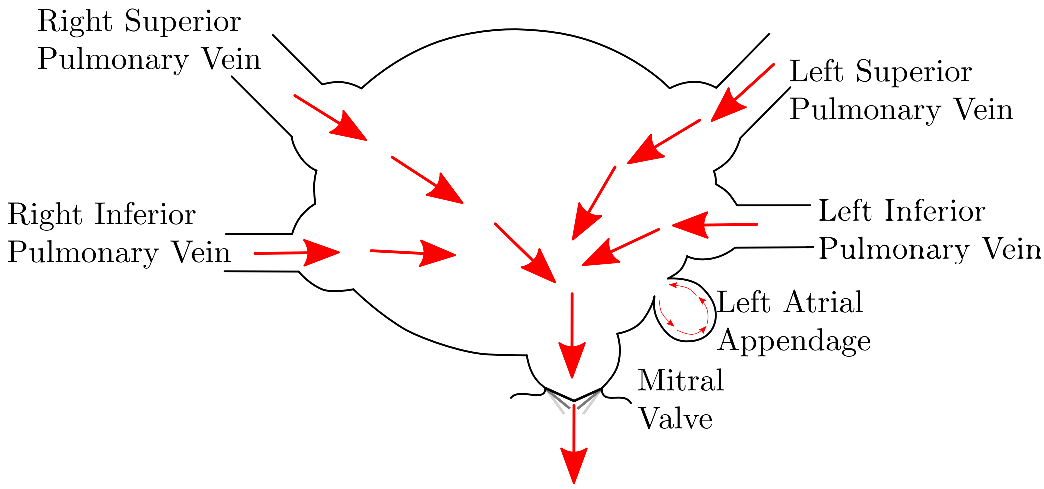

Figure 1.3: Simple illustration of the left atrium with the pulmonary veins, the mitral valve and the indicated blood flow.

vein ablation catheter (PVAC), the multi-array septal catheter (MASC), and the multi-array ablation catheter (MAAC) [Bary 11, Haye 10, Muld 11].

Another subgroup of catheters are balloon catheters [Schm 08]. They are designed to occlude the PV by an inflatable balloon. There are two different balloon catheters available. The first type can be filled with liquid nitrogen to freeze the tissue at the ostium of the pulmonary vein and are named cryo-thermal balloon ablation catheter or in short only cryo-balloon catheter [Avit 03, Bell 07, Neum 08, Thom 11]. The second type are endoscopic laser balloon catheters which ablate the tissue by application of 980-nm laser energy [Gers 10]. This type is equipped with an endoscope to provide a view inside the heart and to visually guide the ablation procedure [Dukk 10, Redd 09]. A single ablation may not be successful for all patients and a second procedure might be required to close re-occurred gaps in the isolation lines [Neum 06, Sart 08]. Furthermore, ablation procedures are not risk-free and complications during the procedure may occur [Andr 05, Calk 07, Sach 07].

Another approach to prevent blood from clotting in the left atrium is the closure of the left atrial appendage by inserting a device that blocks blood from entering, and therefore clotting [Full 11, Sick 07]. Two different devices are currently available, the first is called *WATCHMAN Left Atrial Appendage System* (Atritech Inc., Plymouth, MN, USA) [Land 11], and the second is called *Amplatzer cardiac plug prosthesis* (AGA Medical Corporation, Plymouth, U.S.A.) [Marc 11]. This approach is in discussion because it does not cure the underlying disease and only reduces the risk of an atrial fibrillation induced stroke [McCa 09, Wrig 09]. Surgical ablation is nowadays mostly considered for patients that undergo cardiac surgery anyway [Calk 07, Hais 92, Kay 92]. Catheter ablations are minimally invasive procedures performed to treat patients with arrhythmia and belong to the group of electrophysiology (EP) procedures [Chen 99, Earl 06, Hsu 04, Knec 08a, Ma 06, Mano 94b].

Figure 1.4: Biplane C-arm system equipped with two small detectors. The C-arm depicted in the image is currently used at the *Klinik für Herzrhythmusstörungen* at the *Krankenhaus der Barmherzigen Brüder* in Regensburg, Germany. The photo was taken with permission by Dr. med. Klaus Kurzidim.

1.5 Catheter Ablation

The current state-of-the-art technique to treat atrial fibrillation is the electrical isolation of the pulmonary veins [Calk 07, Camm 10, Gaur 03]. An illustration of the left atrium with the PVs is given in Figure 1.3. The pulmonary veins are surrounded by a sleeve of muscle fibers which are supposed to be a source for ectopic beats. These beats are capable of triggering atrial fibrillation, basically following the focal model. The junction between the pulmonary vein and the atrium can not be distinguished anatomically or histologically from the surrounding myocardium [Scha 05]. The ostium of the PVs is commonly accepted as the area of ablation, although this is not precisely defined. The treatment consists of isolation of the pulmonary veins, either of all four of them, without considering their electrical activation, or only the active PV [Earl 06, Karc 02]. This is often done in combination with a linear ablation [Karc 02, Ma 06]. The linear ablation involves the creation of lesions bridging the two superior PVs within the left atrium or extending lesions from the left inferior PV to the mitral annulus, the area of the mitral valve in the left atrium. A consensus of cardiologists has concluded that optimal treatment consists of ablating all pulmonary veins without respect to their individual electrical activity [Calk 07]. A circumferential mapping (CFM) catheter,

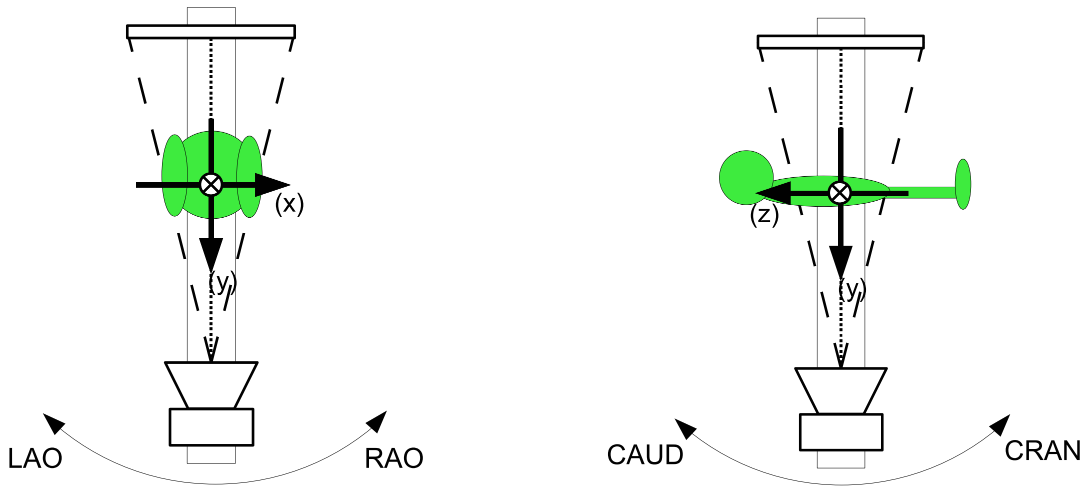

(a) (b)

Figure 1.5: Basic geometry of a C-arm X-ray imaging system. (a) Illustration of the rotation of the C-arm related to a patient's right/left side, right anterior oblique or left anterior oblique (RAO/LAO), viewed from a patient's feet side. (b) Illustration of the rotation towards a patient's cranial or caudal (CRAN/CAUD) direction, viewed from a patient's right side.

also often called lasso catheter, is used for mapping the site of the ablation for each PV [Bahn 04, Katr 08, Nade 04, Oral 06, So 09, Taka 06, Tilz 07].

The catheters for ablation and mapping are positioned via the right femoral vein and the inferior vena cava in the right atrium and are then brought to the left atrium by a trans-septal puncture at the location of the fossa ovalis under fluoroscopic imaging [Mano 99, Mano 94a, Rao 05]. An illustration of the heart is given in Figure 1.1. Electrophysiology labs are usually equipped with modern C-arm systems that provide 2-D fluoroscopic images, but also offer the capability to acquire intra-procedural 3-D data sets, referred to as C-arm CT [Prum 09]. C-arm systems are available in different configurations. Monoplane C-arm systems are equipped with one C-arm, while biplane systems have two C-arms, one floor-mounted and one ceiling-mounted. Different detector sizes are commercially available. Three detector options are currently offered by Siemens AG (Healthcare Sector, Forchheim, Germany). The first size is a big detector with 30 cm $\times$ 40 cm, the second a mid-size detector of 30 cm $\times$ 30 cm, and the third a small detector of 20 cm $\times$ 20 cm [Iwaz 10, Stro 09]. The big version is usually considered for neuro-radiology applications, whereas the small detector is mostly used in cardiac applications. For biplane systems, there also exist a mixed configurations with different detectors for each C-arm. One example of a biplane C-arm system with two small detectors is given in Figure 1.4.

C-arm positions are defined by two angles, the first angle denotes the rotation of the C-arm related to a patient's right/left side, right anterior oblique (RAO/LAO). The second angle denotes the rotation towards a patient's cranial or caudal (CRAN/CAUD) direction. See Figure 1.5 for an illustration. The image guidance during the ablation is either performed by using fluoroscopy, by angiog-

Figure 1.6: An example of an ablation catheter used in electrophysiology procedures. Here, a *Blazer II XP* from Boston Scientific (Natick, MA, USA) with a diameter of 8 F and a tip length of 8 mm is shown.

raphy of the PVs using contrast agent or electro-anatomical mapping [Geps 97, Ma 06, Mano 94a, Nade 04, Papp 00, Sart 08, Wang 07, Witt 02]. A less often reported technique to place the mapping catheter is to move the catheter until the local impedance recorded by the radio frequency generator increases or decreases abruptly. For the ablation itself, a localization of the catheter tip in three dimensions within the left atrium is required. That is achievable by electro-anatomical mapping systems or biplane fluoroscopy [Scha 05].

Inaccuracies during the localization can lead to the ablation of the wrong tissue and to complications for the patient, which include cardiac tamponade, phrenic nerve injury, thromboembolism, mitral valve trauma, and even stenosis may occur.

The position of the esophagus can be marked by a barium sulfate swallow under fluoroscopy or by using pre-operative data [Bour 11a, Bour 11c]. Ablation near the esophagus is also avoided if possible to reduce the risk of an esophageal injury. Other risks, e.g. cardiac emboli, depend on the condition of the patient.

The ablation is performed by using an ablation catheter that has an electrode of about 4 mm at its tip. The electrical current is directly brought to the cardiac wall causing tissue heating and thus performing the ablation. Considering the ablation energy, problems have been reported when the ablation was performed with an effective ablation energy of 50 W resulting in an ablation temperature of 60^oC or more. The protocols used in literature mostly consider an energy of 20 W to 40 W with a resulting heat of 40^oC to 50^oC [Earl 06, Hsu 04, Ma 06, Oral 06, Rao 05, Sart 08, Taka 06]. According to the energy and temperature, the ablation of the tissue is performed for 10 to 60 seconds. The temperature is monitored during the procedure. The energy is generated at a frequency of 350 kHz to 750 kHz from low power 15 V to 60 V [Kay 92, Mano 94a, Mano 94b, Schu 07]. In general, the ablation energy used for AFib procedures is lower than for other ablations in the heart. One example for an ablation catheter is given in Figure 1.6. The diameter of a catheter is measured in F (French) with 1 F = 1/3 mm. In the course of this work, the following catheters are considered during the ablation procedure:

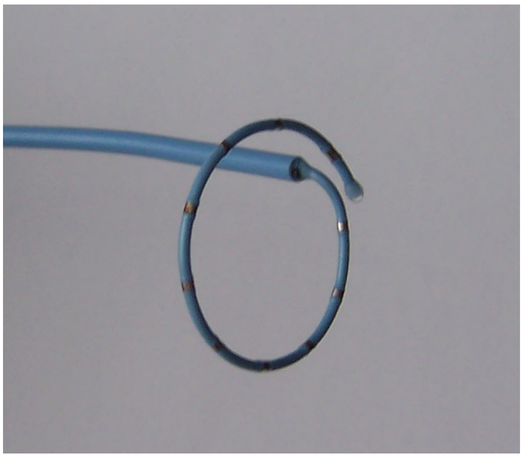

Figure 1.7: An example for a circumferential mapping catheter used in electrophysiology procedures with 10 electrodes and a diameter of 7.5 F. The circular part itself has a diameter of 5 F. This catheter is a previous version of the *Orbiter PV Variable Loop Mapping Catheter* by Bard Medical (Covington, GA, USA). The current version has 14 electrodes.

- **Ablation Catheter:** Ablation catheters have a diameter of 4 F to 6 F and a length of 115 cm. They are equipped with three or four electrodes with a spacing between the electrodes of 1 mm to 7 mm. The ablation tip length itself is 4 mm to 10 mm. In AFib procedures, ablation catheters with an ablation tip of 4 mm are used, which ablate heart tissue by heating. Although ablation catheters that destroy tissue by cooling are available, they are not routinely used for AFib procedures. An example of an ablation catheter is given in Figure 1.6.

- **Diagnostic Catheter:** Diagnostic catheters are equipped with 4 to 24 electrodes with a spacing of 1 mm to 10 mm. These catheters measure potentials within the heart, blood pressure and blood flow as well as the blood temperature. They have a diameter of 4 F to 6 F and a length of 105 cm to 115 cm. During an AFib ablation a diagnostic catheter is placed in the coronary sinus, hence the name CS catheter. Another one may also be placed in the superior vena cava.

- **Circumferential Mapping Catheter:** Mapping catheters for atrial fibrillation are catheters that form a circle at the catheter tip. They have a length of 105 cm to 115 cm, have a diameter of 5 F to 7.5 F, and are equipped with 10 to 20 electrodes to measure potentials. The diameter of the circle is between 14.5 mm and 25.0 mm. The mapping catheter is used to mark the ostium of the pulmonary vein that is considered for ablation and to measure electrical signals during and after the ablation. During the ablation, the catheter is assumed to be stably fixed at the ostium of the PV. Other names for this kind of catheters is lasso catheter or spiral catheter. An example for such a catheter is given in Figure 1.7.

- **Cryo-Balloon Catheter:** This type of catheter belongs to the group of single-shot-devices. A cryo-thermal balloon catheter can be filled with liquid nitro-

Figure 1.8: Inflated cyro-balloon catheter (Arctic Front, Medtronic, Minneapolis, MN, USA). The balloon was manually inflated to its diameter of 28 mm.

gen to freeze the tissue at the ostium of the pulmonary vein [Avit 03, Bell 07, Neum 08, Thom 11]. They are commercially available in two sizes. The inflated balloon can achieve either 23 mm or 28 mm (Arctic Front, Medtronic, Minneapolis, MN, USA). The main problem of these single-shot-devices is that they not always fit to the patient's anatomy. Assessment before the procedure is required, also with respect to the diameter of the balloon catheter [Bros 11a]. An example of a cryo-balloon catheter is given in Figure 1.8

Depending on the manufacturer, the catheters are different in electrode spacing, number of electrodes, size and diameter. In general, the length of the catheters is roughly comparable.

1.6 Intraprocedural Guidance

The guidance of the catheter into the right atrium is performed using fluoroscopy guidance [De B 05, Ecto 08a]. The trans-septal puncture can be performed using fluoroscopy guidance as well, or by using trans-esophageal echocardiography [Bour 11a, Bros 11b]. The ablation procedure itself can be guided by either using fluoroscopy or electro-anatomic mapping systems. Mapping systems are able to visualize the catheter position in 3-D within a registered 3-D data set [Kist 06a, Kist 06b, Kist 08, Witt 99]. While they promise to save X-ray dose, they add effort and cost to the procedure. In addition, mapping systems are virtual reality systems and they do not allow for instant confirmation of catheter positions under real-time X-ray. In some instances, the registration of these systems may even be off with respect to the underlying anatomy [Dacc 07]. Modern C-arm X-ray systems often provide 3-D tomographic imaging to overcome the issue that soft-tissue of the heart is difficult to see in X-ray images [Al A 08, Fahr 00, Isol 08, Nolk 08, Prum 06b, Prum 07, Prum 09, Rohk 08, Stro 09, Stro 03, Orlo 07, Zell 05].

Overlay images rendered from either CT, MR, or C-arm CT 3-D data sets can be superimposed onto live fluoroscopic images. This kind of augmented fluoroscopy can facilitate more precise real-time catheter navigation and also reduce radiation [De B 05, Ecto 08a, Fall 04, Gorg 05, Sier 03, Sra 07, Tops 09]. Unfortunately, catheter navigation under augmented fluoroscopy is compromised by cardiac and respiratory motion. Motion has shown to be problematic in many medical procedures [Keal 06, Klem 07, Ross 08, Shec 04, Shec 06, Shec 05, Ortm 05].

1.7 Scientific Focus and Contributions

In the previous sections, the underlying information about the clinical application and the current state-of-the-art treatment options were presented. The main scientific focus of this work was to develop novel methods for motion compensation for atrial fibrillation ablation procedures. As overlay images rendered from pre-operative data sets have proven to be clinically useful [Ecto 08a, Knec 08b], methods to compensate for cardiac and respiratory motion are required to keep the overlay in sync with live fluoroscopic images. Providing a consistent visual impression for the physician may help to improve the efficiency and safety of the procedure. Furthermore, it might also help to reduce the amount of X-ray used during the procedure. In addition to that, first work to support cryo-balloon ablation procedures was developed. This thesis provides scientific progress within the current research fields regarding electrophysiology procedures and contributions to the community of computer assisted interventions. In the following list, the major scientific contributions are summarized.

- An approach to reconstruct the elliptical part of the circumferential mapping catheter is evaluated in simulations and phantom experiments. This 3-D catheter model is later on used to achieve motion compensation. The details can be found in Chapter 2.

- An novel approach to generate a model of a cryo-balloon catheter from two views is presented in Chapter 3. It has been shown in simulations and experiments that the proposed method outperforms currently available approaches.

- As cryo-balloon ablation procedures gain more and more interest in the medical community, a first approach to provide a planning tool is presented in Chapter 4. Currently, there is no other software available that is able to provide physicians visual feedback about the fit of a cryo-balloon to the considered pulmonary vein.

- To further provide support for cyro-balloon ablation procedures, a first approach to track such a device is presented in Chapter 5. The proposed method is able to visualize the boundary of an inflated balloon catheter on top of live fluoroscopic images. Given a pre-planned position, this could be used to accurately place the cryo-balloon at its desired position.

- In Chapter 7, two novel approaches for motion compensation in atrial fibrillation are proposed. These methods are designed for monoplane C-arm system. As input, a 2-D spline of the circumferential mapping catheter is required. This catheter model is successively registered to fluoroscopic images. As the catheter is firmly placed at the ostium of the pulmonary vein, its motion can directly be applied to the overlay images. The two methods differ only in image pre-processing methods, as presented in Chapter 6. One uses a filter-based approach and the other one makes use of learning-based algorithms. These two methods are compared against each other.

- A novel method for motion compensation for biplane C-arm systems is presented in Chapter 8. As in the previous chapter, a filter-based and a learning-based approach are compared. These approaches require a 3-D catheter model as detailed in Chapter 2 and simultaneously acquired biplane fluoroscopic images.

- In Chapter 9, a new method is proposed that provides 3-D motion compensation when only monoplane fluoroscopic images are available. Therefore, a 3-D catheter model is required that can be registered to monoplane fluoroscopic images. In this case, the monoplane fluoroscopic images are acquired using a biplane C-arm system, but instead of using a simultaneous acquisition approach as in Chapter 8, the underlying assumption is that the images are acquired sequentially.

- A novel approach using a patient-specific motion model is presented in Chapter 10. This method uses a 3-D catheter model and a biplane fluoroscopic sequence to determine a patient-specific motion model. In the subsequent acquired monoplane images, the motion model is used to constrain the motion compensation approach to achieve a compensation for depth information, which is missing in monoplane images.

- As the circumferential mapping catheter needs to be placed at each of the four pulmonary veins considered for ablation, the catheter is moved from one PV to another during the procedure. A first method to detect such kind of non-physiological motion is presented in Chapter 11. The detection is based on the observations of the mapping catheter and the CS catheter. Once their relative distance changes, non-physiological motion is assumed.

- Motion compensation by using the circumferential mapping catheter has been proposed so far. Apart from that, one method to achieve motion compensation using the CS catheter is reported in literature. A new approach to achieve motion compensation by using the coronary sinus catheter is presented in Chapter 12. A training phase is required to obtain the position of the circumferential mapping catheter as an indicator for the pulmonary vein. During this learning phase, an artificial heart cycle value is computed based on the observation of the CS catheter. After the training phase, the position of the mapping catheter is estimated based on the observation of the CS catheter.

1.8 Outline

This thesis is structured in five parts. In the first part, two catheter reconstruction approaches from two views are presented. The second part focuses on tools for cryo-balloon ablation procedures. In the third part, motion compensation methods using the circumferential mapping catheter only are presented. The fourth part extends this by including the coronary sinus catheter. In the last part, future work is considered and the presented methods are summarized.

The reconstruction methods in the first part focus on two catheters, the circumferential mapping catheter and the cryo-balloon catheter. The reconstruction of the elliptical part of the mapping catheter is presented in Chapter 2. Under the assumption that a cryo-balloon catheter can be approximated as a sphere, a reconstruction method is proposed in Chapter 3.

The tools for cryo-balloon ablations presented in the second part consist of the first planning tool for such procedures. The ***A****trial* ***Fi****brillation Ablation Planning* ***T****ool* (AFiT) is presented in Chapter 4. A first approach to track a cryo-balloon catheter is detailed in Chapter 5.

In the third part, motion compensation based on the circumferential mapping catheter is presented. Two methods for catheter segmentation, a filter-based and a learning-based approach, are presented in Chapter 6. In Chapter 7, these segmentation approaches are used for monoplane motion compensation using a model-based 2-D/2-D registration. The same segmentation approaches are presented for biplane motion compensation using a model-based 2-D/3-D registration, using the assumption of simultaneously acquired biplane fluoroscopic images. An approach for a constrained model-based 2-D/3-D registration, if only sequential biplane images are acquired, is presented in Chapter 9. In the next chapter, a first method for a patient-specific motion compensation using a model-based 2-D/3-D registration is detailed. This method requires a training phase to learn the principal motion of the pulmonary vein considered for ablation. The methods in this part were evaluated on the same clinical data set. A comparison on the performance is given in Chapter 10.

In the fourth part, motion compensation methods involving the mapping and the CS catheter are presented. In Chapter 11, a method to detect non-physiological motion of the mapping catheter is presented. In the next chapter, a motion compensation approach using the coronary sinus catheter is presented. This approach uses a training phase and is compared to a currently reported approach in literature. A comparison of the proposed method and the reference method is given in Chapter 12.

In the last part, future work is considered in Chapter 13 and a summary of the presented methods is given in Chapter 14.

Part I

Catheter Reconstruction from Two Views

CHAPTER 2

Circumferential Mapping Catheter Reconstruction

In this chapter, the reconstruction of the circumferential mapping catheter from two views is detailed. The most important part of this catheter is its elliptically shaped tip. It is assumed that this part can be approximated as an ellipse in 2-D as well as in 3-D. The original method was proposed in [Bros 09b]. Parts of this chapter have been published in [Bros 09a, Bros 10b].

2.1 Motivation

The circumferential mapping catheter is a catheter that shapes a circle at its tip [Deis 03]. This catheter is used to measure the electrical activity at the ostium of a pulmonary vein [Capp 05]. The current ablation strategy to treat atrial fibrillation is the electrical isolation of the pulmonary veins [Calk 07]. We can count on the physicians to provide a stable wall contact, as it is in their best interest. Otherwise complete isolation of the pulmonary veins may fail due to undetected residual PV-atrial electrical connections. Image guidance during the procedure is performed by using fluoroscopic imaging. For the reconstruction, we require a biplane C-arm system with two C-arms, one denoted as image plane A and one as image plane B.

2.2 Reconstruction Method

For reconstruction of the elliptical part of the circumferential mapping catheter, we differentiate three cases. In the first case, ellipses are visible in both image planes. The second case assumes that one of the ellipses is degenerated to a line in one projection image. Such a configuration happens when the elliptical part lays in a plane perpendicular to the view direction. The third case, when both ellipses are

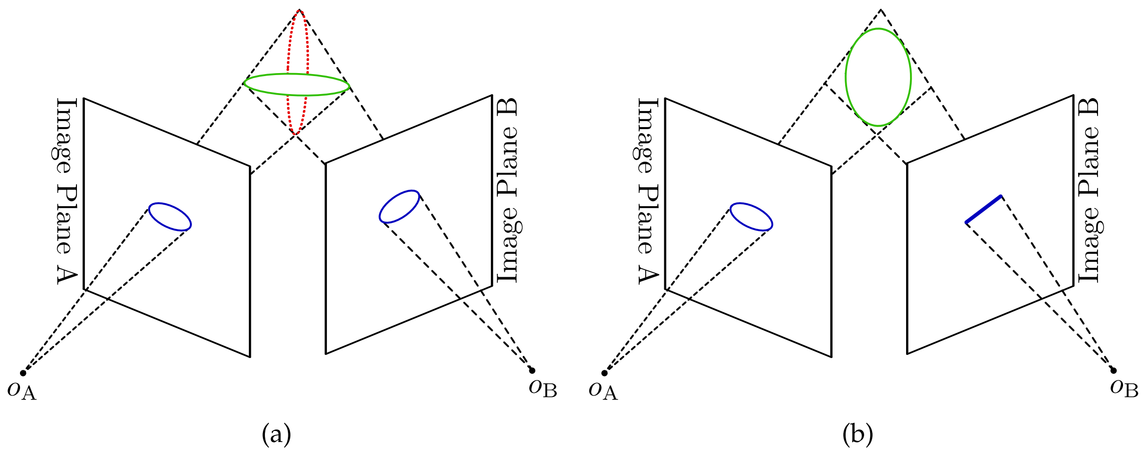

Figure 2.1: Circumferential mapping catheter reconstruction from two views. (a) This *general case* shows two possible solutions when reconstructing a 3-D ellipse from biplane 2-D ellipses. The correct solution can be found by using prior knowledge, e.g., of the diameter of the circumferential mapping catheter. (b) This *degenerated case* reconstructs a 3-D ellipse from one 2-D ellipse in one X-ray view and a line in the other.

degenerated to lines in the projection images, is not further consider as an ellipse reconstruction from such a configuration is not possible. Even a small rotation of one of the C-arms would provide a much better view, such that at least one ellipse becomes visible. From a practical point of view, physicians are very likely to avoid such configurations as the positioning of the ablation with respect to the circumferential mapping catheter is difficult.

This section is structured as follows. In the first subsection, the two-ellipse-case is considered. Two 3-D cones are generated from the 2-D ellipses in the image planes. Their intersection in 3-D yields two intersecting 3-D planes. In the second subsection, the one-ellipse case is considered. If one of the ellipses is degenerated to a line, a reconstruction is still possible.

2.2.1 Two Ellipse Case

The reconstruction method is based on the work in [Quan 96] assuming that ellipses are visible in both image planes. It is shown, that two possible solutions can be computed and prior knowledge about the reconstruction problem is required to find the correct solution. The reconstruction of the circumferential mapping catheter as a circle in 3-D when firmly positioned at the ostium of a pulmonary vein uses the following assumptions:

1. When positioned at the pulmonary vein, the circumferential mapping catheter can be approximated as a circle in 3-D space.

2. The X-ray projection images of the mapping catheter can be modeled as 2-D ellipses.

Using these two assumptions, the elliptical shaped tip of the circumferential mapping catheter can be reconstructed from two views. For simplicity, the equations

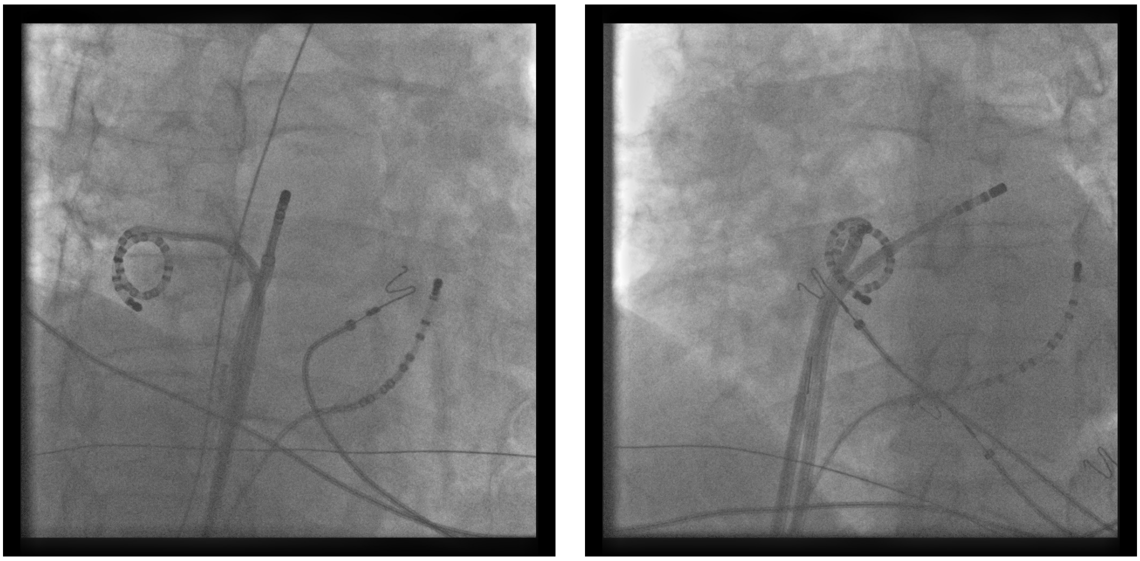

(a) Plane A (b) Plane B

Figure 2.2: The images show an example of the *general case*. The biplane C-arm system is set up such that the circumferential mapping catheter is projected as an ellipse in each view. As the catheter has to be moved through the vessels of the body to reach its target, even this catheter needs to have line-like characteristics including a catheter tip.

in this subsection are valid for both image plane A and image plane B, if not indicated otherwise. When required, the image planes are denoted by A and B. An elliptical cone in 3-D can be spanned using the optical center as vertex $\mathbf{o} \in \mathbb{R}^3$ and the 2-D ellipse $\mathbf{C} \in \mathbb{R}^{3\times 3}$ in the image plane, see Figure 2.3 for an illustration. Given the 2-D input points, an ellipse is fitted to these points. The ellipse parameters are given in matrix notation as $\mathbf{C} \in \mathbb{R}^{3\times 3}$. Assuming a perfect ellipse, a 2-D point on the ellipse would fulfill [Hali 98, Fitz 99, Fitz 95]

$$\widetilde{\mathbf{p}}^T \mathbf{C} \widetilde{\mathbf{p}} = 0 \tag{2.1}$$

with the 2-D point $\mathbf{p} \in \mathbb{R}^2$ in homogeneous coordinates as $\widetilde{\mathbf{p}}^T = (\mathbf{p}^T, 1)^T$. The image point $\mathbf{p}$ is the projection of a point $\mathbf{w} \in \mathbb{R}^3$ in 3-D. The projection of a 3-D point is computed by [Schm 05, Bros 09c, Bros 09d]

$$\widetilde{\mathbf{p}} = \mathbf{P} \cdot \widetilde{\mathbf{w}} \tag{2.2}$$

with the projection matrix $\mathbf{P} \in \mathbb{R}^{3\times 4}$, and a point $\mathbf{w} \in \mathbb{R}^3$ in 3-D given in homogeneous coordinates as $\widetilde{\mathbf{w}} \in \mathbb{R}^4$. The projected point is given as $\widetilde{\mathbf{p}} \in \mathbb{R}^3$ in homogeneous coordinates. To arrive at image coordinates, a dehomogenization is required. Given an ellipse in 3-D, a point $\mathbf{w}$ fulfills

$$\widetilde{\mathbf{w}}^T \cdot \mathbf{P}^T \cdot \mathbf{C} \cdot \mathbf{P} \cdot \widetilde{\mathbf{w}} = 0 \tag{2.3}$$

which is a combination of Eq. (2.1) and Eq. (2.2). The multiplication of the projection matrix and the ellipse parameters yields

$$\mathbf{Q} = \mathbf{P}^T \cdot \mathbf{C} \cdot \mathbf{P} \tag{2.4}$$

(a) Plane A

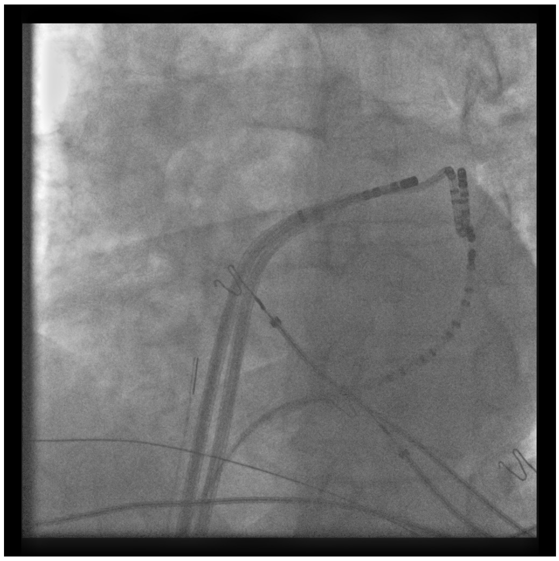

(b) Plane B

Figure 2.3: The images present an example of the *degenerated case*. This view configuration can simplify biplane catheter navigation during ablation, when the circumferential mapping catheter often serves as a visual reference. In this setup, the physician needs to verify that the ablation catheter is in the vicinity of its elliptical projection in one view and close to the line in the other.

which is the resulting quadric $\mathbf{Q} \in \mathbb{R}^{4\times4}$ defining an elliptical cone in 3-D. With the ranks of $\mathbf{P}$ and $\mathbf{C}$ being 3, the quadric $\mathbf{Q}$ is also of rank 3, thus describing a 3-D elliptical cone. Quadrics can be distinguished by considering the ranks of the describing matrix $\mathbf{Q}$ as well as the rank of the left upper 3×3-sub-matrix $\mathbf{Q}^+ \in \mathbb{R}^{3\times3}$, see Table 2.1 [Zwil 06]. Computing the elliptical cones for both image planes results in

$$\widetilde{\mathbf{w}}^T \cdot \mathbf{Q}_A \cdot \widetilde{\mathbf{w}} = 0 \quad (2.5)$$
$$\widetilde{\mathbf{w}}^T \cdot \mathbf{Q}_B \cdot \widetilde{\mathbf{w}} = 0. \quad (2.6)$$

Considering the intersection of these two quadrics, the intersections lay within two intersecting planes. These intersecting planes can be found by combing the two quadrics as

$$\mathbf{Q}(\lambda) = \mathbf{Q}_A + \lambda \cdot \mathbf{Q}_B \quad (2.7)$$

in such a way that

$$\mathrm{rank}(\mathbf{Q}(\lambda)) \stackrel{!}{=} 2. \quad (2.8)$$

The matrix $\mathbf{Q}(\lambda)$ is a function of $\lambda \in \mathbb{R}$ that describes a pencil of matrices [Lanc 66]. Those values of λ_i for which $\mathbf{Q}$ is rank deficient are called latent roots. The eigenvalues of $\mathbf{Q}(\lambda)$ are dependent on the choice of λ. Thus, if a quadratic matrix $\mathbf{Q}(\lambda) \in \mathbb{R}^{\mathcal{N}\times\mathcal{N}}$ has a degeneracy of a, i.e. the rank is $\mathcal{N} - \mathsf{a}$, at least one latent root is of multiplicity $\mathsf{m} = \mathcal{N} - \mathsf{a}$.

rank($\mathbf{Q}$)	rank($\mathbf{Q}^+$)	*Type of Quadric*
4	3	Ellipsoid or Hyperboloid
3	3	Cone
4	2	Paraboloid
3	2	Cylinder
2	2	Intersecting Planes
2	1	Parallel Planes
1	1	Coincident planes

Table 2.1: A Simple classification of quadrics depending on the ranks for their describing matrix $\mathbf{Q}$ and the rank of their corresponding right upper 3×3-sub-matrix $\mathbf{Q}^+$ [Zwil 06].

To achieve that $\mathbf{Q}(\lambda)$ is of rank 2, at least one latent root of multiplicity $\mathsf{m} = 2$ is required. The latent roots are calculated as

$$|\mathbf{Q}(\lambda)| = |\mathbf{Q}_A + \lambda \mathbf{Q}_B| = \mathcal{I}_1 \cdot \lambda^4 + \mathcal{I}_2 \cdot \lambda^3 + \mathcal{I}_3 \cdot \lambda^2 + \mathcal{I}_4 \cdot \lambda + \mathcal{I}_5 = 0 \tag{2.9}$$

with the coefficients $\mathcal{I}_1, \mathcal{I}_2, \mathcal{I}_3, \mathcal{I}_4, \mathcal{I}_5 \in \mathbb{R}$ corresponding to the power of λ that follows. The polynomials $\mathcal{I}_5 = |\mathbf{Q}_A| = 0$ and $\mathcal{I}_1 = |\mathbf{Q}_B| = 0$ can be removed from the equation, corresponding to the latent roots 0 and ∞, respectively. This reduces Eq. (2.9) to

$$\mathcal{I}_2 \cdot \lambda^2 + \mathcal{I}_3 \cdot \lambda + \mathcal{I}_4 = 0. \tag{2.10}$$

As two latent roots with multiplicity $\mathsf{m} = 1$ are given, the remaining latent root λ needs to be of multiplicity $\mathsf{m} = 2$, i.e., there is only one solution for Eq. (2.10). Solving the quadratic equation and assuring that there is only one solution for λ yields to

$$\lambda = \frac{-\mathcal{I}_3}{2\mathcal{I}_2}. \tag{2.11}$$

Given the quadric $\mathbf{Q}(\lambda)$, the 3-D planes, in which each of the solutions lies, are calculated using a transformation $\mathbf{B} \in \mathbb{R}^{4\times4}$, that leads to

$$\mathbf{B}^T \cdot \mathbf{Q}_\lambda \cdot \mathbf{B} = \begin{pmatrix} \mu_1 & & & \\ & \mu_2 & & \\ & & 0 & \\ & & & 0 \end{pmatrix}. \tag{2.12}$$

The points in 3-D space are transformed by the same transformation matrix, resulting to

$$\widetilde{\mathbf{w}}^T \cdot \mathbf{B}^T \cdot \begin{pmatrix} \mu_1 & & & \\ & \mu_2 & & \\ & & 0 & \\ & & & 0 \end{pmatrix} \cdot \mathbf{B} \cdot \widetilde{\mathbf{w}} = 0. \tag{2.13}$$

With the substitution

$$\widetilde{\mathbf{w}}' = \mathbf{B} \cdot \widetilde{\mathbf{w}} \tag{2.14}$$

follows

$$\widetilde{\mathbf{w}}'^T \cdot \begin{pmatrix} \mu_1 & & & \\ & \mu_2 & & \\ & & 0 & \\ & & & 0 \end{pmatrix} \cdot \widetilde{\mathbf{w}}' = 0. \tag{2.15}$$

Rewriting this equation in terms of components of $\widetilde{\mathbf{w}}' = (x', y', z', 1)$ results to

$$\mu_1 \cdot x'^2 + \mu_2 \cdot y'^2 = 0. \tag{2.16}$$

The solution planes in this transformed coordinate system are then calculated by

$$\sqrt{\mu_1} \cdot x' \pm \sqrt{-\mu_2} \cdot y' = 0. \tag{2.17}$$

This describes two planes in the transformed space domain with their normals $\widetilde{\mathbf{n}}'_k \in \mathbb{R}^4$ with $k \in \{1, 2\}$ in homogeneous coordinates as

$$\widetilde{\mathbf{n}}'^T_k \widetilde{\mathbf{w}} = \sqrt{\mu_1} \cdot x' \pm \sqrt{-\mu_2} \cdot y' = 0. \tag{2.18}$$

The back-transformation to normal space is performed by considering the column vectors $\widetilde{\mathbf{e}}_1, \widetilde{\mathbf{e}}_2 \in \mathbb{R}^4$ of $\mathbf{B}$ that leads to

$$(\mathbf{B} \cdot \widetilde{\mathbf{n}}'_k)^T \cdot \widetilde{\mathbf{w}} = (\sqrt{\mu_1} \cdot \widetilde{\mathbf{e}}_1 \pm \sqrt{-\mu_2} \cdot \widetilde{\mathbf{e}}_2)^T \cdot \widetilde{\mathbf{w}} = 0. \tag{2.19}$$

From that, the transformation $\mathbf{B}$ is given by the eigenvectors $\widetilde{\mathbf{e}}_1$ and $\widetilde{\mathbf{e}}_2$ of $\mathbf{Q}(\lambda)$ with the corresponding eigenvalues μ_1 and μ_2. The normals $\widetilde{\mathbf{n}}_1$ and $\widetilde{\mathbf{n}}_2$ of the extracted planes in which the reconstructed ellipses lay are then computed by

$$\begin{aligned} \widetilde{\mathbf{n}}_1 &= \sqrt{\mu_1} \cdot \widetilde{\mathbf{e}}_1 - \sqrt{-\mu_2} \cdot \widetilde{\mathbf{e}}_2 & (2.20)\\ \widetilde{\mathbf{n}}_2 &= \sqrt{\mu_1} \cdot \widetilde{\mathbf{e}}_1 + \sqrt{-\mu_2} \cdot \widetilde{\mathbf{e}}_2. & (2.21) \end{aligned}$$

The normals of the intersecting planes $\widetilde{\mathbf{n}}_1$ and $\widetilde{\mathbf{n}}_2$ are given in homogeneous coordinates. A point in homogeneous coordinates $\widetilde{\mathbf{w}}$ is within a plane $\widetilde{\mathbf{n}}$ if

$$\widetilde{\mathbf{n}}^T \widetilde{\mathbf{w}} = 0 \tag{2.22}$$

is fulfilled. As the normal to the plane is given in homogeneous coordinates, the fourth component is the distance to the coordinate origin $n_d \in \mathbb{R}$. Thus, the normal can be rewritten as

$$\widetilde{\mathbf{n}} = \begin{pmatrix} \mathbf{n} \\ n_d \end{pmatrix}. \tag{2.23}$$

Hence, Eq. (2.22) can be used to formulate a transformation matrix such that all points $\widetilde{\mathbf{w}}$ that lay within the plane are transformed to their corresponding 2-D plane coordinates $\widetilde{\mathbf{q}} \in \mathbb{R}^4$. This transformation is given by

$$\widetilde{\mathbf{q}} = \mathbf{T}_{\widetilde{\mathbf{n}}} \widetilde{\mathbf{w}} \tag{2.24}$$

with the resulting 2-D point given as $\widetilde{\mathbf{q}}^T = (u_q, v_q, 0, 1)^T$ and the 2-D plane coordinates u_q and v_q. The plane matrix $\mathbf{T}_{\widetilde{\mathbf{n}}} \in \mathbb{R}^{4 \times 4}$ is given as

$$\mathbf{T}_{\widetilde{\mathbf{n}}} = \begin{pmatrix} \mathbf{u}^T & 0 \\ \mathbf{v}^T & 0 \\ \mathbf{n}^T & n_d \\ \mathbf{0}^T & 1 \end{pmatrix}. \tag{2.25}$$

The vectors $\mathbf{u} \in \mathbb{R}^3$ and $\mathbf{v} \in \mathbb{R}^3$ are two arbitrary direction vectors of the plane and perpendicular to the normal. Every point that lays within the plane has its third component equal to 0. To calculate the intersection of a plane and a cone, both Eq. (2.1) and Eq. (2.24) need to be fulfilled. Thus, the intersection can be computed by

$$\mathbf{U} = \mathbf{T}_{\widetilde{\mathbf{n}}}^T \mathbf{Q} \mathbf{T}_{\widetilde{\mathbf{n}}}. \tag{2.26}$$

Given a point of the intersection $\widetilde{\mathbf{w}}$, the following equation holds

$$\widetilde{\mathbf{w}}^T \mathbf{U} \widetilde{\mathbf{w}} = 0. \tag{2.27}$$

As every point that within the plane has its third component equal to 0, the third row and third column of $\mathbf{U}$ can be ignored. The remaining entries are then used to compute the implicit parameters of the intersecting ellipse as

$$\mathbf{U} = \begin{pmatrix} a_1 & \frac{a_2}{2} & - & \frac{a_4}{2} \\ \frac{a_2}{2} & a_3 & - & \frac{a_5}{2} \\ - & - & - & - \\ \frac{a_4}{2} & \frac{a_5}{2} & - & a_6 \end{pmatrix}. \tag{2.28}$$

The coefficients $a_1, a_2, a_3, a_4, a_5, a_6 \in \mathbb{R}$ are the implicit parameters of an ellipse in the plane defined by $\widetilde{\mathbf{n}}$. A 2-D point $\mathbf{p}$ of this ellipse fulfills the following equation

$$\widetilde{\mathbf{p}} \begin{pmatrix} a_1 & \frac{a_2}{2} & \frac{a_4}{2} \\ \frac{a_2}{2} & a_3 & \frac{a_5}{2} \\ \frac{a_4}{2} & \frac{a_5}{2} & a_6 \end{pmatrix} \widetilde{\mathbf{p}}^T = 0. \tag{2.29}$$

Given the implicit parameters in this matrix notation as $\mathbf{U}_1$ for the first plane from Eq. (2.20) and $\mathbf{U}_2$ for the second plane from Eq. (2.21), it is not obvious which solution is the correct one. To find the correct solution, we recall the assumption that when positioned at the pulmonary vein, the circumferential mapping catheter can be approximated by a circle in 3-D space. Therefore, the semi-axes, ϕ and ψ, of each solution are obtained from $\mathbf{U}_1$ and $\mathbf{U}_2$, respectively.

Assuming that the correct solution in 3-D actually is a circle, the two semi-axes should be equal or at least be very close to each other. Therefore, we chose that solution $\hat{k}$ out of the two possible 3-D ellipses which is more circular. This is calculated by

$$\hat{k} = \arg\min_k |\phi_k - \psi_k|. \tag{2.30}$$

Once, the best solution $\hat{k}$ is found, the corresponding model points are calculated by sampling the ellipse using the parameters $\mathbf{U}_{\hat{k}}$ and transforming these points to 3-D points $\mathbf{m}_i \in \mathbb{R}^3$ by using $\mathbf{T}_{\widetilde{\mathbf{n}}_{\hat{k}}}^{-1}$.

2.2.2 Degenerated Ellipse Reconstruction

The method so far assumes that an ellipse is visible in both views. Depending on the viewing angle, this might not be true as an ellipse in 3-D space might be projected as a line. To detect the a degenerated ellipse in one of the two 2-D images, principal component analysis (PCA) is used. The principal axes and principal values of the 2-D input points are calculated before ellipse fitting. If one of the principal values is close to zero, it is considered as a degenerated case. If this is detected, two points $\mathbf{q}_1, \mathbf{q}_2 \in \mathbb{R}^2$ on the principal axis are computed. For practical reasons, these two points should have a certain distance between each other. In our case, twice the amount of the principal value was used.

By using the corresponding projection matrix $\mathbf{P} \in \mathbb{R}^{3\times 4}$, two rays in 3-D can be computed from the points $\mathbf{q}_1$ and $\mathbf{q}_2$. The optical center $\mathbf{o} \in \mathbb{R}^3$ can be computed from the projection matrix itself and the direction vector $\mathbf{d} \in \mathbb{R}^3$ can be computed by involving one of the 2-D points [Bros 09c, Bros 09d]. The rays corresponding to $\mathbf{q}_1$ and $\mathbf{q}_2$ are then given by

$$\mathbf{r}_1(\tau) = \mathbf{o} + \tau \cdot \mathbf{d}_1 \tag{2.31}$$
$$\mathbf{r}_2(\tau) = \mathbf{o} + \tau \cdot \mathbf{d}_2. \tag{2.32}$$

These two rays span the 3-D plane in which the elliptical part of the catheter lays. The normal of this plane can be computed by

$$\mathbf{n} = \mathbf{d}_1 \times \mathbf{d}_2. \tag{2.33}$$

To perform an intersection between a cone and a plane as shown in Subsection 2.2.1, the distance n_d to the origin is required. As the optical center $\mathbf{o}$ of the viewing projection is also within that plane, the distance can be calculated as

$$n_d = \mathbf{n}^T \mathbf{o}. \tag{2.34}$$

Finally, the reconstruction problem is reduced to calculating the intersection between a cone $\mathbf{Q}$ and a plane $\mathbf{n}$ without having to deal with two solutions. A summary of the presented circumferential mapping catheter reconstruction method is given in Structogram (2.1).

2.3 Evaluation and Results

For evaluation of our method, we performed simulation studies and experiments using a clinical biplane C-arm X-ray system.

2.3.1 Simulations

In our simulations, five circles in 3-D space were set up, each with a different position, orientation and diameter. These five 3-D circles were forward projected onto 2-D image planes for a set of C-arm projection angles. In the next step, these 3-D circles were reconstructed using the method presented above. The reconstruction was done for the C-arm position angles (RAO/LAO) $\in \{-90°, -60°, \ldots, 60°, 90°\}$ with (CRAN/CAUD) $= 0$. The latter was chosen to be 0 as this is the usual setup for electrophysiology procedures. In other words, the space of all used C-arm detector positions was subsampled in steps of 30°, given a minimum angular difference of 30° and a maximum difference of 150° between two C-arm views used

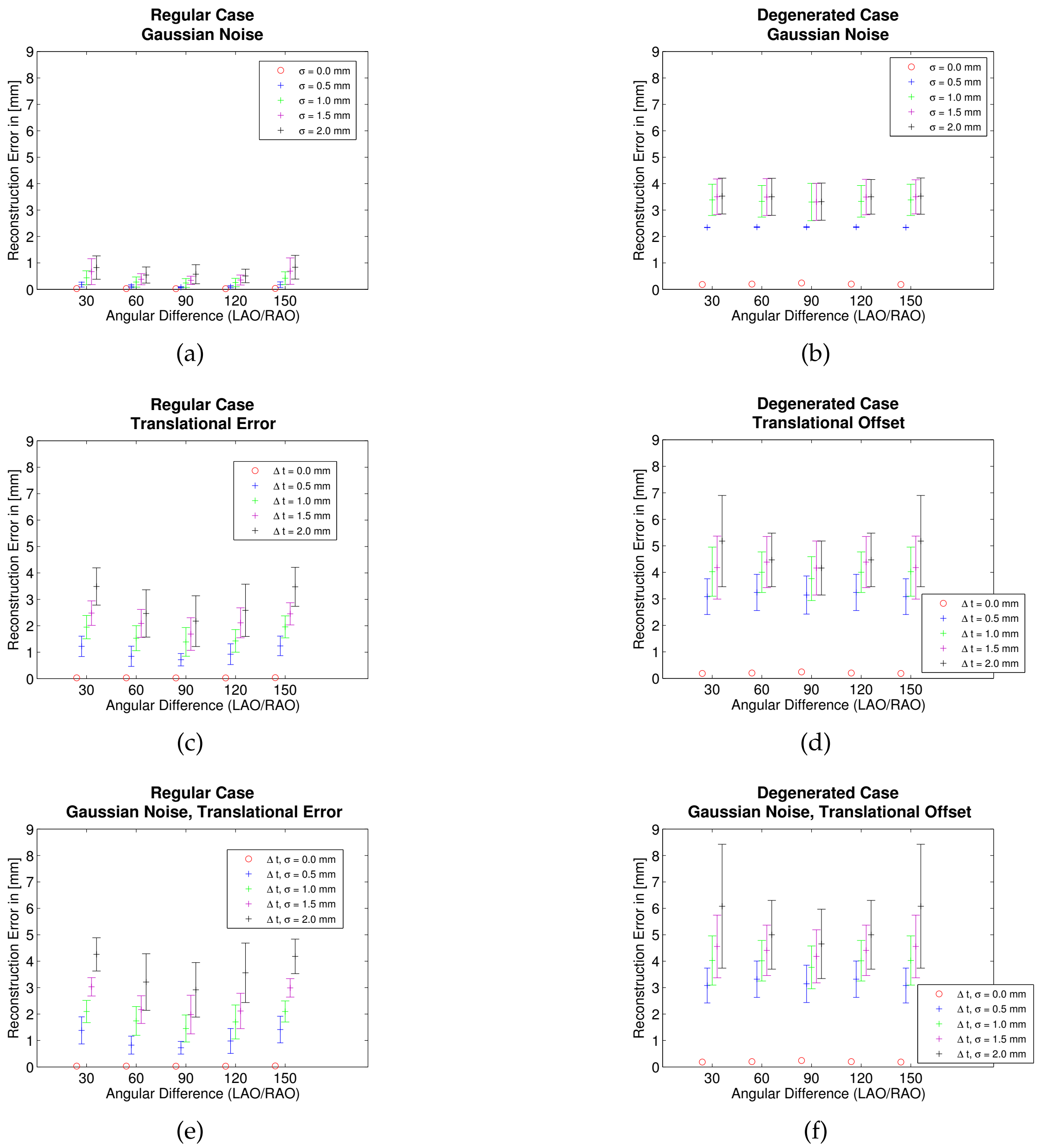

Figure 2.4: Simulation results for elliptical catheter model generation from biplane images. The error is given with its standard deviation. Two three kinds of errors were considered. The first type considers only Gaussian noise with a standard deviation of $\sigma \in \{0.0, 0.5, 1.0, 1.5, 2.0, 2.5\}$ mm added to the 2-D input points. According to the pixel spacing considered for the simulation, a 2-D noise of 1.0 mm equals to about 6 pixels on the image plane. The second type considers a translational offset in v-direction of $\Delta t \in \{0.0, 0.5, 1.0, 1.5, 2.0, 2.5\}$ mm to account for calibration errors. The third kind of error is considered to be a combination of both error types. The errors were calculated by averaging individual errors over the five circles reconstructed from the angulation considered. The results are given for the regular case in which ellipses are visible in both image planes, (a), (c), and (e), as well as for the degenerated case, (b), (d), and (f).

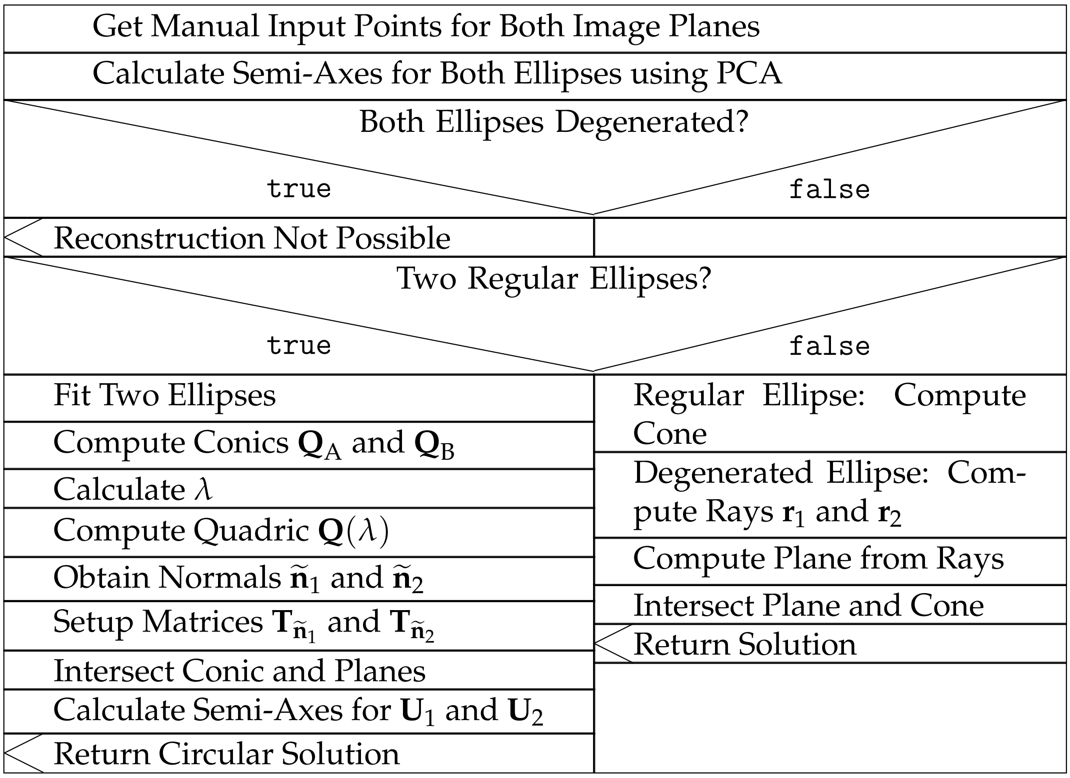

Structogram 2.1: Circumferential Mapping Catheter Reconstruction

for 3-D ellipse reconstruction by triangulation. The cases considering an angular difference of $0°$ and $180°$, respectively, were omitted during the simulation. Not all of these viewing angles are useful in a clinical environment but the results give a systematic evaluation of the accuracy of our reconstruction method. The overall error is calculated as the average distance between points on the original 3-D circle and their nearest-neighbor counterparts on the reconstructed circle. Four cases have been considered for evaluation. In the first case, we simply reconstructed a 3-D circle from the projection images not adding any noise to find out how the reconstruction method works in an idealized scenario. In the other experiments, we added Gaussian noise with zero mean and a standard deviation of up to 2.0 mm to the 2-D points before reconstructing the 3-D object. This is to simulate the potential noise in the mapping catheter point localization step. For a typical EP fluoroscopy image with a size of $1,024 \times 1,024$, 2.0 mm equals to about 12 pixels on the image plane. We also added a translational offset in one image plane of up to 2.0 mm, simulating the potential relative shift in the mapping catheters detected in the two image planes. The relative shift between plane A and plane B images can be either due to the fact that a mapping catheter is not a thin line but of certain width, or because there is inaccuracy in the geometrical calibration between plane A and plane B. Finally, we simulated both Gaussian noise and translational offset. The results are summarized in Figure 2.4. The errors listed in the table were calculated by averaging individual errors over the five circles reconstructed from the biplane C-arm angulations considered. The general case refers to the situation where an ellipse was visible in both image planes. The degenerated case implies that there was

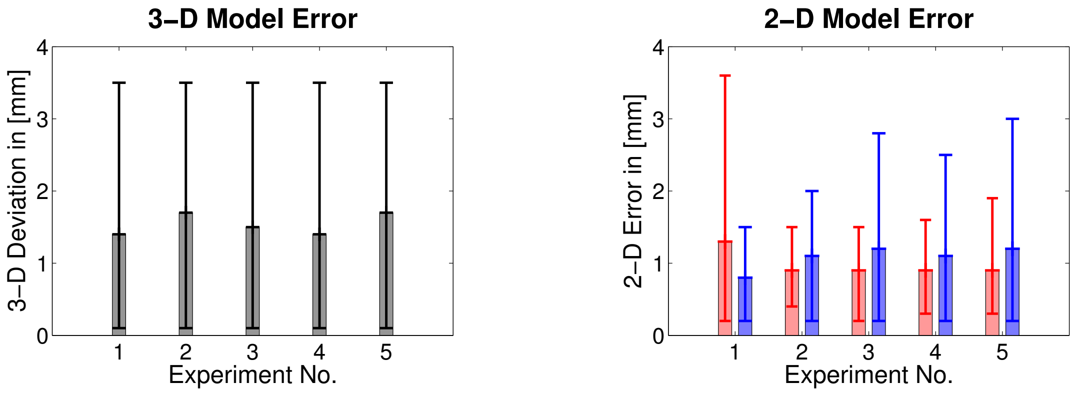

(a) (b)

Figure 2.5: Experimental results for 3-D model generation by triangulation from two views. Five experiments were carried out to evaluate the accuracy. The experimental setup, i.e., the position of the C-Arms and the position and orientation of the mapping catheter, was chosen to be as close as possible to a clinical setup. (a) The 3-D deviation represents the average distance between the reconstructed catheter to a manually outlined catheter in a 3-D data set. The minimum and maximum deviation is also presented. On average over all five experiments a model generation error of 1.5 mm was achieved. (b) The 2-D deviation represents the mean deviation of the projected 3-D model into each image plane from the original 2-D segmentation. The minimum and maximum deviation is also presented. An average deviation over all five experiments of 1.0 mm for plane A and 1.1 mm for plane B was achieved.

one ellipse in one view, while it collapsed to a line in the other view. The projection matrices for the simulation were computed as described in [Bros 09c, Bros 09d].

2.3.2 Experimental Results

To further validate our approach, we acquired biplane fluoroscopic images of a static catheter from different viewing directions and compared the 3-D reconstruction results to a 3-D data set reconstructed using C-arm CT on the same system. C-arm CT involved X-ray data acquisition on an AXIOM Artis dBA biplane system (Siemens AG, Forchheim, Germany). First, the A-plane performed a partial circle scan around the experimental setup. Then, a 3-D data set was reconstructed (*syngo* DynaCT 5sDR, 133 images of size $1,024 \times 1,024$ pixels, pixel spacing 0.1725 mm/pixel, source-detector-distance of 1,200 mm, Siemens AG, Healthcare Sector, Forchheim, Germany). The system was calibrated using the method presented in [Roug 93]. The 3-D coordinates of the circumferential mapping catheter were manually obtained from the 3-D volume and compared to the 3-D reconstruction results obtained from biplane views. To mimic a clinical setup, we varied only the primary angle (LAO/RAO), as it would be during an EP procedure. The secondary angle (CRAN/CAU) was kept constant. The experimental results for catheter model generation are given in Figure 2.5. The 3-D model deviation is mostly influenced by the position and the size of the reconstructed catheter model.

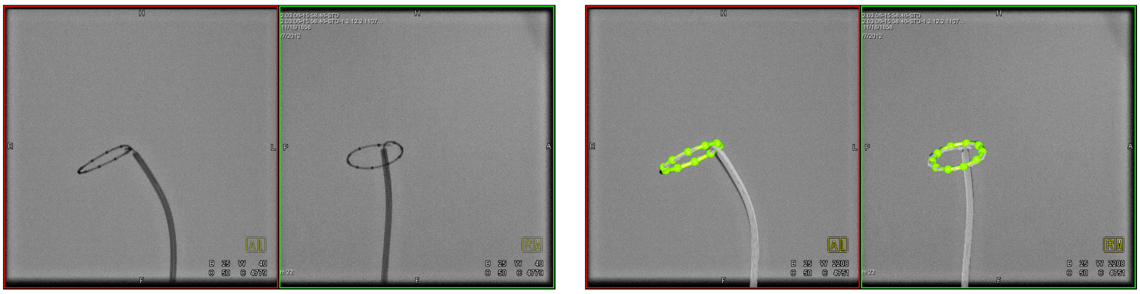

(a) (b)

Figure 2.6: Experiment of 3-D elliptical catheter reconstruction from two views. (a) Original fluoroscopic images. (b) The reconstructed catheter model is forward projected onto the fluoroscopic images.

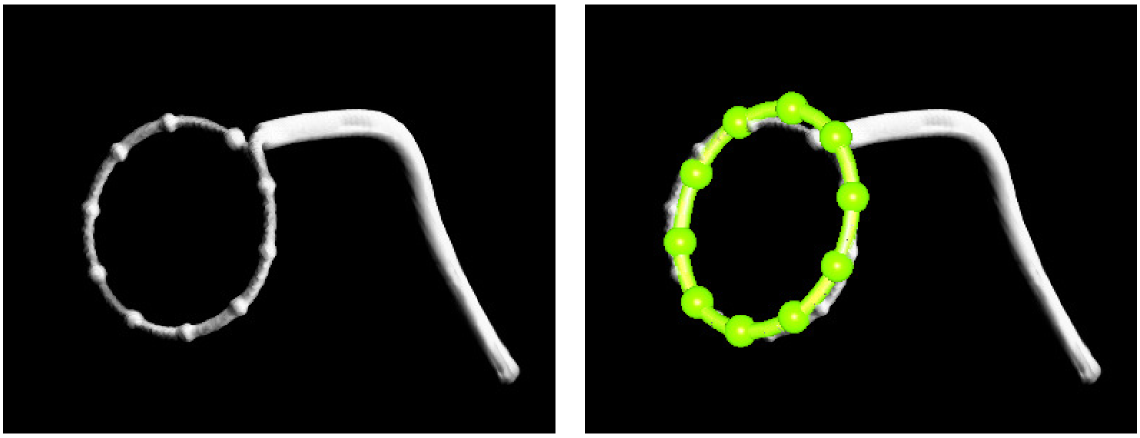

(a) (b)

Figure 2.7: Experiment of 3-D elliptical catheter reconstruction from two views. (a) C-arm CT of the catheter (*syngo* DynaCT, Siemens AG, Healthcare Sector, Forchheim, Germany). (b) Reconstructed ellipse together with the C-arm CT.

2.4 Discussion and Conclusions

Our simulation results show that 3-D reconstruction is very accurate under ideal conditions, but the error increases noticeably when there is noise, see Figure 2.4. Put differently, 3-D ellipse reconstruction from two views is very sensitive to noise in the 2-D points of the detected ellipse, in particular when a translational error is present. To deal with this problem, high-precision ellipse detection and geometrical calibration between plane A and plane B is required for initial model generation in the general case. From our experiments, we conclude that the 2-D model deviation is moreover influenced by the shape of the catheter in the 2-D fluoroscopic images. If the catheter can not be approximated well by an ellipse, a larger model deviation occurs. The 3-D error is almost constant and shows only little variation. The variation in the mean error represents slight shift of the reconstructed 3-D model with respect to the manual segmentation. The maximum error indicates that the size of the ellipse might not be correct reconstructed, but is also

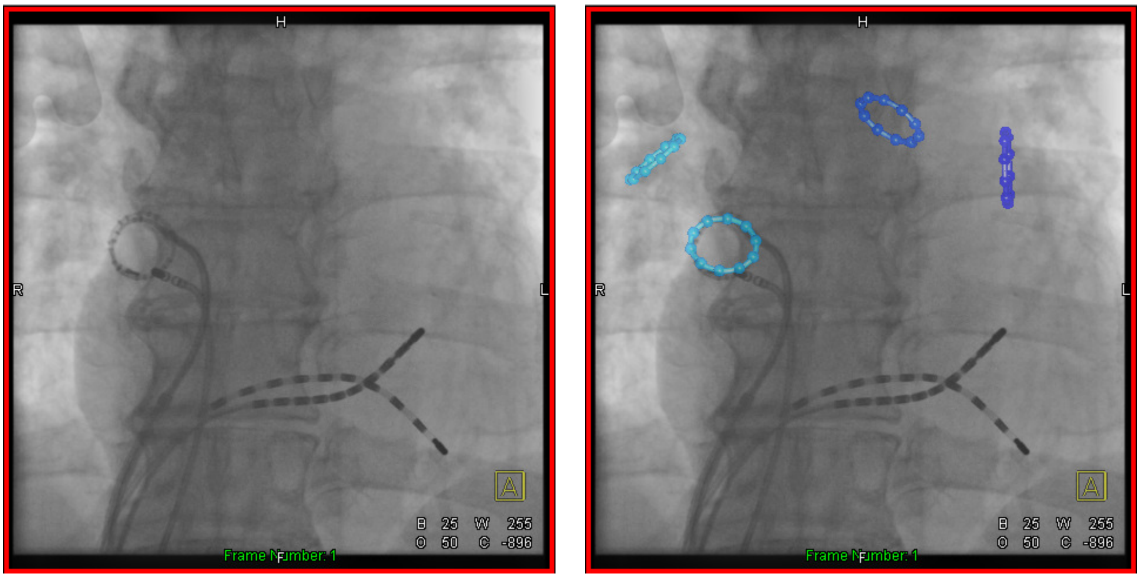

(a) (b)

Figure 2.8: Reconstructed ellipses representing the ostia of the pulmonary veins. (a) Fluoroscopic image without the reconstructed ellipses. (b) Reconstructed ellipses from two views overlaid onto fluoroscopic images. The ellipses were reconstructed from positions of the circumferential mapping catheter positioned at the ostia of the pulmonary veins.

influenced by a shift of the 3-D catheter model. Visual inspection of the forward projected 3-D catheter model onto the fluoroscopic images can be used to verify this, see Figure 2.6. A visual comparison of the 3-D catheter and a C-arm CT is given in Figure 2.7. The results of the simulations and the experiments indicate that the the assumption to chose the more circular solution is valid. In particular, the results of the experiments involving a real catheter as shown in Figure 2.5 support this. The reconstruction of the circumferential mapping catheter can also be used as guidance when no pre-operative 3-D data set is available. The mapping catheter can be positioned as the four ostia of the pulmonary veins and the reconstructed catheters can be overlaid onto the fluoroscopic images. In such a case, the reconstructed ellipses can be used to help the physician orientate himself during the procedure. This idea was presented in [Koch 11, Koch 12]. An illustration is given in Figure 2.8.

CHAPTER 3

Cryo-Balloon Catheter Reconstruction

The use of radio-frequency catheters bears a certain risk for the patient [Calk 07]. To this end, new catheters are being developed. Some of these catheters are so-called single-shot-devices. The idea is to isolate one pulmonary vein with a single application [Avit 03, Bell 07]. One example of such a device is the cyro-balloon catheter. Unfortunately, there is currently no guidance available to support these tools. In this chapter, a method to reconstruct a cryo-balloon catheter from two views is presented. This chapter is the result of the Bachelor Thesis of Andreas Kleinoeder [Klei 11a]. Parts of this work have been published in [Klei 11b, Bour 12b].

3.1 Motivation

Two risk factors of the current radio-frequency catheter ablation approach are pulmonary vein stenosis and esophageal fistula. To reduce these risks, cryo-balloon catheter ablation techniques can be used [Avit 03, Bell 07]. Cryo-balloon catheters perform the isolation of a pulmonary vein by freezing the tissue at the ostium. Unfortunately, current navigation tools do not provide tools to localize and visualize cryo-balloon catheters in 3-D. In our approach, the catheter is modeled as a sphere in 3-D. Methods to reconstruct ellipsoids either require three views [Ma 96] or additional 3-D information [Wije 06a], both is not available in our case. A method for sphere reconstruction has already been proposed in [Wije 06b], but it turns out to be rather sensitive to noise. This is why we present a novel method to reconstruct a cryo-balloon catheter from two views. It is well suited to compute a 3-D model, even in the presence of noise. Used as part of a fluoroscopic overlay image for augmented fluoroscopy applications, we expect that our method can further increase the safety and effectiveness of the cryo-balloon ablation approach.

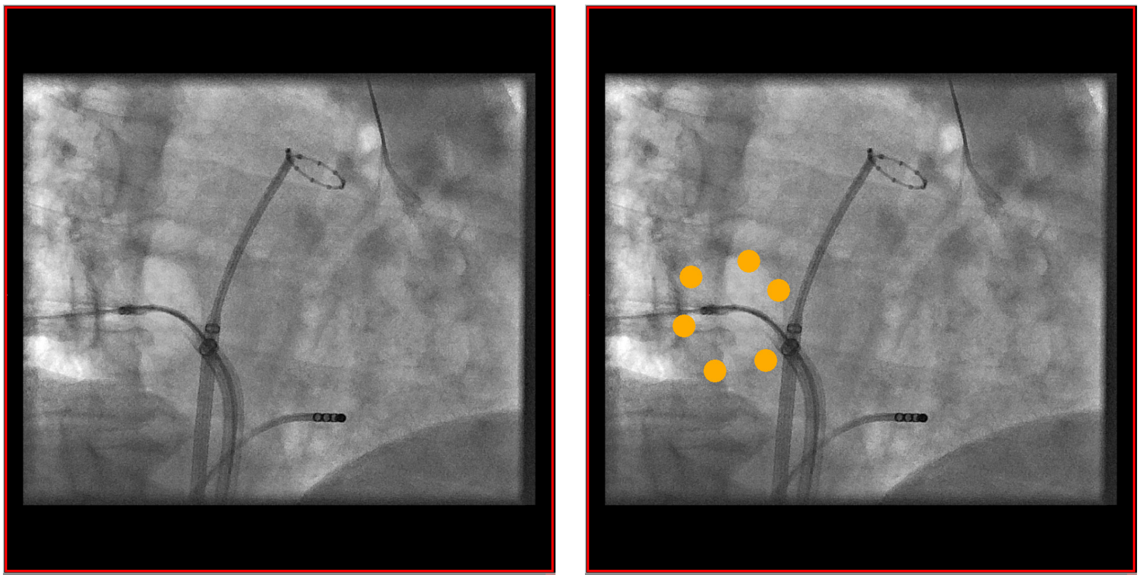

(a) (b)

Figure 3.1: (a) The original fluoroscopic image during a regular atrial fibrillation procedure using a cryo-balloon catheter. (b) The manually selected points of the balloon-catheter are superimposed onto the live fluoroscopic image (orange).

In the next section, the sphere reconstruction is explained. In the third section, the evaluation and the results are presented. In the final section, the approach is discussed and the conclusions are given.

3.2 Reconstruction Method

A method for sphere reconstruction was proposed in [Wije 06b]. Our work closely follows this method but deviates in two steps that improve the accuracy of the reconstruction method. In the first step, the reference method used PCA for ellipse fitting. Our method uses the method proposed in [Hali 98]. In the second step, the method in [Wije 06b] used two points to determine the radius of the sphere. We propose to use about 100 points to get a good estimate of the radius.

As input, manually selected 2-D points on the boundary of the balloon-catheter in both views are needed, see Figure 3.1 for an example of a single view. One point in image plane is denoted as $\mathbf{p}_A \in \mathbb{R}^2$ and as $\mathbf{p}_B \in \mathbb{R}^2$ in image plane B, respectively. Two-dimensional ellipses are fitted to the 2-D input points according to [Hali 98], resulting in the implicit ellipse parameters given in matrix representation as $\mathbf{C}_\mathrm{A}$ for image plane A and $\mathbf{C}_\mathrm{B}$ for image plane B, respectively. The method in [Hali 98] uses a least-squares fitting approach with an additional constraint that ensures an elliptical solution. Using the implicit ellipse parameters, 3-D cones $\mathbf{Q}_A, \mathbf{Q}_B \in \mathbb{R}^{4\times4}$ can be calculated by incorporating the projection matrices $\mathbf{P}_A, \mathbf{P}_B \in \mathbb{R}^{3\times4}$ [Bros 09a, Bros 10b]

$$\mathbf{Q}_A = \mathbf{P}_A^T \mathbf{C}_A \mathbf{P}_A \tag{3.1}$$
$$\mathbf{Q}_B = \mathbf{P}_B^T \mathbf{C}_B \mathbf{P}_B. \tag{3.2}$$

The camera center together with the corresponding ellipse yields a cone in 3-D space. Now, the main axis of the cone, spanned by the camera center and the projected ellipse, is calculated. In the following, we present the calculation only for plane A. The 3-D cones have a structure as follows

$$\mathbf{Q}_A = \begin{pmatrix} \mathbf{Q}_A^+ & \mathbf{a}_A \\ \mathbf{a}_A^T & \chi_A \end{pmatrix} \tag{3.3}$$

with the left upper diagonal sub-matrix $\mathbf{Q}_A^+ \in \mathbb{R}^{3\times3}$, the vector $\mathbf{a}_A \in \mathbb{R}^3$ and the scalar value $\chi_A \in \mathbb{R}$. If a cone has its tip at the origin of the coordinate system and its main axis aligns with one of the coordinate axes, we get [Wije 06b]

$$\mathbf{a}_A = \mathbf{0} \tag{3.4}$$
$$\chi_A = 0. \tag{3.5}$$

To align an arbitrary cone with the coordinate system, we have to find a transformation

$$\mathbf{T}_A = \begin{pmatrix} \mathbf{R}_A & \mathbf{t}_A \\ \mathbf{0}^T & 1 \end{pmatrix} \tag{3.6}$$

with the rotation $\mathbf{R}_A \in \mathbb{R}^{3\times3}$ and the translation $\mathbf{t}_A \in \mathbb{R}^3$. The transformed cone $\hat{\mathbf{Q}}_A \in \mathbb{R}^{4\times4}$ is then given by [Wije 06b]

$$\hat{\mathbf{Q}}_A = \mathbf{T}_A^T \mathbf{Q}_A \mathbf{T}_A \tag{3.7}$$
$$= \begin{pmatrix} \mathbf{R}_A^T \mathbf{Q}_A^+ \mathbf{R}_A & \mathbf{R}_A^T (\mathbf{Q}_A^+ \mathbf{t}_A + \mathbf{a}_A) \\ (\mathbf{t}_A^T \mathbf{Q}_A^+ + \mathbf{a}_A^T) \mathbf{R}_A & \mathbf{t}_A^T \mathbf{Q}_A^+ \mathbf{t}_A + 2\mathbf{a}_A^T \mathbf{t}_A \end{pmatrix}. \tag{3.8}$$

Considering the first element of $\hat{\mathbf{Q}}_A$, the rotation matrix $\mathbf{R}_A$ is given by the matrix of eigenvectors of $\mathbf{Q}_A^+$ which is computed by using singular value decomposition (SVD) [Golu 65]. Using the upper right element of $\hat{\mathbf{Q}}_A$, the translation is given by

$$\mathbf{t}_A = -\left(\mathbf{Q}_A^+\right)^{-1} \mathbf{a}_A. \tag{3.9}$$

Now, that the rotation and translation have been determined, we can intersect the axes of both cones to find the midpoint of the sphere. It is known that the axis of a normalized cone corresponds to the z-axis [Bron 01]. Hence, we can determine the main axis $\mathbf{d}_\mathrm{A} \in \mathbb{R}^3$ of each cone by rotating the z-axis with the rotation matrix $\mathbf{R}_\mathrm{A}$

$$\mathbf{d}_\mathrm{A} = \mathbf{R}_\mathrm{A} \cdot \begin{pmatrix} 0 \\ 0 \\ 1 \end{pmatrix}. \tag{3.10}$$

The cone's axis in 3-D space is represented by a line, using a point and a direction. The translation vector $\mathbf{t}_\mathrm{A}$ corresponds to the apex of the cone and hence is a fixed point on the line. Vector $\mathbf{d}_\mathrm{A}$ describes the direction of the cone's main axis. Computing the translation vector $\mathbf{t}_\mathrm{B}$ and the main axis $\mathbf{d}_\mathrm{B}$ for image plane B as well, the center of the sphere $\mathbf{w}_c \in \mathbb{R}^3$ should lay on the following rays

$$\mathbf{r}_A(\tau_1) = \mathbf{t}_\mathrm{A} + \tau_1 \mathbf{d}_\mathrm{A} \tag{3.11}$$

$$\mathbf{r}_B(\tau_2) = \mathbf{t}_\mathrm{B} + \tau_2 \mathbf{d}_\mathrm{B} \tag{3.12}$$

with the scalar values $\tau_1, \tau_2 \in \mathbb{R}$ as line parameters. These two lines are supposed to intersect with each other at the center of the sphere $\mathbf{w}_c$. Therefore, the ray parameters τ_1 and τ_2 can be calculated by using SVD. In a practical setup, the 2-D input points might not be perfect, thus the lines need not necessarily intersect. The closest point between these two lines is computed as center of the sphere by

$$\mathbf{w}_c = \frac{1}{2}(\mathbf{t}_\mathrm{A} + \tau_1 \mathbf{d}_\mathrm{A} + \mathbf{t}_\mathrm{B} + \tau_2 \mathbf{d}_\mathrm{B}). \tag{3.13}$$

To calculate the radius of the reconstructed sphere, each cone is intersected with a 3-D plane parallel to the image plane at the position of the calculated center $\mathbf{w}_c$. This method is part of the 3-D ellipse reconstruction method Subsection 2.2.1. The plane for the intersection is calculated to be parallel to the image plane and has to pass through the center of the sphere $\mathbf{w}_c$. The intersection of both cones with their corresponding planes yields a set of $W \in \mathbb{Z}$ points $\mathbf{w}_i \in \mathbb{R}^3$. As all these points should lay on the sphere, their distance to the center should be equal to the radius of the sphere $r_s \in \mathbb{R}$. As noise in the input data, in particular the 2-D points, and calibration errors propagate through the presented algorithm, they might be slightly off. An ellipse fitting was used which leads to elliptical cones and not circular cones. Therefore, the intersection of a plane and an elliptical cone yields an ellipse in 3-D, similar to the ellipse reconstruction in Chapter 2. As a sphere is desired as output of this reconstruction algorithm, the mean distance of the computed points $\mathbf{w}_i$ is considered to be the best approximation for the radius. To this end, the radius of the sphere r_s is computed by

$$r_s = \frac{1}{W} \sum_i ||\mathbf{w}_c - \mathbf{w}_i||_2. \tag{3.14}$$

Given the center $\mathbf{w}_c$ and the radius r_s, the sphere is reconstructed in 3-D. A summary of the presented cryo-balloon catheter reconstruction method is given in Structogram (3.1).

3.3 Evaluation and Results

For evaluation of our method, we performed a simulation study and experiments using a clinical biplane C-arm X-ray system.

Get Manual Input Points for Both Image Planes
Calculate Ellipses $\mathbf{C}_\text{A}$ and $\mathbf{C}_\text{B}$
Calculate Cones $\mathbf{Q}_\text{A}$ and $\mathbf{Q}_\text{B}$
Compute $\mathbf{t}_A$ and $\mathbf{t}_B$
Compute $\mathbf{d}_A$ and $\mathbf{d}_B$
Define Rays $\mathbf{r}_A$ and $\mathbf{r}_B$
Obtain Center Point $\mathbf{w}_c$ by Ray Intersection
Compute Planes through $\mathbf{w}_c$ parallel to Image Planes
Intersect Cones with Planes
Use Sample Points to Compute Radius r_s
Return $\mathbf{w}_c$ and r_s

Structogram 3.1: Cryo-Balloon Catheter Reconstruction

3.3.1 Simulations

For the simulation, we computed 500 spheres each at different positions in 3-D space within a maximum distance to the center of the volume of 150 mm and with a radius between 5 mm and 15 mm. Commercially available cryo-balloons have a diameter of either 23 mm or 28 mm. The simulation was performed using ideal C-arm projection matrices as described in [Bros 09c, Bros 09d]. The C-arm positions were chosen to be 90^o apart which is similar to clinical setups in electrophysiology labs. The spheres were forward projected onto the image planes assuming projection images of $1,024 \times 1,024$ pixels with a pixel spacing of 0.308 mm/pixel and a source-detector-distance of 1217 mm. The convex hull of the projection was computed and used as 2-D input for the reconstruction method. We compared our approach to the reference method in [Wije 06b]. Apart from that, Gaussian noise with a standard deviation $\sigma \in \{0\text{ mm}, 0.5\text{ mm}, 1.0\text{ mm}, 1.5\text{ mm}, 2.0\text{ mm}, 2.5\text{ mm}, 3.0\text{ mm}, 3.5\text{ mm}, 4.0\text{ mm}\}$ was added to the 2-D input data before reconstruction to simulate detection errors. The error in the simulations was calculated as the average 3-D distance between the reconstructed sphere and the reference sphere. To this end, $W = 100$ points $\mathbf{w}_{s,i} \in \mathbb{R}^3$ of the original sphere with radius r_s and center $\mathbf{w}_c$ can be calculated. The same number of 3-D points were calculated as $\hat{\mathbf{w}}_{s,i} \in \mathbb{R}^3$ from the estimated center $\hat{\mathbf{w}}_c$ and the estimated radius $\hat{r}_s$. Note that the angles for the point calculations have to be sampled in the same equidistant intervals such that the calculated points correspond to each other. After the points have been calculated, the average 3-D distance $\varepsilon_s \in \mathbb{R}^3$ between the original sphere and the reconstructed sphere can be calculated by

$$\varepsilon_s = \frac{1}{W} \sum_i ||\mathbf{w}_{s,i} - \hat{\mathbf{w}}_{s,i}||_2. \tag{3.15}$$

The advantage of this definition is, that radius and center of the sphere are both considered for this error value. Intuitively this definition can be imagined as the difference between the spheres original surface and the reconstructed surface. The results are shown in Figure 3.2.

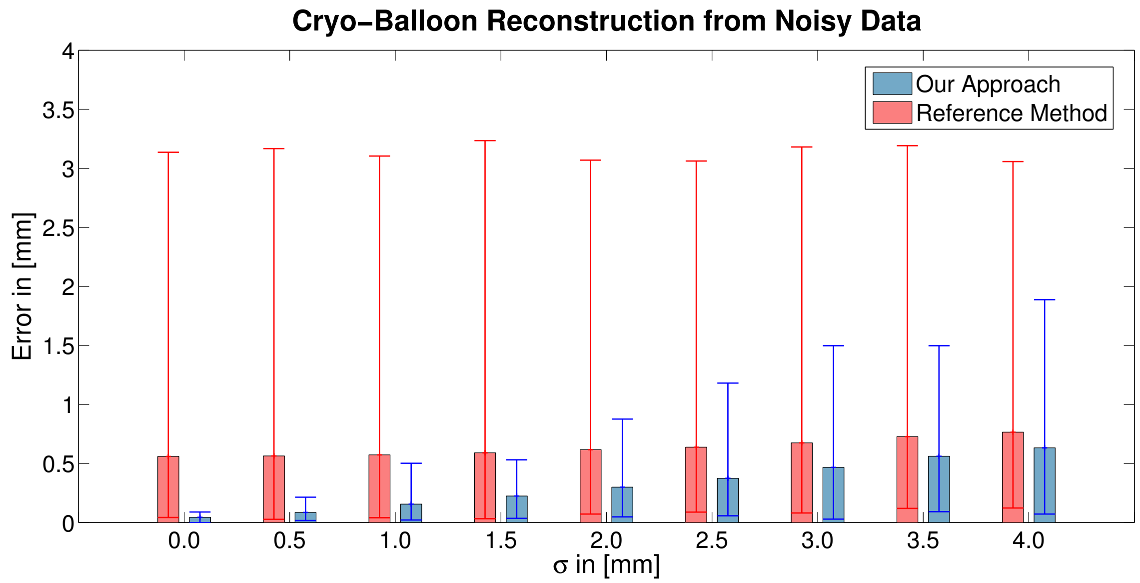

Figure 3.2: Simulation results of our reconstruction approach in comparison to the reference method [Wije 06b]. To disturb the input data, Gaussian noise with a standard deviation $\sigma \in \{0\text{ mm}, 0.5\text{ mm}, 1.0\text{ mm}, 1.5\text{ mm}, 2.0\text{ mm}, 2.5\text{ mm}, 3.0\text{ mm}, 3.5\text{ mm}, 4.0\text{ mm}\}$ was used.

Besides the effect of noise, the angular difference between the two projections was investigated. To this end, the standard deviation of the Gaussian noise was fixed to $\sigma = 2.0$ mm. The C-arm angulations were chosen to mimic the regular setup in EP laps in which (LAO/RAO) is variable and (CRAN/CAUD) is usually fixed to 0^o. In a clinical setup, the angular difference between image plane A and image plane B is close to 90^o. For our simulation, we have varied the absolute angular difference between the two C-arms from 30^o to 150^o in steps of 15^o. The results are shown in Figure 3.3.

3.3.2 Experimental Evaluation

Experimental evaluation was performed in two stages. In the first stage, sphere-shaped objects were used. In the second stage, a real cryo-balloon catheter was available.

Both stages were performed using a real C-arm biplane system (Siemens AG, Healthcare Sector, Forchheim, Germany). In the first stage, sphere-like objects were considered. Therefore, balls of different kinds were used for the experimental evaluation. These included a golf ball, a baseball, a table tennis ball, a squash ball and three handballs. As handballs are available in different sizes, the enumeration behind each handball in the tables states the official size. The results obtained from the reconstruction were compared with multiple measurements of a C-arm CT of the considered object [Noo 07, Rohk 09]. For reconstruction, a commercially available software was used (*syngo* DynaCT 5sDR, 126 images of size $1,024 \times 1,024$ pixels, pixel spacing 0.1725 mm/pixel, source-detector-distance of 1,200 mm, Siemens AG, Healthcare Sector, Forchheim, Germany). For each C-arm CT, ten measure-

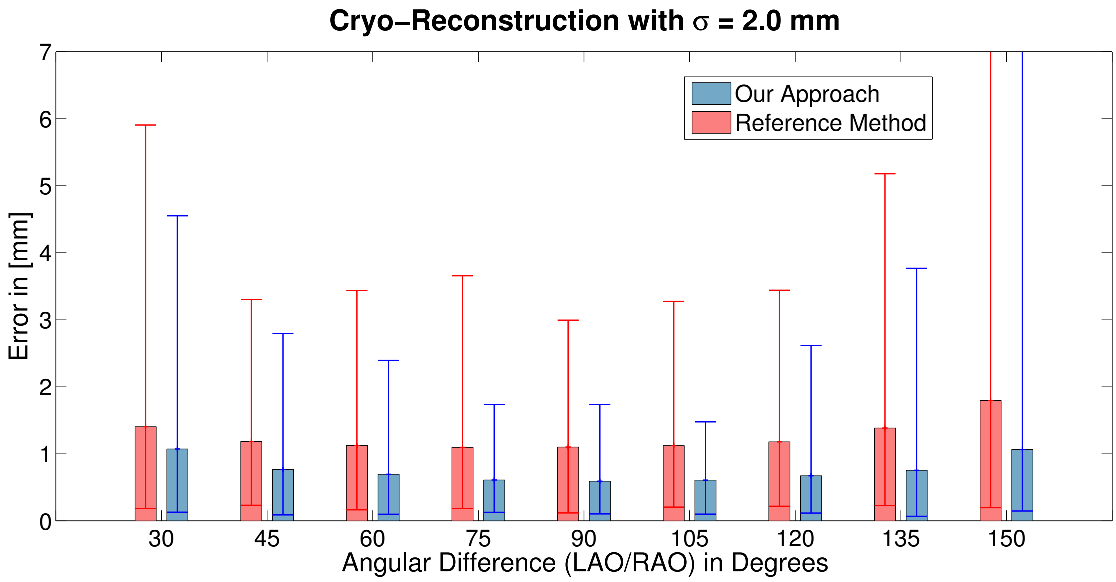

Figure 3.3: Simulation results of our reconstruction approach in comparison to the reference method [Wije 06b]. The input data was disturbed by Gaussian noise with a standard deviation of $\sigma = 2.0$ mm. The maximum error of the reference method was 17.68 mm. The maximum error of our approach was 7.78 mm.

ments of the object diameters were made. The mean of the measurements divided by 2 yields the radius for the comparison. The standard deviation of the measured diameters was in all cases below 1.2 mm. Since the determination of the balls real position in 3-D space with respect to the C-arm system could not be acquired, the evaluation only considers the radii of the spheres as error measurement. The fluoroscopic images used for the reconstruction were of size $1,024 \times 1,024$ pixels, with a pixel spacing of 0.308 mm/pixel and a source-detector-distance of 1,197 mm. The mean error of the proposed reconstruction method is 0.32 mm. The results of the experiments are given in Table 3.1. The objects used for evaluation are shown in Figure 3.4.

In the second stage of the experimental evaluation, a cryo-balloon was reconstructed to gather more applicable results regarding the purpose of the algorithm. The balloon catheter was manually inflated with air, instead of liquid nitrogen, and placed in a small bowl. To make the contour of the catheter visible, the bowl was filled with a mixture of water and contrast agent. The maximal diameter of the catheter is stated to be 28.0 mm leading to a reference radius of 14.0 mm. In the experiment, the catheter was reconstructed six times. The results are given in Table 3.2. The average reconstruction error was 0.26 mm. The images used for reconstruction were of size $1,024 \times 1,024$ pixels, with a pixel spacing of 0.173 mm/pixel and a source-detector-distance of 1,021 mm. On average, the C-arm CT measurements yielded a radius of 9.86 mm. The measurements for the gold-standard diameters were repeated 22 times to obtain reliable results. The standard deviation of the measurements was 1.1 mm. The location to determine the diameter was chosen to be orthogonal to the guidewire of the catheter as this is the part of the balloon that touches the left atrial wall. It is noticeable, that in each catheter recon-

Experimental Evaluation of Sphere Reconstruction				
	Golf	Baseball	T-Tennis	Squash
C-arm CT	19.23 mm	34.74 mm	19.16 mm	20.08 mm
Reconstruction	18.86 mm	34.61 mm	18.77 mm	19.59 mm
Error	0.36 mm	0.13 mm	0.39 mm	0.49 mm
	Handball 0	Handball 1	Handball 2	
C-arm CT	60.09 mm	80.46 mm	86.43 mm	
Reconstruction	59.82 mm	79.93 mm	86.53 mm	
Error	0.27 mm	0.53 mm	0.10 mm	

Table 3.1: Radius comparison between the reference C-arm CT values and the reconstructed radius.

Experimental Evaluation of Cryo-Balloon Reconstruction						
#	1	2	3	4	5	6
C-arm CT	9.86 mm	9.86 mm	9.86 mm	9.86 mm	9.86 mm	9.86 mm
Reconstruction	9.25 mm	9.84 mm	10.18 mm	10.16 mm	10.07 mm	9.99 mm
Error	0.61 mm	0.02 mm	0.32 mm	0.30 mm	0.21 mm	0.13 mm

Table 3.2: Cryo-Balloon reconstructions in [mm]. Comparison between reconstructed radius and cryo-balloon radius measured in C-arm CT. The average reconstruction error is 0.26 mm.

struction and C-arm CT measure, the radius was calculated to be smaller than it should have been. This result might be explained by two factors. First of all, during the experiment the catheter might not have been fully inflated. Another point which falsifies the calculation is due to the fact, that the catheter is more likely to be ellipsoidal, especially when not completely inflated.

An illustration of the experiment is given in Figure 3.5. It shows the cryo-balloon catheter recorded from two different views, observable as the bright round contours. It can be seen, that the balloon catheter is not of perfect spherical shape. While one of the views shows an almost circular contour, the second one is slightly more elliptical and therefore only shows the maximum range of the catheter in one direction. During the radius calculation both views were considered. The minor axis of the elliptical part decreases the result of the radius during the cone-plane intersection. The reconstructed sphere is superimposed with the biplane images. It can be seen that the reconstructed sphere is well aligned with the contour of the balloon catheter in the pure X-ray view. As a 3-D example, a comparison between the original C-arm CT and one with the reconstructed sphere rendered into it is given as well. The position of the balloon catheter is not detected by the C-arm CT, because the catheter was filled with air so that no contrast agent could fill that region. It can be seen, that the reconstructed balloon catheter fits very well into the black gap of the reconstructed 3-D data set.

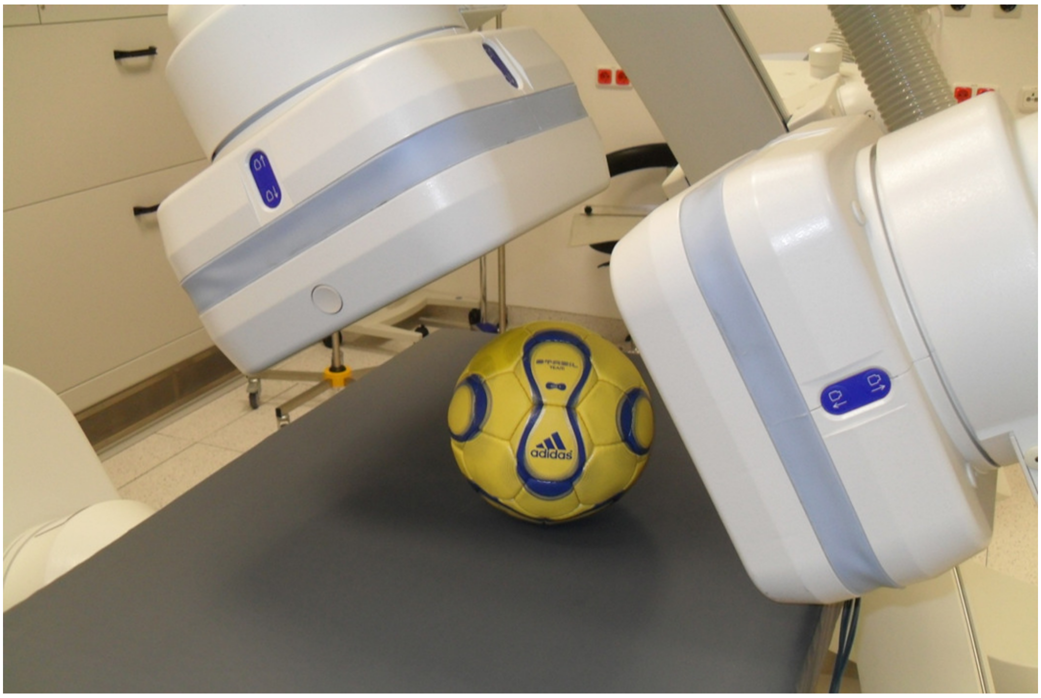

Figure 3.4: Example of a sphere-like object used for experimental evaluation of the sphere or cryo-balloon reconstruction. This setup with the C-arm 90^o degrees apart was used for the experiments.

3.4 Discussion and Conclusions

During the course of this work, we found our sphere reconstruction method from two views robust and easy to use. We contribute the better performance of our method to two factors. First, we do not use principal component analysis for ellipse fitting [Wije 05]. PCA is of advantage if many samples are present that facilitate a robust parameter estimate. In our case, we only require a few points set along object boundaries. Usually five to seven points are sufficient. In such a case, the PCA approach turns out to be very sensitive especially if the samples are not equally distributed along the object boundary. Second, we do not rely on only one or two boundary points, as proposed in [Wije 06b]. Instead, we use about 100 points to determine the radius of the sphere in 3-D. Thanks to these improvements, our 3-D reconstruction is more robust to noise.

From the results in Figure 3.3, it can be concluded that the best angular difference for reconstruction is 90^o. This is consistent with findings for point reconstruction from two views [Bros 09c, Bros 09d]. The high error for the difference of 150^o is due to relative position of the sphere to the cameras. As the cameras are positioned quite opposite to each other, the generated camera cones can happen to lay almost parallel to each other depending on the spheres position from the origin. In this geometrically position and combined with little noise, the calculations are complicated. For the reference method, the calculation of the frontier points to determine the radius gets very difficult. For our approach, the high error is due to the imprecise calculation of the sphere's midpoint. The cones' axes also are al-

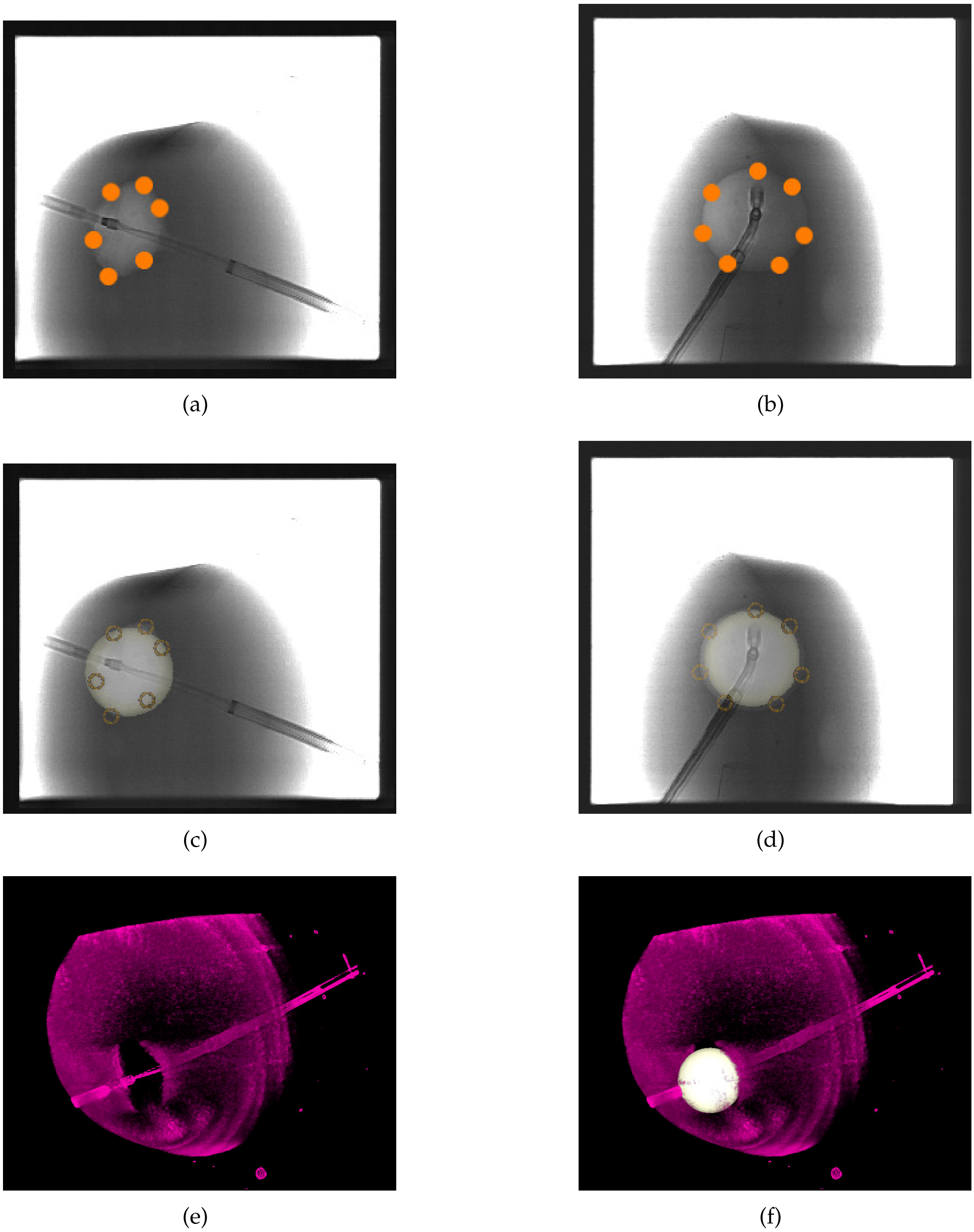

Figure 3.5: (a) Fluoroscopic image in plane A with manually selected 2-D points on the boundary of the cryo-balloon catheter. (b) The same as in (a) for image plane B. (c) The reconstructed sphere model is superimposed on the fluoroscopic. (d) The same is shown for plane B. (e) C-arm CT of a small bucket filled with contrast agent in which the inflated cryo-balloon catheter was placed. (f) The reconstruction of the catheter is shown together with the volumetric data set. For visualization, the volume data is colored in purple.

most parallel to each other. Because of noise and limited calculation accuracy, the cones' axes naturally will not intersect with each other. As mentioned before, the smallest distance between the two axes yields the midpoint. As a consequence, the calculation of the smallest distance between two almost parallel lines gets very difficult. This is why the error becomes large.

As the circumferential mapping catheter is more ellipsoidal shaped, the reconstruction as a sphere can only be seen as an estimate of the dimensions of the balloon catheter. Unfortunately, an ellipsoid reconstruction from two views is not easy to achieve [Ma 96, Wije 06a]. The first clinical trial have not shown to suffer from this [Bour 11b].

The proposed method is likely to be helpful during cryo-balloon catheter ablation procedures as it provides visual feedback to the physician, e.g., about previous balloon positions when multiple freezing treatments are applied to the same pulmonary vein. A clinical evaluation is required to get a better understanding of its utility for cryo-balloon catheter treatments. We expect that the use of our approach will further improve the safety and efficiency of this treatment option.

Part II

Tools for Cryo-Balloon Ablation

CHAPTER 4

AFiT - Atrial Fibrillation Ablation Planning Tool

As mentioned before, there are different catheters to perform atrial fibrillation ablation procedures. Recent studies have shown that the use of cryo-thermal balloon catheters reduce the risk of complications [Defa 11, Neum 08, Bour 10]. Unfortunately, there are currently no guidance tools that support these kind of catheters. To this end, we propose a first planning tool that enables physicians to plan their cryo-balloon ablation procedures. Our ***A**trial **Fi**brillation Ablation Planning **T**ool* (AFiT) provides the functionality to place catheter models of a cryo-balloon catheter and assess their fit to the pulmonary vein. Parts of this work have been published in [Bros 11a, Klei 12].

4.1 Motivation

The current minimally invasive approaches to treat atrial fibrillation typically rely on radio-frequency ablation catheters [Hais 94] or on cryo-balloon catheters [Avit 03, Bell 07]. The cryo-balloon ablation technique was introduced to reduce risks related to radio-frequency catheter ablation such as pulmonary vein stenosis and esophageal fistula [Defa 11, Neum 08, Bour 10]. If balloon catheters fit well to the anatomy of the left atrium, a contiguous circular lesion can be achieved very efficiently, thus, simplifying the procedure and speeding it up as well. A study published in 2008 including 346 patients showed that the use of the cryo-balloon catheter achieves long-term success while exposing the patient to only a minor risk of compilations [Neum 08]. These results are supported by a recent study including 117 patients [Defa 11]. Augmented fluoroscopy using a perspectively forward projected overlay representation of 3-D objects onto live fluoroscopic images has become a useful tool for navigation when performing ablation procedures [Bros 11e, De B 05, Ecto 08a, Ecto 08b]. Unfortunately, current navigation tools do not provide tools to localize and visualize cryo-balloon catheters

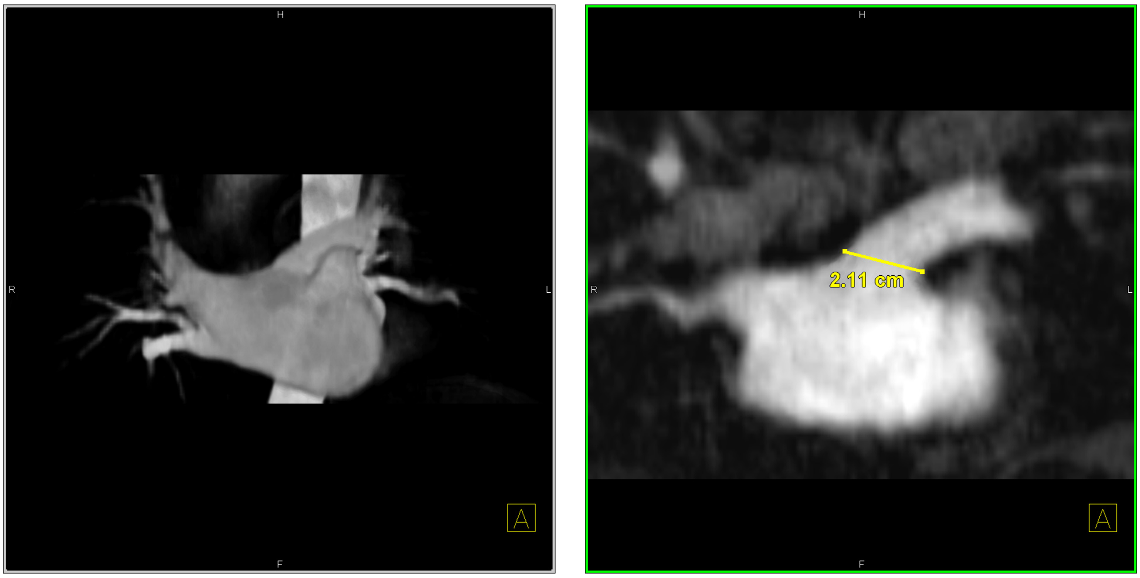

(a) (b)

Figure 4.1: (a) MRI volume data of the left atrium (b) Manual measurement of the diameter of the left superior pulmonary vein. In this case, the diameter was determined to be 2.11 cm.

in 3-D. A first approach to reconstruct a balloon-catheter during the procedure within a pre-operative data set was presented in Chapter 3. Commercially available cryo-balloons come in two different diameters, a 23 mm balloon and a 28 mm balloon [Furn 11]. It mainly depends on the patient's anatomy, especially the configuration of the left atrium and the pulmonary veins, which balloon to choose. Different methods are proposed how to assess which balloon should be used depending on measurements in pre-operative data sets. Most of the time, only the diameter of the pulmonary vein is estimated, see Figure 4.1 for an example. This measurement is cumbersome, and it may even be misleading. We propose to assess 3-D cryo-balloon positions within a pre-operative 3-D data set. Using our proposed method, we can provide information to the physician which catheter size is more likely to fit.

In the second section of this chapter, we briefly describe the standard procedure to determine the diameter of the pulmonary veins. In the third, we introduce our new approach using our atrial fibrillation ablation planning tool. In the last section we discuss the advantages and disadvantages of our approach. As the presented method is purely based on visualization, an objective evaluation could not be performed.

4.2 Default Assessment

A pre-operative data set is required to assess which cryo-balloon catheter type can be used. Commercially available products such as *syngo* InSpace EP (Siemens AG, Healthcare Sector, Forchheim, Germany) are capable of segmenting the left

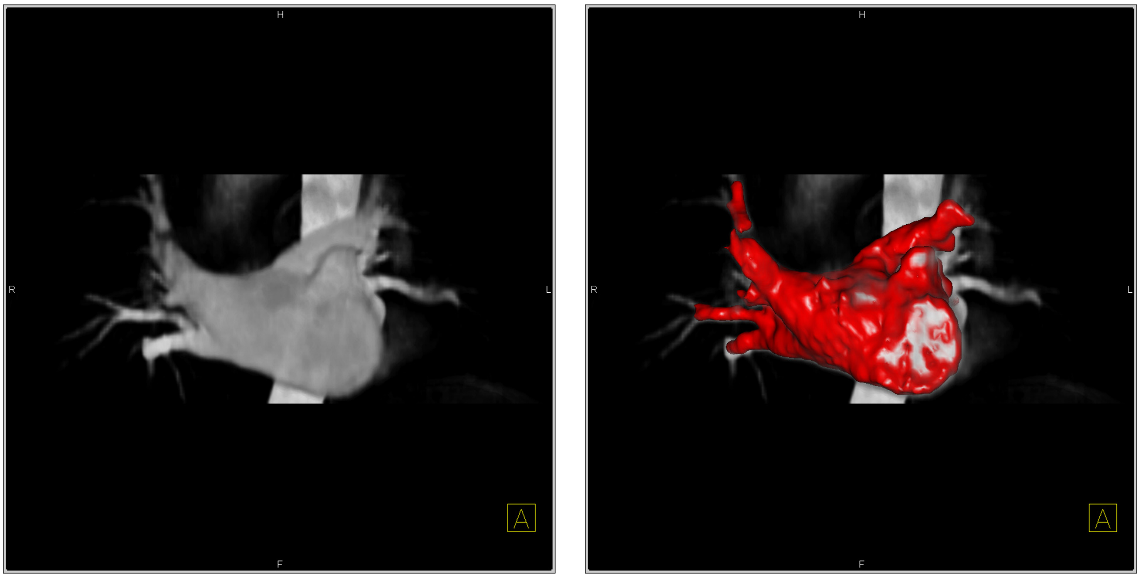

(a) (b)

Figure 4.2: (a) MRI volume data of the left atrium. (b) The same volume data set combined with the segmentation of the left atrium. The segmentation was performed using *syngo* InSpace EP (Siemens AG, Healthcare Sector, Forchheim, Germany).

atrium in pre-operative data sets such as CT [Blan 10], MRI [Miqu 03] or C-Arm CT [Prum 09, Stro 09], see Figure 4.2 for a segmented MRI. This segmentation can also be used to determine the diameter of the ostium of the pulmonary veins. The assessment can be performed by using the combination of the segmentation and the pre-operative data set, see Figure 4.3. Recently *'the ratio between the maximal and minimal PV ostial diameter and the angle between the PV longitudinal and the frontal body axis'* has been proposed to assess which balloon has to be chosen [Furn 11]. But this increases the time required for a physician to determine which catheters are required during the procedure. To reduce this amount of time for the assessment and to provide a better visual feedback, we propose to use a segmented left atrium, visualized in 3-D, and to place a 23 mm or a 28 mm balloon catheter at the ostium of the pulmonary vein to visually perform the assessment.

4.3 AFiT

In this section, we summarize the *Atrial **F**ibrillation **A**blation Planning **T**ool*. First, the visualization methods for the left atrium and the cryo-balloon are explained. Afterwards, some details on the positioning of the balloon and the carving view are presented.

4.3.1 Object Visualization

Left Atrium Visualization is achieved by loading and displaying a segmented 3-D mesh of the left atrium. In our case, *syngo* InSpace EP (Siemens AG, Healthcare

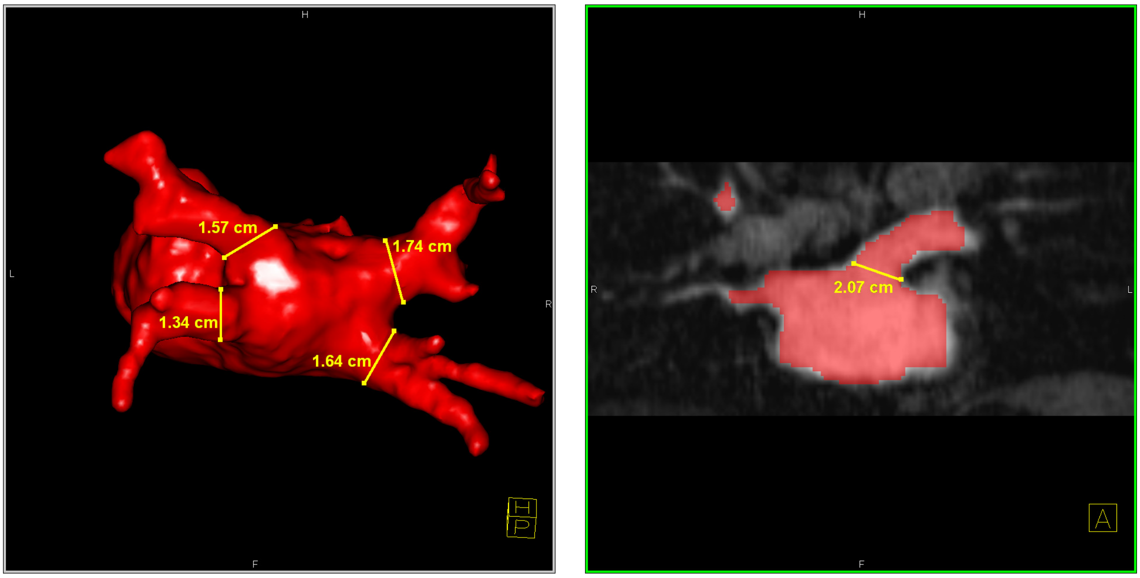

(a) (b)

Figure 4.3: (a) Assessment of the diameter of the four pulmonary veins by considering only the segmentation result. (b) Assessment of the diameter of one pulmonary vein by considering the combination of the segmentation and the pre-operative data set.

Sector, Forchheim, Germany) was used for segmentation. For testing of our software prototype, a MR volume data set with 63 slices and a matrix size of 256 $\times$ 256 was used. Each voxel of the volume was of size 1.03 mm $\times$ 1.03 mm $\times$ 1.62 mm and was represented by 9 Bit. The segmentation result is stored as indexed face set in a .xml format. The .xml file contains information about the position of the object's vertices and normals. Additionally, topological information about which vertices build a triangle may be stored. To be able to display the segmented LA, the indexed face set was read out from the file and stored to a vertex-buffer-object (VBO). The geometry information stored in an VBO is fast accessible and easy to update [Aken 08].

Depending on the usage of the data, the graphics card driver is optimizing the access and placement in the memory. Static data, e.g., is stored in the high speed memory of the graphics card. Highly dynamic data, e.g., data that is changed more often, is allocated in the main memory of the CPU. Independent of the memory type, it is possible to change the stored information by getting a pointer to the stored data. VBOs combine the benefits and the speed of display lists with the flexibility of vertex arrays. By doing so, large objects can be drawn very fast and further extension of the tool can easy be realized. To place the LA around the origin, the position of each vertex was translated by the mean of all vertices. Our tool provides the method to freely rotate the left atrium and also to zoom in and out. This visualization is represented in Figure 4.4.

Cryo-Balloon Visualization is performed by using a sphere with a diameter of either 23 mm or 28 mm as catheter model. These sizes represent the available cryo-balloon diameters of the Arctic Front device (Medtronic, Minneapolis, MN, USA). The cryo-balloon models can be freely moved around and be positioned at

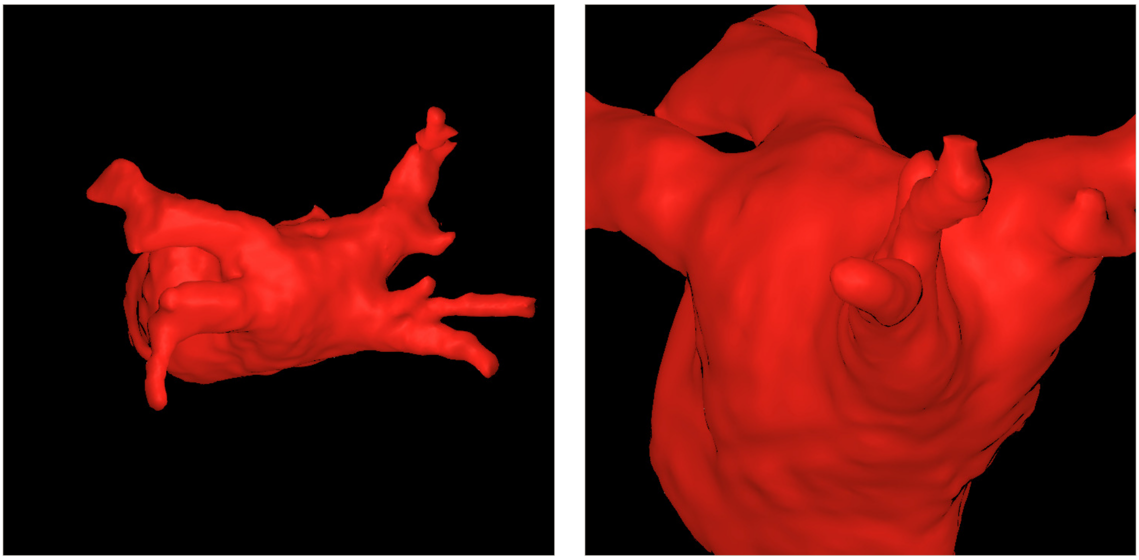

(a) (b)

Figure 4.4: (a) Visualization of the left atrium. (b) Visualization of the left atrium after rotation and zoomed in.

the ostium of the pulmonary veins. To position the catheter, the catheter model needs to be selected and is then moved parallel to the view direction. Hence, our tool requires a rotation of the view to reach the desired position. By doing so, we make sure that the user is required to look from different positions at the left atrium. The balloon automatically occludes the mesh representing the left atrium. The position of the cryo-balloon with respect to the LA can be stored and loaded upon request. An example of the visualization is given in Figure 4.5.

Transparency is achieved by changing the opacity of triangles that are facing towards the camera. Those triangles that are facing away from the observer are not changed. By doing so, we avoid that the left atrium is faded to black. Besides changing the transparency we provide a carving view. Carving means that the front face of the left atrium is partially invisible to a certain degree. In the past years, the use of shaders has evolved to an established method in computer graphics because they provide a huge flexibility. The transparency and later the carving view are done using vertex and fragment shaders [Rost 09]. To achieve a correct visualization of transparency, some drawing aspects have to be considered [Wrig 10]. First of all, the LA has to be divided into two parts, one which consists of all back facing polygons, and one comprising all front facing polygons. The back facing part is usually not visible to the viewer. However, if the front becomes transparent or is cut out, the back face of the object will be visible. To this end, blending has to be enabled [Shre 09]. During blending, the color of already drawn primitives is combined with the color of the incoming primitive which then results in a translucent looking material. An example of the visualization is given in Figure 4.6 (a).

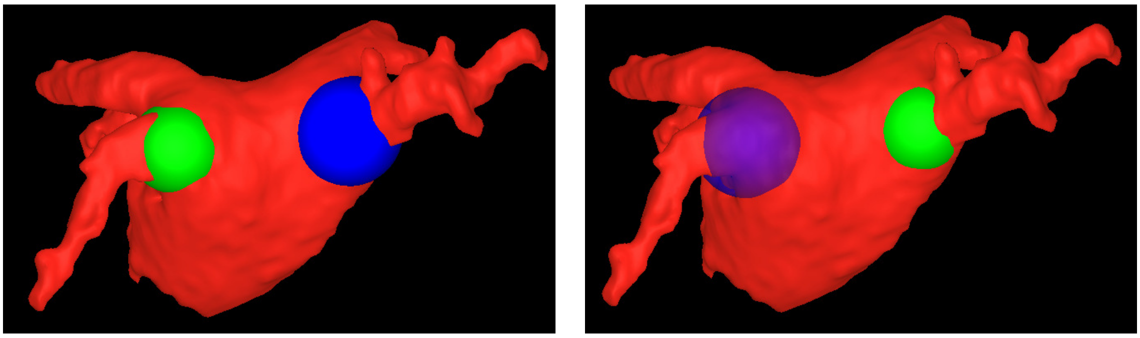

(a) (b)

Figure 4.5: (a) Visualization of a 23 mm (green) and a 28 mm (blue) cryo-balloon positioned at the left and right inferior pulmonary veins. (b) The same setting with the balloon sizes exchanged. In addition to that, transparency was used for the 28 mm balloon to visually assess the placement.

4.3.2 Carving View

In the following section, we consider a fragment $\mathbf{k} \in \mathbb{R}^3$ as an interpolated 3-D point on the mesh which will appear as an image pixel. To realize the carving effect, only the front faces of the LA are affected. The decision, whether a pixel of the mesh is visible or discarded depends on the fragments angle with respect to the view direction $\mathbf{b} \in \mathbb{R}^3$. The view direction $\mathbf{b}$ can be obtained from the projection matrix [Hart 04]. Dependent on the angle between the view direction and vector from the origin to the fragment. In our current implementation, the mesh of the left atrium is centered around the origin. The camera can only be rotated around the origin and only the distance to the origin can be changed. Therefore, the view direction from the camera position will always pass through the origin. Given an interpolated point on the mesh $\mathbf{k}$ the angle ϱ between the fragment and the view direction can be computed by

$$\varrho_i = \arccos\left(\mathbf{b}^T\mathbf{k}\right) \tag{4.1}$$

with $||\mathbf{b}||_2 = 1$ and $||\mathbf{k}||_2 = 1$. Depending on a user-set carving value $\varrho^\star \in [0, \pi]$ a fragment is drawn or discarded. The decision for a fragment $\mathbf{k}$ is based on the following rule:

$$\begin{aligned} \varrho \geq \varrho^\star \quad &\Rightarrow \quad \text{Draw Fragment} \\ \varrho < \varrho^\star \quad &\Rightarrow \quad \text{Discard Fragment.} \end{aligned}$$

An illustration of the carving process is given in Figure 4.7.

4.4 Discussion and Conclusions

By using AFiT, a physician can get direct 3-D visual feedback to determine which type of cryo-balloon catheter should be used for the procedure. The visualization

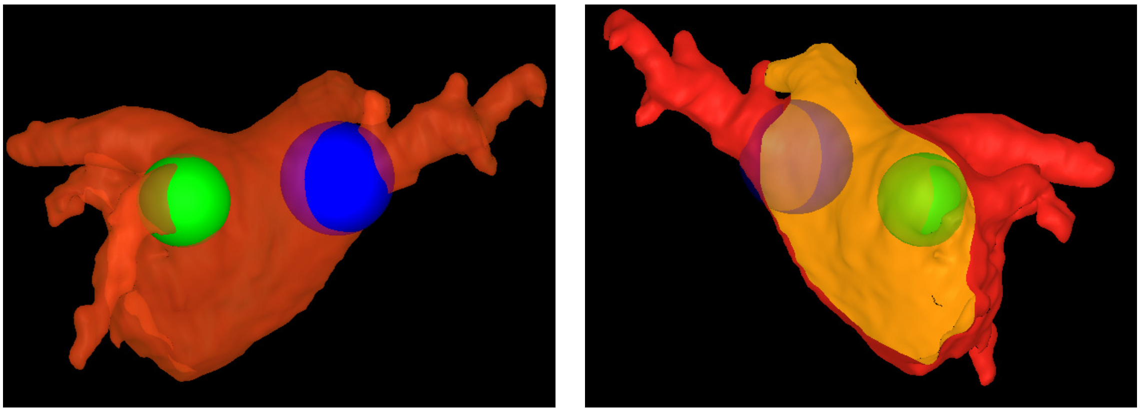

(a) (b)

Figure 4.6: (a) Visualization of the transparency effect. The cryo-balloons are still opaque, but the mesh of the left atrium is somewhat transparent. (b) Carving view of the left atrium with two semi-transparent cryo-balloons in place. The front-face of the left atrium is colored in red, the back-face in amber and the cryo-balloons in green, for 23 mm, and blue, for 28 mm, respectively.

is performed using a segmented left atrium. Our proposed tool is easy to use and the visualization helps to find the correct balloon catheter for the procedure. The current limitation of AFiT is that we do not provide any feedback about wall contact. This has to be assessed manually by the physician. Deformation of the LA up to a certain extent may be beneficial. In addition to that, our catheter models can currently be placed literally anywhere even if the position is not directly accessible. Feedback should be provided automatically if the catheter can be positioned at the planned position or not. Nevertheless, more feedback and a clinical evaluation are needed to quantify the clinical impact of this new planning tool. Still, since AFiT provides interactive visualization features to explore how a cryo-balloon can be deployed in 3-D, we expect that physicians will use this tool to determine if a cryo-balloon ablation strategy makes sense for the LA anatomy at hand.

Focusing on intra-procedural visualization, catheters such as the force-sensing catheter are also of interest [Koch 11, Koch 12]. Further extension could also focus on different interventions, such as transcatheter aortic valve implantation [Scho 11] or stent placements [Rich 07, Rich 09, Zhen 10, John 10]. In general, one could say, our tool could help whenever a 3-D device needs to be placed and the diameter of the device has to be determined beforehand.

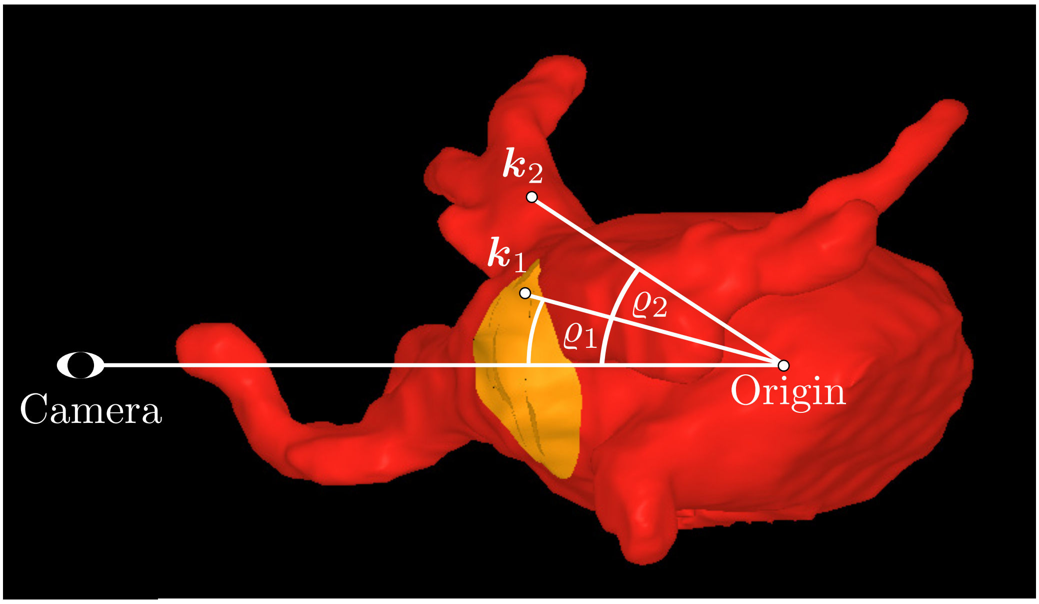

Figure 4.7: Illustration of carving. Please note that the fragment $\mathbf{k}_1$ is discarded.

CHAPTER 5

Cryo-Balloon Catheter Tracking Tool

In Chapter 3, the reconstruction of a cryo-balloon catheter for atrial fibrillation ablation procedures has been described. Chapter 4 detailed about a pre-procedural planning tool that visualizes a cryo-balloon together with a mesh representation of a left atrium in 3-D. To further support ablation procedures that involve a cyro-balloon catheter, we propose a first method to track such a device. This tool is most beneficial if pre-planned cryo-positions and a motion compensation are available. Parts of this chapter have been published in [Kurz 12].

5.1 Motivation

As an alternative to regular ablation catheters which operate on a point-by-point ablation strategy, single-shot-devices have attracted a significant amount of interest. Under ideal conditions, these devices can electrically isolate a pulmonary vein with a single application. One example of such a device is the cryo-balloon catheter. This catheter is inserted through a trans-septal sheath and can be inflated using liquid nitrogen [Koll 09]. Two different catheter types are currently available. They differ only in diameter, which is either 23 mm or 28 mm. The type of catheter is chosen depending on the underlying patient anatomy. As no mapping system is available yet for localizing cryo-balloon catheters without fluoroscopy, these devices are placed and guided under X-ray. Unfortunately, the inflated balloon catheter may be difficult to see using traditional fluoroscopy imaging. Moreover, the diameter of the catheter can only be determined once the balloon is inflated. We propose a method to track and visualize a cryo-balloon device to simplify catheter placement.

5.2 Tracking by Template Matching

The proposed method uses a 2-D template that is manually initialized and then tracked during live fluoroscopy using template matching [Sche 11, Sche 10a]. Once the cryo-balloon catheter position has been found inside an X-ray image, a 2-D ellipse determined from manual initialization is superimposed onto the live fluoroscopic view to better visualize the position and the dimension of the catheter.

On the first frame of the fluoroscopy sequence, manual initialization is required to determine a 2-D tracking template. This template is denoted as $\mathbf{I}_T \in \mathbb{R}^{n \times n}$ with $n \in \mathbb{Z}$. Denoting the fluoroscopic images as $\mathbf{I}_t \in \mathbb{R}^{S \times S}$ with $S \in \mathbb{Z}$ and $t \in [0, T]$ the number of the frame in the sequence, a pixel of the image can be accessed by using $\mathbf{I}_t(u, v)$. The same holds for the template. For simplicity, we assume quadratic images to be considered here, but our method is designed for non-quadratic images. From manual initialization, the first position of the catheter in the first frame of the sequence $t = 0$ is known as $(u_0, v_0) \in \mathbb{N}$, with the image axis denoted as u and v. This information is used to constrain the search region to be of size $2M \times 2M$ with $M \in \mathbb{Z}$. To find the catheter in the next frame $t = t + 1$, we use a multi-scale grid search and the sum of squared distances as cost function. The best translation in u-direction and v-direction such that the template matches best to the current observed fluoroscopic image is found by solving the following minimization problem

$$\hat{u}, \hat{v} = \underset{\substack{u \in [u_{t-1} - M, u_{t-1} + M] \\ v \in [v_{t-1} - M, v_{t-1} + M]}}{\arg\min} \sum_{\substack{i,j \\ \in [-D,D]}} \left(\mathbf{I}_t(u + i, v + j) - \mathbf{I}_T(i - D, j - D) \right)^2 \quad (5.1)$$

with the half size of the template denoted as $D = \lfloor \frac{n-1}{2} \rfloor$ and the floor function $\lfloor \cdot \rfloor$ that maps to the largest integer smaller compared to the argument. Our approach is summarized in Figure 5.1. The first frame of such a sequence is shown in Figure 5.1 (a), the corresponding 2-D template is shown in Figure 5.1 (b). The corresponding position in the successive frames is found by finding the best match for the template. The result for one frame is shown in Figure 5.1 (c). Finally, the superimposed cryo-balloon position is shown in Figure 5.1 (d). A structogram of the presented catheter tracking method is given in Structogram (5.1).

5.3 Evaluation and Results

For the evaluation of the proposed method, 12 clinical sequences were available. The sequences were obtained at one clinical site from 10 patients and were acquired during regular EP procedures on an AXIOM Artis dBC C-arm system (Siemens AG, Forchheim, Germany). Although the data was acquired on a biplane system, our catheter tracking approach is not restricted to such a system and will work on a monoplane device as well. As the sequences were acquired during standard EP procedures, our method is evaluated for a typical setup. It involves one circumferential mapping catheter, one catheter in the coronary sinus and a cryo-balloon catheter. In addition to that, some sequences show one ECG

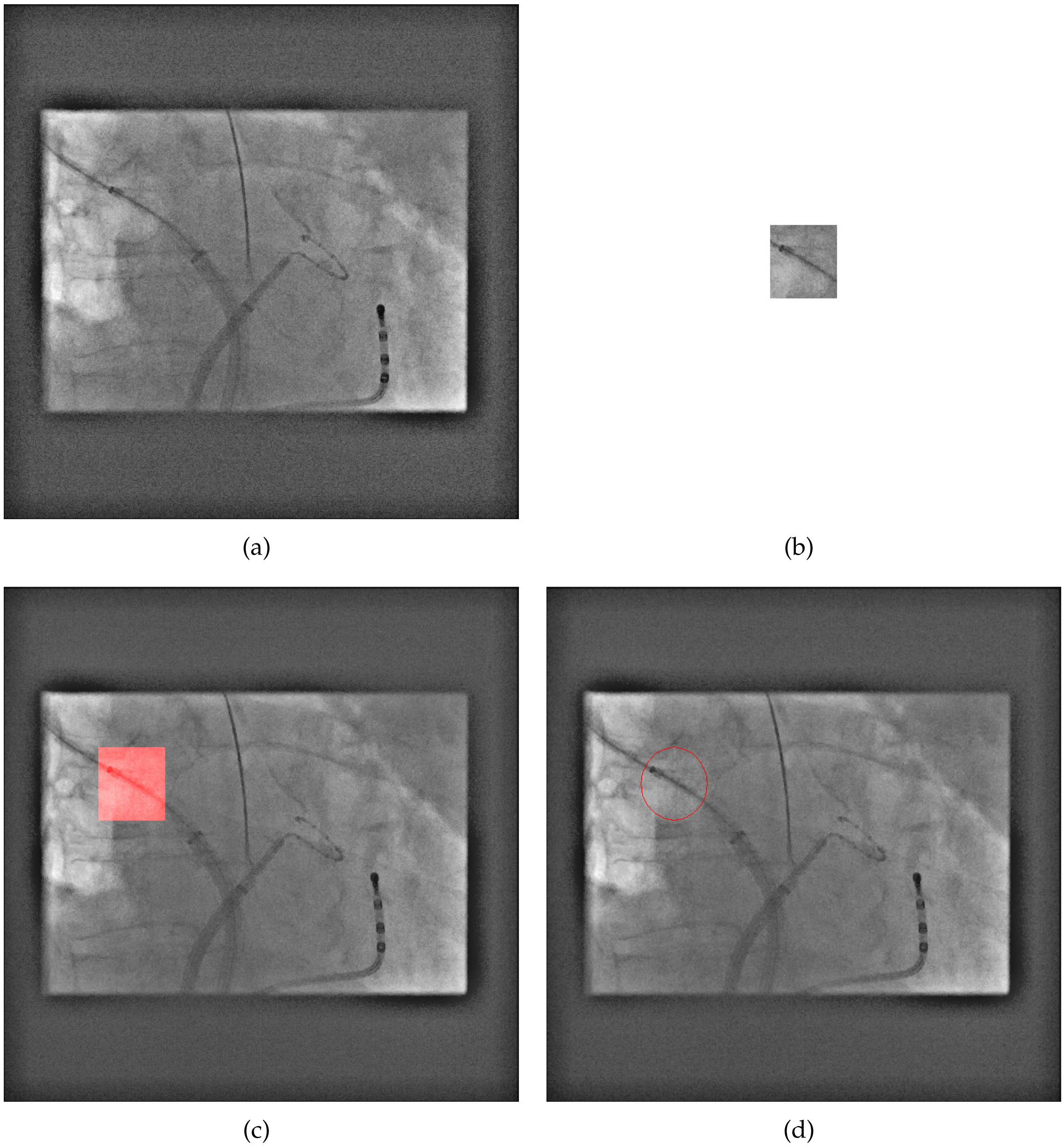

Figure 5.1: (a) First image of one fluoroscopic sequence, $t = 0$. (b) Manually initialized 2-D template for tracking. (c) Matched template highlighted in red in the next frame of the sequence, $t = 1$. (d) A superimposed ellipse was added to the fluoroscopic image to visualize position and dimensions of the cyro-balloon catheter.

Get Manual Input

Determine Template Size n

Extract Template $\mathbf{I}_T$

For Every Frame

$\hat{u} = 0, \hat{v} = 0, \hat{\varepsilon} = 0$

For $u \in [u_{t-1} - M, u_{t-1} + M]$ and $v \in [v_{t-1} - M, v_{t-1} + M]$

$$\varepsilon = \sum_{\substack{i,j \\ \in[-D,D]}} \left(\mathbf{I}_t(u+i, v+j) - \mathbf{I}_T(i-D, j-D)\right)^2$$

$\varepsilon < \hat{\varepsilon}$

true: $\hat{u} = u, \hat{v} = v, \hat{\varepsilon} = \varepsilon$

false:

Update Catheter Position using $\hat{u}$ and $\hat{v}$

Structogram 5.1: Cryo-Balloon Catheter Tracking Tool

leads that were attached to the skin of the patient. The tracking error was calculated as the Euclidean distance between the translation vector from the tracking and translation vectors from the manually segmented catheter by a clinical expert, supervised by an electrophysiologist. The expert was asked to pick the center of the tip of the cryo-balloon catheter. This is actually not a real tip, but the upper end of the catheter to which the balloon is attached. This upper end is also an opening through which contrast agent can be injected into the pulmonary vein. In contrast to the cryo-balloon itself, the opening can easily be seen as a dark spot in fluoroscopic images. Denoting the gold-standard segmentation by $u_t^\star$ and $v_t^\star$, the 2-D error ε_t in mm is calculated by

$$\varepsilon_t = \rho \cdot \sqrt{\left((u_t - u_{t-1}) - (u_t^\star - u_{t-1}^\star)\right)^2 + \left((v_t - v_{t-1}) - (v_t^\star - v_{t-1}^\star)\right)^2} \qquad (5.2)$$

with $t > 0$ and the pixel spacing ρ = 0.183 mm/pixels. The magnification factor was not taken into account. Our proposed method achieved a 2-D tracking error of 0.60 mm $\pm$ 0.32 mm averaged of all frames of all sequences. The results for each sequence are given in Figure 5.2. A total minimum error of 0.01 mm and a total maximum error of 1.64 mm was found.

5.4 Discussion and Conclusions

Our proposed method successfully tracked a cryo-thermal balloon catheter in 12 clinical sequences. It is able to superimpose the position and diameter of the device onto live fluoroscopic images to enhance the visibility of the cryo-balloon catheter. Manual interaction is only required for the initialization of the template and the determination of the size of the cryo-balloon. After that, the catheter is tracked throughout the remainder of the sequence. The visualized outline of the cryo-

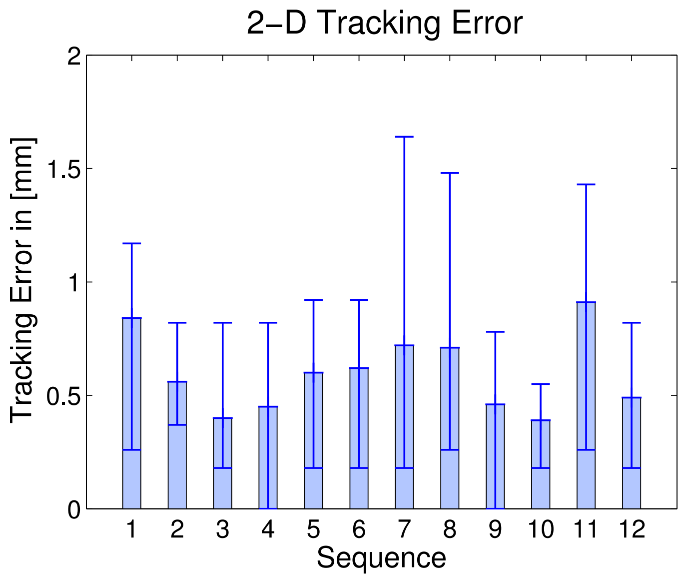

Figure 5.2: Two-dimensional catheter tracking error. The proposed method achieves a 2-D accuracy of 0.60 mm ± 0.32 mm. A total minimum error of 0.01 mm and a total maximum error of 1.64 mm was found.

balloon helps the physician to see the dimensions of the balloon catheter, otherwise hardly visible under X-ray. Our cryo-balloon catheter tracking method could also be combined with a motion-adjusted 3-D overlay rendered from pre-operative data [Bros 11e, Bros 10b]. Such an example is given in Figure 5.3. By doing so, previous balloon catheter positions can be stored and recalled if a second freeze becomes necessary. In addition, a pre-planned cryo-balloon position, e.g., using AFiT [Bros 11a], could be shown to guide the catheter placement. An example is presented in Figure 5.3 (c).

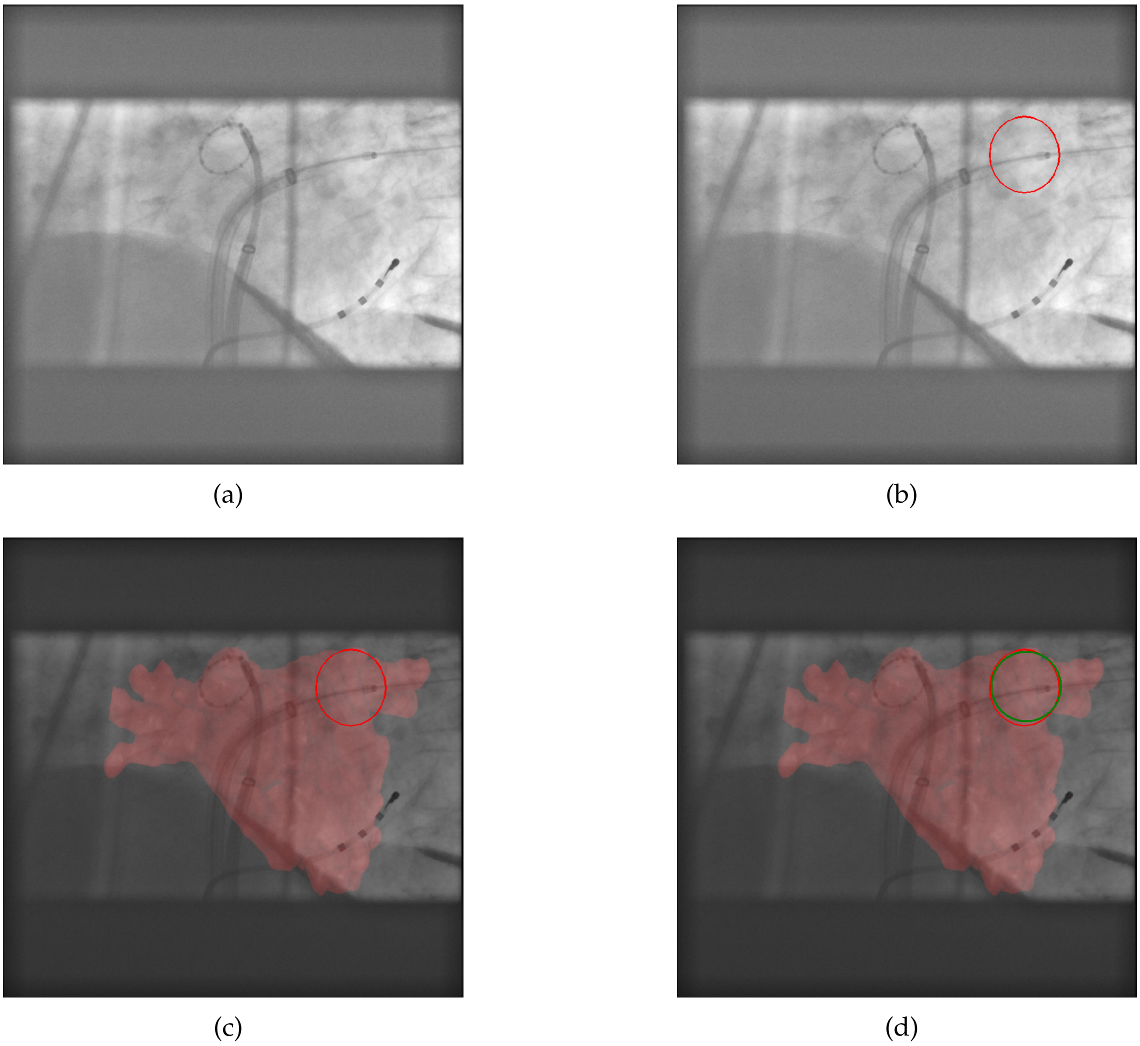

Figure 5.3: (a) Fluoroscopic image of one sequence. (b) The tracked cryo-balloon catheter is overlaid in red. (c) The same fluoroscopic image with motion-adjusted overlay and tracked cryo-balloon. (d) And in addition with a pre-planned target position of the cryo-balloon (green).

Part III

Motion Compensation involving One Catheter

CHAPTER 6

Catheter Segmentation in Fluoroscopic Images

In this chapter, the segmentation steps that are required for the next chapters are briefly summarized. Two different approaches are presented, the first is a filter-based approach and the second a learning-based approach. Both approaches start from a cropped image. Applying either the filter-based or the learning-based method yields a segmentation of the circumferential mapping catheter. The results are thinned using a skeletonization algorithm. A distance transformed image is computed for the skeleton yielding a smooth representation that is used as input for the registration methods used in the chapters hereafter.

6.1 Motivation

The success of image-based tracking methods depends on the image processing steps used to enhance the structure that has to be tracked. The usual candidates that are considered for tracking are guidewires [Baer 03a, Baer 03b, Spie 07], needles [Papa 10], and catheters [Bros 09a]. The methods used in this application are either filter-based or learning-based approaches. Filter-based approach use image filters to enhance the structure of the guidewire, needle, or catheter and try to suppress other structures such as bones or other devices. Most of these approaches make use of Gaussian filter kernels, in particular the second derivatives of Gaussians [Ma 10, Spie 07, Sche 10b]. But also other filter kernels have been proposed [Palt 97], e.g., the Marr-Hildrecht filter [Atas 08]. Learning-based methods use classifiers to determine if a pixel belongs to the desired structure or not.

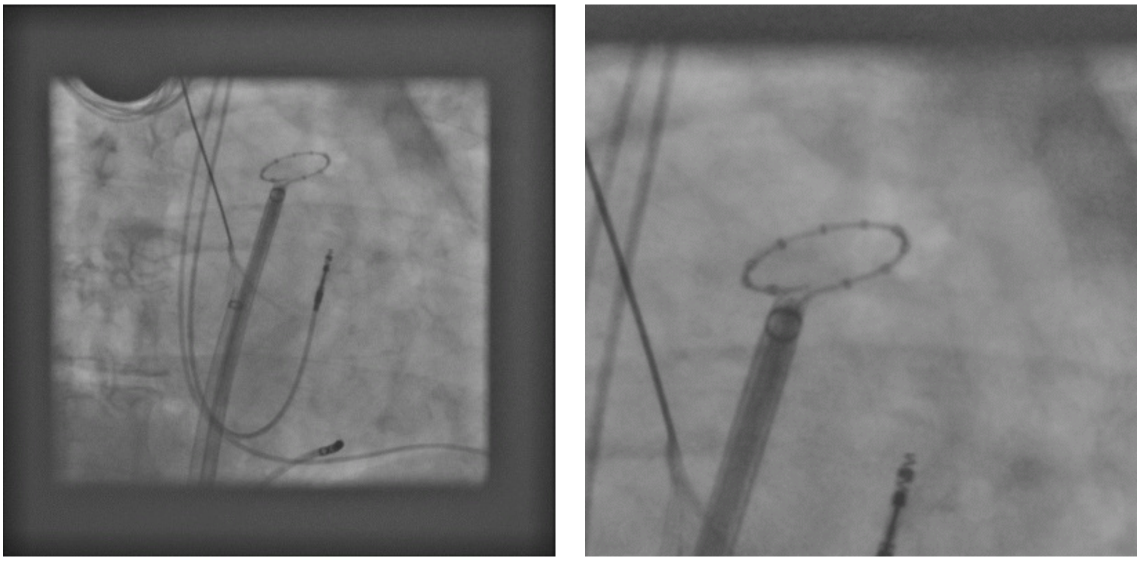

(a) (b)

Figure 6.1: (a) Original fluoroscopic input image of size $1,024 \times 1,024$ pixels. (b) Cropped image around the region of interest. The cropped image is of size 400×400 pixels.

The most recent approaches focus on AdaBoost [Bros 11c, Bros 10c] or probabilistic boosting trees [Wu 11, Wu 12]. The features used for the classifiers are mostly Haar-like features [Viol 04, Viol 01] or SIFT features [Lowe 99]. In comparison to filter-based approaches, the methods using classifiers require a training data set of a certain size to find the best features to classify a pixel. Filter-based approaches are usually considered if only a small data set is available as only the filter kernels and the standard deviation of the Gaussians need to be adjusted. As soon as a larger data base is available, learning-based approaches can be used. Besides these two approaches, template matching has also been proposed [Sche 11, Sche 10a] and, in contrary to other methods, is able to directly output the position of the desired structure. Template matching is based on the assumption that the desired structure is similar to a template of the same structure. The similarity is mostly calculated by using the cross-correlation [Atas 08, Sche 11, Sche 10a] but also the sum of squared differences is used [Kurz 12].

6.2 Image Cropping

The processing steps involved are discussed for one image, but are executed either for one or for two images, dependent on which type of motion compensation approach is considered afterwards. As input images, fluoroscopic images of atrial fibrillation ablation procedures are considered. These images were available as 12-Bit gray scale images with a size of $1,024 \times 1,024$ pixels. Due to implementation constraints, the images were reduced to 8-Bit.

In the first step, of both approaches, the input image is cropped. The region of cropping is considered to be 400×400 pixels, which was found to be suitable. The

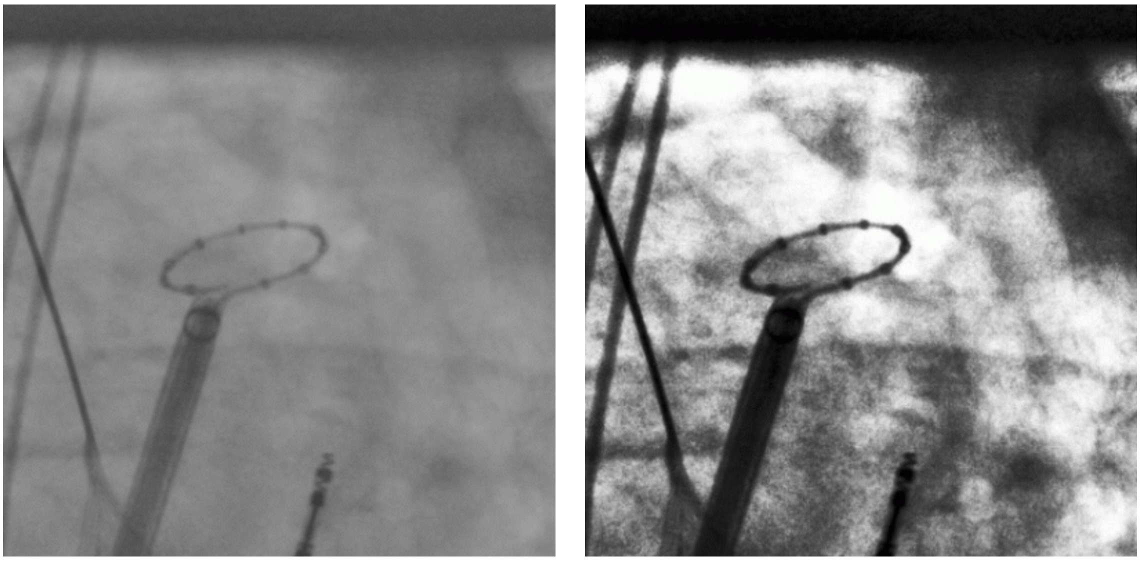

(a) (b)

Figure 6.2: (a) Cropped image of size 400 × 400 pixels. (b) Histogram equalized image.

center of the region is found by either using the manual input of the circumferential mapping catheter reconstruction or the position determined from the tracking result in the previous frame. If the catheter moves close to the boundaries of the image, the size of the region is reduced but only in that dimension that is affect by the boundary of the image. Shutters, which are often used to reduce radiation, are not considered. Their position could be obtained from the system or from file information, but this was not required for the available data. An example of image cropping is given in Figure 6.1.

6.3 Filter-Based Segmentation

The filter-based catheter segmentation is performed in three steps. In the first step, a histogram equalization is performed. This step is done to enhance semi-transparent parts of the circumferential mapping catheter. In the next step, a vesselness filtering is applied to enhance tubular structures. In the third step, the filter response is binarized using Otsu's method.

Histogram Equalization

The contrast difference between the catheter and the surrounding tissue can be rather small. To enhance the catheter, a histogram equalization step is carried out. It is advantageous if an image has a high percentage of low-value intensities and a low percentage of high-value intensities, i.e. the density function of the gray values is not uniform. The histogram equalization calculates a linear mapping of gray-values of one gray-level to another gray-level to achieve a uniformly distributed density function [Prat 07]. The assumption of a uniform distribution may

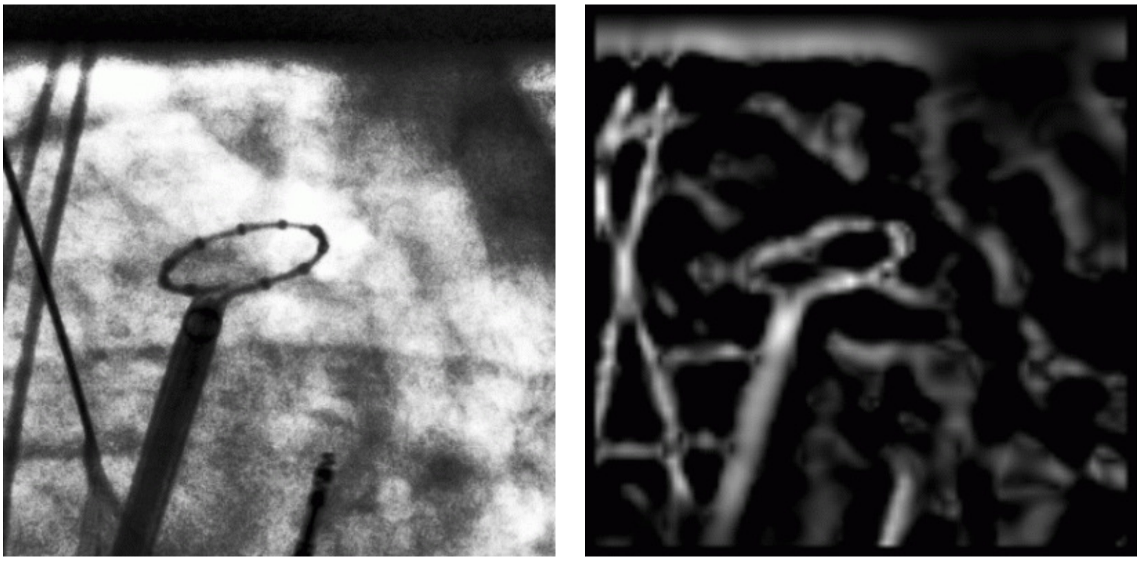

(a) (b)

Figure 6.3: (a) Histogram equalized image. (b) Image after vesselness filtering.

not hold for the probabilities of the gray values, but it may hold for the cumulative density function. The histogram equalization can also be used to reduce the number of gray-levels from the input image to the output image, but this was not considered here. The histogram equalization is only applied to the cropped image. An example of histogram equalization is given in Figure 6.2.

Vesselness Filtering

In the next step, a vesselness filtering is applied to the histogram equalized image. Vesselness filtering, or vessel enhancement filtering, is a multi-scale filter that enhances structures that appear tubular [Fran 98, Sato 98, Spie 07]. This filtering method uses the convolution of second order derivatives of Gaussians with the histogram equalized image. The second derivatives are often used for line enhancement and Gaussian filtering is the method of choice to reduce image noise. Using the second derivatives of a 2-D Gaussian function as filter kernels yields an excellent filter response in areas where a bright spot is surrounded by a dark background. Instead of differentiating the image and convolving it with a Gaussian filter kernel, it is also valid to calculate the derivative of the Gaussian function instead and perform the convolution with the second derivative Gaussian kernels [Koth 03]. The standard deviation σ of the Gaussian filter kernel represents the diameter of the line or tubular structure to be detected. The analysis if a certain point belongs to a vessel-like object or background is done by considering the eigenvalues of the Hessian matrix. Therefore, the neighborhood of a point within the Gaussian filter kernel is considered. The eigenvalues and eigenvectors are interpreted as the semi axes an ellipse around the point. The eigenvalues are sufficient enough to classify the local area around a point. The value of σ is chosen according to the size of the structure that has to be enhanced. This is where knowing

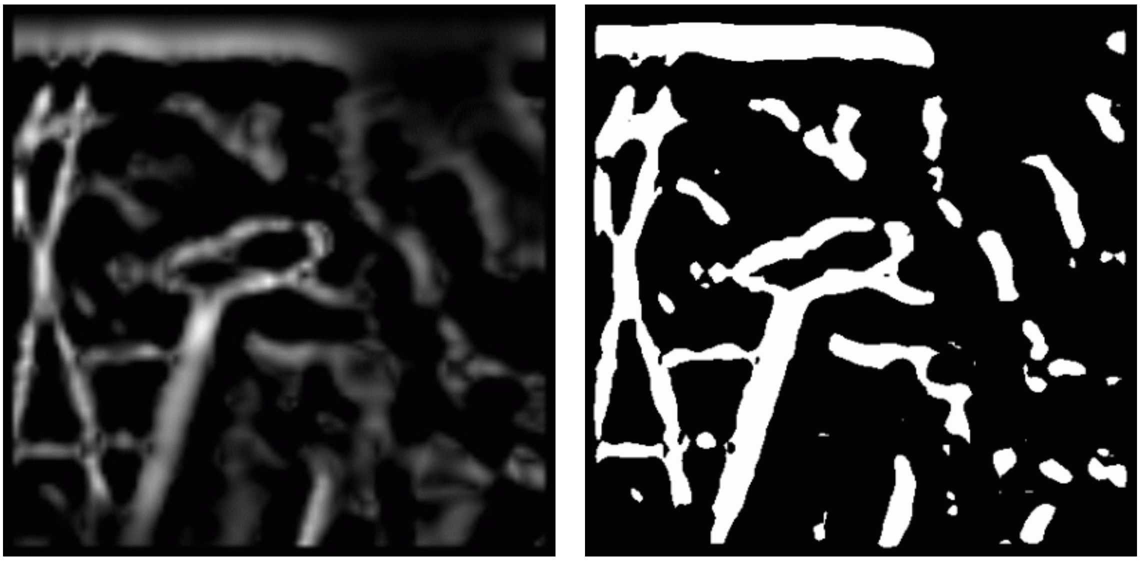

(a) (b)

Figure 6.4: (a) Image after vesselness filtering. (b) Binary image after applying Otsu's method.

the diameter of the catheter would be helpful. Such information could be provided by the physician, but we chose that our method should work independently of such additional information. The Hessian matrix of a function comprises the second partial derivatives [Bron 01]. The classification of a point is then based on its corresponding eigenvalues for a certain scale σ. To calculate a vesselness score for a scale σ, different functions have been proposed in literature [Fran 98, Sato 98]. We followed the method proposed in [Sato 98] which uses a function dependent only on the eigenvalues without additional parameters, which are used in [Fran 98]. As this operation is performed for several values of σ, the overall vesselness score per pixel is then given as the maximum vesselness score over all scales. An example of the result of vesselness filtering is given in Figure 6.3.

Otsu's Method

Otsu's method is an unsupervised and non-parametric algorithm for thresholding gray-valued images [Otsu 79]. Mostly, the threshold is used to separate gray-values in two or more classes. If only two classes are considered, the image is binarized. The calculation is based on second order statistics. The underlying assumption of this method is that the intra-class variance is small and the inter-class variance is large. Further, the two classes are considered as dark and bright pixels. The method tries to find a certain gray value that, when used as threshold to the image, maximizes the inter-class variance while trying to keep the intra-class variances low. Once the threshold is found, the image can be separated into dark pixels, background, and bright pixels, foreground. The vesselness scores are used as input. Assuming that catheter parts have a high filter response and that non-catheter parts have a rather low filter response, they can be separated into high

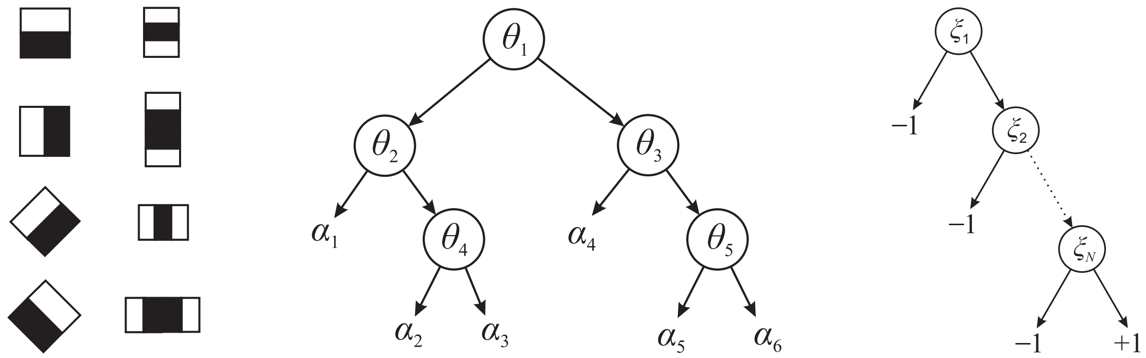

(a) Feature Types (b) Classification and Regression Tree (c) Cascade

Figure 6.5: Features types and classifier structure for catheter segmentation. (a) Several prototypes of Haar-like features. (b) Exemplary classification and regression tree (CART) with five feature nodes $\theta_1, \ldots, \theta_5$ and six leaves $\alpha_1, \ldots, \alpha_6$. (c) A classifier cascade consisting of multiple stages with strong classifiers $\xi_1, \ldots \xi_N$. Each strong classifier ξ_i is a linear combination of weak classifiers, here CARTs.

and low gray values. By maximizing the inter-class variance, these values can be separated into background and foreground. An example is given in Figure 6.4.

6.4 Learning-Based Segmentation

The catheter segmentation method not only has to be reliable, but it needs to be fast as well. Speed is necessary to ensure that the catheter can be tracked in real-time at the frame rate set at the X-ray acquisition system. We found that a combination of Haar-like features and a cascade of boosted classifiers met both requirements to differentiate the live fluoroscopic images into *catheter* and *background*. Haar-like features [Viol 01, Viol 04] calculate various patterns of intensity differences. Several feature prototypes are listed in Figure 6.5(a). Some features detect edges, whereas others focus on line structures. In particular, the latter are useful for detecting the circumferential mapping catheter, which often appears as a thin, elongated object with a loop at its end, see Figure 6.1. Actual features are obtained by shifting and scaling the prototypes within a predefined window. In our case, a window size of 15×15 pixels was found to be sufficient for good results. Thereby, contextual information around the center pixel is considered, which is important to differentiate between catheter and background structures. However, even for moderate window sizes, the resulting number of features is large and easily amounts to several hundreds of thousands. Features are calculated efficiently by using integral images [Viol 04]. To achieve reliable and fast segmentation, the most suitable features for discriminating between catheter and background have to be chosen and integrated into a classifier in a suitable manner. This is carried out by the AdaBoost algorithm [Freu 97]. The idea is to combine several weak classifiers in order to form a strong classifier. The classifier minimizing the classification error is added to a linear combination of weak classifiers until the overall error is below the desired threshold. After each training iteration, the importance of indi-

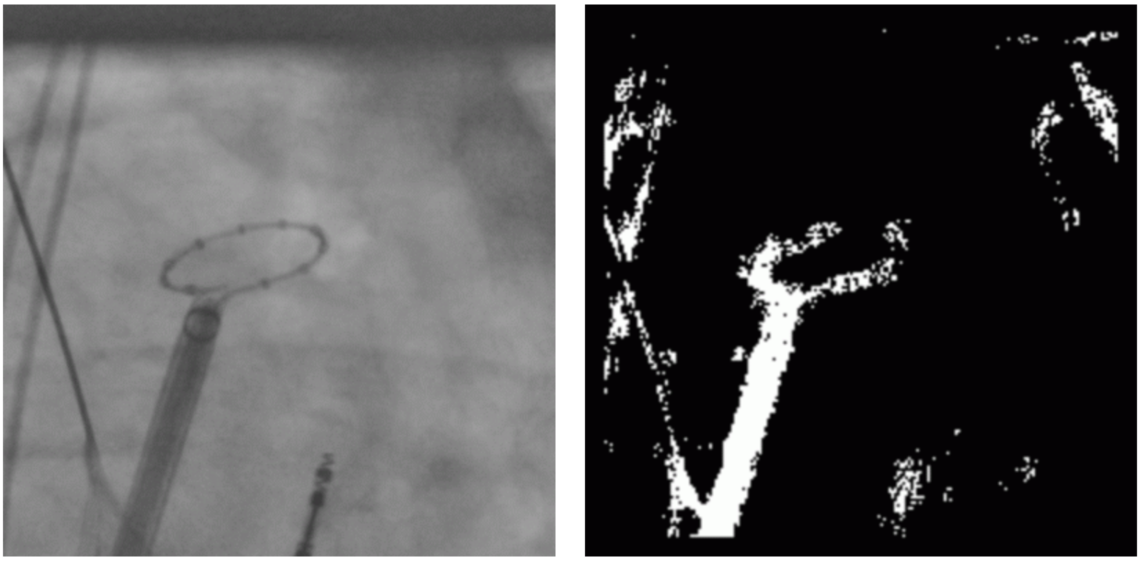

(a) (b)

Figure 6.6: (a) Cropped image. (b) Image after classification using a boosted classifier cascade.

vidual samples is re-weighted to put more emphasis on misclassifications for the next evaluation. Instead of single features and intensity thresholds, we use classification and regression trees (CARTs) [Brei 84] as weak classifiers. A CART is a small tree of fixed size. At each node, a threshold θ associated with a feature partitions the feature space. This way, flexibility is increased and objects with complex feature distributions can be handled. The result of a CART is the value α_k of the classifier reached as leave node. An exemplary CART is shown in Figure 6.5(b). We organize $N \in \mathbb{Z}$ strong classifiers $\xi_1, \ldots, \xi_N$ composed of weighted combinations of CARTs into a cascade, which is illustrated in Figure 6.5(c). In our case, four strong classifiers yielded good results. At each stage, a sample is either rejected (-1) or passed on to the next stage. Only if the sample is accepted $(+1)$ at the final stage, it is accepted as part of the object [Frie 00]. Thus during training, the focus is on maintaining a high true positive rate while successively reducing the false positive rate, either by adding more weak classifiers to a stage or by adding an entirely new stage.

6.5 Skeletonization

Image skeletonization is the erasing of white pixels such that a minimally connected stroke remains. The stroke should be located equidistantly from its nearest outer boundaries [Prat 07]. Several methods have been proposed to obtain such a skeleton. We used the method presented in [Cych 94] which uses the iterative application of morphological operators until the minimal connected skeleton is left. Skeletonization is applied to both, the binarized image after applying Otsu's

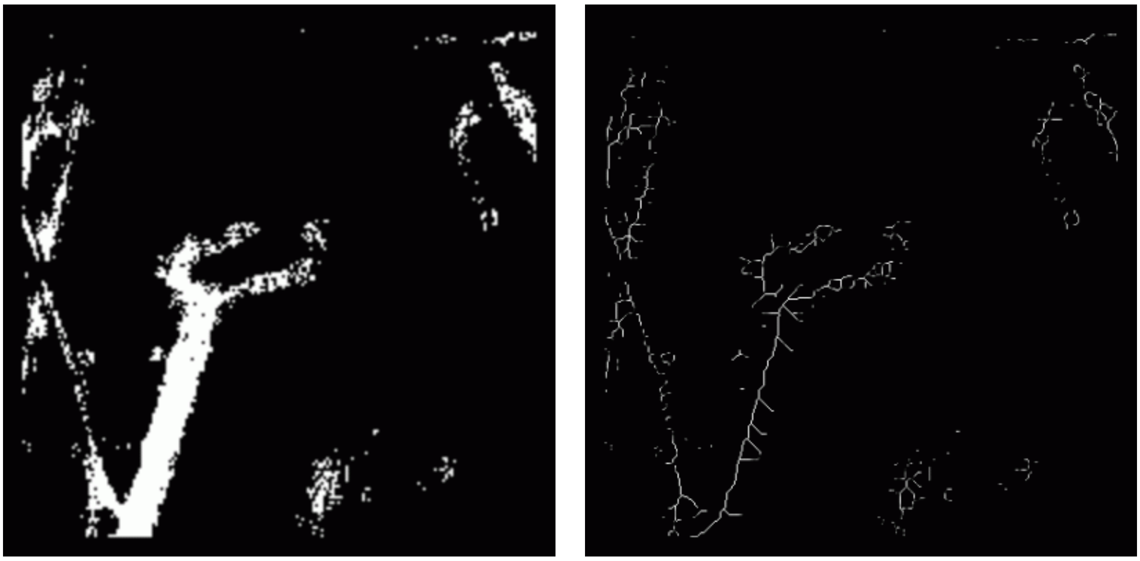

(a) (b)

Figure 6.7: (a) Image after classification using a boosted classifier cascade. (b) Image after skeletonization

method in the filter-based approach, as well as the classified image in the learning-based approach. An example of skeletonization is given in Figure 6.7

6.6 Distance Transform

The distance transform (DT) is applied to the skeleton of the segmentation and calculates the distance for each pixel from the segmented object [Meij 02]. Several algorithms to perform the calculation efficiently are described in literature. In [Pori 07] a wave propagation was used. A graph search algorithm is described in [Lotu 00]. The algorithm in [Breu 95] is based on Voronoi diagrams and, e.g., used in MATLAB (MathWorks, Natick, MA, USA). A comparison between different algorithms is given in [Fabb 08]. The algorithm given in [Meij 02] is said to be the most efficient and fastest version. This is a two step algorithm that can easy be parallelized. A distance transform using morphologic operations is described in [Borg 86, Voss 88]. The algorithm used by OpenCV is proposed in [Felz 04]. It uses a two step approach, calculating rows before columns. In all cases, the result is an image whose values represent the distance to the closest point of the skeleton. The skeleton itself is set to zero. By using the distance transform, a smooth image is obtained that will be used in the next chapters as part of the cost function of the registration methods. The methods presented in the next chapters make use of the algorithm presented in [Felz 04] as it was directly available by using OpenCV. An example of a distance transformed image is given in Figure 6.8. This image is denoted as $\mathbf{I}_{\mathrm{DT}}$ for both, the learning-based and the filter-based approach. One pixel $\mathbf{p} \in \mathbb{R}^2$ is accessed by $\mathbf{I}_{\mathrm{DT}}(\mathbf{p})$.

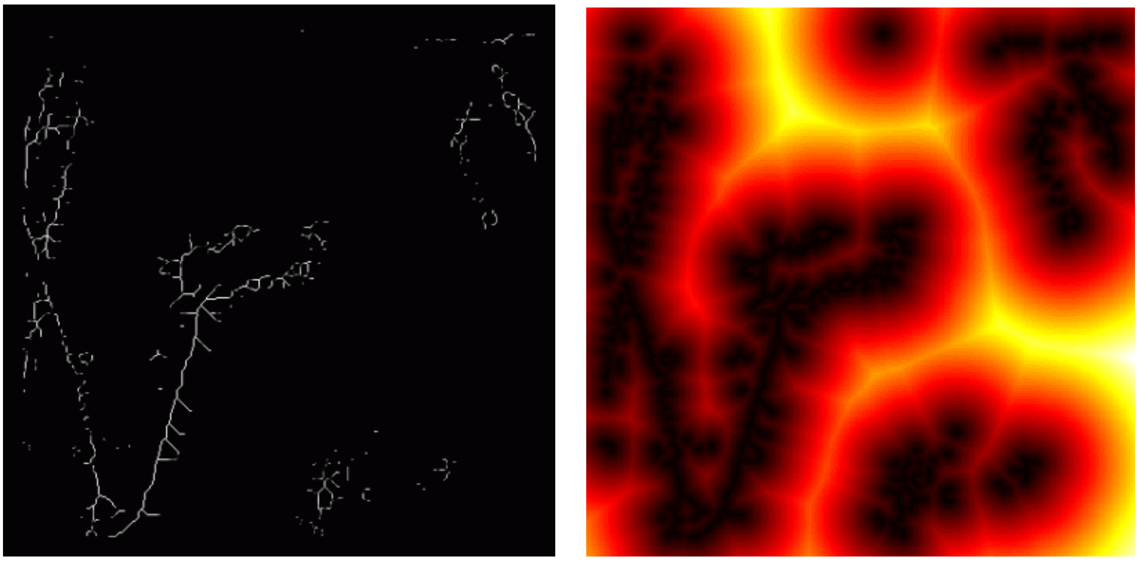

(a) (b)

Figure 6.8: (a) Classified image after skeletonization. (b) Distance transform of the skeleton.

6.7 Segmentation Pipelines

Using the methods presented above, two segmentation pipelines to arrive at the final distance transformed catheter segmentation $\mathbf{I}_{\mathrm{DT}}$ are available. The first method is a filter-based approach, involving a histogram equalization, vesselness filtering, and Otsu's method for binarization. The second method, the learning-based approach, replaces these three steps by using a boosted classifier cascade. These two image processing pipelines are presented in Figure 6.9. In both cases, we end up with a smooth representation of the catheter segmentation, which is found by calculating the distance transform of the skeleton. For simplicity, the distance transform is denoted as $\mathbf{I}_{\mathrm{DT}}$ for both, the filter-based and the learning-based approach.

6.8 Discussion and Conclusions

On first sight, the filter-based method seems to yield better results. In some cases, this might be true. Once, other structures get close to the catheters, the results look different. In addition to that, the filter-based approach requires the knowledge of the size of the catheter, or to be more precise, the diameter of the tubular structure. Even though this information could be obtained at the beginning of the procedure, it would require additional user input. The learning-based approach on the other hand just requires some training data sets but no additional information.

Apart from the two approaches to segment a catheter in fluoroscopic images, other methods have been proposed as well. The approaches are ranging from simple thresholding methods [Rose 01] via template matching [Schm 05] to learning based approaches [Barb 07]. Template matching approaches are usually combined

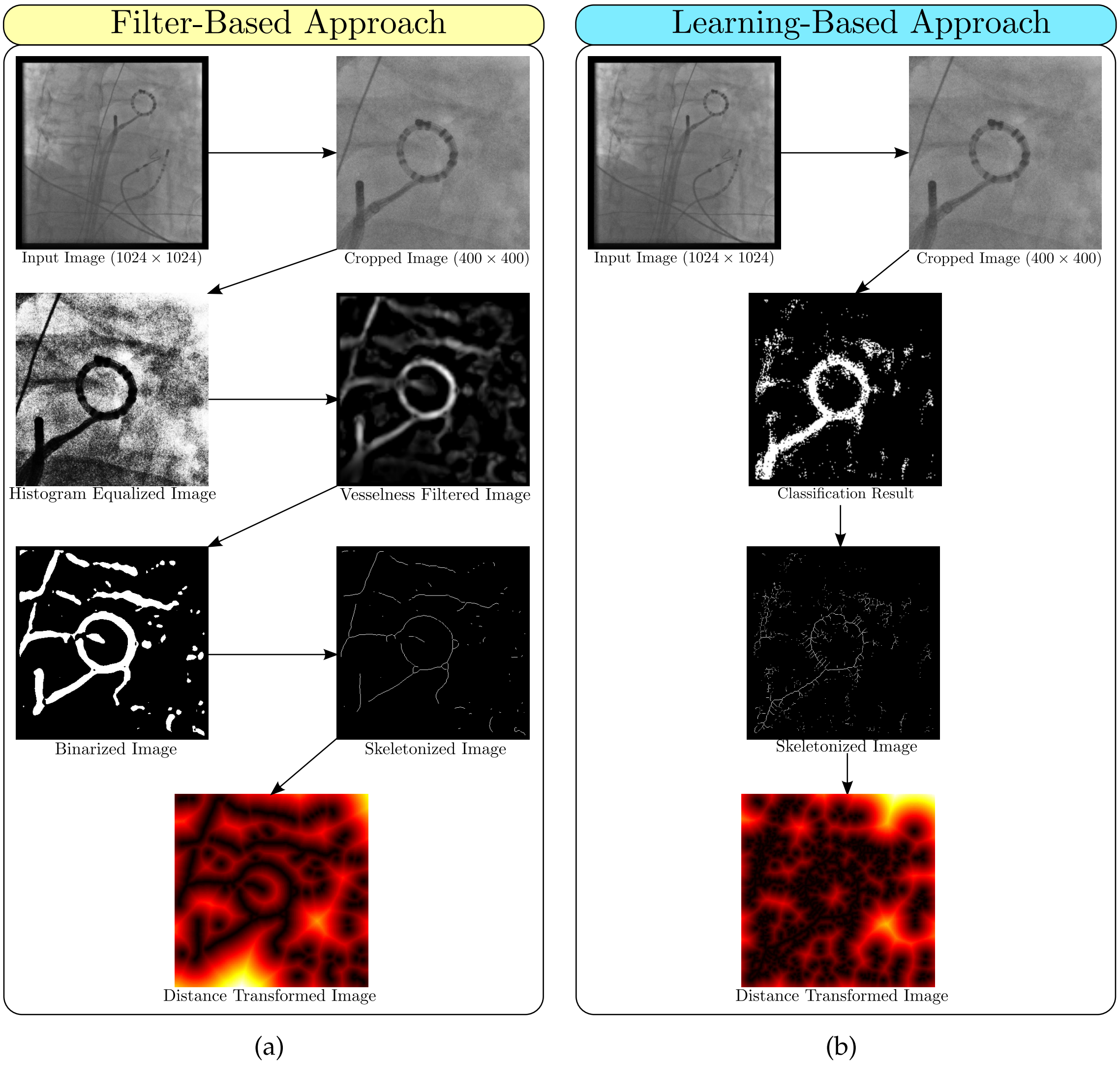

Figure 6.9: (a) Image processing pipeline for the filter-based approach. (b) Image processing pipeline for the learning-based approach.

not directly for segmentation but for position detection of a catheter [Schm 05, Sche 11, Sche 10a, Sche 10b]. These methods have been proposed for electrophysiology procedures. A more sophisticated method for cardiac catheters was proposed in [Fran 06]. Other filter-based methods have been proposed as well [Aufr 95, Aufr 93, Aufr 92, Palt 97]. A new approach proposed in [Hoff 12a, Hoff 12b] used a filter technique called medialness filtering [Guls 08]. Most recently, two approaches for electrophysiology procedures have been proposed. The first is also based on a filter-based approach, specifically designed for blob detection [Ma 10], and a learning based approach using hypothesis testing [Wu 11]. The blob detection method is also based on filtering the image with second derivatives of Gaussians as filter kernels. For now, it will remain an open question whether a filter-based or a learning-based approach yields better results.

CHAPTER 7

Monoplane Motion Compensation by Registration

In this chapter, the focus is on motion compensation for monoplane systems, i.e., C-arm X-ray systems equipped with only one C-arm, instead of biplane systems with two individual C-arms. In the first section a motivation for the approach is given, followed by the presentation of the motion compensation method in section two. The third section focuses on the evaluation and presents the results. The fourth section discusses the results and draws some conclusions. The data sets used for evaluation described here, will be used in Chapters 8, 9, and 10 as well. Parts of this chapter have been published in [Bros 11f, Bros 10d].

7.1 Motivation

A first approach for 3-D respiratory motion compensation based on catheter tracking was proposed in [Bros 09b]. Unfortunately, it required simultaneous biplane fluoroscopy acquisition. There are two problems concerning this approach. First of all, not all EP-Labs are equipped with a biplane C-arm system. See Figure 7.1 for different systems used in interventional cardiology. For monoplane systems, the previously proposed method is not feasible. The second disadvantage is simultaneous biplane acquisition which increases X-ray dose for patient and physician. As exposure for EP procedures is already rather high compared to other interventions, physicians might be unwilling to perform biplane acquisitions [Doss 00]. In this chapter, the focus is to overcome the problem if only a monoplane system is available. Even though the C-arm could be adjusted to image the region of interest from different angles, it is rather unlikely as physicians tend to use their standard angulations [Hais 94]. The presented method requires three steps. In the first step, manual initialization of a 2-D catheter model is performed. In the second step, the input images need to be processed. In the final step, the 2-D catheter model is tracked using a model-based 2-D/2-D registration. The translation obtained from

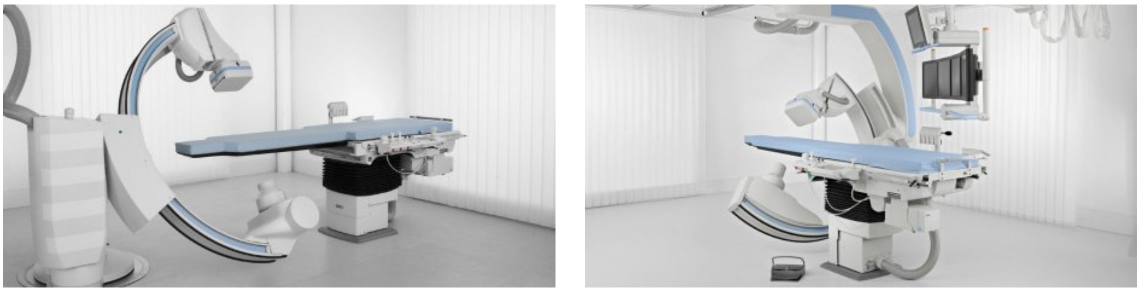

(a) (b)

Figure 7.1: Monoplane C-arm systems for cardiac procedures. Both systems are equipped with a small 20 cm × 20 cm detector. Both systems by Siemens AG, Healthcare Sector, Forchheim, Germany. Images reproduced with permission by Siemens AG, Healthcare Sector, Forchheim, Germany. (a) Artis **zee** floor-mounted system by Siemens. (b) Artis **zee** ceiling-mounted C-arm system by Siemens.

the registration can be applied to the overlay images, thus compensating for the underlying cardiac and respiratory motion.

7.2 Monoplane Model-Based 2-D/2-D Registration

Manual initialization of the catheter model is required. Our first method used an elliptical catheter model [Bros 10d]. Apart from being easy to be mathematically described, the downside of using an ellipse as 2-D catheter model is that in the X-ray projection images, the catheter is not always visible as a circular shaped object. Depending on the catheter in use, the tip part might not form a closed ellipse or might be overlapping. Some examples are given in Figure 7.2. In these cases, a spline model might be preferable as it can be better adapted the to the 2-D projection image. Furthermore, a spline obtained from manual initialization puts less restrictions on the user about setting the points. An elliptical model could be easily converted into a spline model.

Given the 2-D catheter model, the fluoroscopic images need to be processed before being used in the registration step. Catheter segmentation is done according to Chapter 6. The region for cropping is given either by manual initialization in the first frame, or by the tracking result in the previous frame. The resulting image is the distance transformed image of the catheter segmentation denoted as $\mathbf{I}_{\mathrm{DT}}$. It encodes the absolute distance from a pixel to its closest segmented catheter pixel. It also provides a smooth representation of the fluoroscopic image with a pronounced minimum around the shape of the mapping catheter to increase the capture range. One pixel $\mathbf{p}$ is accessed by $\mathbf{I}_{\mathrm{DT}}(\mathbf{p})$. The axes of an image are considered as u and v.

In the next step, tracking is performed by rigid registration of the catheter model to the distance transform of the segmentation result derived from either the filter-based or the learning-based approach [Hill 01]. To this end, the region-of-interest (ROI) of the classification is used. As a 2-D/2-D registration is used, the result is a 2-D pixel offset $\mathbf{l} \in \mathbb{N}^2$. Rotation is not estimated, because 2-D rotation

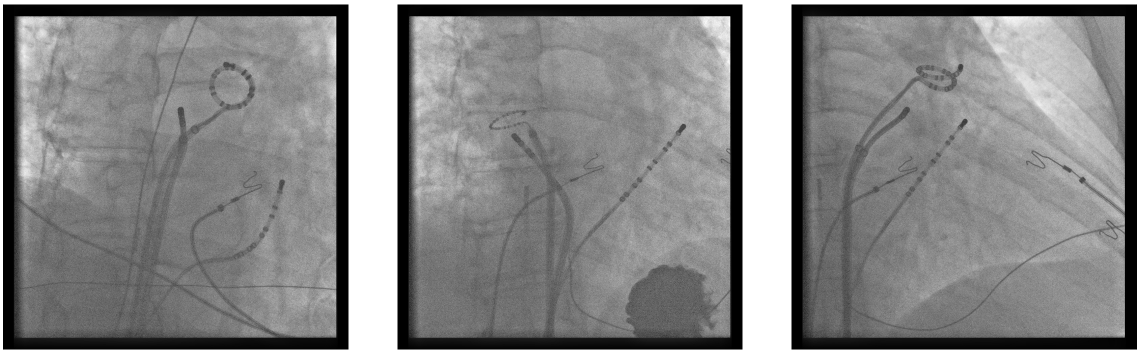

(a) (b) (c)

Figure 7.2: Comparison of different catheter projections. Depending on the resulting 2-D projection, an elliptical or a spline catheter model is preferable. (a) If the projection of the catheter is circular shaped, an elliptical 2-D catheter model can be used. (b) Given a non-closed circular shape, an elliptical catheter model could still be used. (c) In case of a non-elliptical shaped catheter projection, a spline model is preferable.

in typical X-ray images taken during EP procedures is usually very small compared to translation. Furthermore, for cases when the circumferential mapping catheter is very close to being a circle, the estimation of rotation would require additional landmarks. The average distance between catheter model and segmentation derived from the fluoroscopic image is then considered as the cost value. The optimal translation $\hat{\mathbf{l}}$ is found by minimizing

$$\hat{\mathbf{l}} = \arg\min_{\mathbf{l}} \sum_{\omega} \mathbf{I}_{\mathrm{DT}}(\mathbf{s}(\omega) + \mathbf{l}) \tag{7.1}$$

with $\mathbf{s}(\omega)$ denoting a point of the catheter model and the spline parameter $\omega \in [0, 1]$. As optimization strategy, multi-scale grid search is used, i.e., the position of the local optimum on a large scale is taken as starting point for the optimization on a smaller scale [Duda 01]. The search domain is given as $\Omega \subset \mathbb{N}^2$. The estimated 2-D translation $\hat{\mathbf{l}}$ can be directly applied to the 2-D overlay to move it synchronously with the tracked device. A structogram of the presented motion compensation method is given in Structogram (7.1).

7.3 Evaluation and Results

For the evaluation of the proposed method, 23 clinical biplane sequences were available. As the presented approach considers only monoplane motion compensation, the sequences were split in 46 monoplane sequences. The clinical data was collected at two clinical sites and is taken from 16 different patients. The sequences were acquired during EP procedures on AXIOM Artis dBC C-arm systems (Siemens AG, Forchheim, Germany). The pixel spacing of the sequences was either 0.173 mm/pixel or 0.183 mm/pixel. The frame rate varied between 6 frames-per-second (fps) and 15 fps. Although we developed a method for motion compensation that can be used for monoplane systems, it is not restricted to

Get Manual Input Points

Generate Catheter Model $\mathbf{s}(\omega)$

For Every Frame

  Compute Distance Transformed Image $\mathbf{I}_{\mathrm{DT}}$

  $\hat{\mathbf{l}} = \mathbf{0}$, $\hat{\varepsilon} = \infty$

  For $\mathbf{l} \in \Omega$

    $\varepsilon = \sum_{\omega} \mathbf{I}_{\mathrm{DT}}(\mathbf{s}(\omega) + \mathbf{l})$

    $\varepsilon < \hat{\varepsilon}$

    true: $\hat{\mathbf{l}} = \mathbf{l}$, $\hat{\varepsilon} = \varepsilon$

    false:

  Update Catheter Model $\mathbf{s}(\omega)$ using $\hat{\mathbf{l}}$

  Update Overlay using $\hat{\mathbf{l}}$

Structogram 7.1: Monoplane Motion Compensation by Registration

such a system and could be used for biplane systems as well. As the sequences were acquired during standard EP procedures, our method is evaluated for a typical clinical setup. It involves one circumferential mapping catheter, one ablation catheter and one catheter in the coronary sinus. Two different types of circumferential mapping catheter were used. The evaluation was performed using two-fold cross validation, i.e., two sequences, actually being one biplane sequence, were excluded for training of the classifier and used for evaluation. The tracking error is considered in 2-D only, as only monoplane motion compensation is considered here. The 2-D error was calculated as the average distance between the motion-compensated catheter model and the manually segmented mapping catheter. Manual segmentation was supervised by an electrophysiologist. This distance was averaged over all frames of a particular sequence to arrive at an overall tracking error for each sequence. To calculate the error in mm, the pixel scaling at the detector of either 0.183 mm/pixel or 0.173 mm/pixel was used. The magnification factor was not taken into account. In Figure 7.3, we present the mean tracking error together with the minimum and maximum values for each sequence compared to an uncompensated overlay. Over all 46 sequences with a total of 1,288 frames, the mean tracking error was 0.58 mm with a minimum of 0.21 mm and a maximum of 1.92 mm. This is small considering that the thickness of circumferential mapping catheters varies between 1.3 mm and 2.4 mm. The observed motion was on average 1.83 mm with a minimum of 0.14 mm and a maximum of 6.82 mm. Errors of the same range could be assumed for the uncompensated case, but will depend on the initial registration. The proposed tracking method reduced the motion difference in all sequences.

Besides the learning-based approach used, we compared our method to a filter-based approach similar to the one used in [Bros 09b]. The filter-based method yielded a 2-D average error of 0.61 mm with a total minimum error of 0.21 mm

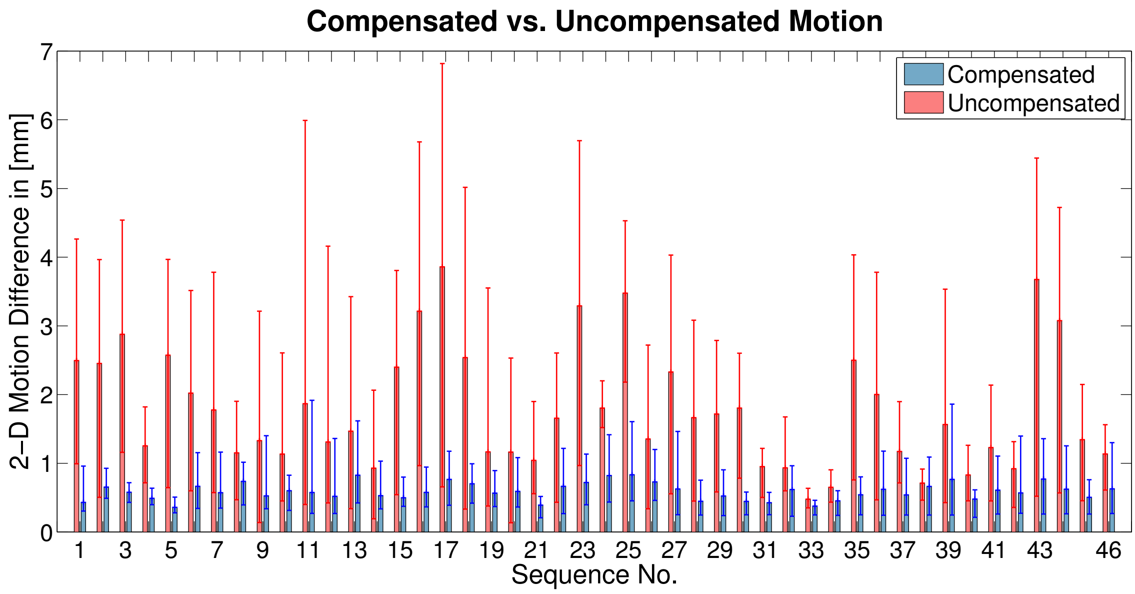

Figure 7.3: Comparison of the learning-based monoplane motion compensation to an uncompensated overlay. The 2-D motion compensation yields a mean tracking error was 0.58 mm with a minimum of 0.21 mm and a maximum of 1.92 mm. The observed motion was on average 1.83 mm with a minimum of 0.14 mm and a maximum of 6.82 mm.

and a total maximum error of 4.02 mm. The comparison between the learning-based and the filter-based approach are given in Figure 7.4.

For the clinical sequences, different mapping catheters with a thickness ranging between 1.3 mm and 2.1 mm were used. Our method is optimized for multi-core CPUs and achieves a frame rate of 16 fps on an Intel Quad Core with 2.20 GHz, for the filter-based approach. The learning-based method yields a frame rate of 10 fps. For both methods, the same optimization strategy and the same optimization parameters were used. The optimization of the objective function in Eq. (7.1) was performed by a multi-scale grid search using three scales. The function was evaluated 16,588 times for each frame in 0.27 ms on the aforementioned architecture.

7.4 Discussion and Conclusions

We developed a method for motion compensation in radio-frequency catheter ablation of atrial fibrillation. Our method is fast enough to compensate for cardiac and respiratory motion. The presented catheter tracking approach involves registration of a catheter model to a catheter segmented by a boosted classifier cascade. The target device for tracking is a circumferential mapping catheter. After manual initialization, the catheter model is tracked throughout the remainder of the sequence. Our evaluation comprising 46 clinical data sets yielded an average tracking error of 0.58 mm, with a minimum error of 0.21 mm and a maximum error of 1.92 mm for the learning-based approach. From this, we conclude that our method has the potential to significantly improve the accuracy of fluoroscopy overlay techniques for EP navigation. Verification can be achieved only by consid-

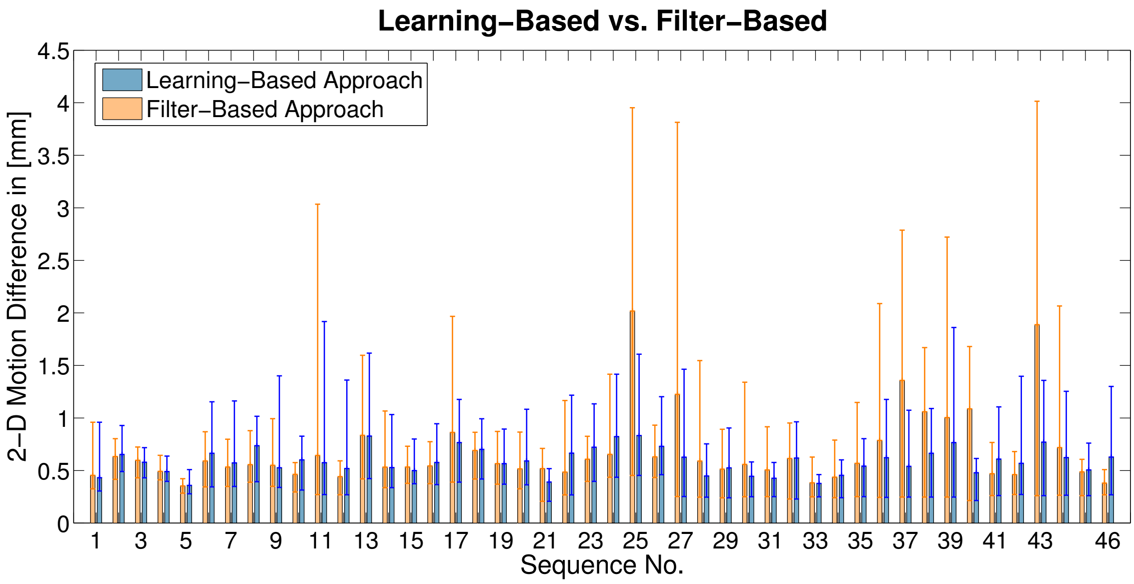

Figure 7.4: Comparison of the filter-based and the learning-based approach. The filter-based method yielded an average 2-D motion error of 0.61 mm with a minimum of 0.21 mm and a maximum of 4.02 mm. The learning-based method yielded an average 2-D motion error of 0.58 mm with a minimum of 0.21 mm and a maximum of 1.92 mm.

ering sequences that show the administration of contrast agent. This is a standard step during the procedure to enhance the structure of the left atrium. Figure 7.5 shows a comparison between a static overlay and a motion compensated overlay for a fluoroscopic sequence involving contrast agent. It has to be noted that the amount of contrast agent used for the angiogram of the left atrium, may hamper the segmentation of the circumferential mapping catheter.

The filter-based approach has on average a larger error of 0.61 mm $\pm$ 0.43 mm compared to the learning-based approach. This is mostly due to contrast agent injected into the left atrium, as shown in Figure 7.6 (b), or a barium swallow close to the catheter as in Figure 7.6 (a). Nevertheless, it can be seen that the learning-based approach is more robust in comparison to the filter-based approach. Even though the filter-based method works slightly better on some sequences, the overall mean and the number of outliers clearly favors the learning-based approach. The filter-based approach failed in a total number of 19 frames, compared to 1 frame for the learning-based method. A tracking fail is assumed if the error is larger than 2.00 mm. A clinically accepted error for cardiac applications is stated in [Este 08] as 2 mm. Even though this error is stated for 2-D/3-D registration of MRI data, we will use the same amount of 2.00 mm as a threshold to differentiate between success and failure. The filter-based method yielded a tracking success of 97.83 % compared to the 100.00 %[1] of the learning-based approach. A direct comparison between the two approaches is given in Table 7.1. As each frame is considered almost independently, our method does not suffer from drift - an often discussed issue for tracking algorithms relying on online updating of the appearance model.

[1]Please note that the success rate of 100.00 % for the learning-based approach was achieved on the available data only.

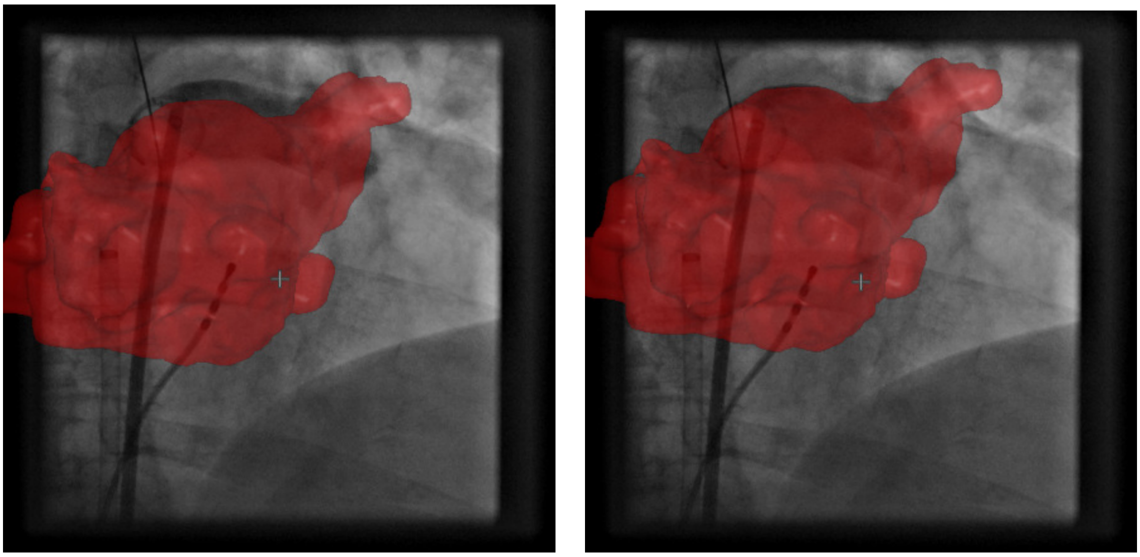

(a) (b)

Figure 7.5: Administration of contrast agent to outline the left atrium used to verify our motion compensation approach. The image to the left shows a left atrium segmented from a pre-operative MRI overlayed onto a fluoroscopic image without motion compensation. The image to the right shows the same fluoroscopic image, but the overlay image had been moved by our motion compensation approach, resulting in an apparently improved match of the outlines of the left atrium.

The proposed approach does not provide 3-D tracking as depth information is difficult to determine from a single view. Nevertheless, since the motion of the LA can be approximated by a 3-D rigid-body transform [Ecto 08b] and because the LA offers only limited space for a catheter to move about, 2-D motion estimation in the image plane may offer an acceptable approximation to arrive at a dynamic overlay.

The advantages of motion compensation by tracking the mapping catheter that is routinely used during catheter ablation has been demonstrated in [Bros 09a]. A direct comparison between an overlay with and without motion compensation is presented in Figure 7.7. Robust and efficient tracking is achieved using a hybrid method involving learning-based catheter classification and model-based registration. We do neither require a complex segmentation approach nor a complex registration algorithm. Instead, we found that the combination of both can also achieve remarkably good results. Furthermore, due to the fact that registration is used, motion estimation and compensation is essentially done in one step.

Due to the slow frame rates during EP procedures, usually 1 to 3 fps, the previous tracking result is used only to constrain the search region. Our current implementation achieves a frame rate of 10 fps, on the available data set. During EP procedures, a rather low dose is used to avoid high X-ray exposures to patients and to physicians. In turn, this leads to a lower image quality in comparison to other applications, e.g., guidewire-tracking in neuro-applications [Baer 03b, Barb 07, Palt 97]. Therefore, a more sophisticated but more robust catheter tracking algorithm is required to achieve a good performance. The tip of the ablation

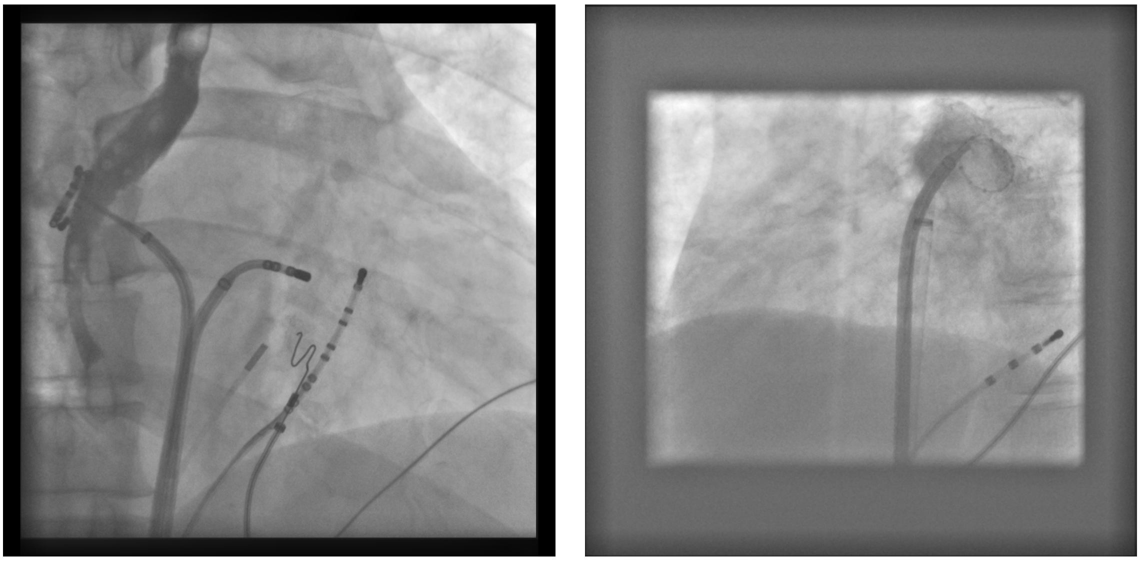

(a) (b)

Figure 7.6: Tracking failure for the filter-based approach. (a) In this frame of Seq. 11 the filter-based catheter tracking approach of the circumferential mapping catheter failed. For the same frame, the learning-based approach achieved its worst tracking result with an error of 1.92 mm. (b) In this frame of Seq. 27, when contrast agent is administered to the pulmonary vein, the tracking of the filter-based approach failed, but the learning-based approach worked.

catheters used for atrial fibrillation have a diameter between 1.2 mm and 1.8 mm. Considering a maximum error of 1.92 mm, the overlay would be wrongly translated by the same amount. This would roughly refer to one diameter of the ablation catheter. Our method is able to stay below the threshold of 2.00 mm in all frames in the data set.

For the remainder of this work, these two approaches will be referred to as monoplane methods for motion compensation. At some points, it will be differentiated between the filter-based and the learning-based approach.

Monoplane Tracking Approaches		
	Filter-Based	Learning-Based
Mean 2-D Error	0.61 mm $\pm$ 0.43 mm	**0.58 mm $\pm$ 0.22 mm**
Max 2-D Error	4.02 mm	**1.92 mm**
2-D Success Rate	97.83 %	**100.00 %**

Table 7.1: Comparison of the two monoplane tracking approaches. Please note that the success rate of 100.00 % for the learning-based approach was achieved on the available data only.

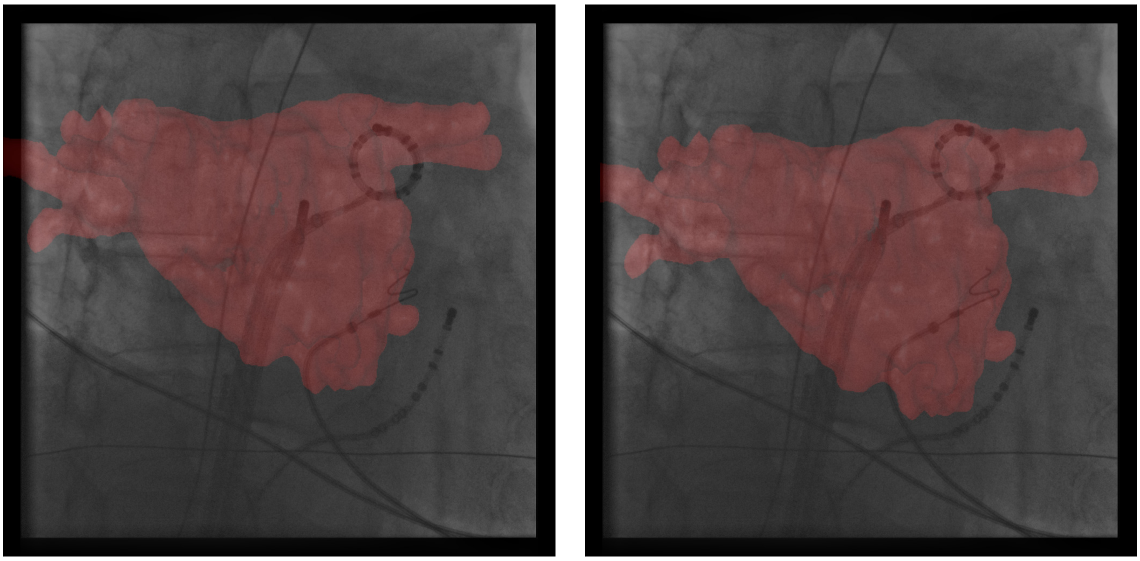

(a) (b)

Figure 7.7: Comparison of an overlay with and without motion compensation. (a) The current overlay approach involving a static image, rendered from the pre-procedural 3-D data set. It can be seen that a static overlay may not always exactly align with the current patient anatomy. Please note how the circumferential mapping catheter is starting to move outside the volume, here a segmented left atrium. (b) Here, the result of our proposed method for motion compensation can be seen. The rendered overlay moves synchronously with the circumferential mapping catheter firmly anchored at the upper left pulmonary vein, and it fits well.

CHAPTER 8

Biplane Motion Compensation by Registration

This chapter describes an image-based method to detect and compensate respiratory and cardiac motion in 3-D using simultaneous biplane fluoroscopy. Motion compensation is achieved by tracking the circumferential, ring-shaped mapping catheter from two views. First, we discuss model-based catheter tracking by 2-D/3-D image registration. Afterwards, we evaluate our method. Finally, we present our results, discuss them, and draw some conclusions. Parts of this chapter have been published in [Bros 09a, Bros 10a, Bros 10b, Bros 10c].

8.1 Motivation

The circumferential mapping catheter is one of the most prominent structures visible in EP fluoroscopy scenes providing a good feature for robust tracking. During the isolation of the four pulmonary veins using radio-frequency catheter ablation, the mapping catheter is typically fixed at the ostium of the PV that is considered for electrical isolation. By tracking the circumferential mapping catheter, we can obtain a motion estimate right at the ablation site, without the need of a pre-constructed motion model. Since we are using a biplane imaging system, the motion estimation takes place directly in 3-D and not only in 2-D. Once an estimate of the 3-D motion is available, we can translate and rotate the 3-D data set accordingly and recompute a new fluoroscopic overlay using perspective rendering methods.

8.2 Biplane Model-Based 2-D/3-D Registration

In the first frame of a biplane sequence, the circumferential mapping catheter is reconstructed from two views, as described in Chapter 2. Given the 3-D catheter model as $\mathbf{m}_i \in \mathbb{R}^3$, $i \in \{1,\ldots,E\}$ and $E \in \mathbb{N}$ the number of catheter model points. This catheter model is then successively registered to the remaining biplane frames of the sequence. The elliptical shape of the circumferential mapping catheter is used for tracking. Catheter tracking itself is performed by rigid registration [Hill 01] of the catheter model to a segmentation result derived from either a learning-based segmentation or a filter-based approach, as presented in Section 6.7. A distance map $\mathbf{I}_{\mathrm{DT,A/B}}$ is calculated for each image plane, denoted with the index $_{\mathrm{A}}$ for image plane A and $_{\mathrm{B}}$ for image plane B, respectively. It encodes the absolute distance from a pixel to its closest segmented catheter pixel. It also provides a smooth representation of the fluoroscopic image with a pronounced minimum around the shape of the mapping catheter to increase the capture range. Model-based catheter tracking in 3-D is achieved by performing 2-D/3-D registration. Hence, the reconstructed catheter model is translated by $\mathbf{T}_{\mathrm{u}}(\mathbf{h}) \in \mathbb{R}^{4\times 4}$ first. This translation is given by

$$\mathbf{T}_{\mathrm{u}}(\mathbf{h}) = \begin{pmatrix} 1 & 0 & 0 & h_x \\ 0 & 1 & 0 & h_y \\ 0 & 0 & 1 & h_z \\ 0 & 0 & 0 & 1 \end{pmatrix} \tag{8.1}$$

with the translation parameters in vector notation $\mathbf{h} = (h_x, h_y, h_z)^T$ and $h_x, h_y, h_z \in \mathbb{R}$. The catheter model is then projected onto the two image planes of the biplane C-arm system. The average distance between the projected points and the closest feature point, i.e., the circumferential mapping catheter in fluoroscopic images is efficiently calculated using the distance map introduced above. A suitable translation is found by optimizing

$$\hat{\mathbf{h}} = \arg\min_{\mathbf{h}} \sum_i \mathbf{I}_{\mathrm{DT,A}}(\mathbf{P}_A \cdot \mathbf{T}_{\mathrm{u}}(\mathbf{h}) \cdot \widetilde{\mathbf{m}}_i) + \sum_i \mathbf{I}_{\mathbf{DT,B}}(\mathbf{P}_B \cdot \mathbf{T}_{\mathrm{u}}(\mathbf{h}) \cdot \widetilde{\mathbf{m}}_i) \tag{8.2}$$

with the elliptical 3-D catheter model points $\widetilde{\mathbf{m}}_i \in \mathbb{R}^4$ in homogeneous coordinates. The projection matrices $\mathbf{P}_{\mathrm{A}}$ and $\mathbf{P}_{\mathrm{B}}$ do not need to be identical to the ones used for the 3-D model generation. A grid search was used for optimization. The search domain is given as $\Psi \subset \mathbb{R}^3$. Rotation was not considered, as an analysis of the left atrium performed by Ector, *et al.* [Ecto 08b] found that the rotation observed from the pulmonary vein ostia is mostly due to the contraction and expansion of the left atrium and the actual degree of rotation of the ostium was found to be much less. Previous studies found similar results [McLe 02]. Once the 3-D translation is estimated, it can be directly applied to the 3-D data set to move it in sync with the tracked device. A structogram of the presented motion compensation method is given in Structogram (8.1).

8.3 Evaluation and Results

The biplane motion compensation approaches were evaluated on the same data sets as the monoplane methods in Chapter 7. As the proposed methods are based

- Get Manual Input
- Generate Catheter Model $\mathbf{m}_i$
- For Every Frame
  - Compute Distance Transformed Images $\mathbf{I}_{\mathbf{DT},\mathrm{A}}$ and $\mathbf{I}_{\mathbf{DT},\mathrm{B}}$
  - $\hat{\mathbf{h}} = \mathbf{0}$, $\hat{\varepsilon} = \infty$
  - For $\mathbf{h} \in \Psi$
    - $\varepsilon = \sum_i \mathbf{I}_{\mathrm{DT,A}}(\mathbf{P}_A \cdot \mathbf{T}_{\mathrm{u}}(\mathbf{h}) \cdot \widetilde{\mathbf{m}}_i) + \sum_i \mathbf{I}_{\mathbf{DT},\mathrm{B}}(\mathbf{P}_B \cdot \mathbf{T}_{\mathrm{u}}(\mathbf{h}) \cdot \widetilde{\mathbf{m}}_i)$
    - $\varepsilon < \hat{\varepsilon}$
      - `true`: $\hat{\mathbf{h}} = \mathbf{h}$, $\hat{\varepsilon} = \varepsilon$
      - `false`:
  - Update Catheter Model $\mathbf{m}_i$ using $\hat{\mathbf{h}}$
  - Update Overlay using $\hat{\mathbf{h}}$

Structogram 8.1: Biplane Motion Compensation by Registration

on biplane images, the sequences were used as biplane sequences, yielding 23 clinical data sets for evaluation. Furthermore, these approaches facilitate motion compensation in 3-D. Hence, a 2-D tracking error and a 3-D tracking can be computed. The 2-D tracking error is calculated, similar to the 2-D error in Chapter 7, as the average 2-D distance between the projection of the 3-D catheter model and a 2-D gold-standard segmentation. We compare the result of the filter-based approach to the learning-based method. Since catheter tracking is performed in 3-D, we follow the evaluation in [Bros 10a, Bros 10b] to estimate the 3-D motion correction. Therefore, the tip of the mapping catheter was manually localized throughout all sequences by triangulating its 3-D position from biplane frames to get a reference point. In the next step, we applied our motion estimation approach to the catheter tip to move it from its 3-D position in the previous frame to the next frame. Because of that, we can compare the 3-D position reached by applying the estimated motion to the actual 3-D reference point obtained by triangulation [Bros 09c, Bros 09d]. Finally, the error was calculated as the Euclidean distance in 3-D space. Moreover, an error without performing motion compensation can be calculated was well. To this end, the 3-D distance between the first frame to all remaining frames is used to estimate the observed 3-D motion. As mentioned before, rotation was not considered.

For both approaches, the 2-D tracking errors for each sequence are given in Figure 8.1. Considering image plane A, the filter-based approach yielded a mean tracking error of 0.71 mm with a minimum error of 0.26 mm and a maximum of 5.30 mm. The results for image plane B were similar, with a mean error of 1.06 mm, a minimum of 0.33 mm and a maximum of 5.30 mm. Averaged over all frames and both image planes, the filter-based method yielded a mean 2-D error of 0.89 mm $\pm$ 0.58 mm.

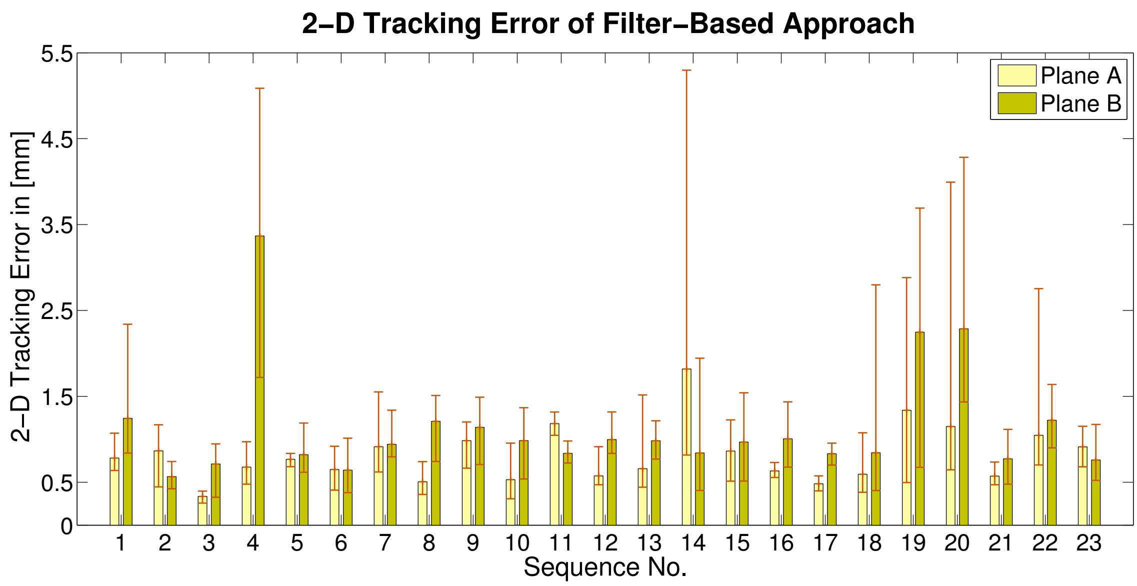

(a)

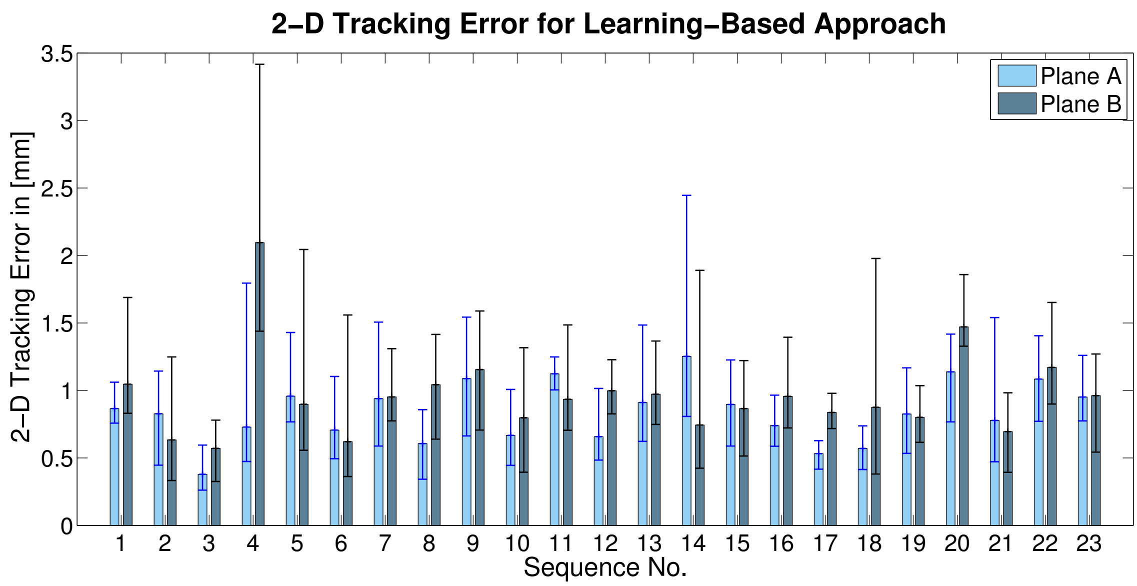

(b)

Figure 8.1: (a) The Two-dimensional tracking error of the filter-based approach yielded a mean tracking error of 0.89 mm $\pm$ 0.58 mm. (b) The tracking error of the learning-based approach yielded an average 2-D tracking error of 0.84 mm $\pm$ 0.35 mm.

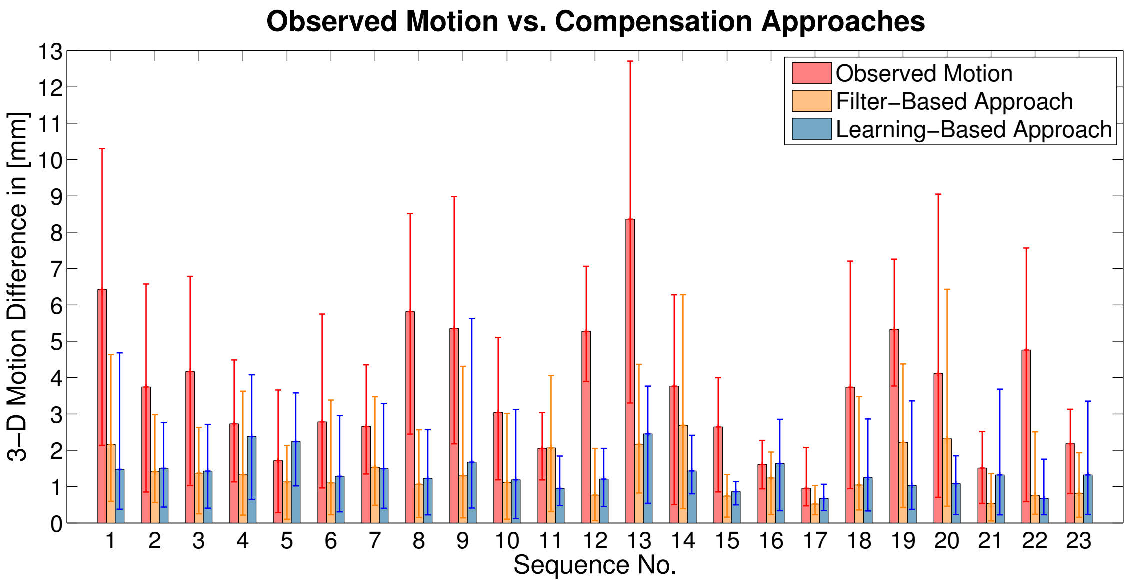

(a)

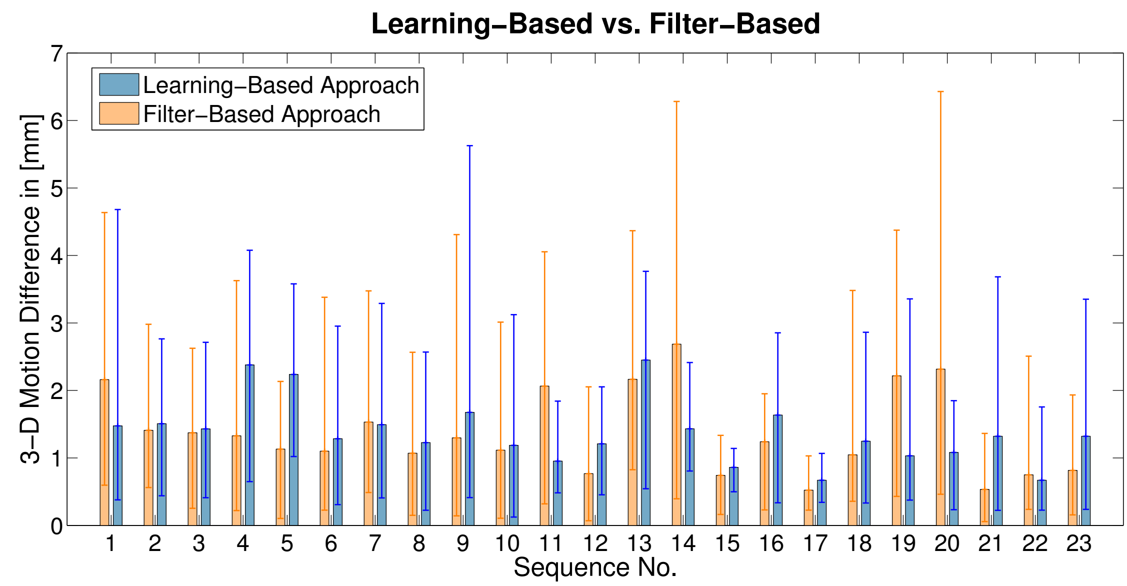

(b)

Figure 8.2: (a) Three-dimensional tracking error of the filter-based and the learning-based approach compared to the observed motion. (b) Comparison of the 3-D tracking error between the filter-based and the learning-based approach.

The learning-based approach yielded a mean tracking error of 0.77 mm with a minimum of 0.26 mm and a maximum of 2.45 mm for image plane A, and a mean error of 0.91 mm with a minimum of 0.33 mm and a maximum of 3.42 mm, for plane B, respectively. On average, the learning based method achieved a mean 2-D tracking error of 0.84 mm $\pm$ 0.35 mm.

To estimate the 3-D tracking, the motion of the circumferential mapping catheter was analyzed. The mean 3-D motion of the catheter was found to be 3.64 mm with a minimum observed motion of 2.09 mm and a maximum of 12.71 mm. The results compared to the tracking results of the filter-based and the learning-based method are presented in Figure 8.2 (a). The filter-based method yielded an average 3-D tracking error of 1.22 mm with a total minimum error of 0.06 mm and a total maximum of 6.43 mm. The learning-based method yielded an average error of 1.35 mm with a total minimum of 0.12 mm and a total maximum of 5.63 mm. A direct comparison between the filter-based and the learning-based approach are presented in Figure 8.2 (b).

Our method is optimized for multi-core CPUs and achieved a frame rate of 3 fps on an Intel Quad Core with 2.20 GHz, for the filter-based approach. The learning-based method yielded a frame rate of 2 fps. For both methods, the same optimization strategy and the same optimization parameters were used. The optimization of the objective function was performed by a grid search. The function was evaluated 62,197 times for each frame in 188.65 ms on the aforementioned architecture.

8.4 Discussion and Conclusions

Two methods for biplane catheter tracking have been presented and were compared against each other. Their application is 3-D motion compensation for radiofrequency catheter fibrillation. The methods are based on tracking of a circumferential mapping catheter in biplane fluoroscopy imaging. Catheter tracking is performed by 2-D/3-D registration of a 3-D elliptical catheter model to 2-D biplane images. During our experiments, we found that a catheter model consisting of 50 points yielded good results. Increasing the number of model points further did not provide an increase tracking accuracy. Both methods assume that the circumferential mapping catheter remains anchored at the pulmonary vein during ablation. Our clinical data suggests that the circumferential mapping catheter indeed moves very little with respect to the PV ostia when used to measure the electrical signals at the pulmonary ostia. When comparing the two tracking approaches, it can be seen, that the learning-based approach performs slightly better than the filter-based approach. The 2-D tracking error for the filter-based approach yielded 0.89 mm $\pm$ 0.58 mm, and the learning-based method yielded 0.84 mm $\pm$ 0.35 mm. The success rate of both methods is 95.50 % for the filter-based approach, and 98.99 % for the learning-based approach. Failure is considered, if the 2-D error is larger than 2.00 mm. Unfortunately, there is no clear statement about an acceptable tracking error. As in Chapter 7, we use a threshold of 2.00 mm as proposed for 2-D/3-D registration in [Este 08]. Given a 3-D error of 2.00 mm, this error would be magnified onto the fluoroscopic images by the projection geometry of the C-arm.

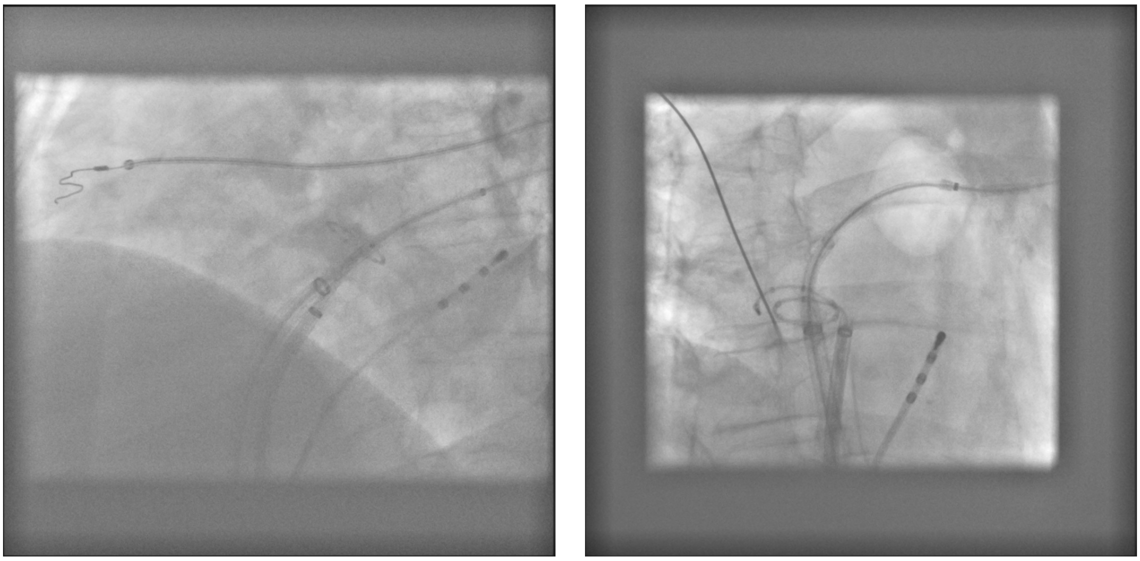

(a) (b)

Figure 8.3: Two frames of two different sequences in which catheter tracking was not as successful as in other sequences. (a) One frame of Seq. 19 which was acquired using a lower dose protocol than all other sequences. (b) One frame of Seq. 20 in which a cable from a defibrillation patch interferes with the catheter.

We will use the threshold of 2.00 mm for both, 2-D and 3-D, regardless of the magnification factor. The filter-based approach fails in a total of 58 frames over all sequences. Failures are due to different interference with contrast agent or other structures. The catheter is not well tracked in Seq. 11, partially due the nature of a non-perfect catheter model. It needs to be noted here, that the learning-based approach does not have this issue. In Seq. 14, contrast agent is injected into the PV such that the filter method fails to obtain a good segmentation and fails in 11 out of 21 frames. The same holds for Seq. 18, but the method quickly recovers after one or two frames. Seq. 19 was acquired with a lower dose protocol than all other sequences, see Figure 8.3 (a) for one frame of that sequence. In this case, the filter response is not as good as for the other sequences. In Seq. 20, a cable from a defibrillation patch is visible close to the circumferential mapping catheter, thus disturbing the tracking, see Figure 8.3 (b). The structure of this cable is similar to a catheter and therefore has the same filter response as the catheter. The learning-based method is able to suppress this structure. In 3-D, the method has a success rate of 86.63 %, using the same threshold value of 2.00 mm to determine a tracking failure. The error in 3-D is higher due to the reason, that errors in 2-D might add up for the 3-D error. In particular, the failures in Seq. 14 and Seq. 20 directly affect the 3-D accuracy. In addition to that, only translation was considered for tracking, but the localization of the catheter tip also incorporates its rotation. An example of a frame with and without motion compensation is given in Figure 8.4.

The learning-based approach only fails in 13 frames and performs slightly better than the filter-based approach. The higher tracking errors in Seq. 4 are partially due the nature of a non-perfect catheter model. In Seq. 14 and Seq. 18, the injec-

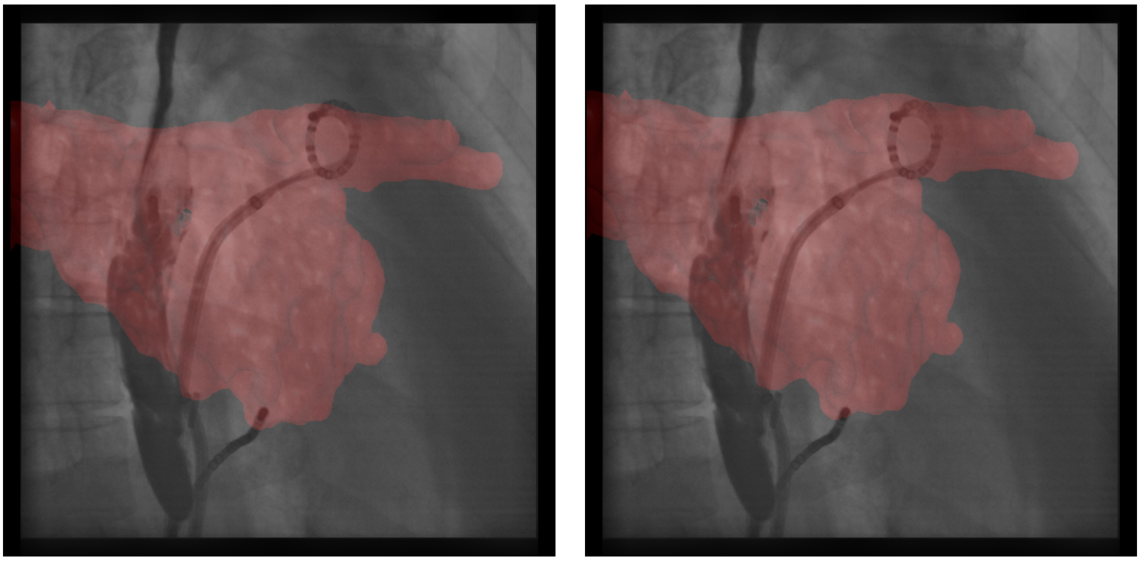

(a) (b)

Figure 8.4: Comparison of an overlay with and without motion compensation, shown for one image plane only. (a) Static overlay without motion compensation. (b) The same fluoroscopic image with motion compensation enabled.

Biplane Tracking Approaches		
	Filter-Based	Learning-Based
Mean 2-D Error	0.89 mm ± 0.58 mm	**0.84 mm ± 0.35 mm**
Max 2-D Error	5.30 mm	**3.42 mm**
2-D Success Rate	95.50 %	**98.99 %**
Mean 3-D Error	**1.22 mm ± 0.92 mm**	1.35 mm ± 0.81 mm
Max 3-D Error	6.43 mm	**5.63 mm**
3-D Success Rate	**86.63 %**	82.61 %

Table 8.1: Comparison of the two biplane tracking approaches.

tion of contrast agent leads to a tracking failure in one frame. In both cases, the tracking recovers after one frame.

When comparing the methods with the motion present in the available sequences, both methods are able to reduce the motion, see Figure 8.2 (a). Only in Seq. 16 an improvement is hardly observable, as the motion within the sequence is limited compared to the other data sets available. The reason hereof is unknown. As it is only a small sequence of 11 frames and it might have been acquired during breathold. Comparing the learning-based and the filter-based approaches in Figure 8.2 (b), it is not clear which method performs best. In some cases, the filter-based method performs better, in other cases, the learning-based method performs better. Nevertheless, the learning-based method seems preferable, as it has less outliers and has a maximal 3-D error of 5.63 mm.

In a direction comparison to the motion compensation methods in Chapter 7, it seems that the biplane methods are less accurate in 2-D. Unfortunately, the best 3-D positions may not automatically coincide with the best projected 2-D positions. This can be attributed to three factors. First of all, the segmentation is not perfect and therefore misclassifications may impair the results. Second, the model error from the elliptical reconstruction may add to this 2-D error, and third, calibration errors between image plane A and image plane B may affect the projection geometry. The last factor may be the major one, as the low 3-D error suggests. Nevertheless, the average 2-D error differs at about 0.40 mm which results in 2 to 3 pixels in the image.

The downside of the presented method is that it requires simultaneously biplane fluoroscopy acquisition. This is hardly performed in clinical practice as it results in a higher exposure of X-ray dose to the patient and to the physician. It might be used if a high accuracy is required as both images at the same time provide a better visualization of the ablation catheter. Considering the maximum error of the learning-based approach with 5.63 mm and the diameter of the ablation catheter being about 2.3 mm, a misplacement by the same amount would only be twice the diameter of the catheter. Considering the average 3-D error of 1.35 mm, it would be close to only half the size of the catheter. A direct comparison between the filter-based and the learning-based approach is given in Table 8.1. The use of more clinical data, in particular, with other structures such as surgical clips or trans-esophageal ultra-sound probes, would improve the quality of the classifier. Incorporating rotation into the tracking, as previously done in [Bros 10c, Bros 10b, Bros 09a] would also improve the tracking accuracy, but it might be questionable if the motion compensation would also be more accurate. A study involving 4-D data sets needs to be performed to further evaluate the behavior of the circumferential mapping catheter compared to the motion of the left atrium and the pulmonary veins. Unfortunately, such data was not available.

For the remainder of this work, these two approaches will be referred to as biplane methods for motion compensation. If not indicated otherwise, the learning-based approach is considered.

CHAPTER 9

Constrained Motion Compensation by Registration

This chapter describes an image-based method to detect and compensate respiratory and cardiac motion in 3-D using only monoplane fluoroscopy acquisition. Once, a 3-D catheter model had been generated, motion compensation is achieved by tracking the circumferential, ring-shaped mapping catheter from one view. This is facilitated by using a constrained 2-D/3-D registration that restricts the search directions in 3-D to be parallel to the imaging plane. Parts of this chapter have been published in [Bros 11e].

9.1 Motivation

Two different methods for motion compensation in atrial fibrillation ablation procedures have been proposed in Chapter 7 and in Chapter 8. Unfortunately, both methods have their advantages and disadvantages. The monoplane approach, on the one hand, works with monoplane image acquisitions, but each rotation of the C-arm requires a reinitialization of the catheter model. The biplane approach, on the other hand, uses a 3-D model, that would not require reinitialization, but it works only with simultaneous biplane fluoroscopy, which is rarely used in clinical practice. To improve the monoplane situation, we propose a constrained 2-D/3-D registration to perform motion compensation using a 3-D catheter model. The unconstrained method is similar to the biplane method in Chapter 8, but uses only one image plane. The generation of a 3-D catheter model requires only a single biplane shot and is performed as described in Chapter 2. This way, the increase of X-ray radiation to the patient is kept to a minimum. In the next section, the approach for a constrained registration of a 3-D catheter model to 2-D fluoroscopic images is described. In Section 9.3 an approach for an unconstrained registration to achieve motion compensation is briefly described. The results of both methods are given in Section 9.4 and are discussed in Section 9.5.

9.2 Constrained Model-Based 2-D/3-D Registration

In the registration step of our method, the actual motion compensation is performed by a constrained model-based 2-D/3-D registration. The catheter model is manually initialized in the first image pair of a biplane sequence. This manual input is used to reconstruct the catheter model in 3-D, as described in Chapter 2. The catheter model is tracked throughout the remainder of one monoplane sequence. Tracking itself is performed by rigid 2-D/3-D registration. The constraint used for registration is that the search range is restricted to all directions parallel to the imaging plane. No search is performed perpendicular to the optical plane, i.e., along the optical axis. This is not a major issue, because shifts along the optical axis merely result in size changes of the motion-compensated fluoroscopic overlay. A motion analysis of the LA, performed by Ector *et al.* [Ecto 08b], revealed that the dominant motion is in anterior-posterior and superior-inferior direction. They found that the degree of rotation is much less, and they contributed it to the deformation of the left atrium. The mismatch in depth between the 3-D overlay and the live fluoroscopic images mainly results in small changes of the LA size which we found negligible for augmented fluoroscopy applications in clinical practice. Therefore, we focused on the remaining dominant motion directions in superior-inferior and anterior-posterior directions. To carry out this constrained 2-D/3-D registration, the view direction $\mathbf{b} \in \mathbb{R}^3$ with $||\mathbf{b}||_2 = 1$ is obtained from the projection matrix $\mathbf{P} \in \mathbb{R}^{3\times4}$. The view direction is perpendicular to all vectors that are parallel to the image plane. Thus, two vectors $\mathbf{u} \in \mathbb{R}^3$ and $\mathbf{v} \in \mathbb{R}^3$ that are parallel to the image plane can be computed. For simplicity, we assume that both vectors have unity length, $||\mathbf{u}||_2 = 1$ and $||\mathbf{v}||_2 = 1$. Moving a point $\mathbf{w} \in \mathbb{R}^3$ parallel to the imaging plane is achieved by

$$\mathbf{w}^\star = \mathbf{w} + \eta\mathbf{u} + \zeta\mathbf{v} \tag{9.1}$$

with the translated point $\mathbf{w}^\star \in \mathbb{R}^3$ and the amount of translation defined by $\eta, \zeta \in \mathbb{R}$. We compute a transformation matrix $\mathbf{T}_\mathrm{c}(\eta,\zeta) \in \mathbb{R}^{4\times4}$ as

$$\mathbf{T}_\mathrm{c}(\eta,\zeta) = \begin{pmatrix} 1 & 0 & 0 & \eta u_x + \zeta v_x \\ 0 & 1 & 0 & \eta u_y + \zeta v_y \\ 0 & 0 & 1 & \eta u_z + \zeta v_z \\ 0 & 0 & 0 & 1 \end{pmatrix} \tag{9.2}$$

with $\mathbf{u} = (u_x, u_y, u_z)^T$ and $\mathbf{v} = (v_x, v_y, v_z)^T$. The objective function for the constrained registration is then defined by using the values of the distance transformed image $\mathbf{I}_\mathrm{DT}$ as cost function by

$$\hat{\eta}, \hat{\zeta} = \arg\min_{\eta,\zeta} \sum_i \mathbf{I}_\mathrm{DT}\left(\mathbf{P} \cdot \mathbf{T}_\mathrm{c}(\eta,\zeta) \cdot \mathbf{m}_i\right). \tag{9.3}$$

A grid search was used for optimization. The search domain is given as $\Phi \subset \mathbb{R}^2$. The catheter segmentation that results in the distance transformed image $\mathbf{I}_\mathrm{DT}$ was

- Get Manual Input
- Generate Catheter Model $\mathbf{m}_i$
- Compute Constrained Translation Matrix $\mathbf{T}_{\mathrm{c}}$
- For Every Frame
  - Compute Distance Transformed Image $\mathbf{I}_{\mathrm{DT}}$
  - $\hat{\eta} = \mathbf{0}, \hat{\varepsilon} = \infty$
  - For $(\eta, \zeta)^T \in \Phi$
    - $\varepsilon = \sum_i \mathbf{I}_{\mathrm{DT}} \left(\mathbf{P} \cdot \mathbf{T}_{\mathrm{c}}(\eta, \zeta) \cdot \mathbf{m}_i \right)$
    - $\varepsilon \quad < \quad \hat{\varepsilon}$
      - true: $\hat{\eta} = \eta, \hat{\zeta} = \zeta, \hat{\varepsilon} = \varepsilon$
      - false:
  - Update Catheter Model $\mathbf{m}_i$ using $\mathbf{T}_{\mathrm{c}}(\hat{\eta}, \hat{\zeta})$
  - Update Overlay using $\mathbf{T}_{\mathrm{c}}(\hat{\eta}, \hat{\zeta})$

Structogram 9.1: Constrained Motion Compensation by Registration

described in Chapter 6. Rotation is not considered, as we are primarily interested in the compensation of breathing motion which occurs in axial direction. The projection matrix considered for projecting the model into the imaging plane is not required to be one of the projection matrices used for model generation, i.e., the C-arm can be moved in between model generation and tracking. Given the parameters $\hat{\eta}, \hat{\zeta}$, found by a grid search, the catheter model can be updated using $\mathbf{T}_{\mathrm{c}}(\hat{\eta}, \hat{\zeta})$. The same transformation is then applied to the 3-D volumetric data set that is used for the image overlay. This way, we can achieve a 3-D motion compensation for monoplane fluoroscopic images. A structogram of the constrained approach for motion compensation is given in Structogram (9.1).

9.3 Unconstrained Model-Based 2-D/3-D Registration

One might consider using an unconstrained approach to perform catheter tracking for motion compensation. This can be achieved by using the transformation matrix

$$\mathbf{T}_{\mathrm{u}}(\mathbf{h}) = \begin{pmatrix} 1 & 0 & 0 & h_x \\ 0 & 1 & 0 & h_y \\ 0 & 0 & 1 & h_z \\ 0 & 0 & 0 & 1 \end{pmatrix} \tag{9.4}$$

with the translation parameters in vector notation $\mathbf{h} = (h_x, h_y, h_z)^T$, as used for biplane motion compensation in Chapter 8. Incorporating this into Eq. (9.3) yields a three-dimensional optimization problem, which can be formulated as

$$\hat{\mathbf{h}} = \arg\min_{\mathbf{h}} \sum_i \mathbf{I}_{\mathrm{DT}} \left(\mathbf{P} \cdot \mathbf{T}_{\mathrm{u}}(\mathbf{h}) \cdot \mathbf{m}_i \right). \tag{9.5}$$

Get Manual Input

Generate Catheter Model $\mathbf{m}_i$

For Every Frame

- Compute Distance Transformed Image $\mathbf{I}_{\mathbf{DT}}$
- $\hat{\mathbf{h}} = \mathbf{0}$, $\hat{\varepsilon} = \infty$
- For $\mathbf{h} \in \Psi$
  - $\varepsilon = \sum_i \mathbf{I}_{\mathrm{DT}} \left(\mathbf{P} \cdot \mathbf{T}_{\mathrm{u}}(\mathbf{h}) \cdot \mathbf{m}_i \right)$
  - $\varepsilon \quad < \quad \hat{\varepsilon}$
    - `true`: $\hat{\mathbf{h}} = \mathbf{h}$, $\hat{\varepsilon} = \varepsilon$
    - `false`
- Update Catheter Model $\mathbf{m}_i$ using $\hat{\mathbf{h}}$
- Update Overlay using $\hat{\mathbf{h}}$

Structogram 9.2: Unconstrained Motion Compensation by Registration

A grid search was used for optimization. The search domain is given as $\Psi \subset \mathbb{R}^3$. The resulting 3-D translation given by $\mathbf{T}_{\mathrm{u}}(\hat{\mathbf{h}})$ could then be applied to the 3-D volume instead of $\mathbf{T}_{\mathrm{c}}(\hat{\eta}, \hat{\zeta})$. A structogram of the unconstrained approach for motion compensation is given in Structogram (9.2).

9.4 Evaluation and Results

For evaluation, the same 23 biplane fluoroscopic sequences as in Chapter 7 and Chapter 8 were used. As the proposed method facilitates 3-D motion compensation using only monoplane fluoroscopy, the 23 biplane sequences were split into 46 monoplane sequences, as before in Chapter 7. This way, we obtained a total frame number of 1,288 frames to evaluate catheter tracking. The 2-D tracking error is calculated as the average 2-D distance between the projection of the 3-D catheter model and a 2-D gold-standard segmentation as described in Chapter 7. Since catheter tracking is performed in 3-D, we follow the evaluation in Chapter 8 to estimate the 3-D motion correction. Therefore, the tip of the mapping catheter was manually localized throughout all sequences by triangulating its 3-D position from biplane frames to get a reference point. In this case, the 3-D position of the mapping catheter for one biplane sequence was use to evaluate the two corresponding monoplane sequences. The motion estimation approach was applied to the catheter tip to move it from its 3-D position in the previous frame to the next frame. Because of that, the 3-D position could be compared by applying the estimated motion to the actual 3-D reference point obtained by triangulation [Bros 09c, Bros 09d]. The initial 3-D information about the position of the circumferential mapping catheter was obtained from the 3-D reconstruction of the mapping catheter. Finally, the error was calculated as the Euclidean distance in 3-D space. Moreover, an error without performing motion compensation can

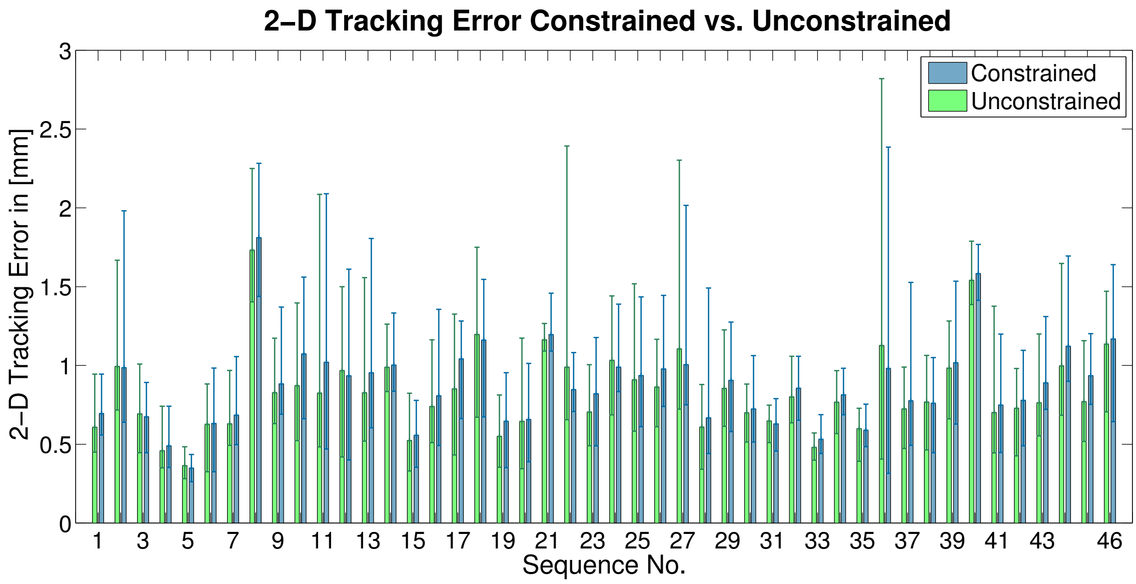

Figure 9.1: Two-dimensional tracking error for all 46 sequences. For each sequence, the average error, minimum error, and maximum error is given. The unconstrained approach yielded an average error of 0.80 mm ± 0.32 mm, compared to 0.85 mm ± 0.34 mm for the constrained approach.

be calculated as well. To this end, the 3-D distance between the first frame to all remaining frames is used to estimate the observed 3-D motion. In addition to that, we compare our constrained approach with an unconstrained approach.

The unconstrained approach yielded an average 2-D tracking error of 0.80 mm with a total minimum of 0.28 mm and a total maximum of 2.82 mm. Considering the 2.00 mm threshold for success or failure in tracking as used in Chapter 7 and Chapter 8, the unconstrained method achieved a success rate of 99.46 %. The proposed constrained approach yielded an average error of 0.85 mm with a total minimum of 0.26 mm and a total maximum of 2.39 mm. The constrained method tracked the catheter successfully in 99.38 % of the frames. A comparison for each sequence is given in Figure 9.1. Both tracking methods fail in Sequence #36. This is mainly due the injection of contrast agent injected into the pulmonary vein via the catheter sheath that holds the circumferential mapping catheter. One frame of Sequence #36 is given in Figure 9.2.

The unconstrained method yielded an average 3-D error of 2.45 mm with a total minimum of 0.16 mm and a total maximum of 8.40 mm. Considering the same 2.00 mm threshold, the unconstrained method achieved a success rate of 36.80 %. The constrained method yielded an average 3-D error of 1.50 mm with a total minimum of 0.06 mm and a total maximum of 7.48 mm. We found the success rate to be 77.62 %. The results of both methods are given in Figure 9.3. In addition to that, a comparison to the observed motion was also performed. The results are shown in Figure 9.4. As biplane motion compensation methods are also available, Figure 9.5 shows a comparison with the learning-based biplane approach from Chapter 8.

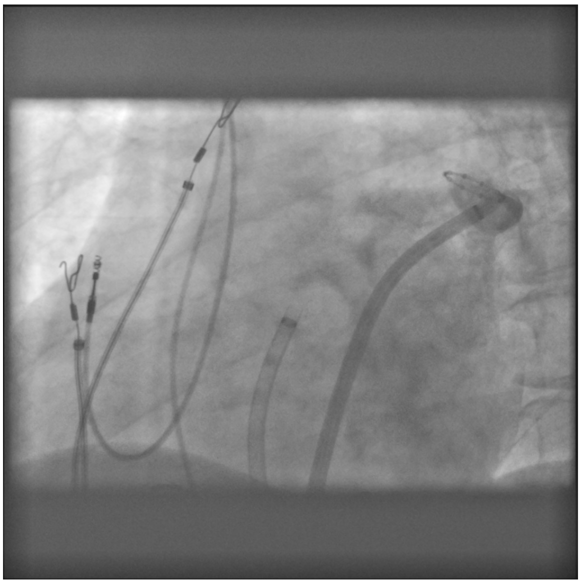

Figure 9.2: One frame of Sequence #36. Catheter tracking is mainly compromised when contrast agent is injected into the pulmonary vein via the catheter sheath that holds the circumferential mapping catheter.

Performing motion compensation in 3-D using only monoplane imaging is difficult as depth information is hard to determine from only one view direction [Fall 09, Fall 10a, Fall 10b]. The amount of the error in view direction can be used to further judge the performance of the motion estimation method. The average 3-D error along the view direction for the unconstrained method was 2.12 mm with a total minimum of 0.01 mm and a total maximum of 8.35 mm. The comparison of the 3-D errors for the unconstrained approach are given in Figure 9.6. The same evaluation for the constrained method yielded an average 3-D error along the view direction of 0.82 mm with a total minimum of 0.01 mm and a total maximum of 7.43 mm. The results are given in Figure 9.7. Our method is optimized for multi-core CPUs and achieves a frame rate of 8 fps on an Intel Quad Core with 2.20 GHz. The optimization of the objective function was performed by a grid search. The function was evaluated 3,240 times for each frame in 7.36 ms on the aforementioned architecture.

9.5 Discussion and Conclusions

The constrained method performs better compared to the unconstrained method in 3-D. This is not the fact regarding the 2-D tracking errors. The unconstrained method performed slightly better than the constrained method, with 0.80 mm$\pm$ 0.32 mm versus 0.85 mm $\pm$ 0.34 mm in 2-D. The same holds for the success rates of 99.46 % versus 99.38 %. An example of motion compensation is given in Figure 9.8. Both methods have their largest 2-D tracking errors in Sequence #36 when contrast agent is injected into the pulmonary vein via the catheter sheath that holds the circumferential mapping catheter. Considering the 3-D errors of 2.45 mm $\pm$ 1.26 mm versus 1.50 mm $\pm$ 0.94 mm, the constrained method performs much better than

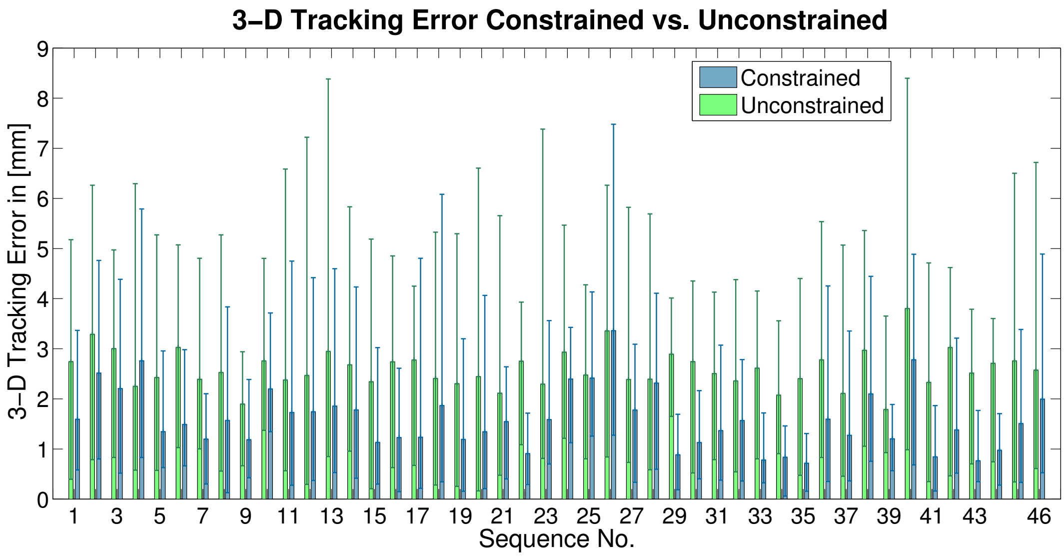

Figure 9.3: Comparison of 3-D tracking errors between the constrained and the unconstrained approach. The tracking errors are given for all 46 sequences. For each sequence, the average, minimum, and maximum for the tracking error is given. The unconstrained approach yielded 2.45 mm ± 1.26 mm, compared to the constrained approach yielding 1.50 mm ± 0.94 mm.

the unconstrained approach. This becomes even more clear when taking a look at the success rate of 77.62 % for the constrained approach versus the success rate of 36.80 % for the unconstrained method. As shown in Figure 9.4, the constrained method is able to reduce the 3-D error compared to the observed motion. The observed motion can be interpreted as the 3-D error of a static overlay. The unconstrained method performs much worse and, in some cases, even increases the error. This is not true for all cases, as in some of our data sets, the maximum error of the constrained approach is larger when compared to the unconstrained approach, see Sequences #18 and #26 in Figure 9.1.

On average, however, the constrained method easily outperforms the unconstrained approach. Taking into account the error along the view direction in Figure 9.6 and Figure 9.7, the largest part of the 3-D error is along the view direction. For the unconstrained method, this can be interpreted as failure to correctly estimate the depth from a single view. The constrained method, however, is not trying to perform any kind of depth estimation, explaining the high error along the view direction. When comparing the error in view direction, Figure 9.7, with the 2-D tracking error, Figure 9.1, one can see that if the tracking in 2-D was accurate, the 3-D error is mostly along the view direction. If the tracking failed in 2-D, the error in 3-D might not be only along the view direction. The comparison to the learning-based biplane approach in Figure 9.5 shows that the constrained method performs nearly as good as the biplane approach, whereas the unconstrained approach yields much larger errors. A direct comparison between the constrained and unconstrained approaches is given in Table 9.1.

The proposed method, when compared to the previous proposed methods, has some advantages. The monoplane approach in Chapter 7 can not deal with C-arm

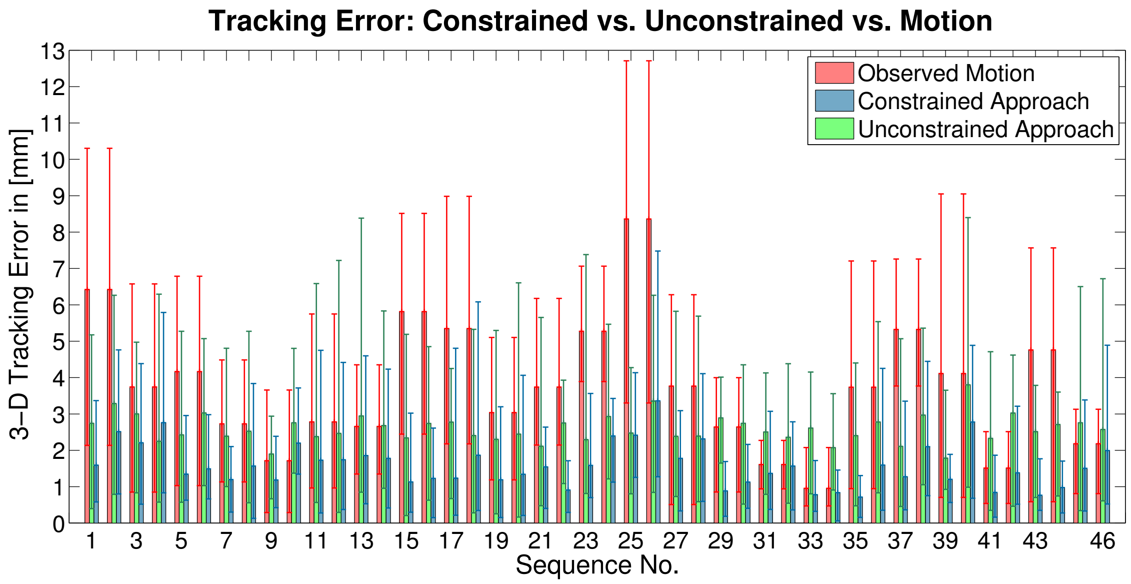

Figure 9.4: Comparison of 3-D tracking errors between the constrained and the unconstrained approach as well as the observed 3-D motion. The tracking errors are given for all 46sequences. For each sequence, the average, minimum, and maximum for the tracking error is given. The unconstrained approach yielded 2.45 mm ± 1.26 mm, compared to the constrained approach yielding 1.50 mm ± 0.94 mm. The observed motion was 3.64 mm ± 0.29 mm.

rotation and requires re-initialization of the catheter model before tracking and motion compensation can be continued. The biplane approach in Chapter 8 requires simultaneous biplane fluoroscopy, which would mean more dose for patient and physician. The proposed constrained method requires only a single biplane fluoroscopic shot for model generation. Once the model is generated, the C-arms can be rotated and motion compensation is still feasible. The limitation of our method is mainly related to the fact that motion along the view direction cannot be taken into account as depth information is hard to determine from monoplane projection images. To achieve a depth correction, a perfect segmentation of the catheter would be required and, in addition, we would also need to know the exact dimensions of the catheter in 3-D, i.e., its diameter and its thickness. Any noise in the 2-D segmentation or at the 3-D model would decrease the accuracy of the depth estimate, as can be seen when considering the results for the unconstrained approach. To avoid this problem we have chosen to use only search directions parallel to the imaging plane. As a price to pay, we accept that the 3-D error will not be as good as it is for the biplane approach. As in the previously presented methods, ours approach does not require a perfect segmentation of the circumferential mapping catheter, because the registration method can compensate for segmentation errors. For the remainder of this work, this approach will be referred to as constrained methods for motion compensation.

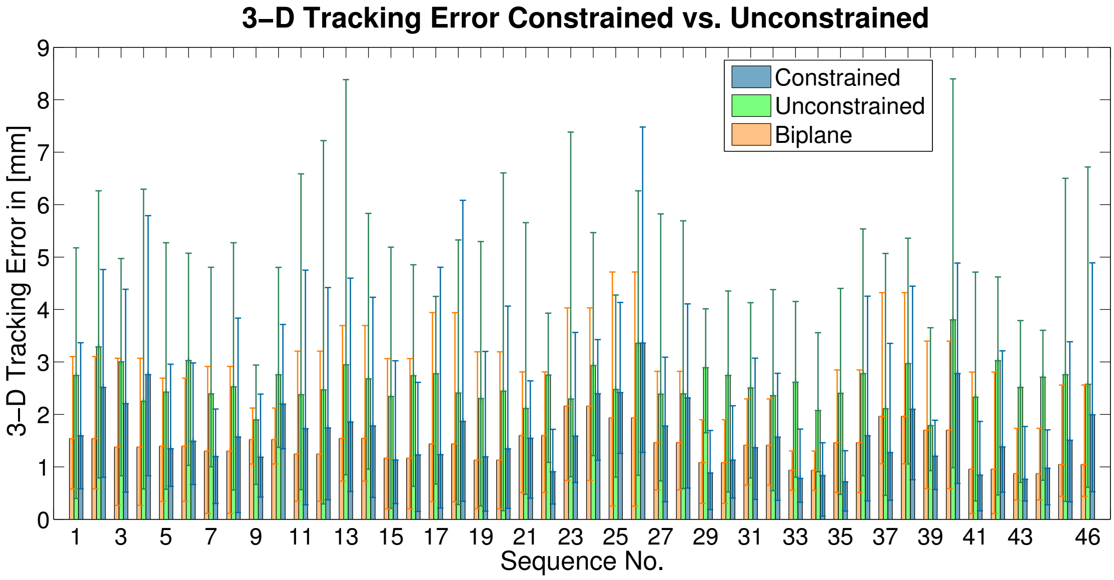

Figure 9.5: Comparison of 3-D tracking errors between the constrained and the unconstrained approach as well as the learning-based biplane appraoch.

Constrained vs. Unconstrained		
	Unconstrained	Constrained
Mean 2-D Error	**0.80 mm ± 0.32 mm**	0.85 mm ± 0.34 mm
Max 2-D Error	2.82 mm	**2.39 mm**
2-D Success Rate	**99.46 %**	99.38 %
Mean 3-D Error	2.45 mm ± 1.26 mm	**1.50 mm ± 0.94 mm**
Max 3-D Error	8.40 mm	**7.48 mm**
3-D Success Rate	36.80 %	**77.62 %**

Table 9.1: Comparison of constrained and unconstrained motion compensation approaches.

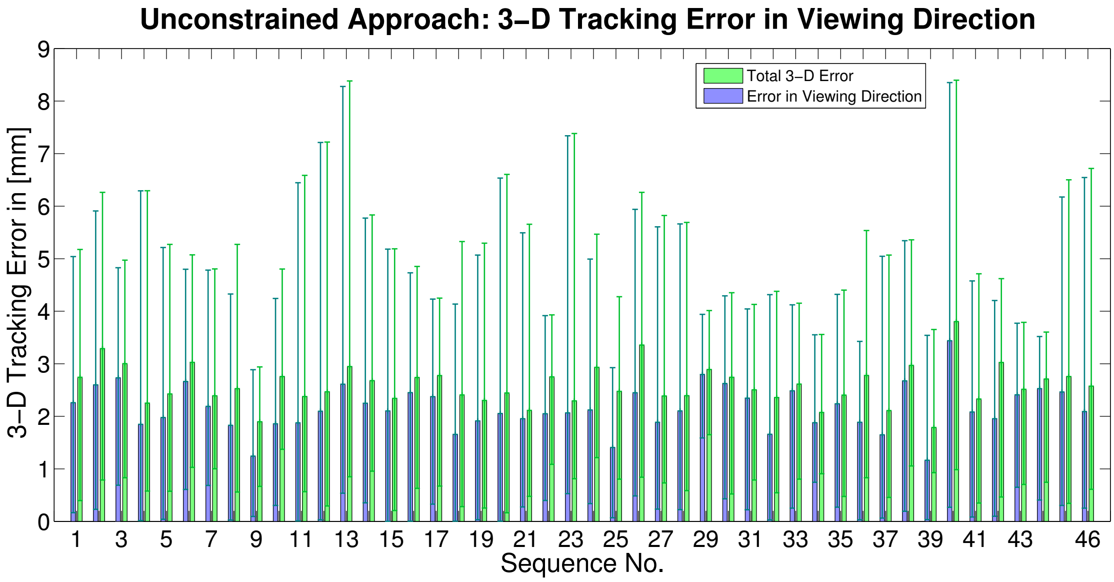

Figure 9.6: The 3-D error of the unconstrained method compared to the total 3-D error. The error in view direction was 2.12 mm ± 1.37 mm, compared to the total error of 2.45 mm ± 1.26 mm.

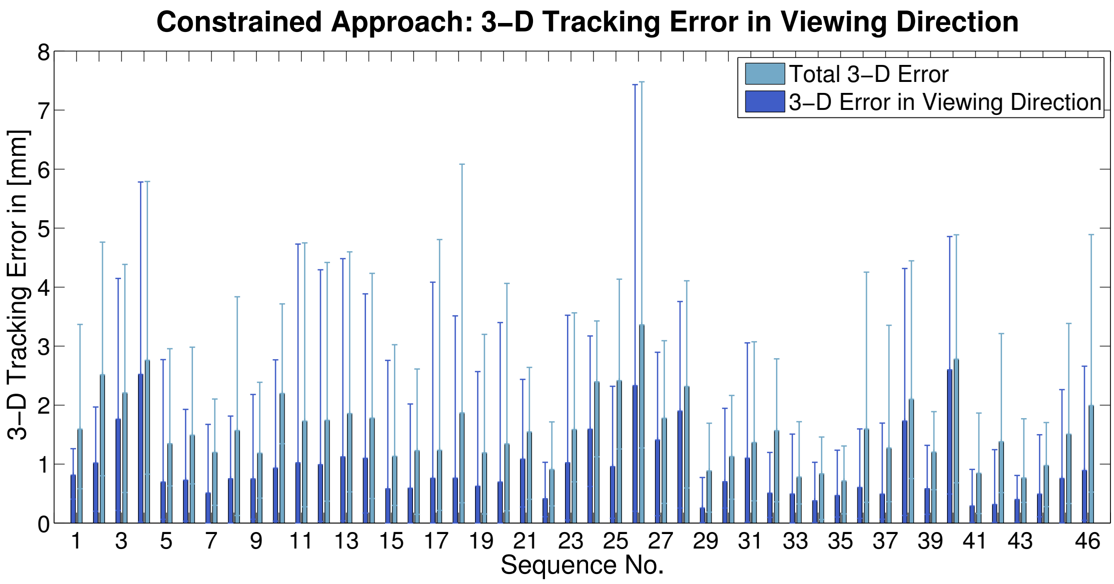

Figure 9.7: The 3-D error of the constrained method compared to the total 3-D error. The error in view direction was 0.82 mm ± 0.85 mm, compared to the total error of 1.50 mm ± 0.94 mm.

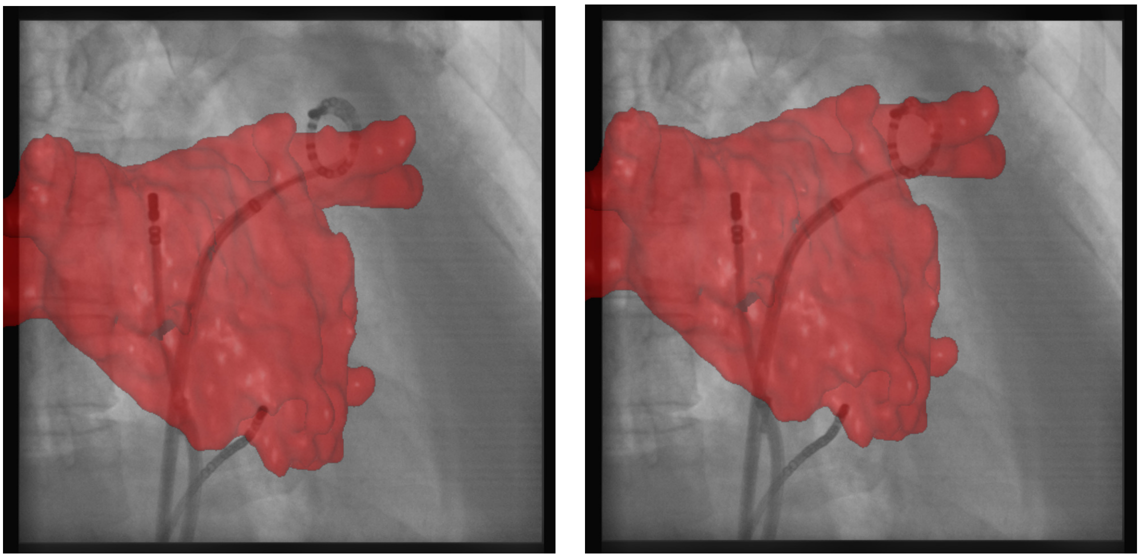

(a) (b)

Figure 9.8: A comparison showing the difference if motion compensation is considered or not. (a) One frame of a sequence without motion compensation. (b) The same frame as in (a) but this time with motion compensation.

CHAPTER 10

Patient-Specific Motion Compensation by Registration

In this chapter, an image-based method to detect and compensate respiratory and cardiac motion in 3-D using only monoplane fluoroscopy is detailed. This method consists of three steps. First, a 3-D catheter model needs to be generated. Second, a biplane training phase is required to train a patient-specific motion model. The third step is the application of the motion model. The motion model is used to constrain the search region of the 2-D/3-D registration used for motion compensation. Parts of this chapter have been published in [Bros 11d].

10.1 Motivation

The method described in Chapter 9 has shown, that it is advantageous to constrain the 2-D/3-D registration when used for motion compensation. This was achieved by restricting the search region for registration to directions parallel to the image plane. Compensation for movement parallel to the view direction is omitted. To achieve motion compensation in this direction, prior knowledge about the movement of the circumferential mapping catheter needs to be incorporated. Such information can be gathered when using a training phase. The training phase estimates the motion of the CFM catheter at the PV using a biplane sequence in which the mapping catheter is tracked using an unconstrained 2-D/3-D registration. The principal motion axis is determined from the trajectory established during the tracking training phase. This axis is considered a patient-specific motion model. As the main axis of the motion by itself is not sufficient to provide a good search space for a constrained registration, another axis is needed. We decided to use a vector perpendicular to the view direction and the main axis, because the search region for the constrained registration can then be reduced to a 2-D search space, spanned by the principal axis and a vector parallel to the image plane. This allows us to not only to track motion that is parallel to the image plane, but also to capture some depth information with respect to the pre-acquired motion model. Our constrained approach can be simply stated as dimension reduction of the search space from 3-D to 2-D.

Our method works as follows. As input, a 3-D catheter model of the circumferential mapping catheter is required. The generation of the model is described in Chapter 2. A short biplane sequence is used to generate 3-D samples of the position of the circumferential mapping catheter recorded during a training phase. The principal axis derived from the sample positions is taken as main direction of PV motion. The motion model should be acquired in the same state with respect to heart rate and presence of arrhythmia that will be present during the application of the motion model. In the next step, we apply a constrained model-based 2-D/3-D registration to track the circumferential mapping catheter in 3-D using only monoplane fluoroscopy. To this end, the motion model estimated during the training phase limits the allowed motion to two directions. The first motion is parallel to the principal motion axis. The second allows motion parallel to the image plane.

The patient-specific motion model is presented in the next section. This model is estimated during a training phase in which the circumferential mapping catheter is tracked using biplane fluoroscopic imaging. The training is performed on a biplane sequence to obtain the main motion axis. In the third section, the constrained 2-D/3-D registration based on the motion model is introduced. In the last section, we discuss our results.

10.2 Motion-Model Generation

The motion model is set up using a biplane 2-D/3-D registration of the previously generated 3-D catheter model to biplane fluoroscopic images acquired during a training phase. The catheter is segmented using the learning-based method as presented in Chapter 6, which leads to the distance transformed images $\mathbf{I}_{\mathrm{DT,A},t}$ for plane A, and $\mathbf{I}_{\mathrm{DT,B},t}$ for plane B, respectively, at time t. We allow for a full 3-D search of the catheter model to get the best fit of the catheter model to each 2-D fluoroscopic image, as described in Chapter 8. In this case, the transformation matrix is written as

$$\mathbf{T}_{\mathrm{u}}(\mathbf{h}) = \begin{pmatrix} 1 & 0 & 0 & h_x \\ 0 & 1 & 0 & h_y \\ 0 & 0 & 1 & h_z \\ 0 & 0 & 0 & 1 \end{pmatrix} \tag{10.1}$$

with the translation parameters $\mathbf{h} = (h_x, h_y, h_z)^T$. The cost function can be formulated as

$$\begin{aligned} \hat{\mathbf{h}} = \arg\min_{\mathbf{h}} \sum_i \; & \mathbf{I}_{\mathrm{DT,A},t+1}\left(\mathbf{P}_A \cdot \mathbf{T}_{\mathrm{u}}(\mathbf{h}) \cdot \mathbf{m}_{i,t}\right) \\ + \; & \mathbf{I}_{\mathrm{DT,B},t+1}\left(\mathbf{P}_B \cdot \mathbf{T}_{\mathrm{u}}(\mathbf{h}) \cdot \mathbf{m}_{i,t}\right) \end{aligned} \tag{10.2}$$

with the projection matrices $\mathbf{P}_A$ for image plane A, and $\mathbf{P}_B$ for plane B, as well as the 3-D catheter model, $\mathbf{m}_{i,t}$, at time t. Optimization is performed using a grid search approach [Duda 01]. The search domain is given as $\Psi \subset \mathbb{R}^3$. The projection matrix used during the training phase tracking is not required to be one of the projection matrices used for model generation, i.e., the C-arm can be moved in between catheter model generation and the training phase. The same holds for the actual motion compensation. Given the parameters $\hat{\mathbf{h}}$ found by the nearest-neighbor search, the catheter model can be updated to $\mathbf{m}_{i,t+1} \in \mathbb{R}^4$ by

$$\forall i : \mathbf{m}_{i,t+1} = \mathbf{T}_\mathrm{u}(\hat{\mathbf{h}}) \cdot \mathbf{m}_{i,t}. \tag{10.3}$$

During the training phase, the same transformation $\mathbf{T}_u(\hat{\mathbf{h}})$ can be applied to the 3-D volumetric data set that is used for image overlay. This way, a 3-D motion compensation can be shown during the training phase.

The patient specific motion model is calculated from the circumferential mapping catheter positions. To this end, the catheter model for every time step is reduced to the center of the model by

$$\overline{\mathbf{m}}_t = \frac{1}{E} \sum_i \mathbf{m}_{i,t}. \tag{10.4}$$

The principal axis for the catheter centers $\overline{\mathbf{m}}_t$ is calculated by a principal component analysis, representing the main motion vector $\mathbf{g}_m \in \mathbb{R}^3$ with $||\mathbf{g}_m||_2 = 1$. For the motion model, only the principal axis is considered, as tracking inaccuracies during the training phase might produce outliers.

10.3 Model-Constrained 2-D/3-D Registration

In this section, motion compensation by model-constrained registration is introduced. The assumption for our approach is that only monoplane fluoroscopic imaging is available. Our proposed constraint is the reduction of the 3-D search space to a 2-D search space, by introducing a second feasible vector that is perpendicular to the view direction and the principal motion vector. This results in a 2-D search plane for the catheter model to be semi-parallel to the image plane. The cost function is the distance transform $\mathbf{I}_\mathrm{DT}$ of the post-processed segmentation result, as detailed in Chapter 6. By using the main motion vector, the 2-D search space also allows some depth estimation from a single X-ray view.

Physicians position their C-arms in standard view positions, usually only angulations in left-anterior-oblique (LAO), posterior-anterior (PA), or right-anterior-oblique (RAO) direction are used. Angulations towards cranial or caudal directions are, at least to the knowledge of the authors, not common for EP procedures. The angle between the two C-arm is usually between 60^o degrees and 90^o degrees. This enables us to capture most of the motion during the training phase. During the application of the patient specific motion model, the common positions of the the C-arm in an LAO, PA, or RAO position, provides enough information that most of the motion is captured.

To carry out our constrained 2-D/3-D registration, we determine the view direction $\mathbf{b} \in \mathbb{R}^3$ with $||\mathbf{b}||_2 = 1$ from the projection matrix $\mathbf{P} \in \mathbb{R}^{3\times 4}$ [Hart 04]. The second vector required to estimate the second search direction, which is perpendicular to the view direction and the main motion axis, is given by

$$\mathbf{g}_p = \mathbf{g}_m \times \mathbf{b}. \tag{10.5}$$

The vector $\mathbf{g}_p$ can also be considered as plane-specific translation vector. Any point on that plane can be represented by a linear combination of these two vectors $\mathbf{g}_p$ and $\mathbf{g}_m$. This translation can be rewritten in matrix notation as

$$\mathbf{T}_\mathrm{c}(\eta, \zeta) = \begin{pmatrix} 1 & 0 & 0 & \eta g_{p,x} + \zeta g_{m,x} \\ 0 & 1 & 0 & \eta g_{p,y} + \zeta g_{m,y} \\ 0 & 0 & 1 & \eta g_{p,z} + \zeta g_{m,z} \\ 0 & 0 & 0 & 1 \end{pmatrix} \tag{10.6}$$

with $\mathbf{g}_p = (g_{p,x}, g_{p,y}, g_{p,z})^T$ and $\mathbf{g}_m = (g_{m,x}, g_{m,y}, g_{m,z})^T$ similar to the constrained registration matrix in Chapter 9. The objective function for the constrained registration is then defined by the distance transformed image $\mathbf{I}_{\mathrm{DT,A}}$ for image plane A, or $\mathbf{I}_{\mathrm{DT,B}}$ for plane B, respectively. In the remainder of this section, the indices A and B are omitted, and $\mathbf{P}$ stands either for $\mathbf{P}_\mathrm{A}$ or $\mathbf{P}_\mathrm{B}$. The same holds for $\mathbf{I}_{\mathrm{DT},t}$.

The cost function for the constrained registration can then be stated as

$$\hat{\eta}_t, \hat{\zeta}_t = \arg\min_{\eta,\zeta} \sum_i \mathbf{I}_{\mathrm{DT},t+1} \left(\mathbf{P} \cdot \mathbf{T}_\mathrm{c}(\eta, \zeta) \cdot \mathbf{m}_{i,t} \right). \tag{10.7}$$

Optimization was performed using a nearest-neighbor search, as for the training phase [Duda 01]. Given the parameters $\hat{\eta}_t, \hat{\zeta}_t$, the catheter model can be updated to $\mathbf{m}_{i,t} \in \mathbb{R}^4$ by

$$\forall i : \mathbf{m}_{i,t+1} = \mathbf{T}_\mathrm{c}(\hat{\eta}_t, \hat{\zeta}_t) \cdot \mathbf{m}_{i,t}. \tag{10.8}$$

A grid search was used for optimization. The search domain is given as $\Omega \subset \mathbb{R}^2$. A structogram of the presented motion compensation method is given in Structogram (10.1). The same transformation $\mathbf{T}_c(\hat{\eta}_t, \hat{\zeta}_t)$ is then applied to the 3-D volumetric data set that is used to compute the image overlay by 2-D forward projection of the 3-D model based on the known projection geometry. This way, we can achieve a 3-D motion compensation for monoplane fluoroscopic images.

The results of the constrained registration are compared to an unconstrained method that uses full 3-D translation as a motion model, as stated in Section 9.3. To this end, an unconstrained registration to monoplane fluoroscopy is performed. In this case, Eq. (10.2) is adapted to the monoplane case by rewriting it as

$$\hat{\mathbf{h}}' = \arg\min_{\mathbf{h}} \sum_i \mathbf{I}_{\mathrm{DT},t+1} \left(\mathbf{P} \cdot \mathbf{T}_\mathrm{u}(\mathbf{h}) \cdot \mathbf{m}_{i,t} \right). \tag{10.9}$$

Motion compensation is then performed using $\hat{\mathbf{h}}'$ to update the catheter model as in Eq. (10.3) and applying the same transformation to the 3-D data set used to generate the overlay images. A structogram of the unconstrained approach is given in Structogram (9.2).

- Get Manual Input Points
- Generate Catheter Model $\mathbf{m}_{i,t=0}$
- Compute $\overline{\mathbf{m}}_{t=0}$
- For Training Phase $t > 0$
  - Compute Distance Transformed Images $\mathbf{I}_{\mathbf{DT},A,t}$ and $\mathbf{I}_{\mathbf{DT},B,t}$
  - $\hat{\mathbf{h}} = \mathbf{0}$, $\hat{\varepsilon} = \infty$
  - For $\mathbf{h} \in \Psi$
    - $\varepsilon = \sum_i \mathbf{I}_{\mathrm{DT},A,t}\left(\mathbf{P}_A \cdot \mathbf{T}_\mathrm{u}(\mathbf{h}) \cdot \mathbf{m}_{i,t-1}\right) + \mathbf{I}_{\mathrm{DT},B,t}\left(\mathbf{P}_B \cdot \mathbf{T}_\mathrm{u}(\mathbf{h}) \cdot \mathbf{m}_{i,t-1}\right)$
    - $\varepsilon \quad < \quad \hat{\varepsilon}$
      - `true`: $\hat{\mathbf{h}} = \mathbf{h}$, $\hat{\varepsilon} = \varepsilon$
      - `false`:
  - Update Catheter Model $\mathbf{m}_{i,t}$ using $\mathbf{T}_\mathrm{u}(\hat{\mathbf{h}})$
  - Update Overlay using $\hat{\mathbf{h}}$
  - Compute Model Center $\overline{\mathbf{m}}_t$
- Compute Main Motion Vector $\mathbf{g}_m$ from $\overline{\mathbf{m}}_t$
- Obtain View Direction $\mathbf{b}$ from Projection Matrix $\mathbf{P}$
- Compute Plane-Specific Translation Vector $\mathbf{g}_p$
- Setup $\mathbf{T}_\mathrm{c}(\eta, \zeta)$ using $\mathbf{g}_m$ and $\mathbf{g}_p$
- For Application Phase
  - Compute Distance Transformed Image $\mathbf{I}_{\mathbf{DT},t}$
  - $\hat{\eta} = 0$, $\hat{\zeta} = 0$, $\hat{\varepsilon} = \infty$
  - For $(\eta, \zeta)^T \in \Omega$
    - $\varepsilon = \sum_i \mathbf{I}_{\mathrm{DT},t+1}\left(\mathbf{P} \cdot \mathbf{T}_\mathrm{c}(\eta, \zeta) \cdot \mathbf{m}_{i,t}\right)$
    - $\varepsilon \quad < \quad \hat{\varepsilon}$
      - `true`: $\hat{\eta} = \eta$, $\hat{\zeta} = \zeta$, $\hat{\varepsilon} = \varepsilon$
      - `false`:
  - Update Catheter Model $\mathbf{m}_{i,t}$ using $\mathbf{T}_\mathrm{c}(\hat{\eta}, \hat{\zeta})$
  - Update Overlay using $\mathbf{T}_\mathrm{c}(\hat{\eta}, \hat{\zeta})$

Structogram 10.1: Patient-Specific Motion Compensation by Registration

10.4 Evaluation and Results

In this section, we evaluate the performance of our proposed motion-model constrained 2-D/3-D registration algorithm for motion compensation and present the results. The tracking accuracy of the constrained and unconstrained methods were calculated by comparison to a gold-standard segmentation. For evaluation, 23 clinical biplane sequences were available. The fluoroscopic sequences were acquired during standard electrophysiology procedures. The circumferential mapping catheter was placed at the ostium of the pulmonary vein during image acquisition. The catheter is usually firmly placed to ensure a good wall contact. A suboptimal wall contact may lead to undetected residual PV-atrial electrical connections, and potentially to an incomplete pulmonary vein isolation. One gold-standard segmentation was available for each sequence, i.e., the catheter was segmented by one expert observer in each frame of the whole sequence. Our data was taken from 16 different patients at two clinical sites. All fluoroscopic sequences were recorded on AXIOM Artis dBC biplane C-arm systems (Siemens AG, Healthcare Sector, Forchheim, Germany). The training of the classifier was performed on a two-fold cross validation, i.e., the biplane sequence considered for evaluation was excluded from the training data set. For each sequence, a 3-D model was generated as described in Chapter 2. Afterwards, the constrained method was evaluated by using each image plane of the biplane sequences independently. The frames used for the generation of the motion model were excluded from evaluation. For the unconstrained approach, the same frames were used for evaluation to achieve comparable results. The constrained method used a training phase of 50 % of the sequence. The shortest sequence available comprised 10 frames, and the longest 117. Individual sequences for training of the motion model were not available.

A 2-D tracking error was obtained by calculating the average 2-D distance of the projected catheter model to the gold-standard segmentation. The unconstrained method achieved an average 2-D tracking error of 0.78 mm with a total minimum of 0.28 mm and a total maximum of 2.82 mm. The performance of the constrained method did not differ much and yielded an average 2-D tracking error of 0.86 mm with a total minimum of 0.27 mm and a total maximum of 3.24 mm. The frames of the training phase were not included. The frame with the maximum error is presented in Figure 10.2. Tracking in this frame is compromised by a barium sulfate swallow to obtain the position of the esophagus. The evaluation of the unconstrained method was performed on the same frames as for the method using the patient-specific motion model. The comparison of the 2-D tracking accuracy of both methods is shown in Figure 10.1.

As the motion estimation and compensation is performed in 3-D, and for each case we have biplane sequences to derive the ground truth position in 3-D, a 3-D error can be estimated as well. We use the same methods for evaluation as in Chapter 8 and Chapter 9. The tip of the circumferential mapping catheter was manually localized in 3-D by triangulation from two views and is used as an estimation of the real 3-D motion. For the 46 tested sequences, the observed motion on the frames used for evaluation was on average 3.88 mm $\pm$ 2.05 mm with a max-

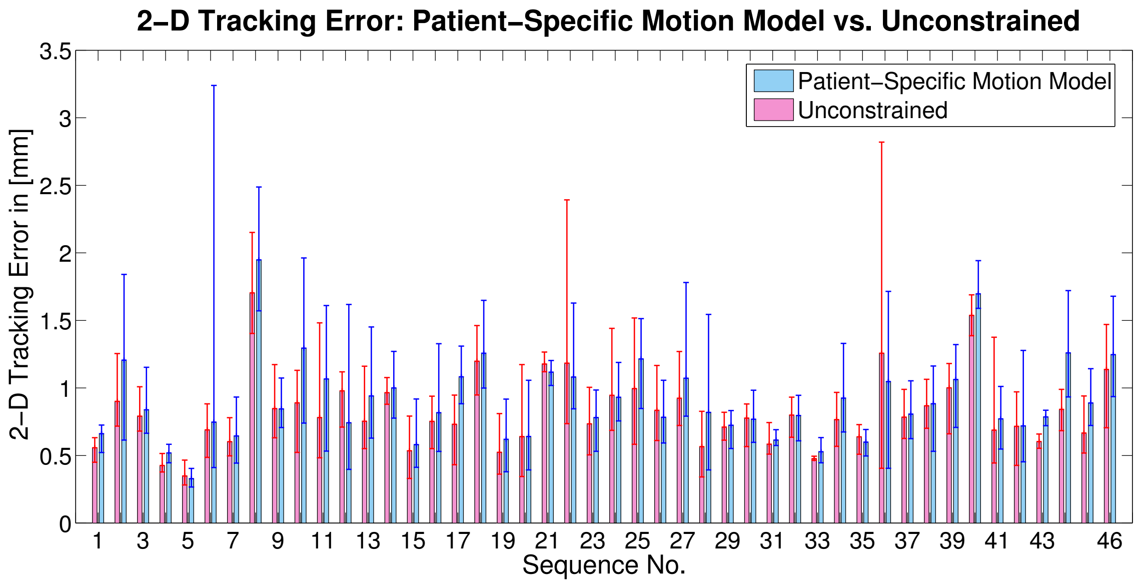

Figure 10.1: Comparison of the 2-D tracking accuracy of the patient-specific motion model and the unconstrained 2-D/3-D registration. The patient specific motion model yielded an average 2-D error of 0.86 mm ± 0.37 mm. On the same frames, the unconstrained method yielded an average 2-D error of 0.78 mm ± 0.30 mm.

imum observed motion of 10.31 mm. These motion errors exclude the training phase. The patient-specific motion compensation approach yielded a 3-D tracking error of 1.63 mm with a total minimum of 0.08 mm and a total maximum of 6.98 mm. The unconstrained approach performed considerably worse with an average 3-D error of 2.44 mm with a total minimum of 0.16 mm and a total maximum of 8.38 mm. A comparison of the 3-D error between the patient-specific motion compensation and the unconstrained approach is given in Figure 10.3. A comparison between the observed motion and the patient-specific compensation approach is given in Figure 10.4.

Even though the patient-specific motion compensation method performed well, the gold-standard biplane method in Chapter 8 is still superior regarding the 3-D accuracy. Evaluating the biplane approach on the same frames and excluding the training phase, yielded an average error of 1.29 mm ± 0.72 mm. However, its better accuracy comes at the cost of increased X-ray dose. A comparison of our constrained approach and the biplane approach is given in Figure 10.5.

As drift is an often discussed issue when evaluating tracking methods, we also considered the tracking error over time. This question is especially interesting, as only one previous frame is considered when tracking the current frame. In particular, the tracking result of the previous frame is used for cropping the region-of-interest in the current frame. Apart from that, all frames are treated independently. For example, the 2-D tracking error for sequence # 19 is given in Figure 10.6. Both, the unconstrained and the constrained approach, achieved comparable results with the constrained method yielding a slightly higher 2-D error. Specifically, in this particular sequence the 2-D tracking error was 0.62 mm ± 0.14 mm for the patient-specific method and 0.52 mm ± 0.81 mm for the unconstrained

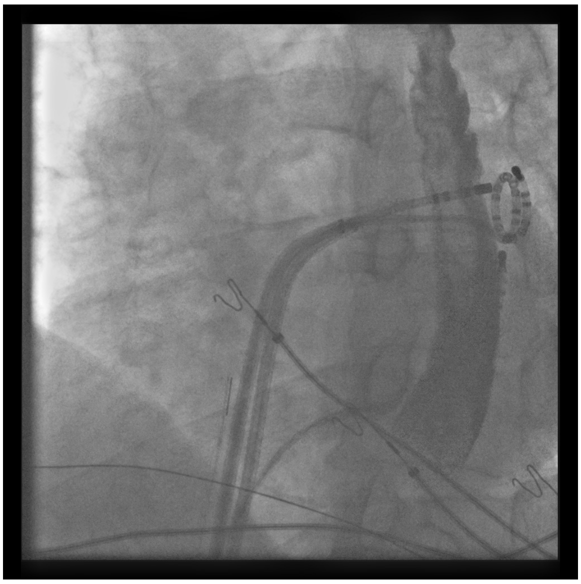

Figure 10.2: One frame of Sequence #6. Catheter tracking is compromised by a barium sulfate swallow. This is performed to obtain the position of the esophagus.

approach, respectively. The patient-specific motion compensation yielded a 3-D tracking error of 1.36 mm $\pm$ 0.69 mm, in comparison to the 3-D tracking error of 2.14 mm $\pm$ 1.02 mm for the unconstrained method. Both methods did not suffer from drifting issues, suggesting that our model-based 2-D/3-D registration using a pre-generated 3-D catheter model is robust with respect to sporadic tracking errors.

The error along the view direction was also evaluated. As this approach tries to somewhat compensate for movements in this direction by using the patient-specific motion model, the question is if this can be achieved by the proposed method. The mean error in view direction yielded 1.03 mm with a total minimum of 0.01 mm and a total maximum of 6.97 mm. On the same frames, the unconstrained method also had an average 3-D along the view direction of 2.05 mm with a total minimum of 0.01 mm and a total maximum of 8.35 mm. The results are given in Figure 10.8. This confirms that estimating object depth from monoplane fluoroscopy is a challenging task as pointed out in [Fall 10a, Fall 10b, Fall 09]. It also confirms that the patient-specific motion model approach is a reasonable choice for tracking a mapping catheter when put firmly in place at the ostium of a pulmonary vein. The large errors in Sequence #40 are due to the high tracking error in the 2-D images. If the position in 2-D is not found correctly, an estimation of the 3-D position is also not very accurate.

To evaluate the influence of the number of frames used during the training phase, we took the three longest biplane sequences available, consisting of 79, 95 and 117 frames, respectively. These three biplane sequences are split into the six monoplane Sequences #11, #12, #15, #16, #19, and #20. The training phases for this evaluation were chosen to comprise 5, 10, 20, 30, and 40 frames, respectively. The 3-D tracking error versus the number of frames using in the training phase is shown in Figure 10.9.

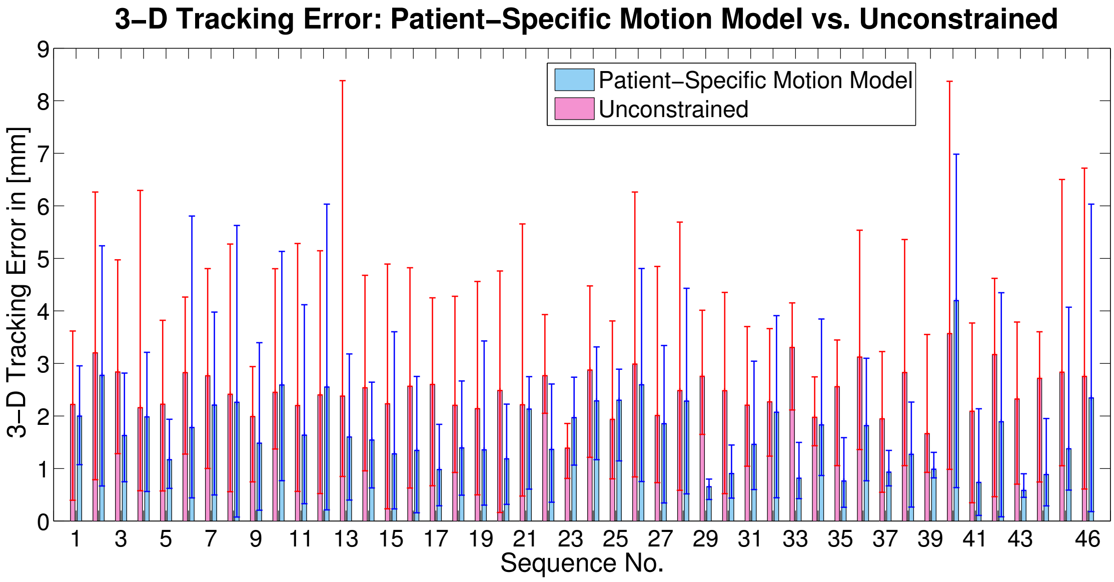

Figure 10.3: Comparison of the 3-D tracking accuracy of the patient-specific motion model and the unconstrained 2-D/3-D registration. The patient-specific motion model yielded an average 3-D error of 1.63 mm ± 1.16 mm. On the same frames, the unconstrained method yielded an average 3-D error of 2.44 mm ± 1.24 mm.

To further evaluate how robust our method behaves against catheter model errors, the longest available sequence was chosen and the respective 3-D model was disturbed by Gaussian noise with a standard deviation $\sigma \in \{0.0\text{ mm}, 0.5\text{ mm}, 1.0\text{ mm}, 1.5\text{ mm}, 2.0\text{ mm}, 2.5\text{ mm}, 3.0\text{ mm}\}$. Afterwards, tracking was performed and evaluated. The 2-D and 3-D tracking with respect to the Gaussian noise are shown in Figure 10.10. Our method is optimized for multi-core CPUs and achieves a frame rate of 5 fps on an Intel Quad Core with 2.20 GHz. The optimization of the objective function in Eq. (10.7) was performed by a grid search. The function was evaluated 25,921 times for each frame in 54.65 ms on the aforementioned architecture.

10.5 Discussion and Conclusions

The initialization of the circumferential mapping catheter model used for motion compensation is required only once. The 2-D/3-D registration incorporates the projection matrix, so no model re-initialization is required if the view direction of a C-arm is changed. Although, model re-initialization is usually not time consuming, it does interrupt the workflow because manual interaction involving the user is required. In fact, while the catheter model can be calculated in less than 55 ms on our PC platform, user feedback for model initialization carries the risk that things are slowed down considerably. The accuracy of the model generation has already been evaluated in Chapter 2. To further investigate the effect of catheter model errors, one sequence was tested with noisy input models. Gaussian noise with zero mean was used to disturb the model in 3-D. The results are shown in Figure 10.10. While the average 3-D error is almost constant, the maximum error varies a lot.

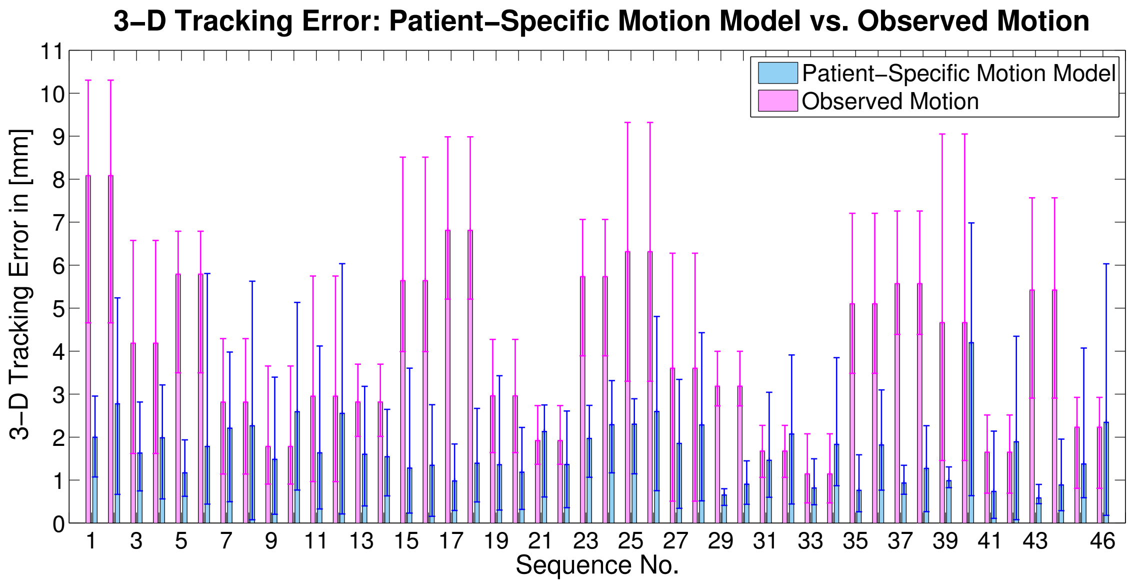

Figure 10.4: Comparison of the patient-specific motion compensation to the observed motion. The patient-specific motion model yielded an average 3-D error of 1.63 mm $\pm$ 1.16 mm. The observed motion was 3.88 mm $\pm$ 2.05 mm.

We attribute this to the randomness of the noise as in one case might be more destructive than in another case. The same holds for the errors in 2-D. The average errors are increasing and tracking fails in more frames with increasing noise. The increase in average errors is also partially due to the projection of the distorted 3-D model. The larger the amount of noise used, the farther away the projection gets from the ideal 2-D position. The good performance of the proposed method is due to the combination of a distance transformed segmentation and a 2-D/3-D registration. Both methods on its own would probably not be able to handle such errors, but their combination increases the robustness of this motion compensation approach.

The computation of the motion model requires a training phase. We used 50 % of the available biplane sequence to compute the principal motion axis. In clinical practice, this could be included into the workflow. At the beginning of each AFib ablation procedure, the signals at the PVs are documented and the correct position of the circumferential mapping catheter is verified by contrast injection and, if available, using a short biplane sequence. Given the amount of contrast agent, this sequence might already be sufficient to set up our proposed motion model. As four pulmonary veins are to be ablated during the procedure, it might be necessary to train four individual motion models, i.e., one for each of the PVs. Evaluating the 3-D tracking error with respect to number of frames used during the training phase, we conclude that our method is insensitive to the length of the training phase, as shown in Figure 10.9. Even though a short sequence might be sufficient to estimate the principle direction of the motion, a full breathing cycle should be used for best results. For example, if the patient is consciously sedated, the physician could ask the patient perform a deep inhale and exhale during the

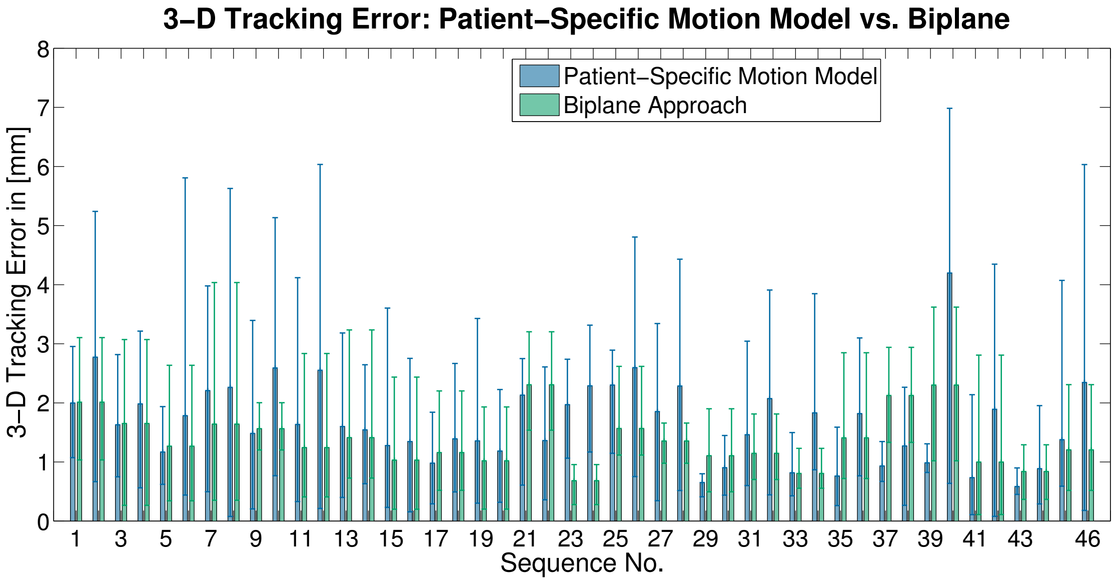

Figure 10.5: Comparison of the patient-specific motion compensation to the learning-based biplane approach as presented in Chapter 8. The patient-specific motion model yielded an average 3-D error of 1.63 mm ± 1.16 mm. The biplane approach yielded an average 3-D error of 1.29 mm ± 0.72 mm.

training sequence for the motion model. Using general anesthesia, this might not be required.

Our proposed method is able to achieve a 3-D accuracy of about 1.63 mm ± 1.16 mm. As before, we use a threshold of 2.00 mm to determine tracking failures. The patient-specific approach yielded a 2-D success rate of 98.89 % and a 3-D success rate of 72.22 %. In comparison, the unconstrained approach yielded a better 2-D success rate of 99.52 %, but a much more worse 3-D success rate, being 41.11 %. Nevertheless, to reduce the 3-D error, one could employ simultaneous biplane imaging which comes at the cost of a higher dose for patient and the medical staff [Bros 10c]. The learning-based biplane approach from Chapter 8 yielded an average 3-D error of 1.29 mm ± 0.72 mm and a success rate of 85.71 %. A comparison between the patient-specific motion model and the unconstrained approach is given in Table 10.1. As physicians are used to 2-D projection images and the 2-D error is lower, it is an open question whether a 3-D error of 2.00 mm can be accepted or not. It seems as if a clinical evaluation of the proposed method should be performed in order to evaluate the clinically required accuracy.

The limitation of our method is mainly related to the fact that motion along the view direction can not be fully accounted for, because it is difficult to estimate depth information reliably from monoplane projection images [Fall 09, Fall 10a, Fall 10b]. Using an unconstrained approach, the 3-D error remains high, especially along the view direction, see Figure 10.8. Depth correction could be performed by analyzing the width of the object, as mentioned in Chapter 9. But this requires a perfect segmentation of the catheter and the exact knowledge of the catheter's dimensions. Any noise or inaccuracy in the 2-D segmentation or the 3-D model would significantly deteriorate the accuracy of depth estimation. Even

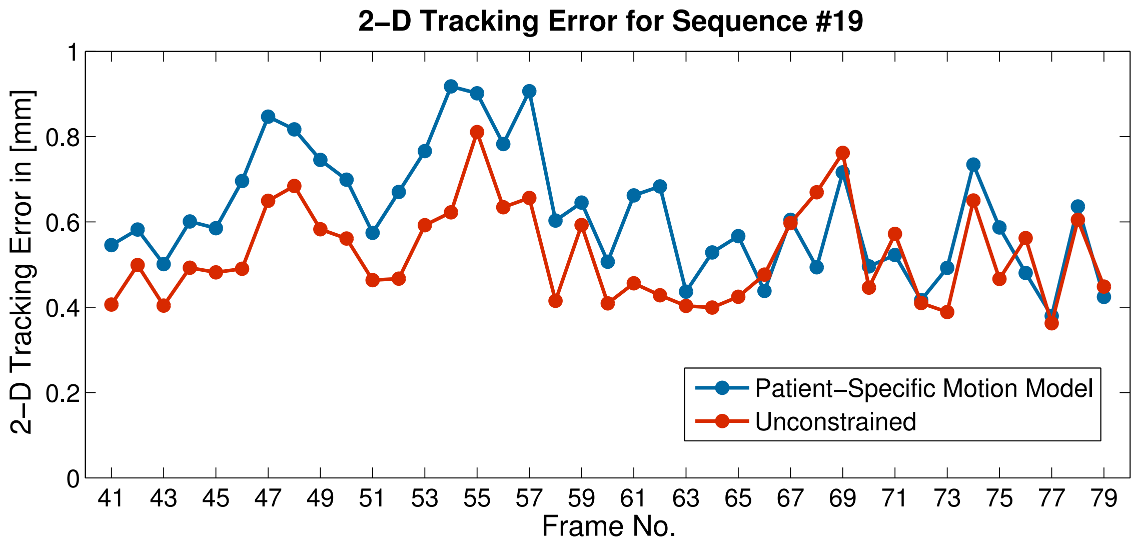

Figure 10.6: Comparison of the patient-specific motion compensation and the unconstrained approach for Sequence #19. The patient-specific motion model yielded a 2-D tracking error of 0.62 mm ± 0.14 mm. The unconstrained approach yielded a 2-D error of 0.52 mm ± 0.81 mm.

Patient-Specific Motion Model vs. Unconstrained		
	Unconstrained	Constrained
Mean 2-D Error	**0.78 mm± 0.30 mm**	0.86 mm± 0.37 mm
Max 2-D Error	**2.82 mm**	3.24 mm
2-D Success Rate	**99.52 %**	98.89 %
Mean 3-D Error	2.44 mm± 1.24 mm	**1.63 mm± 1.16 mm**
Max 3-D Error	8.38 mm	**6.98 mm**
3-D Success Rate	41.11 %	**72.22 %**

Table 10.1: Comparison of the patient-specific motion compensation and the unconstrained approach.

if the depth information could be accurately estimated, the effect would probably not be clearly visible because the size of the overlay would only change slightly. Nevertheless, 3-D motion errors in X-ray view direction are a major contributing factor why the unconstrained method yields significantly worse results, see Figure 10.3. Our proposed method does not need an explicit depth-estimation step thanks to the motion-model. If there is a significant motion in X-ray view direction, then it will be captured by the main motion axis. It depends on the preferences of the physician how to set the C-arm views, if there is motion in the view direction. Physicians might set their C-arm such that most of the motion is captured in their fluoroscopic images. The distance transform provides the main input for the cost function. As long as only one circumferential mapping catheter appears in the image, there is only one global optimum for the cost function. Using our grid-search approach, we did not run into local optima. Some of these occur around the region

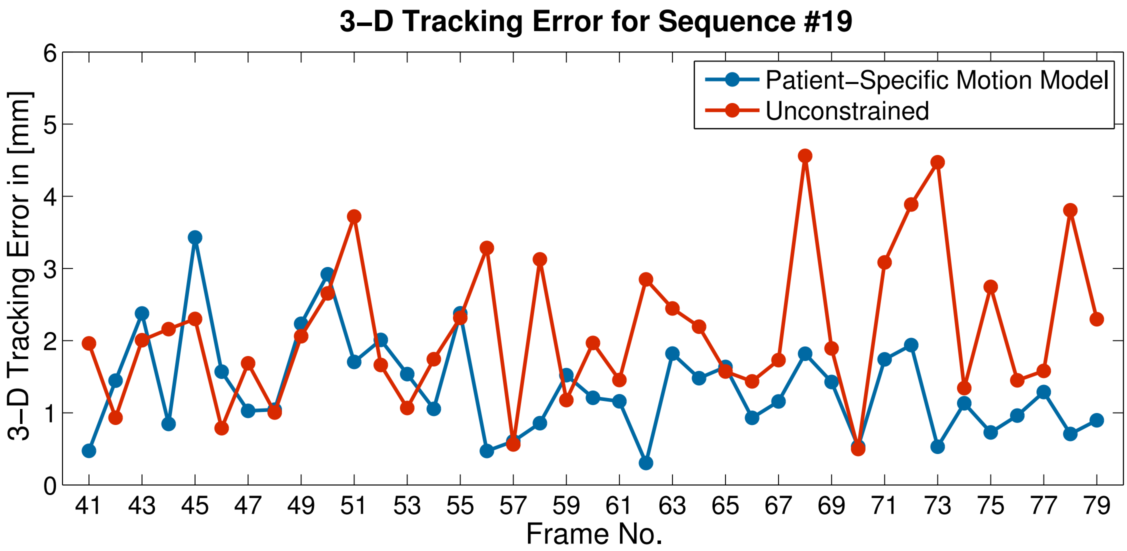

Figure 10.7: Comparison of the patient-specific motion compensation and the unconstrained approach for Sequence #19. The patient-specific motion model yielded a 3-D tracking error of 1.36 mm $\pm$ 0.69 mm. The unconstrained approach yielded a 3-D error of 2.14 mm $\pm$ 1.02 mm.

of the correct position. If multiple elliptical shaped catheters were used, more local optima would appear and our optimization strategy could run into one of these. The same holds if the shape of the circumferential mapping catheter degenerates and gets closer to a line-like object. Currently, this restricts our method to cases using a single circumferential mapping catheter. Fortunately, the majority of AFib cases belong to this category.

Other 2-D/3-D registration approaches [Turg 05, Yao 03] have not been tried yet. Since we are dealing with a very small structure, they are difficult to apply. Although the method in [Herm 07, Mahf 03] are similar to our approach in spirit, they involve a direct image-to-image similarity measure which we find more difficult to evaluate than our current approach.

One gold-standard database comprising 1,288 frames was available for training. The training on a larger database would further improve the segmentation results. The more training samples we have, the more likely we are to capture most of the subtle differences. This is particularly important in difficult cases where contrast may be low. This can happen when treating heavy patients, e.g., due to scatter radiation [Stro 09]. Our data set comprised biplane fluoroscopic images of six patients. We encountered two different types of circumferential mapping catheters. One type was used in 11 biplane sequences, and a second type was used in two more sequences.

Other methods for image-based respiratory motion compensation in electrophysiology procedures have been proposed as well [King 09, Ma 10]. The first method uses a different catheter and the second involves a pre-operative data set. The main shortcoming of these methods is that they do not estimate the motion at the site of ablation directly. Therefore, they require either a patient-specific model built beforehand as well, or a heuristic prior to infer the motion at the site of ab-

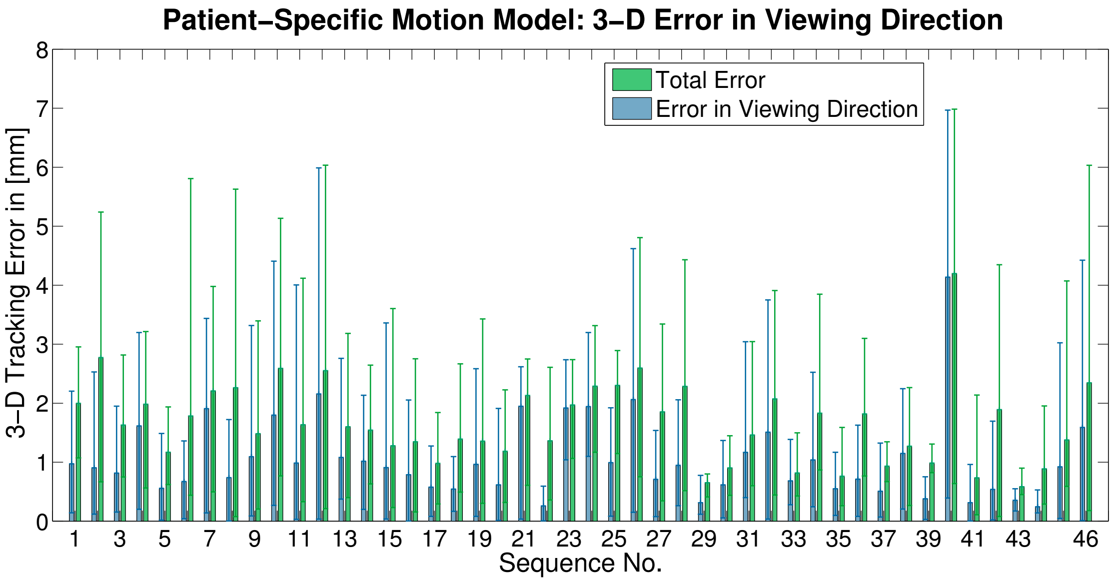

(a)

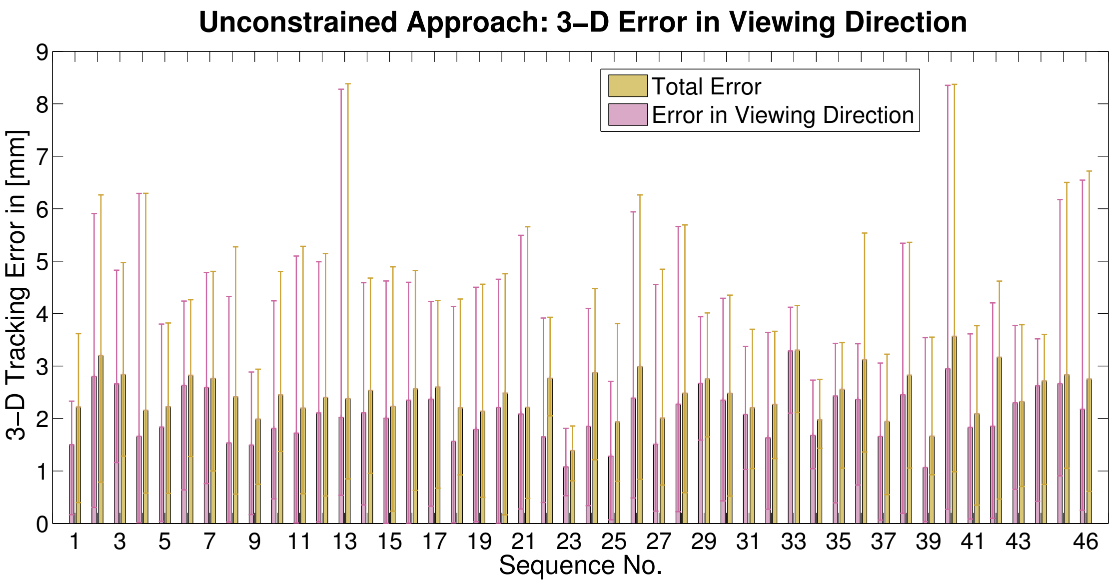

(b)

Figure 10.8: Visualization of the motion compensation error in view direction. (a) The motion compensation error along the view direction of the constrained method. On average, an error in view direction of 1.03 mm ± 1.06 mm was achieved. (b) The same graph for the unconstrained method with an average error of 2.05 mm ± 1.35 mm.

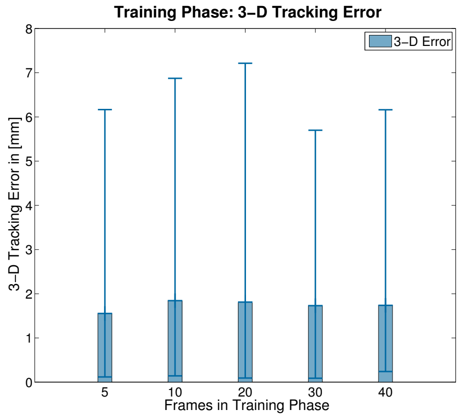

Figure 10.9: Mean 3-D tracking error with minimum and maximum error calculated over three sequences with 79, 95, and 117 frames versus different frame numbers used during the training phase.

lation from the motion estimates. Since the motion estimates appear to be joint estimates of heart and breathing motion, the two motion components need to be separated for respiratory motion correction. When the motion is estimated in 2-D, re-initialization is required whenever when the C-arm position changes. Our proposed method, on the other hand, captures the relevant motion right at the site of ablation and takes it into account real-time. Since our approach uses a 3-D catheter model, re-initialization after repositioning the C-arm can be avoided. For comparison, non-image-based methods for motion compensation involving electro-anatomic mapping systems provide a 3-D mean tracking error of 0.7 mm [Geps 97] which is comparable to our mean 2-D tracking error of 0.55 mm. Since we do not need to record the ECG signal, a stand-alone version of our motion-compensated fluoroscopy system is more straightforward. A comparison of different methods to perform motion compensation is given in [Ma 11].

Our method is purely image driven. Considering the catheters available during AFib ablation procedures, the only other possible catheter candidate to perform motion compensation with is the catheter in the coronary sinus, as proposed in [Ma 10]. Our proposed method could be extended to learn the motion difference between the circumferential mapping and the CS catheter. The same idea could be applied to using the diaphragm for motion compensation. Our current implementation for motion estimation relies on the assumption that the circumferential mapping catheter is firmly placed at the PV where ablation takes place. If the mapping catheter floated around freely within the left atrium, we would not get a reliable motion estimate with our current method. In such a case, we would need to introduce an additional motion analysis stage to detect the free motion.

A comparison between an overlay with and without motion compensation is presented in Figure 10.11. In Figure 10.12, a fluoroscopic image with a motion-compensated 3-D overlay is compared to the original X-ray frame using a contrast injection. In a clinical setup, a physician working on a biplane system is likely to use the two X-ray image planes in an alternating way. Furthermore, a combination of the proposed patient-specific method and the previous biplane reference

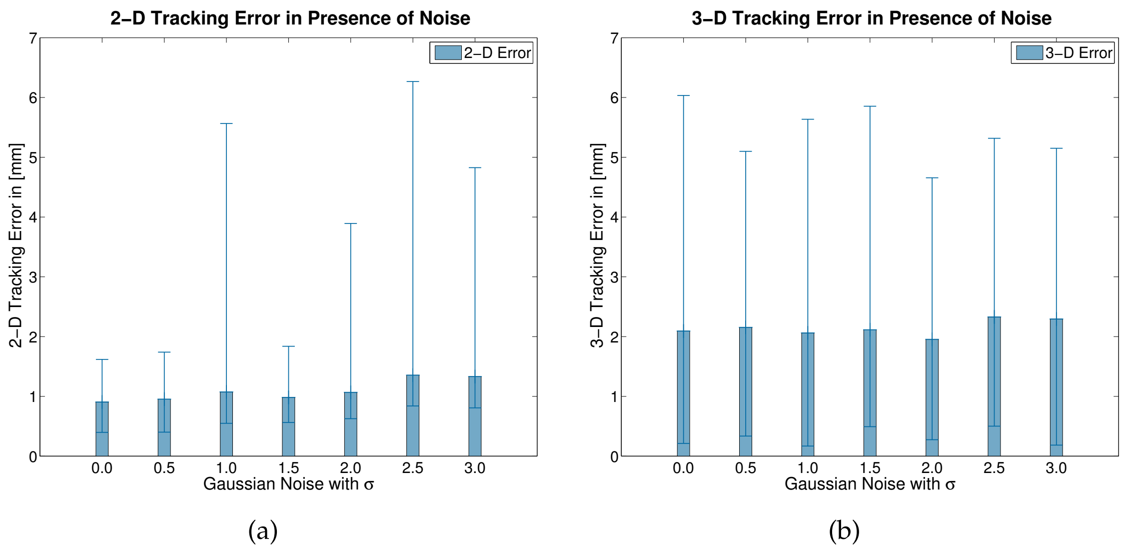

Figure 10.10: Tracking error with respect to a noisy catheter model. Gaussian noise with different standard deviations was used. (a) The 2-D tracking error with respect to Gaussian noise. (b) The 3-D tracking error with respect to Gaussian noise.

approach in Chapter 8 might provide a seamless workflow and high degree of flexibility to the physicians. For example, during regular procedures, the constrained method could be used. If a higher accuracy is required, physicians can switch to a biplane fluoroscopy and the biplane method may start automatically from the initial position provided by the constrained method.

As the methods presented in this part were evaluated using the same data sets. The patient-specific motion compensation requires biplane training to generate the motion model. To arrive at a direct comparison of all motion compensation, the evaluation was restricted to the same frames. In total, all methods were evaluated on 630 monoplane frames. A detailed comparison of the methods is given in Table 10.2. It can be concluded that the best 2-D error can be achieved by using the learning-based method for monoplane motion compensation as proposed in Chapter 7. The 3-D error is best for the biplane method in Chapter 8, although this method requires simultaneously biplane fluoroscopy. The filter-based approach performs better, but the outliers are more sever than for the learning-based approach. Regarding the methods for monoplane 2-D/3-D motion compensation, the constrained approach in Chapter 9 and the patient-specific motion compensation as proposed here, perform equally. The patient-specific motion model performs slightly better regarding the 2-D error, but has a slightly higher 3-D error. Here, the question is, which method is preferred by the physician. To what extent is a better 3-D performance required. Is this the preferred option, even if it might come at the cost of an additional training phase? So far, physicians were used to work with 2-D projection images only. The proposed method enables a 3-D visualization overlaid onto the live X-ray images that also moves in 3-D. Nevertheless, clinical trials are required to compare the visual impression of motion compensation in 2-D and in 3-D.

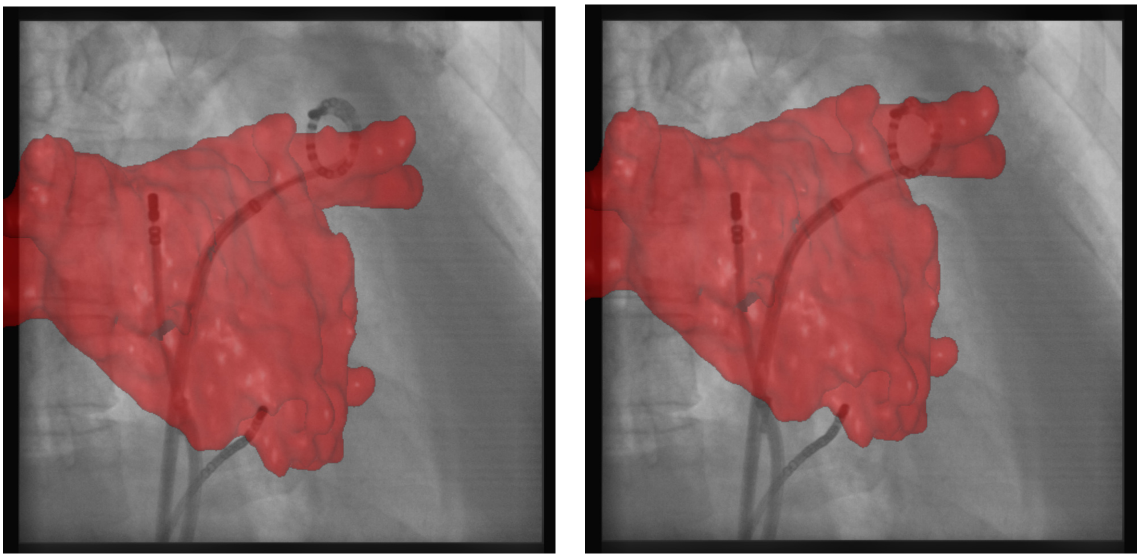

(a) (b)

Figure 10.11: A comparison showing the difference whether or not motion compensation is applied on the fluoroscopic overlay. (a) One frame of sequence 17 without motion compensation. (b) The same frame of sequence 17 with motion compensation.

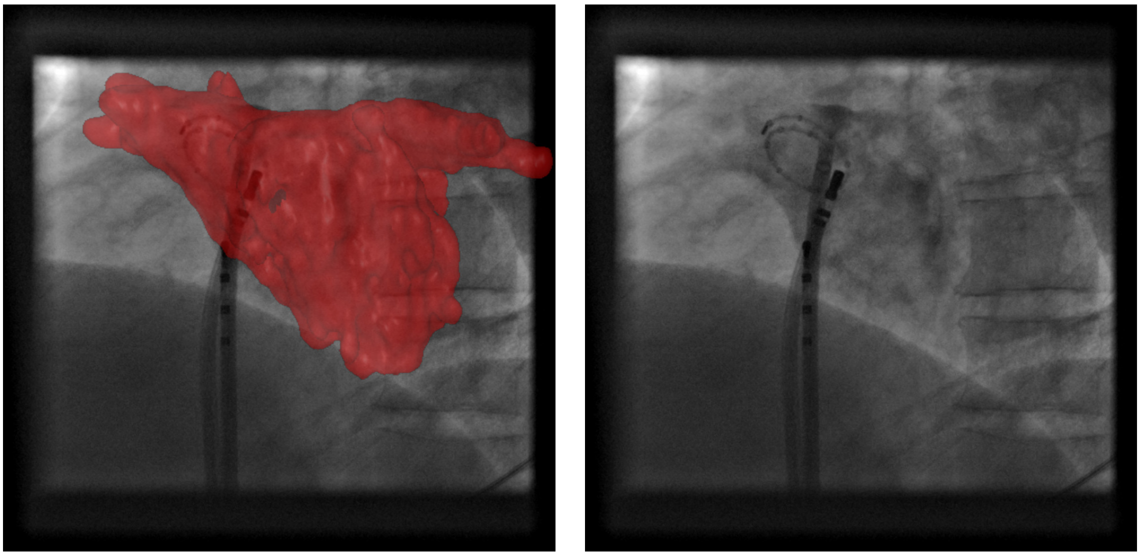

(a) (b)

Figure 10.12: Visual inspection of the motion compensation method. (a) One motion compensated frame of one sequence with 3-D overlay during contrast injection close to one pulmonary vein. (b) The same frame without the 3-D overlay.

	Motion Compensation Approaches			
	Monoplane Filter-Based	Monoplane Learning-Based	Biplane Filter-Based	Biplane Learning-Based
Mean 2-D Error	0.65 mm ± 0.44 mm	**0.59 mm ± 0.61 mm**	0.90 mm ± 0.61 mm	0.84 mm ± 0.33 mm
Max 2-D Error	4.02 mm	**1.86 mm**	5.30 mm	3.00 mm
2-D Success Rate	97.78 %	**100.00 %**	95.56 %	99.05 %
Mean 3-D Error	-/-	-/-	**1.16 mm ± 0.93 mm**	1.29 mm ± 0.72 mm
Max 3-D Error	-/-	-/-	6.43 mm	**4.68 mm**
3-D Success Rate	-/-	-/-	**89.84 %**	85.71 %

	Unconstrained	Constrained	Patient-Specific
Mean 2-D Error	0.78 mm ± 0.30 mm	0.84 mm ± 0.34 mm	0.86 mm ± 0.37 mm
Max 2-D Error	2.82 mm	2.39 mm	3.24 mm
2-D Success Rate	99.52 %	99.24 %	98.89 %
Mean 3-D Error	2.44 mm ± 1.24 mm	1.42 mm ± 1.24 mm	1.63 mm ± 1.16 mm
Max 3-D Error	8.38 mm	5.79 mm	6.98 mm
3-D Success Rate	41.11 %	80.79 %	72.22 %

Table 10.2: Comparison of the proposed motion compensation approaches. All methods were evaluated on the same data set. Please note that the success rate of 100.00 % for the monoplane learning-based approach was achieved on the available data only.

Part IV

Motion Compensation involving Two Catheters

CHAPTER 11

Dynamic Detection of Catheter Displacement

The motion compensation methods presented in Chapters 7, 8, 9, 10 have the advantage, that the circumferential mapping catheter is directly placed at the pulmonary vein considered for ablation. Therefore, the motion of the catheter can be applied directly to the overlay images, either in 2-D or in 3-D. The disadvantage of these methods is that the mapping catheter needs to be moved from one pulmonary vein to another pulmonary vein for mapping the next pulmonary ostium. The circumferential mapping needs to be positioned at each PV individually to ensure that each is electrically isolated. The approaches so far, can not directly deal with this problem. In this chapter, a method is presented that is able to detect non-physiological movement of the circumferential mapping catheter by using the information of catheter placed in the coronary sinus. In this chapter, different data sets than in the previous chapters were used for evaluation. It was required that both catheters are available in the images without obstructions by contrast agent, devices, or shutters. Parts of this work have been published in [Bros 11c].

11.1 Motivation

The methods in Chapters 7, 8, 9, 10 involve tracking of a commonly used circumferential mapping (CFM) catheter which has been firmly positioned at the ostium of the pulmonary vein in simultaneous biplane images. The drawback of this method is a lack to detect when the CFM catheter is moving from one PV to another. Another method has been introduced that tracks a catheter placed in the coronary sinus (CS) vein for respiratory motion compensation [Ma 10]. The placement of the CS catheter is usually performed before the trans-septal puncture and is used during the procedure to stimulate a certain heart rate. The method in [Ma 10] uses a blob-detection algorithm to find the electrodes of the circumferential mapping catheter. Motion compensation is facilitated by using the most proximal electrode. This electrode is used to estimate the motion of the pulmonary veins using a low-pass filter. For motion compensation, we settled on the CFM approach, because our data did not reveal a sufficiently strong correlation between the motion at the CS catheter and the PV ostium. To explain our findings, let us first recall that the CS catheter, placed in the coronary sinus vein, lies between the left atrium and the left ventricle. As a result, its motion may be highly influenced by the motion of the ventricle as well, i.e., the heart beat. The motion of the circumferential mapping catheter, on the other hand, is restricted because the left atrium is connected to the lungs via the pulmonary veins. Although we decided against using the CS for motion estimation directly, we found it very useful as an anchor, i.e., to detect if the CFM catheter is moved from one PV ostium to the next. To this end, we assumed that the absolute distance between CS catheter and CFM catheter remains sufficiently stable to classify whether the CFM catheter has been moved away from a PV ostium. To achieve a reliable and robust motion compensation, we track both catheters at the same time and compare the absolute 2-D distance between the virtual electrode and the loop's center of the circumferential mapping catheter between two consecutive frames. If the distance changes by more than a certain percentage, we assume that the CFM catheter has been moved from one pulmonary vein to another. To obtain a good anchor point along the CS catheter, we decided to introduce a virtual electrode (VE). It is placed on the CS catheter more proximal than any other electrode. Below, we briefly explain motion compensation first. Then we turn to our evaluation and the results. Afterwards, we discuss our results and draw conclusions from this work.

The proposed algorithm consists of two catheter tracking approaches, one for the circumferential mapping catheter and one for the CS catheter, and the detection of non-physiological movement. The tracking of the coronary sinus catheter includes the tracking of the virtual electrode as well. In the first subsection, the tracking of the circumferential mapping catheter is briefly summarized. In Subsection 11.3, the tracking of the CS catheter as well as the virtual electrode is briefly described. The approach for tracking the CS catheter has been proposed in [Wu 11]. An implementation of this work was made available by the authors of [Wu 11]. In the next section, the detection of non-physiological movement based on the position of both catheters is described.

11.2 Circumferential Mapping Catheter Tracking

The tracking of the circumferential mapping catheter follows the learning-based approach in Chapter 7. In this case, only a 2-D catheter model is available from manual initialization. Image processing is performed as described in Chapter 6 following the learning-based catheter segmentation. As a 2-D/2-D registration is

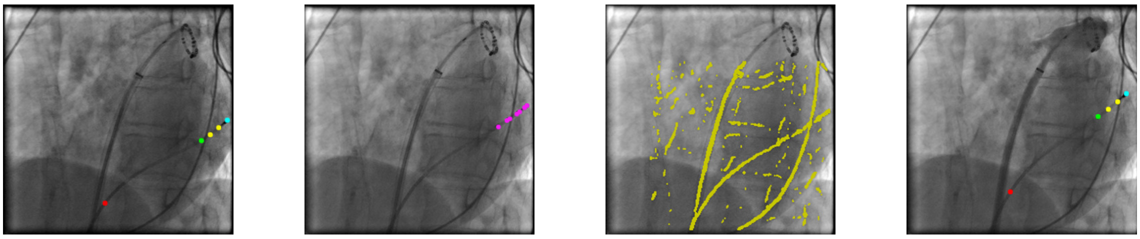

(a) (b) (c) (d)

Figure 11.1: CS catheter detection and VE tracking. (a) Fluoroscopic image with user inputs, electrodes and VE. (b) Automatically detected electrode positions without decision which electrode is the tip and which electrodes belong to the body. (c) Detected catheter body points. (d) Tracked electrodes and VE. The most distal electrode in cyan, the most proximal in green, and all other electrodes in yellow. The virtual electrode is presented in red.

used to register a 2-D catheter model to the segmentation of the circumferential mapping catheter. The optimal translation $\hat{\mathbf{l}}$ is found by minimizing

$$\hat{\mathbf{l}} = \arg \min_{\mathbf{l}} \sum_{\omega} \mathbf{I}_{\mathrm{DT}}(\mathbf{s}(\omega) + \mathbf{l}) \tag{11.1}$$

with $\mathbf{s}(\omega)$ denoting a point of the catheter model and the spline parameter $\omega \in [0, 1]$. As optimization strategy, multi-scale grid search was used [Duda 01].

11.3 Virtual Electrode Tracking

The CS catheter is modeled by a set of electrodes, starting from the tip of the catheter going through each individual electrode and the most proximal electrode (MPE), to the virtual electrode (VE). Figure 11.1 (a) illustrates an example of a CS catheter with 3 electrodes (yellow, and green) other than the tip (cyan). The electrode of the CS catheter are usually clearly visible. The CS tracking method presented in [Ma 10] used a simple blob-detection to find these electrodes. The virtual electrode, red in Figure 11.1 (a), is a reference point on the CS catheter initialized by the user clicking on an arbitrary proximal position along the catheter. The reason to introduce a virtual electrode is to have a reference point which is proximal enough to serve as a better motion estimation reference. The CS catheter is placed in the coronary sinus at the beginning of the procedure and usually not moved during the procedure. Similar to the circumferential mapping catheter, manual interaction is used for the first frame in the sequence to generate the initial CS catheter model. For the remaining frames, we track all the electrodes, including the virtual electrode. At the end, we use the virtual electrode as a reference point to indicate the change of circumferential mapping catheter position from one PV to another. Tracking of the virtual electrode is conducted in a two-stage process. In the first stage, we robustly track all the real electrodes between the tip and the most proximal electrode on the CS catheter. In the second stage, the virtual electrode is inferred by the MPE along the CS catheter using a geodesic constraint. By

Displacement Detection

	$\Delta^\star$	2 %	5 %	6 %	7 %	10 %	15 %	20 %
VE	*FP*	22.7 %	5.8 %	4.2 %	2.7 %	0.5 %	0.0 %	0.0 %
	FN	0.0 %	0.0 %	14.3 %	57.1 %	42.9 %	57.1 %	85.7 %

Table 11.1: Displacement detection using the absolute difference between the CFM catheter and the VE on the CS catheter. False positive (FP) is the percentage of wrongly detected motion and false negative (FN) of undetected motion.

our experiment, we demonstrate that the motion of the virtual electrode is much more consistent with the circumferential mapping catheter compared to the MPE or other electrodes on the catheter.

In our work, catheter tip, electrodes and catheter body points are detected at each frame using trained classifiers. The classifiers use Haar-like features, and steerable features. Each classifier is a probabilistic boosting tree [Tu 05]. The set of detected electrodes and tips at each frame is fed to a non-maximal suppression stage that cleans-up clustered detections. Robust hypothesis matching through a Bayesian framework is then used to select the best hypothesis for each frame. Please refer to [Wu 11] for the detail of the algorithm. Figure 11.1 shows an example of input data with user initialization, detected electrodes, detected body points and tracking results.

11.4 Displacement Detection

Motion compensation was performed by tracking the circumferential mapping (CFM) catheter. The center of the elliptical part of the circumferential mapping catheter for time t is given as $\bar{\mathbf{s}}_t \in \mathbb{R}^2$. The virtual electrode of the CS catheter is given as $\mathbf{c}_{\mathrm{VE},t} \in \mathbb{R}^2$. The relative change $\Delta_{\mathrm{VE},t+1}$ between the catheters from frame t to frame $t+1$ is computed by

$$\Delta_{\mathrm{VE},t+1} = \left| \frac{||\bar{\mathbf{s}}_t - \mathbf{c}_{\mathrm{VE},t}||_2 - ||\bar{\mathbf{s}}_{t+1} - \mathbf{c}_{\mathrm{VE},t+1}||_2}{||\bar{\mathbf{s}}_t - \mathbf{c}_{\mathrm{VE},t}||_2} \right| . \tag{11.2}$$

If the relative change $\Delta_{\mathrm{VE},t+1}$ increase more than a certain threshold $\Delta^\star_{\mathrm{VE}} \in \mathbb{R}$, we assume non-physiological movement, i.e., the CFM catheter is moved from one PV to another. In this case, no motion compensation is applied to the fluoroscopic images, even though catheter tracking is still performed. As soon as the absolute distance becomes stable again, i.e., the distance change is less than $\Delta^\star \in \mathbb{R}$, the motion of the tracked CFM catheter is again applied to the fluoroscopic overlay. A summary of the presented catheter displacement detection method for motion compensation is given in Structogram (11.1).

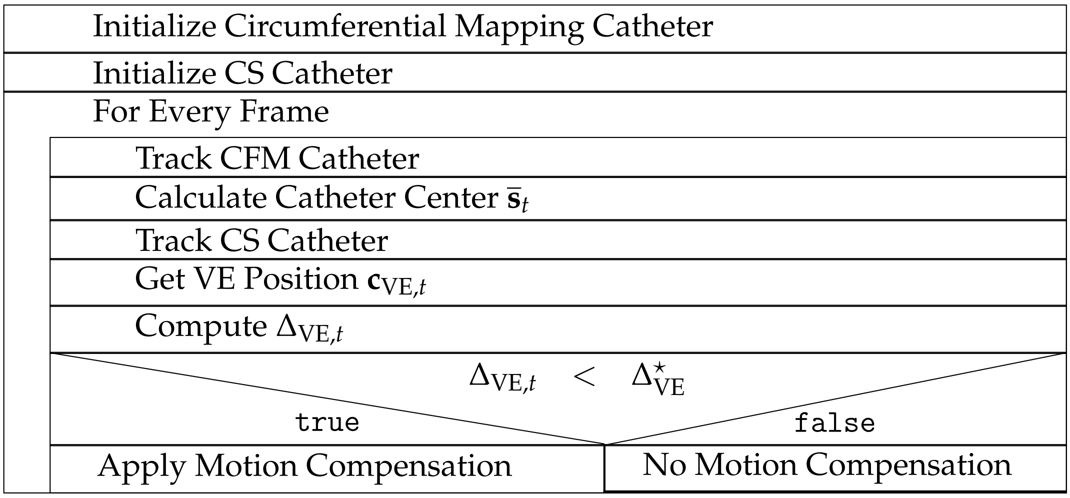

Structogram 11.1: Dynamic Detection of Catheter Displacement

11.5 Evaluation and Results

Our methods were evaluated on 14 clinical data sets from two different hospitals and from 10 different patients using leave-one-out validation. During three of these sequences, a 10-electrode CS catheter was used. In the remaining data sets, 4-electrode catheters were chosen. The images were either 512×512 pixels or 1024×1024 pixels. The pixel size varied between 0.173 mm and 0.345 mm. Image acquisition was performed without using ECG-triggered fluoroscopy. Hence, both respiratory and cardiac motion were present. At first, we evaluated the accuracy of the tracking methods. The gold-standard segmentations of both catheters were manually generated for each frame in every sequence. The segmentation was supervised by an electrophysiologist. For the CS catheter, a gold-standard segmentation of the whole catheter and the individual electrodes as well is available. The tracking errors were computed by considering the 2-D Euclidean distance of the catheter models to the gold-standard segmentations, as detailed in Chapter 7. The results are given in Figure 11.2(a). The CFM localization yielded an average 2-D error of 0.55 mm, which includes the inherent model error. The detection of the MPE on the CS catheter yielded an average 2-D error of 0.52 mm. The VE detection yielded an average 2-D error of 0.49 mm. The detection error of the virtual electrode was computed as the distance to the closest point on the catheter. Further, we compared the motion calculated from the catheter detection methods to the motion observed at the PV ostia. This motion was obtained by using a gold-standard segmentation of the circumferential mapping catheter. The center of the 2-D catheter model was used to calculate the underlying motion of the PV between successive frames. The comparison is given in Figure 11.2(b). The circumferential mapping catheter is considered as point of reference regarding the motion compensation. The catheter is stably fixed at the ostium of the pulmonary vein and therefore represents the motion of the left atrium. The motion obtained by CFM catheter detection differs on average by about 0.48 mm from the real motion, whereas the motion from the most proximal CS electrode had a mean error of

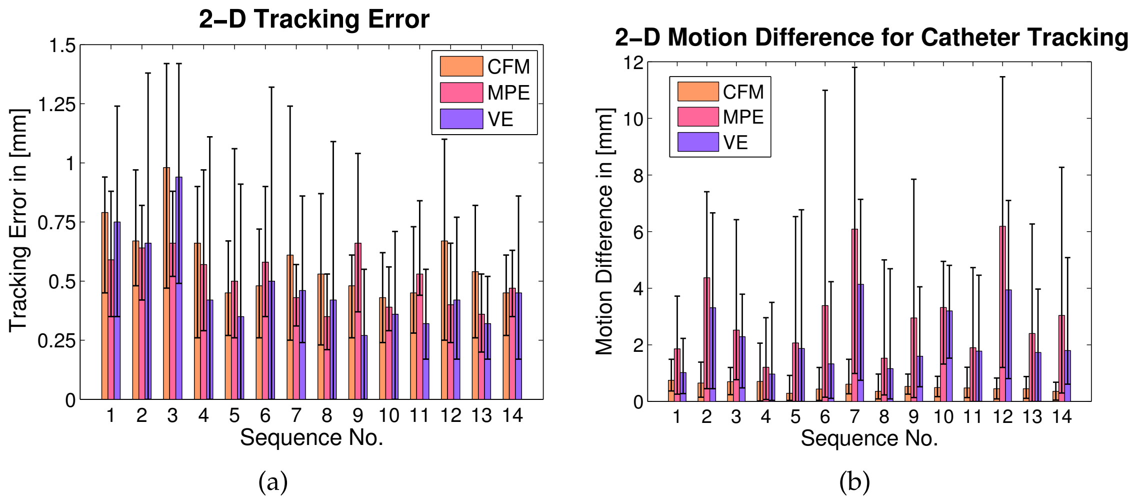

Figure 11.2: (a) Accuracy for the catheter tracking methods. Tracking of the circumferential mapping (CFM) catheter, the most proximal electrode (MPE) on the CS catheter, and the virtual electrode (VE) on the CS catheter. (b) Difference between the observed motion by the circumferential mapping catheter and the catheter tracking methods.

about 2.61 mm. Using the virtual electrode, we could reduce the mean error from 2.61 mm to 1.68 mm. The maximum difference between the true and the estimated motion using the CFM catheter was 2.06 mm. The MPE was off by up to 11.80 mm and the VE by up to 7.14 mm, see Figure 11.2(b). The 14 fluoroscopic sequences used for evaluating the tracking performance had the CFM catheter firmly placed at a single pulmonary vein, i.e., the CFM catheter was not moved from one PV to the next. To evaluate our displacement detection method, five further sequences were added to our data set. For each of these sequences, a gold-standard segmentation is available. In addition to that, the frames between which the CFM catheter was moved away from the PV were annotated. To detect CFM catheter displacement, we introduced a displacement threshold. The displacement threshold is a percentage of the distance between VE and the center of the loop representing the CFM catheter. Results for different displacement thresholds are given in Figure 11.1. A change in the absolute distance of 5 % from one frame to the next turned out to be the best threshold for detecting catheter repositioning in our experiments. In this case, the false positive rate was 5.8 %, i.e., in 5.8 % of the frames non-physiological was wrongly detected. We decided on the VE for displacement detection, because it turned out to be a much more stable reference than the MPE. This can be seen, e.g., by taking a look at their mean errors and maximum differences, see Figure 11.2(b).

11.6 Discussion and Conclusions

The results indicate that our catheter localization and tracking algorithms are accurate enough to meet clinical needs, as the tracking errors are below the threshold of 2.00 mm. The tracking results are given in Figure 11.2(a). In our experiments, involving non-ECG-triggered fluoroscopic data acquired under free breathing con-

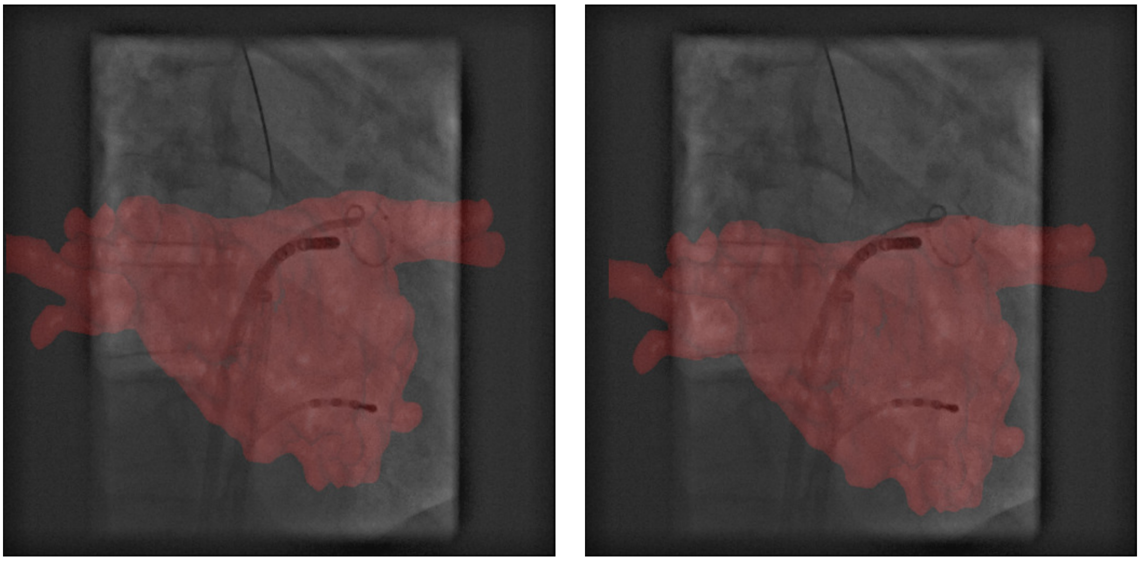

(a) (b)

Figure 11.3: (a) Motion compensation using the circumferential mapping catheter. (b) Motion compensation using the most proximal electrode on the coronary sinus catheter.

ditions, only tracking of the CFM was accurate enough to be directly applicable to motion compensation without any need for a more sophisticated motion model, see Figure 11.2(b). The tracking of the circumferential mapping catheter yielded an overall average error of 0.55 mm. Since this error also contains some model error of the underlying spline catheter model, which is not adapted over time, the actual tracking performance of the distance-transform-based method might even be better. The number of spline points were selected between 50 and 100, depending on the manual initialization. The motion difference between the real motion at the PV ostia and the estimated motion, yielded a maximum error of 2.06 mm. The same error for the MPE was 11.80 mm and 7.14 mm for the VE, respectively, see Figure 11.2(b). From these numbers, we conclude that the circumferential mapping catheter is the best surrogate for the motion of the left atrium. At first sight, our observations seem to contradict the results reported in [Ma 10]. Here, a motion compensation error based on the CS catheter is reported to be as small as 1.6 mm $\pm$ 0.9 mm. Maybe the varying results are due to differences in how the procedures were performed. For example, some centers apply general anesthesia while only mild sedation was used in our cases. Some clinical sites also provide a setup where ECG signals can be recorded on the fluoroscopy system. The ECG could be exploited to select proper fluoroscopic frames. As our cases came from multiple sites using different ECG recording equipment, we decided to not take advantage of any ECG signals to keep things consistent. The choice for one method or the other may come down to how well you control the procedure. For example, if there is general anesthesia, stable sinus rhythm, and available ECG information, the approach presented in [Ma 10] may be the method of choice. However, in the general case it might not be straightforward to apply it as successfully. Although we found it difficult to rely on the CS catheter for motion compensation, we observed that it can be used to detect displacement of the CFM catheter. If the distance between the circumferential mapping catheter and the virtual electrode changes by a certain amount, we assume that the mapping catheter has been moved from one PV to the other. From our experiments, using the absolute distance between the CFM and the VE yielded the best results to detect that the CFM moved away from a particular PV. A change in the absolute distance of 5 % was the best threshold in our experiments yielding a false positive rate of 5.8 %. Compared to a mis-detection which may lead to incorrect fluoroscopic overlays, a false detection is preferred. In the worst case, there are a few frames without motion correction.

CHAPTER 12

Motion Compensation using Coronary Sinus Catheter

In this chapter, a motion compensation approach is proposed that is based on the observation of the coronary sinus (CS) catheter. It requires a training phase during which the circumferential mapping catheter is tracked together with the CS catheter. Features extracted from the CS catheter are used to compute an artificial heart value and are stored together with the position of the circumferential mapping catheter. Assuming that the circumferential mapping catheter is not available after the training phase, an artificial heart cycle value is determined from the observed coronary sinus catheter and an estimation of the position of the circumferential mapping catheter is computed. This chapter summarizes the result of the Bachelor Thesis of Sebastian Kaeppler [Kaep 12a]. Parts of this chapter have been published in [Kaep 12b].

12.1 Motivation

The targets of atrial fibrillation ablation procedures are the ostia of the pulmonary veins. In general, three catheters are used during the procedure. At first a mapping catheter is placed in the coronary sinus vein. The coronary sinus vein lies in the sulcus between the left ventricle and the left atrium. An ablation catheter and a circumferential mapping catheter are brought into the left atrium using trans-septal punctures. The circumferential mapping catheter is positioned at the ostium of the pulmonary vein (PV) considered for ablation. By doing so, the electrophysiologist performing the procedure can guarantee a successful isolation of the pulmonary vein. Unfortunately, the overlay images are compromised by cardiac and respiratory motion. Recent approaches for motion compensation involve catheter tracking of at least one of these catheters. They have shown to improve the quality of these overlay images [Bros 11c, Ma 10]. The work in [Ma 10] facilitates motion compensation using the CS catheter, whereas the work presented in the previous chapters uses the circumferential mapping catheter. The downside of using the CS catheter is the fact that this catheter is not inside the left atrium. Therefore, its motion is more influenced by the left ventricle than the left atrium. Furthermore, this catheter might not always be visible depending on collimator or zoom settings of the imaging system. The circumferential mapping catheter on the other hand is moved on purpose during the procedure and is usually positioned at the PV considered for ablation. This movement requires either user interaction or a movement detection algorithm, as presented in the previous chapter. In addition, if only one trans-septal puncture is performed, only one catheter is inside the left atrium. By doing so, the circumferential mapping catheter is brought to the left atrium before and after the ablation of one PV, to measure the signals, switching places with the ablation catheter.

We present a new method that reduces the disadvantages of both previous methods. To this end, we use a training phase during which both catheters are tracked. After the training phase, a motion prediction model is calculated. After that, the prediction model can be used to estimate the cardiac and respiratory motion by observing only the CS catheter.

Our method is separated into three steps. The first step is the training phase in which both catheters are tracked. In the second step, the features to estimate the motion are computed. The third step is the actual motion compensation during the procedures.

12.2 Training Phase

For every image in the training phase, the circumferential mapping catheter and the CS catheter are tracked. Their positions are stored for later computations. Tracking of the catheters themself is performed by using the method proposed in [Wu 11]. This approach was briefly summarized in Subsection 11.3.

The catheters are modeled by a set of electrodes, starting from the tip of the catheter going through each individual electrode. Manual interaction is used for the first frame in the sequence to generate the initial catheter models. For the remaining frames, all electrodes are tracked. The electrodes are detected in each frame using trained classifiers. The classifiers use Haar-like and steerable features. Each classifier is a probabilistic boosting tree [Tu 05]. The set of detected electrodes and tips at each frame is fed to a non-maximal suppression stage that cleans-up clustered detections. Robust hypothesis matching through a Bayesian framework is then used to select the best hypothesis for each frame. Please refer to [Wu 11] for the details of the algorithm.

12.3 Motion Prediction Model Generation

In order to build our motion model, we need to determine the cardiac phase for each training image. One could use ECG data to determine the cardiac phase for a given frame. Unfortunately, this data is not always readily available at the imaging system. Additionally, its accuracy may be affected by irregularities of the heart beat. Here, the computation of the cardiac phase is based on a pattern recognition approach instead. In particular, we exploit the fact that respiration causes only a slight rotational movement of the heart [McLe 02, Shec 04], while the electrodes of the CS catheter show a large relative rotative movement during the cardiac cycle. We try to capture this movement due to the cardiac cycle using a feature set based on the positions of the electrodes of the CS catheter. The tracked electrodes of the CS catheter are denoted as $\mathbf{c}_i^{(t)} = (u_i^{(t)}, v_i^{(t)})^T$ with $i \in [1, K]$ and K being the number of electrodes, and $t \in \{1, \ldots, L, \ldots, T\}$ and L the number of images in the training sequence. The image coordinate system is defined by u and v. For simplicity, we denote the most distal electrode as $\mathbf{c}_1^{(t)}$ and the most proximal one as $\mathbf{c}_N^{(t)}$. The center of the mapping catheter in frame t is denoted as $\overline{\mathbf{m}}_t \in \mathbb{R}^2$. The following features $f_1^{(t)}, \ldots, f_5^{(t)}$ for image t are computed for all images in the training set from the tracked positions of the CS electrodes:

- The first feature is the u-position of the most distal electrode divided by the u-position of the most proximal electrode. The positions are in absolute image coordinates and not related to a reference frame. The computation is done as

$$f_1^{(t)} = \frac{u_1^{(t)}}{u_N^{(t)}}. \tag{12.1}$$

- The second feature is calculated similar to the first feature, but instead of using the u-coordinates, the v-coordinates are used. This feature is calculated by

$$f_2^{(t)} = \frac{v_1^{(t)}}{v_N^{(t)}}. \tag{12.2}$$

- The third feature is the angle between the u-axis of the image and the line spanned by the most proximal and most distal electrode. The computation of this features is

$$f_3^{(t)} = \tan^{-1}\left(\frac{|u_1^{(t)} - u_N^{(t)}|}{|v_1^{(t)} - v_N^{(t)}|}\right). \tag{12.3}$$

- The fourth feature is the angle between the u-axis of the image and the line spanned by the most proximal electrode and the one next to the most distal electrode. This feature is computed as

$$f_4^{(t)} = \tan^{-1}\left(\frac{|u_2^{(t)} - u_N^{(t)}|}{|v_2^{(t)} - v_N^{(t)}|}\right). \tag{12.4}$$

- The fifth and last feature is the angle between the u-axis of the image and the line spanned by the most proximal electrode and the one second next to the most distal electrode. Its computation is done by

$$f_5^{(t)} = \tan^{-1}\left(\frac{|u_3^{(t)} - u_N^{(t)}|}{|v_3^{(t)} - v_N^{(t)}|}\right). \tag{12.5}$$

These features capture CS catheter rotations and deformations, which are typical for cardiac motion. Yet, they are relatively invariant to translation motion, which is characteristically for respiratory motion. As these feature values have different ranges, they are normalized to the range $[0,1]$. This normalization is stored for later use. The resulting features $\tilde{f}_1, \ldots, \tilde{f}_5$ are combined to feature vectors $\mathbf{f}_t$ as

$$\mathbf{f}_t = (\tilde{f}_1^{(t)}, \tilde{f}_2^{(t)}, \tilde{f}_3^{(t)}, \tilde{f}_4^{(t)}, \tilde{f}_5^{(t)})^T. \tag{12.6}$$

To reduce the dimensionality of the feature vector, a principle component analysis is performed. First, the mean feature vector is calculated by

$$\bar{\mathbf{f}} = \frac{1}{L}\sum_t^L \mathbf{f}_t. \tag{12.7}$$

In the next step, the covariance matrix is calculated by

$$\Sigma = \frac{1}{L-1}\sum_t^L (\mathbf{f}_t - \bar{\mathbf{f}}) \cdot (\mathbf{f}_t - \bar{\mathbf{f}})^T. \tag{12.8}$$

Now, the eigenvalues and eigenvectors of Σ are computed. Let $\mathbf{e}_\mu$ be the eigenvector corresponding to the largest eigenvalue of the covariance matrix Σ. The unitless cardiac cycle value $\vartheta_t \in \mathbb{R}$ for every image in the training sequence is then computed by

$$\vartheta_t = \mathbf{e}_\mu^T \cdot (\mathbf{f}_t - \bar{\mathbf{f}}), \tag{12.9}$$

which is the length of the orthogonal projection of the feature vector onto the first eigenvector. Thus, a correspondence between the calculated cardiac cycle value ϑ_t and the stored position of the mapping catheter $\overline{\mathbf{m}}_t$ has been established

$$\vartheta_t \longrightarrow \overline{\mathbf{m}}_t. \tag{12.10}$$

To summarize the training step, an artificial heart cycle value ϑ_t is computed from the observations of the electrode on the CS catheter and associated with the position of the center of the circumferential mapping catheter $\overline{\mathbf{m}}_t$. For the use of the training data, two parts of information need to be stored. The first is the normalization of the feature values from f_i to $\tilde{f}_i$. The second piece of information is the triplet of the heart cycle value ϑ_t, the position of the circumferential mapping catheter $\overline{\mathbf{m}}_t$, and the position of the most proximal electrode $\mathbf{c}_N^{(t)}$.

12.4 Motion Compensation using Motion Prediction Model

For motion compensation, we assume that the circumferential mapping catheter is no longer available. Therefore, only the tracking results for the CS catheter are required. To apply the compensation, the features need to be computed for the new image. The features are computed as described above and the same normalization as for the training data is applied. The features are then combined to the new feature vector $\mathbf{f}_{\text{new}}$. The new heart cycle value ϑ_{new} corresponding to the new feature vector is calculated by

$$\vartheta_{\text{new}} = \mathbf{e}_{\mu}^{T} \cdot (\mathbf{f}_{\text{new}} - \bar{\mathbf{f}}). \tag{12.11}$$

In the next step of the motion compensation, two training samples that are closest to the current image with respect to cardiac phase need to be found. The first one, denoted β, is earlier in the cardiac cycle than the new image. The other one, denoted γ, is later. To do so, the following minimization problem is considered for the sample index β

$$\beta = \arg \min_{\substack{t \\ \vartheta_t < \vartheta_{\text{new}}}} (|\vartheta_t - \vartheta_{\text{new}}|)^2 + \iota \cdot (u_N^{(t)} - u_N^{(\text{new})})^2 \tag{12.12}$$

with the regularization parameter $\iota \in \mathbb{R}$. For the sample γ, the constraint $\vartheta_t < \vartheta_{\text{new}}$ in Eq. (12.12) is replaced by $\vartheta_t \geq \vartheta_{new}$. The position of the most proximal electrode in u-direction, $u_N^{(\text{new})}$, is used for regularization. The idea behind this term is to reduce the effect of errors in the calculation of the heart cycle, which may, for example, arise from slight inaccuracies in the catheter tracking. The cardiac cycle values ϑ_β and ϑ_γ correspond to the two samples closest to the new frame with the observed cardiac cycle value ϑ_{new}. These two values are used to compute estimates for the position of the circumferential mapping catheter

$$\hat{\mathbf{m}}_{\text{new},\beta} = \mathbf{m}_\beta + \left(\mathbf{c}_N^{(\text{new})} - \mathbf{c}_N^{(\beta)}\right), \tag{12.13}$$

$$\hat{\mathbf{m}}_{\text{new},\gamma} = \mathbf{m}_\gamma + \left(\mathbf{c}_N^{(\text{new})} - \mathbf{c}_N^{(\gamma)}\right). \tag{12.14}$$

The difference terms in Eq. (12.13) and Eq. (12.14) provide the compensation for respiratory motion. For two images in the same cardiac phase, we assume that any remaining motion must be due to respiration. Since we also assume that the CS and the mapping catheter are equally affected by respiratory motion, we simply apply the difference vector between the proximal electrodes of the CS catheter in the two images to the estimate of the position of the mapping catheter. The proximal electrode was chosen because it shows the least intra-cardiac motion with respect to the mapping catheter. These two values are combined to calculate the final estimate as

$$\hat{\mathbf{m}}_{\text{new}} = \kappa \cdot \hat{\mathbf{m}}_{\text{new},\beta} + (1 - \kappa) \cdot \hat{\mathbf{m}}_{\text{new},\gamma} \tag{12.15}$$

- Initialize Circumferential Mapping Catheter
- Initialize CS Catheter
- For Training Phase $t \in \{1, \dots, L\}$
  - Track CFM Catheter
  - Store Catheter Center $\overline{\mathbf{m}}_t$
  - Track CS Catheter
  - Compute Feature Vector $\mathbf{f}_t$
  - Store Feature Vector $\mathbf{f}_t$
  - Store Most Proximal Electrode Position $\mathbf{c}_N^{(t)}$
- Compute Principal Vector $\overline{\mathbf{f}}$
- Compute Artificial Heart Cycle Value ϑ_t for all t
- For Frames $t > L$
  - Track CS Catheter
  - Compute Feature Vector $\mathbf{f}_{\text{new}}$
  - Compute Artificial Heart Cycle Value ϑ_{new}
  - Find Indices β and γ
  - Compute $\hat{\mathbf{m}}_{\text{new}}$ using Linear Interpolation
  - Input Frame Rate ≥ 15 fps
    - `true`: Apply Temporal Lowpass Filter
    - `false`:
  - Perform Motion Compensation using $\hat{\mathbf{m}}_{\text{new}}$

Structogram 12.1: Motion Compensation using Coronary Sinus Catheter

representing a linear interpolation with respect to the heart cycle values. The scaling value $\kappa \in \mathbb{R}$ between the two estimates is calculated by

$$\kappa = \frac{|\vartheta_\gamma - \vartheta_{\text{new}}|}{|\vartheta_\gamma - \vartheta_\beta|}. \tag{12.16}$$

In case of high acquisition frame rates ≥ 15 frames-per-second, we apply a temporal lowpass filter

$$\hat{\mathbf{m}}'_{\text{new}} = \delta \cdot \hat{\mathbf{m}}_{\text{new}} + (1 - \delta) \cdot \hat{\mathbf{m}}_{\text{new}-1} \tag{12.17}$$

with the smoothing parameter $\delta \in [0, 1]$. This is motivated by the fact that the motion of the heart is smooth in high frame rate image sequences. A summary of the presented motion compensation method is given in Structogram (12.1).

12.5 Evaluation and Results

For evaluation, 6 sequences from two different hospitals were available. The available data set comprises a total of 508 frames. The length of the sequences varied between 49 and 117 frames. Each sequence was split into two disjoint sets of

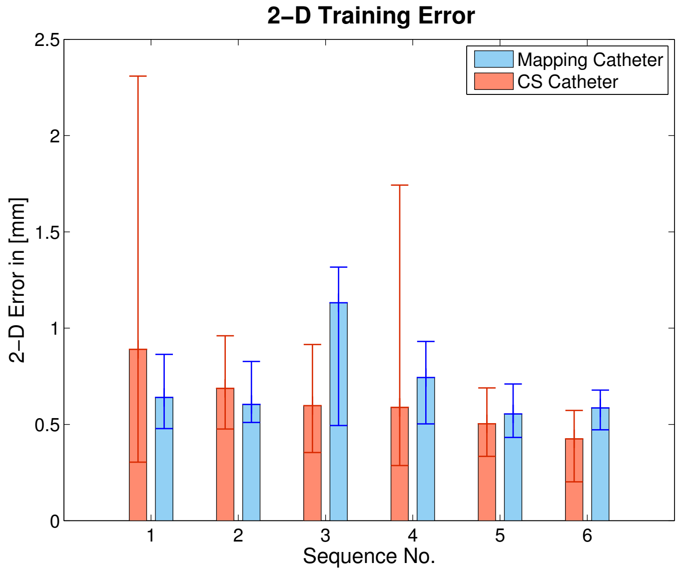

Figure 12.1: Tracking errors during the training phase. The CS catheter was tracked with an average error of 0.62 mm ± 0.34 mm. The circumferential mapping catheter was tracked with an accuracy of 0.71 mm ± 0.22 mm.

frames. One set, comprising the first 30 frames of the sequence, was used for the patient-specific training of the model. The remaining set was used for evaluation. This resulted in a total number of 328 frames available for evaluation. In a clinical scenario, usually more time passes between training and compensation phase. The first sequence was acquired using ECG-triggered fluoroscopy. We chose to include this sequence to see how our method handles respiratory motion with only residual cardiac motion. The other sequences were acquired with either 15 or 30 frames-per-second. We compare our results to an uncompensated overlay as well as to the method proposed in [Ma 10], which uses only the CS catheter for motion compensation. The values of 0.01 for regularization parameter ι and 0.7 for the smoothing parameter δ were determined by performing a grid search on a subsample of the available sequences.

For evaluation, gold-standard segmentations of the CS and the circumferential mapping catheter were available. These segmentations are used to evaluate the tracking accuracy. The segmentation of the mapping catheter is further used as gold-standard for the motion to be compensated for and is compared to the motion estimate derived from our new approach. Due to its proximity to the ablation target, the motion of the mapping catheter is considered to be the motion that needs to be estimated. We further compare our results to the observed 2-D motion as well as to the reference method in [Ma 10]. In the training phase, the circumferential mapping catheter was tracked with an average error of 0.71 mm with a total minimum of 0.43 mm and a total maximum of 1.32 mm. The CS catheter was tracked with an average error of 0.62 mm with a total minimum of 0.20 mm and a total maximum of 2.31 mm. The results are given in Figure 12.1.

After the training phase, the coronary sinus catheter was tracked with an average error of 0.59 mm with a total minimum of 0.21 mm and a total maximum of

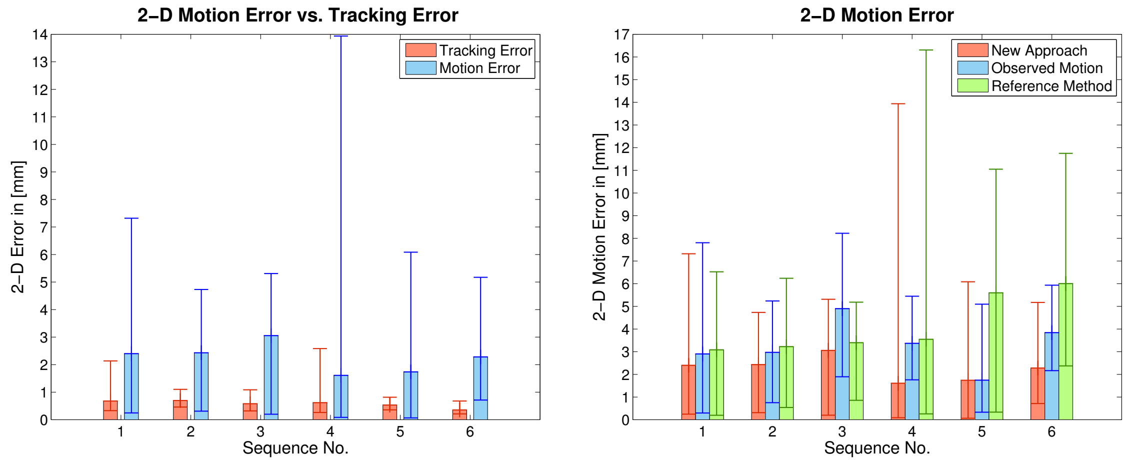

(a) (b)

Figure 12.2: Motion compensation error by using the CS catheter. (a) Comparison between the tracking error of the CS catheter and the motion estimate. The CS catheter was tracked with an average error of 0.59 mm ± 0.30 mm. The motion estimation error was on average 3.14 mm ± 1.67 mm. (b) A comparison to the observed 2-D motion and the reference method. The observed motion was 3.14 mm ± 1.67 mm. The reference method yielded an average error of 4.07 mm ± 2.25 mm. However, our data sets might have been acquired using a different protocol.

2.58 mm. The estimation of the motion of the PV ostium yielded an average error of 2.20 mm with a total minimum of 0.06 mm and a total maximum of 13.94 mm. A comparison of the tracking error of the CS catheter and the motion estimation is given in Figure 12.2(a). The reference method [Ma 10] yielded an average motion estimation error of 4.07 mm with a total minimum of 0.20 mm and a total maximum of 16.31 mm. The observed 2-D motion was on average 3.14 mm with a total minimum of 0.30 mm and a total maximum of 8.22 mm. A comparison is given in Figure 12.2(b)

12.6 Discussion and Conclusions

Considering the available data, it can be concluded that motion compensation using the CS catheter is possible, but not as accurate as it could be using the circumferential mapping catheter. The outlier in our motion compensation approach that can be observed when taking a look at Figure 12.2 is due to a tracking failure of the CS catheter. Considering a threshold of 2.00 mm for the motion estimation error, the proposed method achieves a success rate of 53.96 %. On the same data set, our implementation of the reference method by Ma, *et al.* [Ma 10] yielded a success rate of only 13.41 %.

Our method has shown to perform better as the current motion compensation approach based on the CS catheter, as proposed in [Ma 10]. A direct comparison is given in Table 12.1. Our implementation of the reference method performs surprisingly less accurate than reported in literature. There, an average error of

Comparison to Reference Method		
	Our Approach	Reference Method [Ma 10]
Mean 2-D Error	**2.20 mm ± 1.59 mm**	4.07 mm ± 2.25 mm
Max 2-D Error	**13.94 mm**	16.31 mm
2-D Success Rate	**53.96 %**	13.41 %

Table 12.1: Comparison of the proposed CS motion compensation approach to the reference method as proposed in [Ma 10].

1.6 mm ± 0.9 mm was stated. This might be due to the fact, that our data was acquired with different settings, either regarding frames-per-second, or C-arm position, or both. The data used in [Ma 10] was not available for comparison.

The presented approach performs not as good as the approaches involving the circumferential mapping catheter as presented in previous chapters. The advantage of our new approach is defined by the incorporation of a training phase to calculate a prediction model. By doing so, our method easily outperforms the only other approach involving the coronary sinus catheter. As the error is still higher than reported by using the circumferential mapping catheter a combination of both methods should be considered. As presented in Chapter 11, the CS catheter can be used to detect non-physiological movement of the circumferential catheter. This method could be used to switch from a motion compensation approach based on the circumferential mapping catheter to a compensation using the CS catheter. Once the mapping catheter is stable again, one could switch back from the CS to the mapping catheter. Motion compensation derived from the CS catheter would already be better than a static overlay [Klem 07].

Apart from that, a 3-D training phase using a biplane sequence might also improve the results. Our method deals only with 2-D images and is prone to foreshortening which is difficult to observe in monoplane images. The CS catheter may not be the best surrogate for motion compensation in atrial fibrillation ablation procedures, but the presented method could be used as a fall-back option. In particular, when non-physiological movement of the circumferential mapping catheter is detected as proposed in Chapter 11, motion compensation using the CS catheter could be used until the mapping catheter gets stable again. An example of the motion compensation using the CS catheter is presented in Figure 12.3.

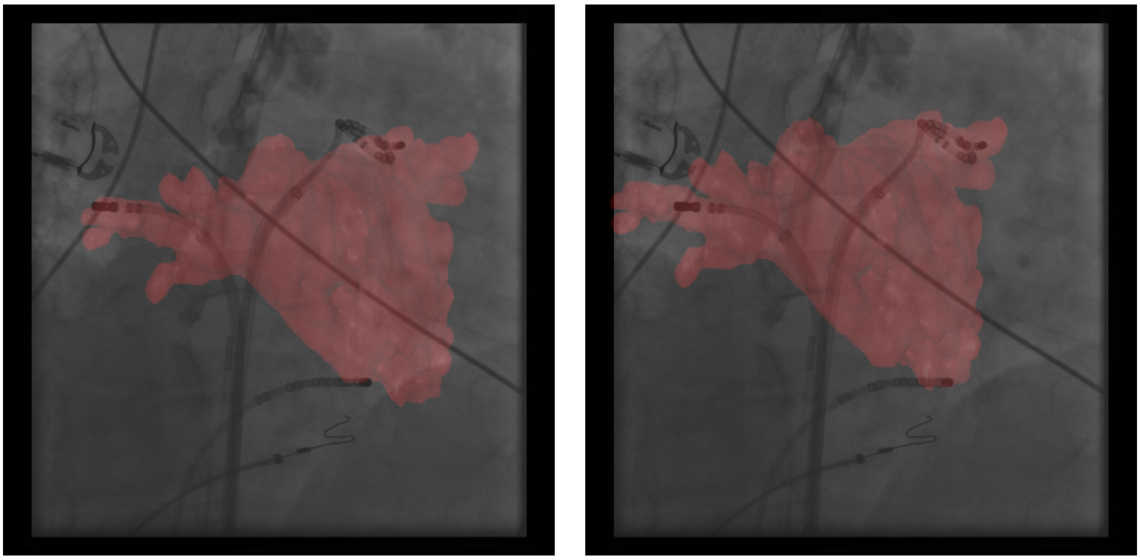

(a) (b)

Figure 12.3: A comparison showing the difference if motion compensation for overlay images is considered or not. (a) Single frame without motion compensation. (b) The same frame with applied motion compensation.

Part V

Outlook and Summary

CHAPTER 13

Outlook

In this chapter, the discussions of the previous chapters are recalled and directions for future work are presented.

13.1 Catheter Reconstruction from Two Views

Circumferential Mapping Catheter Reconstruction

The reconstruction of the circumferential mapping catheter, in particular considering only the circular part of the mapping catheter, has shown to be sufficiently accurate and useful. When using the reconstruction result as catheter model for the motion compensation approaches, it has proven to be of advantage. Currently, manual initialization is required. Automatic detection of ellipses has been proposed in [Jian 06, Kana 01, Kawa 98, Libu 06, Xie 02, Yao 05, Yao 04]. These methods could be adapted to the elliptical part of the circumferential mapping catheter. Also, an extension of the electrode detection and tracking as presented in [Wu 11, Wu 12] should also be considered. It has to be taken into account that different catheter types that are commercially available.

A spline-based reconstruction has been recently proposed in [Hoff 12b]. This could further improve the accuracy of the reconstruction method and the motion compensation methods as well. Besides a 3-D spline model, a physically motivated model incorporating material properties could be used. The circumferential mapping catheter can not always be considered as a perfect ellipse in 3-D. Using a parametric catheter model adapted to the 2-D observations could improve the localization in 3-D. If required, the type of catheter could be known at the beginning of the procedure. But an automatic detection of the catheter type should also be considered if a parametric model is used.

Cryo-Balloon Catheter Reconstruction

The method also requires manual initialization before the reconstruction is performed. An automatic detection of the cryo-balloon could be more difficult compared to the circumferential mapping catheter, but would significantly improve the clinical workflow. The proposed method in Chapter 3 assumes a spherical shape of the catheter. In reality, the catheter might be distorted or not completely inflated, thus being more ellipsoidal shaped than spherical. Unfortunately, an ellipsoid reconstruction from two views is not easy achievable and requires more information [Ma 96, Wije 06a]. Considering a detection of the balloon catheter, the required information could be automatically obtained from the fluoroscopic images.

In a next step, a physically motivated catheter model is worthwhile considering. By doing so, the required parameters to describe this catheter in 3-D could be adapted from a fluoroscopic biplane image pair. By doing so, the balloon itself could more likely be shaped as an ellipsoid.

13.2 Tools for Cryo-Balloon Ablation

AFiT - Atrial Fibrillation Ablation Planning Tool

Considering the *Atrial Fibrillation Ablation Planning Tool* (AFiT), the following aspects should be considered for future work. A visualization of the pre-operative data set is also desirable. So far, only the mesh representation of the left atrium is considered. Furthermore, currently only one mesh data set can be visualized. Current research in atrial fibrillation focuses on scar tissue information [Perr 12]. Such information should be taken into account for visualization as well.

Our current implementation features only one view of the 3-D scene. Hence, it requires a rotation of the 3-D data set to position the cryo-balloon catheter. A second view with 90^o degrees apart could be added to provide a stereo view of the 3-D scene. This would not require the operator to rotate the scene, but would provide two views at the same time.

Apart from that, one could assess the clinical value using a study where a certain number of cases is performed with and without using the tool. There might be a difference in procedure time and possibly even outcome. Further research will focus on making the planned cryo-balloon positions part of the live fluoroscopic images employing augmented fluoroscopy techniques. A first approach to reconstruct a balloon-catheter during the procedure within a pre-operative data set is presented in [Klei 11b]. The value of fluoroscopic overlay images for radiofrequency catheter ablations has been proven [Ecto 08a, De B 05, Bros 09a, Bros 10c, Bros 10b, Bros 10d]. An extension of AFiT to cover other single-shot devices is also conceivable. The current version does not provide other than visual feedback about the position. One could think of mesh deformation or force-feedback approaches to help the physician.

To make the planning step fully automatic, further clinical data is required. The planning should not only focus on single-shot-devices but also on the traditional ablation approach. A first approach for an automatic planning using a C-arm CT was proposed in [Keus 11]. In addition to that, proposals for the trans-septal puncture could also be made. Or at least an indicator if the planned positions are reachable with the considered type of catheter. If, due to the rigidness of the catheter, a position that is not within reach, a different catheter could be automatically proposed. To do so, information about the properties of the available catheters are required.

Cryo-Balloon Catheter Tracking Tool

The proposed method uses template matching and sum-of-squared-difference to determine the catheter position. Learning-based approaches as mentioned in [Bros 11e, Wu 11], should be considered for detection and tracking as well. An automatic detection of the catheter is desirable to avoid manual initialization. If the type of catheter, 23 mm or 28 mm, could be performed automatically, might be questionable, but this should be considered as well. This automatic detection was already mentioned for the reconstruction of cryo-balloon.

13.3 Motion Compensation involving One Catheter

First of all, some general aspects regarding motion compensation should be mentioned. In Chapter 7 and Chapter 8, it has been shown, that the learning-based approach is more accurate than the filter-based approach. However, the filter-based method is not completely outperformed. Other learning-based approaches apart from the boosted classifier cascade used in this work should be considered to improve the results, e.g., probabilistic boosting trees [Tu 05]. Even a combination of the filter-based and the learning-based might lead to new insights.

In addition to that, the problem of the initial alignment of the pre-operative data set to the fluoroscopic images is not yet solved. The current approach uses manual registration of the 3-D data set to sequences showing a contrast injection into the left atrium. A first approach towards initial registration has been proposed in [Bour 12a]. Other methods for automatic alignment have also been proposed [Liao 08, Penn 98, Penn 99, Prum 06a, Plui 03, Prum 05, Zago 07]. This initial registration should be considered, in particular as the motion compensation afterwards can not improve this registration.

Monoplane Motion Compensation

This method was specifically designed for monoplane C-arm systems. To further improve this method, an automatic detection of the circumferential mapping catheter is required. This would make the manual initialization obsolete. The registration itself could also be improved. One might considered different methods to solve the registration. Apart from a multi-scale grid search, a gradient-descent approach might yield the same results, but might be faster. A 2-D patient-specific motion model could be considered as well, either using a 2-D training phase similar to the one mentioned in Chapter 10, or on the fly by using a continuous regression.

It has been shown that the learning-based approach for motion compensation performs better than a filter-based approach. This could be further investigated, in particular, regarding the computation speed. The method presented here was optimized for multi-core CPUs. The use of the GPU might reduce the overall computation time. Furthermore, the quality of the segmentation should also be considered. It was shown that the current bottle neck is the skeletonization [Bros 12]. A method would be required that directly computes the centerline. A 2-D patient-specific motion model could be considered as well, either using a 2-D training phase, or on the fly by using a continuous regression.

Biplane Motion Compensation

Biplane motion compensation has shown to be the most accurate approach. Unfortunately, this comes at a very high price. It requires simultaneously biplane fluoroscopy which means an increased dose for patient and physician. As physicians might not be willing to pay such a high price, it was later used to generate a patient-specific motion model. Nevertheless, in certain phases during a procedure, in particular when a very high accurate catheter placement is required, one might consider this approach. In such cases, the method should be fast and robust, even more robust as the method presented here. To achieve a more robust method, one could use the patient-specific motion model to further improve the accuracy. Currently, no results from previous frames are considered. Adding this information might lead to a more stable method. To further improve these methods, a better 3-D catheter model would be required. In our case, only a 3-D ellipse had been used, but a 3-D spline representation as in [Hoff 12b] of the circular part might improve the accuracy. Furthermore, a deformable 3-D model might not improve the accuracy but could improve the stability of the algorithm [Sarr 01].

Constrained Motion Compensation

The constrained approach is more accurate than an unconstrained approach. But it suffers from the missing depth information. To achieve compensation for the missing depth information, the patient-specific motion model had been proposed. It should be considered if this model could be generated from sequentially acquired sequences as well. One could use the artificial heart cycle value from Chapter 12 to determine in which heart phase the images were acquired. Using such an approach, one could reduce the cost for the patient-specific model. Furthermore, the model could also be redefined during the procedure.

Patient-Specific Motion Model

The current motion model is considered to be linear. It is an open question, if this is really the case, or if a higher dimensional model is required. In addition to that, the question regarding the length of the training sequence is an open question. Using a higher dimensional model, the length of the training phase should be reconsidered as well. As additional information, the artificial heart cycle value from Chapter 12 could be used to achieve more stable results. Further investigation is required to answer the question if one motion model is enough, or if individual motion models for all four pulmonary veins are required. Assuming that one model is not sufficient, a motion model of the heart could be derived from the motion patterns of the PVs, which could be used to generate a 4-D overlay by deforming the current 3-D mesh representation.

13.4 Motion Compensation involving Two Catheters

Dynamic Detection of Catheter Displacement

The detection of non-physiological motion is based on 2-D observations of 3-D catheters. It should be considered to perform a similar analysis in 3-D. As the motion might be influenced by the patient's anatomy, one could consider a training phase for the motion patterns of the different catheters to detect non-physiological motion. Also, the artificial heart cycle value could be included. One could also implement the use or prediction methods such as Kalman filters to further improve the estimation of the PV position [Ramr 07, Welc 95].

Motion Compensation using CS Catheter

As mentioned before, a 3-D training phase using a biplane sequence might also lead to better results. This method deals only with 2-D images and is prone to foreshortening which is difficult to observe in monoplane images. Using 3-D information as input, one could further improve the results. If ECG-signals would be available, this method might also perform better, but synchronization between the fluoroscopic images and the ECG signal is then required. Furthermore, a 4-D overlay as proposed for coronary interventions could be considered as well [Shec 05].

CHAPTER 14

Summary

The focus of this work was on image processing for fluoroscopy guided atrial fibrillation ablation procedures. Atrial fibrillation is the most common arrhythmia and is associated with an increased risk of stroke. If drug therapy fails, then the state-of-the-art treatment option is catheter ablation. These procedures are performed as minimally invasive interventions inside of electrophysiology labs equipped with C-arm systems. To facilitate navigation for this kind of catheter procedures, imaging technology is essential. In Chapter 1, an overview of the human heart, cardiac arrhythmias and atrial fibrillation was presented. If drug therapy is ineffective or not well tolerated, then the standard treatment of atrial fibrillation is the electrical isolation of the four pulmonary veins attached to the left atrium. To this end, an ablation catheter and a circumferential mapping catheter are inserted into the left atrium. The mapping catheter measures the electrical signals around the ostium of a pulmonary vein. The ablation catheter is used to ablate tissue at the ostium and after the successful ablation render the pulmonary vein electrically isolated.

To support atrial fibrillation ablation procedures, two methods for catheter reconstruction from two views were developed. In Chapter 2, the reconstruction of the circumferential mapping catheter was presented. The reconstruction method requires manual initialization in the two image planes. The reconstruction can be performed from either two ellipses in the two images, or from one ellipse and one ellipse degenerated to a line. This method was evaluated in simulations and in experiments as well. In Chapter 3, we presented a method for the reconstruction of a cryo-balloon catheter. This kind of catheter belongs to the group of so-called single-shot-devices. They are designed to electrically isolate a pulmonary vein with a single application. The cryo-balloon ablation technique was introduced to reduce risks related to radio-frequency catheter ablation such as pulmonary vein stenosis and esophageal fistula. Our method yields superior results for sphere reconstruction from two views when compared to other methods known from literature. Using simulation studies, we also found that the best angular difference for reconstruction is 90^o. This is consistent with findings for point reconstruction from two views reported in literature.

If cryo-balloon catheters fit well to the underlying anatomy of the left atrium, a contiguous circular lesion can be achieved very efficiently, thus, simplifying the procedure and speeding it up as well. Since a good fit to the patient anatomy is key for an efficient cryo-balloon procedure, a planning tool was developed to verify it. This ***A****trial* ***Fi****brillation Ablation Planning* ***T****ool* (AFiT) was presented in Chapter 4. It tool provides direct visual feedback about the fit of a cyro-balloon to a patient's anatomy. The visualization is performed using a segmented left atrium and cryo-balloon catheter models with a diameter of 23 mm and 28 mm, respectively. Depending on the anatomy at hand, a physician can now make an informed decision about whether to perform cryo-ablation at all and which catheters to use.

As no navigation system is yet available for localizing cryo-balloon catheters without fluoroscopy, these devices are placed and applied under fluoroscopy. To provide support for ablation procedures involving cryo-balloon catheters, we proposed a method to track and visualize a cryo-balloon device to simplify catheter placement in Chapter 5. In involves a manual initialization to arrive at a 2-D template that is tracked by means of template matching. Our method successfully tracked a cryo-thermal balloon catheter in 12 clinical sequences. It is able to superimpose the position and diameter of the device onto live fluoroscopic images to enhance the visibility of the cryo-balloon catheter. The visualized outline of the cryo-balloon helps the physician to see the dimensions of the balloon catheter, otherwise hardly visible under X-ray. Our proposed method achieved an average 2-D tracking error of 0.60 mm $\pm$ 0.32 mm.

In Chapters 7, 8, 9, and 10 we present our research on motion compensation methods for atrial fibrillation ablation procedures were presented. To this end, a filter-based and a learning-based method for catheter segmentation in fluoroscopic images were presented in Chapter 6. These two methods were then used as basis for the motion compensation methods in Chapters 7 and 8. The method in Chapter 7 is designed for monoplane C-arm systems. This approach is based on model-based 2-D/2-D registration of a 2-D catheter model to the segmented circumferential mapping catheter in fluoroscopic images. The proposed method was evaluated on 46 monoplane sequences and yielded a mean tracking error of 0.58 mm $\pm$ 0.22 mm. This method achieved a frame rate of 10 fps. The method in Chapter 8 uses a model-based 2-D/3-D registration. To this end, the method from Chapter 2 is used to generate a 3-D model of the circumferential mapping catheter. This catheter is then tracked by means of a 2-D/3-D registration in simultaneous biplane images. The proposed method achieves an average 3-D tracking error of 1.35 mm $\pm$ 0.81 mm. Our implementation achieves a frame rate of 2 fps. The methods in Chapters 7 and 8 have their advantages and disadvantages. The monoplane approach, on the one hand, works with monoplane image acquisitions, but each rotation of the C-arm requires a reinitialization of the catheter model. The biplane approach, on the other hand, uses a 3-D model, thus eliminating the need for reinitialization, but it requires simultaneous biplane fluoroscopy, which is rarely used in clinical practice due to dose concerns. To improve the situation for sequential biplane acquisitions, we proposed in Chapter 9 a constrained 2-D/3-D registration to perform motion compensation using a 3-D catheter model. The search region is constrained to a direction parallel to the image plane. By doing so, our method yielded an average 3-D error of 1.50 mm $\pm$ 0.94 mm and achieves a frame rate of 8 fps. This method has shown, that it is advantageous to constrain the 2-D/3-D registration when used for motion compensation. To achieve motion compensation in view direction, prior knowledge about the movement of the circumferential mapping catheter needs to be taken into account. In Chapter 10 such information was obtained by a training phase which tracked the mapping catheter in simultaneous biplane images. Afterwards, the principal motion axis is determined from the trajectory established during the tracking training phase. This axis is considered a patient-specific motion model. In addition, another vector perpendicular to the view direction and the motion axis is used computed. This vector and the main motion axis are used to constrain a model-based 2-D/3-D registration to track the circumferential mapping catheter in 3-D using only monoplane fluoroscopy. This method yielded an average 3-D error of 1.63 mm $\pm$ 1.16 mm while achieving a frame rate of 5 fps. The methods in Chapters 7, 8, 9, and 10 were all evaluated on the same data set. A comparison of all motion compensation methods is given at the end of Chapter 10 in Table 10.2.

The drawback of the proposed methods so far, is a lack to detect when the circumferential mapping catheter is moved from one PV to another. To detect such motion, we proposed in Chapter 11 the use of a virtual electrode on the coronary sinus catheter as a point of reference. To achieve a reliable and robust motion compensation, we track both catheters, the circumferential mapping catheter and the coronary sinus catheter, at the same time and compare the absolute 2-D distance between the virtual electrode and the loop's center of the mapping catheter between two consecutive frames. If the distance changes by more than 5 %, we can assume that the circumferential mapping catheter has been moved from one pulmonary vein to another. In this case, the false positive rate was 5.8 %, i.e., in 5.8 % of the frames non-physiological was wrongly detected. In Chapter 12 we further investigated the use of the coronary sinus catheter for motion compensation. The circumferential mapping catheter is moved on purpose and may not always be available. To this end, we proposed a training phase during which both catheters, the circumferential mapping and coronary sinus catheter, are tracked. After the training phase, a motion prediction model is calculated. After that, the prediction model can be used to estimate the cardiac and respiratory motion at the ostium of the pulmonary vein by using the CS catheter only. On the available data set, this method achieved an average 2-D motion estimation of 2.20 mm $\pm$ 1.59 mm and outperforms a similar method reported in literature. We can conclude that motion compensation using the CS catheter is possible, but it is not as accurate as it could be using the circumferential mapping catheter. Nevertheless, such kind of motion compensation is still better than no motion compensation at all.

In Chapter 13 we summarize ideas on future work to improve and further investigate the methods presented in this thesis.

List of Acronyms

AFib	Atrial Fibrillation
AFiT	Atrial Fibrillation Ablation Planning Tool
AV	Atrio-Ventricular
CART	Classification and Regression Tree
CFM	Circumferential Mapping
CS	Coronary Sinus
CT	Computed Tomography
DT	Distance Transform
ECG	Electrocardiogram
EP	Electrophysiology
FN	False-Negative
FP	False-Positive
fps	frames-per-second
LA	Left Atrium
MPE	Most Proximal Electrode
MRI	Magnetic Resonance Imaging
PCA	Principal Component Analysis
PV	Pulmonary Vein
ROI	Region-Of-Interest
VBO	Vertex-Buffer-Object
VE	Virtual Electrode

List of Figures

List of Structograms

List of Symbols

a	Implicit ellipse parameters	25
f	Single feature	135
k	Number of possible ellipse solution	24
n	Size of template	56
n_d	Distance of a plane to the origin	24
r_s	Radius of sphere	36
t	Time step	56
D	Half size of image template	56
E	Number of 3-D catheter model points	84
K	Number of electrodes on the CS catheter	135
L	Number of images in training phase	135
M	Search range for template matching	56
N	Number of strong classifiers in a boosted cascade	69
S	Size of a fluoroscopic image	56
T	Length of fluoroscopic sequence	56
W	Number of 3-D points	36

$\mathbf{a}$	Parameter for cones	35
$\mathbf{b}$	Viewing direction	52
$\mathbf{c}$	Electrode of the coronary sinus catheter	135
$\mathbf{d}$	Direction vector in 3-D	26
$\mathbf{e}$	Eigenvector	24
$\mathbf{f}$	Feature vector	136
$\mathbf{g}_m$	Main motion vector of catheter model in 3-D	107
$\mathbf{g}_p$	Vector perpendicular to main motion vector and view direction	108
$\mathbf{h}$	Translation parameters for an unconstrained 3-D translation	84
$\mathbf{k}$	Interpolated 3-D point of a mesh	52
$\mathbf{m}$	Model point in 3-D	25
$\overline{\mathbf{m}}$	Center of elliptical catheter model in 3-D	107
$\mathbf{n}$	Normal in 3-D space	24
$\tilde{\mathbf{n}}$	Normal in homogeneous coordinates	24
$\mathbf{o}$	Optical Center	21
$\mathbf{p}$	Point in 2-D	21
$\tilde{\mathbf{p}}$	Point in 2-D in homogeneous coordinates	21
$\mathbf{q}$	Point in 2-D	26
$\mathbf{r}$	Ray in 3-D	26
$\mathbf{s}$	Spline in 2-D coordinates	75
$\mathbf{l}$	Translation vector in 2-D	74
$\mathbf{t}$	Translation vector	35
$\mathbf{u}$	Spanning vector of a plane in 3-D	25

$\mathbf{v}$	Spanning vector of a plane in 3-D	25
$\mathbf{w}$	Point in 3-D space	21
$\widetilde{\mathbf{w}}$	Point in 3-D in homogeneous coordinates	21
$\mathbf{w}_c$	Center of a sphere	36
$\mathbf{w}_s$	Sampled point on a sphere	37

$\mathbf{B}$	Transformation matrix	23
$\mathbf{C}$	Ellipse Parameters in Matrix Notation	21
$\mathbf{I}_T$	Image template	56
$\mathbf{I}_t$	Fluoroscopic image at time t	56
$\mathbf{I}_{\mathrm{DT}}$	Distance transformed image	70
$\mathbf{P}$	Projection Matrix	21
$\mathbf{Q}$	Matrix describing quadric	22
$\mathbf{Q}^+$	Left upper 3×3-sub-matrix of a quadri.c	22
$\mathbf{R}$	Rotation matrix	35
$\mathbf{T}_{\mathrm{u}}$	Translation matrix for unconstrained registration	84
$\mathbf{T}_{\mathrm{c}}$	Translation matrix for constrained registration	94
$\mathbf{T}_{\widetilde{\mathbf{n}}}$	Normal $\widetilde{\mathbf{n}}$ in matrix notation	24
$\mathbf{U}$	Quadric describing intersection between Cone and Plane	25

α	Leaf of a CART	68
β	Index for heart cycle value	137
γ	Index for heart cycle value	137
δ	Smoothing parameter	138
ε	Error value	58
ε_s	Error of sphere reconstruction	37
ε_t	Error for template matching at time t	58
ζ	Parameter for constrained translation	94
η	Parameter for constrained translation	94
θ	Node of a CART	68
ϑ	Heart cycle value	136
ι	Regularization parameter	137
κ	Scaling parameter	138
λ	Latent root of Lambda-Matrices	22
μ	Eigenvalues	23
ξ	Strong classifier in a cascade	68
ρ	Pixel spacing of an image	58
ϱ	Angle between a point and the viewing direction	52
σ	Standard deviation of Gaussian noise	27
τ	Ray parameter for ray $\mathbf{r}$	26
ϕ	Length of one semi axis of ellipse	25
χ	Parameter for cones	35
ψ	Length of one semi axis of ellipse	25
ω	Spline parameter	75

List of Tables

Bibliography

[Aken 08] T. Akenine-Möller, E. Haines, and N. Hoffman. *Real-Time Rendering*. AK Peters, Natick, MA, USA, 3rd Ed., July 2008.

[Al A 08] A. Al-Ahmad, L. Wigström, D. Sandner-Porkristl, P. Wang, P. Zei, J. Boese, G. Lauritsch, T. Moore, F. Chan, and R. Fahrig. "Time-resolved three-dimensional imaging of the left atrium and pulmonary veins in the interventional suite: A comparison between multi-sweep gated rotational three-dimensional reconstructed fluoroscopy and multislice computed tomography". *Heart Rhythm*, Vol. 5, No. 4, pp. 513–519, April 2008.

[Alle 13] H. Allen. "Auricular Fibrillation". *California State Journal of Medicine*, Vol. XI, No. 12, pp. 496–499, December 1913.

[Andr 05] R. Andres, P. Berdal, H.-R. Baur, and T. Carrel. "Schwere embolische Komplikation nach chirugischer Radiofrequenz-Ablation eines Vorhofflimmerns". *Kardiovaskuläre Medizin*, Vol. 8, No. 6, pp. 241–245, June 2005.

[Ante 09] E. Anter and D. Callans. "Pharmacological and Electrical Conversion of Atrial Fibrillation to Sinus Rhythm Is Worth the Effort". *Circulation*, Vol. 120, No. 14, pp. 1436–1443, October 2009.

[Arru 07] M. Arruda, D. He, P. Friedman, H. Nakagawa, C. Bruce, K. Azegami, R. Anders, P. Kozel, A. Chiavetta, P. Marad, D. Macadam, W. Jackman, and D. Wilber. "A Novel Mesh Electrode Catheter for Mapping and Radiofrequency Delivery at the Left Atrium-Pulmonary Vein Junction: A Single-Catheter Approach to Pulmonary Vein Antrum Isolation". *Journal of Cardiovascular Electrophysiology*, Vol. 18, No. 2, pp. 206–211, February 2007.

[Atas 08] S. Atasoy, M. Groher, D. Zikic, B. Glocker, T. Waggershauser, M. Pfister, and N. Navab. "Real-Time Respiratory Motion Tracking: Roadmap Correction for Hepatic Artery Catheterizations". In: M. I. Miga and K. R. Cleary, Eds., *Proceedings of SPIE Medical Imaging 2008: Visualization, Image-guided Procedures, and Modeling, San Diego, CA, USA, February 16–21*, p. 691815, 2008.

[Aufr 92] R. Aufrichtig and D. Wilson. "Marking Arteries and Catheters in X-Ray Fluoroscopy Using Morphological Filtering". *14th Annual International Conference of the IEEE Engineering in Medicine and Biology Society, Paris, France, October 29 – November 1*, Vol. 5, pp. 1854–1855, October 1992.

[Aufr 93] R. Aufrichtig, D. Geiger, A. Singh, and D. Wilson. "Spatio-Temporal X-ray Fluoroscopy Filteringusing Object Detection". In: *IEEE Proceedings: Computers in Cardiology 1993, London, UK, September 5–8*, September 1993.

[Aufr 95] R. Aufrichtig and D. Wilson. “X-Ray Fluoroscopy Spatio-Temporal Filtering with Object Detection”. *IEEE Transactions on Medical Imaging*, Vol. 14, No. 4, pp. 733–746, December 1995.

[Avit 03] B. Avitall, D. Urboniene, G. Rozmus, D. Lafontaine, R. Helms, and A. Urbonas. “New Cryotechnology for Electrical Isolation of the Pulmonary Veins”. *Journal of Cardiovascular Electrophysiology*, Vol. 14, No. 3, pp. 281–286, March 2003.

[Back 04] T. Back, M. Schaeg, C. Back, Y. Epifanov, T. Hemmen, R. Dodel, and O. Schöffski. “Kosten der Stroke-Unit-Care in Deutschland - Ressourcenverbrauch und Erlöse mit deutschen Diagnosis Related Groups”. *Der Nervenarzt*, Vol. 10, No. 75, pp. 991–999, October 2004.

[Baer 03a] S. Baert, E. van de Kraats, T. van Walsum, M. Viergever, and W. Niessen. “Three-Dimensional Guide-Wire Reconstruction From Biplane Image Sequences for Integrated Display in 3-D Vasculature”. *IEEE Transactions On Medical Imaging*, Vol. 22, No. 10, pp. 1252–1258, October 2003.

[Baer 03b] S. Baert, M. Viergever, and W. Niessen. “Guide Wire Tracking During Endovascular Interventions”. *IEEE Transactions On Medical Imaging*, Vol. 22, No. 8, pp. 965–972, August 2003.

[Bahn 04] T. Bahnson and A. Grant. “To Be or Not To Be in Normal Sinus Rhythm: What Do We Really Know?”. *Annals of Interal Medicine*, Vol. 141, No. 9, pp. 727–729, November 2004.

[Barb 07] A. Barbu, V. Athitsos, B. Georgescu, S. Boehm, P. Durlak, and D. Comaniciu. “Hierarchical Learning of Curves: Application to Guidewire Localization in Fluoroscopy”. In: *IEEE Conference on Computer Vision and Pattern Recognition (CVPR 2007), Minneapolis, MN, USA, June 18–23*, pp. 1–8, June 2007.

[Bary 11] C. von Bary, S. Weber, C. Dornia, C. Eissnert, C. Fellner, P. Latzin, S. Fredersdorf, S. Stadler, and O. Hamer. “Evaluation of Pulmonary Vein Stenosis After Pulmonary Vein Isolation Using a Novel Circular Mapping and Ablation Catheter (PVAC)”. *Circulation: Arrhythmia and Electrophysiology*, Vol. 4, No. 5, pp. 630–636, October 2011.

[Bell 07] Y. van Belle, P. Janse, M. Rivero-Ayerza, A. Thornton, E. Jessurun, D. Theuns, and L. Jordaens. “Pulmonary vein isolation using an occluding cryoballoon for circumferential ablation: feasibility, complications, and short-term outcome”. *European Heart Journal*, Vol. 28, No. 18, pp. 2231–2237, September 2007.

[Blan 10] P. Blanke, T. Baumann, M. Langer, and G. Pache. “Imaging of pulmonary vein anatomy using low-dose prospective ECG-triggered dual-source computed tomography”. *European Radiology*, Vol. 20, No. 8, pp. 1851–1855, August 2010.

[Borg 86] G. Borgefors. “Distance transformations in digital images”. *Computer Vision, Graphics, and Image Processing*, Vol. 34, No. 3, pp. 344–371, June 1986.

[Bour 10] F. Bourier, A. Brost, L. Yatziv, J. Hornegger, N. Strobel, and K. Kurzidim. "Coronary Sinus Extraction for Multimodality Registration to guide Transseptal Puncture". In: T. Kahn, F. Jolesz, and J. Lewin, Eds., *8th Interventional MRI Symposium, Leipzig, Germany, September 24–25*, pp. 311–313, 2010.

[Bour 11a] F. Bourier, A. Brost, M. Koch, A. Kleinoeder, A. Kiraly, J. Hornegger, N. Strobel, N. Zorger, H.-J. Schneider, and K. Kurzidim. "Guiding transseptal puncture by 3D-overlay of the left atrium and ascending aorta by a new softwareprototype". In: European Society of Cardiology, Ed., *Congress of the European Society of Cardiology (ESC 2011), Paris, France, August 27–31*, 2011.

[Bour 11b] F. Bourier, A. Brost, J. Hornegger, A. Kiraly, J. Barbot, N. Strobel, N. Zorger, H.-J. Schneider, F. Heissenhuber, and K. Kurzidim. "Augmented fluoroscopy-based navigation on a biplane angiography system for pulmonary vein isolation". In: European Society of Cardiology, Ed., *ESC Congress (ESC 2011), Paris, France, August 27–31*, 2011.

[Bour 11c] F. Bourier, H.-J. Schneider, F. Heissenhuber, P. Ganslmeier, R. Fischer, A. Brost, M. Koch, N. Strobel, J. Hornegger, and K. Kurzidim. "Frühzeitige Registrierung eines 3D-Overlays des linken Atriums während linksatrialen Ablationen mittels Koronarsinuskatheter". In: D. G. für Kardiologie, Ed., *77. Jahrestagung (Frühjahrestagung der Deutschen Gesellschaft für Kardiologie), Mannheim, Deutschland, April 27–30*, 2011.

[Bour 12a] F. Bourier, A. Brost, A. Kleinoeder, T. Kurzendorfer, M. Koch, A. Kiraly, H.-J. Schneider, J. Hornegger, N. Strobel, and K. Kurzidim. "Navigation for fluoroscopy-guided cryo-balloon ablation procedures of atrial fibrillation". In: D. Holmes and K. Wong, Eds., *Proceedings of SPIE Medical Imaging 2012: Image-Guided Procedures, Robotic Interventions, and Modeling, San Diego, CA, USA, Febuary 4–9*, p. 831627, 2012.

[Bour 12b] F. Bourier, A. Brost, A. Kleinoeder, T. Kurzendorfer, M. Koch, A. Kiraly, H.-J. Schneider, J. Hornegger, N. Strobel, and K. Kurzidim. "Navigation for Fluoroscopy-Guided Cryo-Balloon Ablation Procedures of Atrial Fibrillation". In: D. Holmes and K. Wong, Eds., *Proceedings of SPIE Medical Imaging 2012: Image-Guided Procedures, Robotic Interventions, and Modeling, San Diego, CA, USA, Febuary 4–9*, p. 831627, 2012.

[Brei 84] L. Breiman, J. Friedman, R. Olshen, and C. Stone. *Classification and Regression Trees*. Chapman & Hall, New York, NY, USA, 1984.

[Breu 95] H. Breu, J. Gil, D. Kirkpatrick, and M. Werman. "Linear time Euclidean distance transform algorithms". *IEEE Transactions on Pattern Analysis and Machine Intelligence*, Vol. 17, No. 5, pp. 529–533, May 1995.

[Bron 01] I. Bronstein, K. Semendjajew, G. Musiol, and H. Mühlig. *Taschenbuch der Mathematik*. Verlag Harri Deutsch, Frankfurt am Main, Germany, 5th Ed., 2001.

[Bros 09a] A. Brost, R. Liao, J. Hornegger, and N. Strobel. "3-D Respiratory Motion Compensation during EP Procedures by Image-Based 3-D Lasso Catheter Model Generation and Tracking". *Lecture Notes in Computer*

Science (12th International Conference on Medical Image Computing and Computer-Assisted Intervention, MICCAI 2009), London, UK, September 20–24, Vol. 5761, pp. 394–401, 2009.

[Bros 09b] A. Brost. *Model-Based Catheter Tracking in Bi-Plane Fluoroscopic Sequences*. Master's thesis, Pattern Recognition Lab, Department of Computer Science, Friedrich-Alexander-Universität Erlangen-Nürnberg, Germany, April 2009.

[Bros 09c] A. Brost, N. Strobel, L. Yatziv, W. Gilson, B. Meyer, J. Hornegger, J. Lewin, , and F. Wacker. "Geometric Accuracy of 3-D X-Ray Image-Based Localization from Two C-Arm Views". In: *Workshop on Geometric Accuracy in Image Guided Interventions (MICCAI 2009), London, UK, September 20*, pp. 1–8, 2009.

[Bros 09d] A. Brost, N. Strobel, L. Yatziv, W. Gilson, B. Meyer, J. Hornegger, J. Lewin, and F. Wacker. "Accuracy of x-ray image-based 3D localization from two C-arm views: a comparison between an ideal system and a real device". In: M. Miga and K. Wong, Eds., *Proceedings of SPIE Medical Imaging 2009: Visualization, Image-Guided Procedures, and Modeling, Lake Buena Vista, FL, USA, February 7–12*, p. 72611Z, 2009.

[Bros 10a] A. Brost, R. Liao, J. Hornegger, and N. Strobel. "3D model-based catheter tracking for motion compensation in EP procedures". In: *Proceedings of SPIE Medical Imaging 2010: Visualization, Image-Guided Procedures, and Modeling, San Diego, CA, USA, March 4–10*, p. 762507, 2010.

[Bros 10b] A. Brost, R. Liao, N. Strobel, and J. Hornegger. "Respiratory motion compensation by model-based catheter tracking during EP procedures". *Medical Image Analysis*, Vol. 14, No. 5, pp. 695–706, October 2010.

[Bros 10c] A. Brost, A. Wimmer, R. Liao, J. Hornegger, and N. Strobel. "Catheter Tracking: Filter-Based vs. Learning-Based". In: M. Goesele, S. Roth, A. Kuijper, B. Schiele, and K. Schindler, Eds., *Lecture Notes in Computer Science (Proceedings of 32nd DAGM Symposium, Darmstadt, Germany, September 22–24)*, pp. 293–302, 2010.

[Bros 10d] A. Brost, R. Liao, J. Hornegger, and N. Strobel. "Model-Based Registration for Motion Compensation during EP Ablation Procedures". In: B. Fischer, B. Dawant, and C. Lorenz, Eds., *Lecture Notes in Computer Science, Workshop on Biomedical Image Registration (WBIR 2010) Lübeck, Germany, July 11–13*, pp. 234–245, 2010.

[Bros 11a] A. Brost, F. Bourier, A. Kleinoeder, J. Raab, M. Koch, M. Stamminger, J. Hornegger, N. Strobel, and K. Kurzidim. "AFiT - Atrial Fibrillation Ablation Planning Tool". In: *16th International Workskhop on Vision, Modeling, and Visualization (VMV 2011), Berlin, Germany, October 4–6*, pp. 223–230, 2011.

[Bros 11b] A. Brost, F. Bourier, L. Yatziv, M. Koch, J. Hornegger, N. Strobel, and K. Kurzidim. "First steps towards initial registration for electrophysiology procedures". In: K. Wong and D. Holmes, Eds., *Proceedings of SPIE Medical Imaging 2011: Visualization, Image-Guided Procedures, and Modeling, Lake Buena Vista, FL, USA, February 12–17*, p. 79641P, 2011.

[Bros 11c] A. Brost, W. Wu, M. Koch, A. Wimmer, T. Chen, R. Liao, J. Hornegger, and N. Strobel. “Combined Cardiac and Respiratory Motion Compensation for Atrial Fibrillation Ablation Procedures”. *Lecture Notes in Computer Science (14th International Conference on Medical Image Computing and Computer-Assisted Intervention, MICCAI 2011), Toronto, Canada, September 18–22*, Vol. 6891, pp. 540–547, 2011.

[Bros 11d] A. Brost, A. Wimmer, F. Bourier, M. Koch, R. Liao, K. Kurzidim, N. Strobel, and J. Hornegger. “Constrained Registration for Motion Compensation in Atrial Fibrillation Ablation Procedures ”. *IEEE Transactions on Medical Imaging*, Vol. [Epub ahead of print], p. [n/a], December 2011.

[Bros 11e] A. Brost, A. Wimmer, R. Liao, J. Hornegger, and N. Strobel. “Constrained 2-D/3-D Registration for Motion Compensation in AFib Ablation Procedures”. In: R. Taylor and G.-Z. Yang, Eds., *Lecture Notes in Computer Science (2nd International Conference on Information Processing in Computer-Assisted Interventions, IPCAI 2011), Berlin, Germany, June 22*, pp. 133–144, 2011.

[Bros 11f] A. Brost, A. Wimmer, R. Liao, J. Hornegger, and N. Strobel. “Motion Compensation by Registration-Based Catheter Tracking”. In: K. Wong and D. Holmes, Eds., *Proceedings of SPIE Medical Imaging 2011: Visualization, Image-Guided Procedures, and Modeling, Lake Buena Vista, Florida, USA, February 12–17*, p. 79641O, 2011.

[Bros 12] A. Brost, F. Bourier, A. Wimmer, M. Koch, A. Kiraly, R. Liao, K. Kurzidim, J. Hornegger, and N. Strobel. “Real-time circumferential mapping catheter tracking for motion compensation in atrial fibrillation ablation procedures”. In: D. Holmes and K. Wong, Eds., *Proceedings of SPIE Medical Imaging 2012: Image-Guided Procedures, Robotic Interventions, and Modeling, San Diego, CA, USA, Febuary 4–9*, p. 83162V, 2012.

[Calk 07] H. Calkins, J. Brugada, D. Packer, R. Cappato, S.-A. Chen, H. Crijns, J. R. Damiano, D. Davies, D. Haines, M. Haïssaguerre, Y. Iesaka, W. Jackman, P. Jaïs, H. Kottkamp, K. Kuck, B. Lindsay, F. Marchlinski, P. McCarthy, J. Mont, F. Moradi, K. Nademanee, A. Natale, C. Pappone, E. Prystowsky, A. Raviele, J. Ruskin, and R. Shemin. “HRS/EHRA/ECAS Expert Consensus Statement on Catheter and Surgical Ablation of Atrial Fibrillation: Recommendations for Personnel, Policy, Procedures and Follow-Up”. *Europace*, Vol. 9, No. 6, pp. 335–379, June 2007.

[Camm 10] A. Camm, P. Kirchhof, G. Lip, U. Schotten, I. Savelieva, S. Ernst, I. van Gelder, N. Al-Attar, G. Hindricks, B. Prendergast, H. Heidbüchel, O. Alfieri, A. Angelini, D. Atar, P. Colonna, R. de Caterina, J. de Sutter, A. Goette, B. Gorenek, M. Heldal, S. Hohloser, P. Kolh, J.-Y. L. Heuzey, P. Ponikowski, and F. Rutten. “Guidelines for the management of atrial fibrillation: The Task Force for the Management of Atrial Fibrillation of the European Society of Cardiology (ESC)”. *European Heart Journal*, Vol. 31, No. 19, pp. 2369–2429, October 2010.

[Capp 05] R. Cappato, H. Calkins, S.-A. Chen, W. Davies, Y. Iesaka, J. Kalman, Y.-H. Kim, G. Klein, D. Packer, and A. Skanes. "Worldwide Survey on the Methods, Efficacy, and Safety of Catheter Ablation for Human Atrial Fibrillation". *Circulation*, Vol. 111, No. 9, pp. 1100–1105, March 2005.

[Chen 99] S.-A. Chen, M.-H. Hsieh, C.-T. Tai, C.-F. Tsai, V. Prakash, W.-C. Yu, T.-L. Hsu, Y.-A. Ding, and M.-S. Chang. "Initiation of Atrial Fibrillation by Ectopic Beats Originating From the Pulmonary Veins". *Circulation*, Vol. 100, No. 2, pp. 1879–1886, November 1999.

[Cron 04] P. Cronin, M. Sneider, E. Kazerooni, A. Kelly, C. Scharf, H. Oral, and F. Morady. "MDCT of the Left Atrium and Pulmonary Veins in Planning Radiofrequency Ablation for Atrial Fibrillation: A How-To Guide". *American Journal of Roentgenology*, Vol. 183, No. 3, pp. 767–778, September 2004.

[Cych 94] J. Cychosz. "Efficient Binary Image Thinning using Neighborhood Maps". In: P. Heckbert, Ed., *Graphics Gems IV*, pp. 465–473, Academic Press, San Diego, CA, USA, 1994.

[Dacc 07] M. Daccarett, N. Segerson, J. Günther, G. Nölker, K. Gutleben, J. Brachmann, and N. Marrouche. "Blinded correlation study of three-dimensional electro-anatomical image integration and phased array intra-cardiac echocardiography for left atrial mapping". *Europace*, Vol. 9, No. 10, pp. 923–926, October 2007.

[De B 05] S. De Buck, F. Maes, J. Ector, J. Bogaert, S. Dymarkowski, H. Heidbüchel, and P. Suetens. "An Augmented Reality System for Patient-Specific Guidance of Cardiac Catheter Ablation Procedures". *IEEE Transactions on Medical Imaging*, Vol. 24, No. 11, pp. 1512–1524, November 2005.

[Defa 11] P. Defaye, A. Kane, A. Chaib, and P. Jacon. "Efficacy and safety of pulmonary vein isolation by cryoablation for the treatment of paroxysmal and persistend atrial fibrillation". *Europace*, Vol. 13, No. 6, pp. 789–795, June 2011.

[Deis 03] I. Deisenhofer, M. Schneider, M. Böhlen-Knauf, B. Zrenner, G. Ndrepepa, S. Schmieder, S. Weber, J. Schreieck, S. Weyerbrock, and C. Schmitt. "Circumferential Mapping and Electric Isolation of Pulmonary Veins in Patients With Atrial Fibrillation". *American Journal of Cardiology*, Vol. 91, No. 2, pp. 159–163, January 2003.

[Deis 06] I. Deisenhofer, H. Estner, and A. Pustowoit. *Catheter Ablation of Cardiac Arrhythmias*. Steinkopff Verlag, Darmstadt, Germany, 2006.

[Dela 07] E. Delacrétaz, J. Seiler, M. Schwerzmann, and H. Tanner. "Electroanatomic imaging to guide ablation of multiple intra-atrial reentrant circuits in congenital heart disease". *Kardiovaskuläre Medizin*, Vol. 10, No. 10, pp. 339–341, October 2007.

[Doss 00] O. Dössel. *Bildgebende Verfahren in der Medizin*. Springer Verlag, Heidelberg, Germany, 2000.

[Duda 01] R. Duda, P. Hart, and D. Stork. *Pattern Classification*. Wiley, New Yorkn NY, USA, 2nd Ed., 2001.

[Dukk 10] S. Dukkipati, P. Neuzil, J. Skoda, J. Petru, A. d'Avila, S. Doshi, and V. Reddy. "Visual balloon-guided point-by-point ablation: reliable, reproducible, and persistent pulmonary vein isolation". *Circulation: Arrhythmia and Electrophysiology*, Vol. 3, No. 3, pp. 266–273, June 2010.

[Earl 06] M. Earley, D. Abrams, A. Staniforth, S. Sporton, and R. Schilling. "Catheter ablation of permanent atrial fibrillation: medium term results". *Heart*, Vol. 92, No. 2, pp. 233–238, February 2006.

[Ecke 02] R. Eckert, D. Randall, W. Burggren, and K. French. *Tierphysiologie*. Georg Thieme Verlag, Stuttgart, Germany / New York, NY, USA, 4th Ed., 2002.

[Ecto 08a] J. Ector, S. de Buck, W. Huybrechts, D. Nuyens, S. Dymarkowski, J. Bogaert, F. Maes, and H. Heidbüchel. "Biplane three-dimensional augmented fluroroscopy as single navigation tool for ablation of atrial fibrillation: Accuracy and clinical value". *Heart Rhythm*, Vol. 5, No. 7, pp. 957–964, July 2008.

[Ecto 08b] J. Ector, S. de Buck, D. Loeckx, W. Coudyzer, F. Maes, S. Dymarkowski, J. Bogaert, and H. Heidbüchel. "Changes in left atrial anatomy due to respiration: Impact on three-dimensional image integration during atrial fibrillation ablation". *Journal of Cardiovascular Electrophysiology*, Vol. 19, No. 8, pp. 828–834, August 2008.

[Este 08] M. Esteghamatian, Z. Azimifar, P. Radau, and G. Wright. "Real-time 2D-3D MR cardiac image registration during respiration using extended Kalman filter predictors". In: *9th International Conference on Signal Processing (ICSP 2008), Beijing, China, October 26–29*, pp. 1325–1328, 2008.

[Fabb 08] R. Fabbri, L. Costa, J. Torelli, and O. Bruno. "2D Euclidean Distance Transform Algorithms: A Comparative Survey". *ACM Computing Surveys (CSUR)*, Vol. 40, No. 1, pp. 1–44, February 2008.

[Fahr 00] R. Fahrig and D. W. Holdsworth. "Three-dimensional computed tomographic reconstruction using a C-arm mounted XRII: Image-based correction of gantry motion nonidealities". *Medical Physics*, Vol. 27, No. 1, pp. 30–38, January 2000.

[Fall 04] P. Fallavollita, P. Savard, and G. Sierra. "Fluoroscopic navigation to guide RF catheter ablation of cardiac arrhythmias". In: *26th Annual International Conference of the IEEE Engineering in Medicine and Biology Society (IEMBS 2004), San Francisco, CA, USA, September 1–5*, pp. 1929–1932, September 2004.

[Fall 09] P. Fallavollita. "Monoplane 3D reconstruction of mapping ablation catheters: a feasibility study". *Biomedical Imaging and Intervention Journal*, Vol. 6, No. 2, p. e17, April 2009.

[Fall 10a] P. Fallavollita. “2D/3D registration using only single-view fluoroscopy to guide cardiac ablation procedures: a feasibility study”. In: K. H. Wong and M. I. Miga, Eds., *Proceedings of SPIE Medical Imaging 2010: Visualization, Image-Guided Procedures, and Modeling, San Diego, CA, USA, February 4–9*, p. 762507, February 2010.

[Fall 10b] P. Fallavollita. “Is Single-View Fluoroscopy Sufficient in Guiding Cardiac Ablation Procedures?”. *Journal of Biomedical Imaging*, Vol. 2010, No. 631264, pp. 1:1–1:13, March 2010.

[Felz 04] P. Felzenszwalb and D. Huttenlocher. “Distance Transforms of Sampled Functions”. Tech. Rep., Cornell Computing and Information Science, September 2004.

[Fitz 95] A. Fitzgibbon and R. Fisher. “A Buyer’s Guide to Conic Fitting”. In: *Proceedings of the 6th British Conference on Machine Vision (BMVC ’95), Birmingham, UK, September 11–14*, pp. 513–522, 1995.

[Fitz 99] A. Fitzgibbon, M. Pilu, and R. Fisher. “Direct Least Square Fitting of Ellipses”. *IEEE Transactions On Pattern Analysis And Machine Intelligence*, Vol. 21, No. 5, pp. 476–480, May 1999.

[Fran 06] E. Franken, P. Rongen, M. van Almsick, and B. Romeny. “Detection of Electrophysiology Catheters in Noisy Fluoroscopy Images”. *Lecture Notes in Computer Science (9th International Conference on Medical Image Computing and Computer-Assisted Intervention, MICCAI 2006), Copenhagen, Denmark, October 1–6*, Vol. 4191, pp. 25–32, 2006.

[Fran 98] A. Frangi, W. Niessen, K. Vincken, and M. Viergever. “Multiscale Vessel Enhancement Filtering”. *Lecture Notes in Computer Science (1st International Conference on Medical Image Computing and Computer-Assisted Interventation, MICCAI 1998), Cambridge, MA, USA, October 11–13*, Vol. 1496, pp. 130–137, 1998.

[Freu 97] Y. Freund and R. Schapire. “A Decision-Theoretic Generalization of On-Line Learning and an Application to Boosting”. *Journal of Computer and System Sciences*, Vol. 55, No. 1, pp. 119–139, August 1997.

[Frie 00] J. Friedman, T. Hastie, and R. Tibshirani. “Additive Logistic Regression: a Statistical View of Boosting”. *Annals of Statistics*, Vol. 28, No. 2, pp. 337–407, April 2000.

[Full 11] C. Fuller and M. Reisman. “Stroke Prevention in Atrial Fibrillation: Atrial Appendage Closure”. *Current Cardiology Reports*, Vol. 13, No. 2, pp. 159–166, April 2011.

[Furn 11] A. Fürnkranz and F. Ouyang. “Non-invasive imaging prior to cryoballoon ablation of atrial fibrillation: what can we learn?”. *Europace*, Vol. 13, No. 2, pp. 153–154, February 2011.

[Gage 01] B. Gage, A. Waterman, W. Shannon, M. Boechler, M. Rich, and M. Radford. “Validation of Clinical Classification Schemes for Predicting Stroke”. *Journal of the American Medical Association*, Vol. 285, No. 22, pp. 2864–2870, June 2001.

[Gaur 03] A. Gauri and B. Knight. "Catheter Ablation for Atrial Fibrillation". *Indian Pacing and Electrophysiology Journal*, Vol. 3, No. 4, pp. 210–223, October 2003.

[Geps 97] L. Gepstein, G. Hayam, and S. Ben-Haim. "A Novel Method for Non-fluoroscopic Catheter-Based Electroanatomical Mapping of the Heart: In Vitro and In Vivo Accuracy Results". *Circulation*, Vol. 95, No. 6, pp. 1611–1622, March 1997.

[Gers 10] E. Gerstenfeld and J. Michele. "Pulmonary vein isolation using a compliant endoscopic laser balloon ablation system in a swine model". *Journal of Interventional Cardiac Electrophysiology*, Vol. 29, No. 1, pp. 1–9, October 2010.

[Ghat 04] O. Ghatnekar, U. Persson, E.-L. Glader, and A. Terént. "Cost of stroke in Sweden: An incidence estimate". *International Journal of Technology Assessment in Health Care*, Vol. 20, No. 3, pp. 375–380, August 2004.

[Golu 65] G. Golub and W. Kahan. "Calculating The Singular Values And Pseudo-Inverse Of A Matrix". *Journal of the Society for Industrial and Applied Mathematics, Series B: Numerical Analysis*, Vol. 2, No. 2, pp. 205–224, 1965.

[Gorg 05] S. Gorges, E. Kerrien, M. Berger, Y. Trousset, J. Pescatore, R. Anxionnat, and L. Picard. "Model of a Vascular C-Arm for 3D Augmented Fluoroscopy in Interventional Radiology". *Lecture Notes in Computer Science (8th International Conference on Medical Image Computing and Computer-Assisted Intervention, MICCAI 2005), Palm Springs, CA, USA, October 26–30*, Vol. 3750, pp. 214–222, 2005.

[Guls 08] A. Gülsün and H. Tek. "Robust Vessel Tree Modeling". *Lecture Notes in Computer Science (11th international conference on Medical Image Computing and Computer-Assisted Intervention (MICCAI 2008), New York, NY, USA, September 6–10*, Vol. 5241, pp. 602–611, 2008.

[Hais 92] M. Haïssaguerre, F. Gaita, B. Fischer, D. Commenges, P. Montserrat, D. d'Ivernois, P. Lemetayer, and J. Warin. "Elimination of atrioventricular nodal reentrant tachycardia using discrete slow potentials to guide application of radiofrequency energy". *Circulation*, Vol. 85, No. 6, pp. 2162–2175, June 1992.

[Hais 94] M. Haïssaguerre, L. Gencel, B. Fischer, P. le Metayer, F. Poquet, F. Marcus, and J. Clémenty. "Successful Catheter Ablation of Atrial Fibrillation". *Journal of Cardiovascular Electrophysiology*, Vol. 5, No. 12, pp. 1045–1052, December 1994.

[Hali 98] R. Halir and J. Flusser. "Numerically Stable Direct Least Squares Fitting Of Ellipses". In: *Proceedings of 6th International Conference in Central Europe on Computer Graphics, Visualization and Computer Vision, February 9–13, Plzen, Czech Republic*, February 1998.

[Hank 99] G. Hankey and C. Warlow. "Treatment and secondary prevention of stroke: evidence, costs, and effects on individuals and populations". *The Lancet*, Vol. 354, No. 9188, pp. 1457–63, October 1999.

[Hart 04] R. Hartley and A. Zisserman. *Multiple View Geometry in Computer Vision*. Cambridge University Press, Cambridge, UK, 2nd Ed., March 2004.

[Haye 10] C. Hayes and D. Keane. "Safety of atrial fibrillation ablation with novel multi-electrode array catheters on uninterrupted anticoagulation Ů a single-center experience". *Journal of Interventional Cardiac Electrophysiology*, Vol. 27, pp. 117–122, March 2010.

[Herm 07] J. Hermans, P. Claes, J. Bellemans, D. Vandermeulen, and P. Suetens. "A robust optimization strategy for intensity-based 2D/3D registration of knee implant models to single-plane fluoroscopy". In: J. P. W. Pluim and J. M. Reinhardt, Eds., *Proceedings of SPIE Medical Imaging 2007: Image Processing, San Diego, CA, USA, Feburary 17–22*, p. 651227, 2007.

[Hill 01] D. Hill, P. Batchelor, M. Holden, and D. Hawkes. "Medical image registration". *Physics in Medicine and Biology*, Vol. 46, No. 3, pp. R1–R45, March 2001.

[Hoff 12a] M. Hoffmann. *3-D Catheter Reconstruction from Two Views for Electrophysiology Procedures*. Master's thesis, Pattern Recognition Lab, Department of Computer Science, Friedrich-Alexander-University Erlangen-Nuremberg, January 2012.

[Hoff 12b] M. Hoffmann, A. Brost, C. Jakob, F. Bourier, M. Koch, K. Kurzidim, J. Hornegger, , and N. Strobel. "Semi-Automatic Catheter Reconstruction from Two Views". In: *15th International Conference on Medical Image Computing and Computer Assisted Intervention (MICCAI 2012), Nice, France, October 1–5*, p. [accepted], 2012.

[Hsu 04] L.-F. Hsu, P. Jaïs, P. Sanders, S. Garrigue, M. Hocini, F. Sacher, Y. Takahashi, M. Rotter, J.-L. Pasquié, C. Scavée, P. Bordachar, J. Clémenty, and M. Haïssaguerre. "Catheter Ablation for Atrial Fibrillation in Congestive Heart Failure". *The New England Journal of Medicine*, Vol. 351, No. 23, pp. 2373–2383, December 2004.

[Isol 08] A. Isola, A. Ziegler, T. Koehler, W. Niessen, and M. Grass. "Motion-compensated iterative cone-beam CT image reconstruction with adapted blobs as basis functions". *Physics in Medicine and Biology*, Vol. 53, No. 23, pp. 6777–6797, November 2008.

[Iwaz 10] J. Iwazawa, S. Ohue, H. Abe, and T. Mitani. "Visualization of gastric varices using angiographic C-arm CT during retrograde transvenous sclerotherapy". *Indian Journal of Radiology and Imaging*, Vol. 20, No. 1, pp. 39–41, February 2010.

[Jian 06] M. Jianfei, X. Rong, and D. Weilong. "A Compound and Robust Algorithm for Ellipse Detection". In: *16th International Conference on Artificial Reality and Telexistence–Workshops (ICAT 2006), Hangzhou, China, November 29 – December 1*, pp. 381–386, 2006.

[John 10] M. John, R. Liao, Y. Zheng, A. Nöttling, J. Boese, U. Kirschstein, J. Kempfert, and T. Walther. "System to guide transcatheter aortic valve implantations based on interventional c-arm CT imaging". *Lecture Notes in Computer Science (13th International Conference on Medical Image Computing and Computer-Assisted Intervention, MICCAI 2010), Beijing, China, September 20 – 14*, Vol. 6361, pp. 375–382, 2010.

[Kaep 12a] S. Kaeppler. *Model-Based Motion Compensation for Electrophysiology Procedures*. Master's thesis, Pattern Recognition Lab, Department of Computer Science, Friedrich-Alexander-University Erlangen-Nuremberg, January 2012.

[Kaep 12b] S. Kaeppler, A. Brost, W. Wu, M. Koch, F. Bourier, T. Chen, M. Ostermeier, K. Kurzidim, J. Hornegger, and N. Strobel. "Motion Estimation Model for Cardiac and Respiratory Motion Compensation". In: *3rd International Conference on Information Processing in Computer-Assisted Interventions (IPCAI 2012), Pisa, Italy, June 27 [accepted]*, p. [n/a], 2012.

[Kana 01] K. Kanatani and N. Ohta. "Automatic Detection of Circular Objects by Ellipse Growing". *Memoirs of the Faculty of Engineering, Okayama University*, Vol. 36, No. 1, pp. 107–116, December 2001.

[Karc 02] M. Karch, J. Schreieck, and B. Zrenner. "Gegenwärtiger Stand der Vorhofflimmerablation". *Herzschrittmachertherapie und Elektrophysiologie*, Vol. 13, No. 4, pp. 178–185, Dezember 2002.

[Katr 08] D. Katritsis, M. Wood, E. Giazitzoglou, R. Shepard, G. Kourlaba, and K. Ellenbogen. "Long-term follow-up after radiofrequency catheter ablation for atrial fibrillation". *Europace*, Vol. 10, No. 4, pp. 419–424, April 2008.

[Kawa 98] T. Kawaguchi and R. ich Nagata. "Ellipse Detection Using A Genetic Algorithm". In: *Fourteenth International Conference on Pattern Recognition (ICPR 1998), Brisbane, Qld., Australia, August 16–20*, pp. 141–145, 1998.

[Kay 92] G. Kay, A. Epstein, S. Dailey, and V. Plumb. "Selective radiofrequency ablation of the slow pathway for the treatment of atrioventricular nodal reentrant tachycardia. Evidence for involvement of perinodal myocardium within the reentrant circuit". *Circulation*, Vol. 85, No. 5, pp. 1675–1688, May 1992.

[Keal 06] P. Keall, G. Mageras, J. Balter, R. Emery, K. Forster, S. Jiang, J. Kapatoes, D. Low, M. Murphy, B. Murray, C. Ramsey, M. Van Herk, S. Vedam, J. Wong, and E. Yorke. "The management of respiratory motion in radiation oncology report of AAPM Task Group 76.". *Medical Physics*, Vol. 33, No. 10, October 2006.

[Keus 11] J. Keustermans, S. D. Buck, H. Heidbüchel, and P. Suetens. "Automated planning of ablation targets in atrial fibrillation treatment". In: B. M. Dawant and D. R. Haynor, Eds., *Proceedings of SPIE Medical Imaging 2011: Image Processing, Lake Buena Vista, FL, USA, February 12–17*, p. 796207, 2011.

[Khea 03] B. Khealani, Z. Javed, N. Syed, S. Shafqat, and M. Wasay. "Cost of Acute Stroke Care at a tertiary care hospital in Karachi, Pakistan". *Journal of Pakistan Medical Association*, Vol. 53, No. 6, pp. 552–555, June 2003.

[King 09] A. P. King, R. Boubertakh, K. S. Rhode, Y. L. Ma, P. Chinchapatnam, G. Gao, T. Tangcharoen, M. Ginks, M. Cooklin, J. S. Gill, D. J. Hawkes, R. S. Razavi, and T. Schaeffter. "A subject-specific technique for respiratory motion correction in image-guided cardiac catheterisation procedures". *Medical Image Analysis*, Vol. 13, No. 3, pp. 419–331, June 2009.

[Kist 06a] P. Kistler, M. Earley, S. Harris, D. Abrams, S. Ellis, S. Sporton, and R. Schilling. "Validation of Three-Dimensional Cardiac Image Integration: Use of Integrated CT Image into Electroanatomic Mapping System to Perform Catheter Ablation of Atrial Fibrillation". *Journal of Cardiovascular Electrophysiology*, Vol. 17, No. 4, pp. 341–348, April 2006.

[Kist 06b] P. Kistler, K. Rajappan, M. Jahngir, M. Earley, S. Harris, D. Abrams, D. Gupta, R. Liew, S. Ellis, S. Sporton, and R. Schilling. "The Impact of CT Image Integration into an Electroanatomic Mapping System on Clinical Outcomes of Catheter Ablation of Atrial Fibrillation". *Journal of Cardiovascular Electrophysiology*, Vol. 17, No. 10, pp. 1093–1101, October 2006.

[Kist 08] P. Kistler, K. Rajappan, S. Harris, M. Earley, L. Richmond, S. Sporton, and R. Schilling. "The impact of image integration on catheter ablation of atrial fibrillation using electroanatomic mapping: a prospective randomized study". *European Heart Journal*, Vol. 29, No. 24, pp. 3029–3036, December 2008.

[Klee 11] T. Kleemann, C. Urbanek, M. D. Santos, F. Buggle, A. Safer, H. Becher, R. Zahn, A. Grau, and F. Palm. "Clinical Characterization of Patients with Acute First-Ever Ischemic Stroke and Atrial Fibrillation by Using the CHADS2 Score: Results From the German Ludwigshafen Stroke Study (LuSSt)". *Clin Res Cardiol*, Vol. 100, No. Suppl 1, p. n/a, April 2011.

[Klei 11a] A. Kleinoeder. *Catheter Reconstruction from Two X-Ray Projections*. Master's thesis, Pattern Recognition Lab, Department of Computer Science, Friedrich-Alexander-University Erlangen-Nuremberg, May 2011.

[Klei 11b] A. Kleinoeder, A. Brost, F. Bourier, M. Koch, K. Kurzidim, J. Hornegger, and N. Strobel. "Cryo-balloon reconstruction from two views". In: *18th IEEE International Conference on Image Processing (ICIP 2011), Brussels, Belgium, September 11–14*, pp. 223–230, 2011.

[Klei 12] A. Kleinoeder, A. Brost, F. Bourier, M. Koch, K. Kurzidim, J. Hornegger, and N. Strobel. "Cryo-balloon catheter position planning using AFiT". In: D. Holmes and K. Wong, Eds., *Proceedings of SPIE Medical Imaging 2012: Image-Guided Procedures, Robotic Interventions, and Modeling, San Diego, CA, USA, Febuary 4–9*, p. 83162R, 2012.

[Klem 07] H. Klemm, D. Steven, C. Johnsen, R. Ventura, T. Rostock, B. Lutomsky, T. Risius, T. Meinertz, and S. Willems. "Catheter motion during atrial ablation due to the beating heart and respiration: Impact on accuracy and spatial referencing in three-dimensional mapping". *Heart Rhythm*, Vol. 4, No. 5, pp. 587–592, May 2007.

[Knec 08a] S. Knecht, K.-T. Lim, M. O'Neil, S. Matsuo, L. Arantes, N. Derval, F. Sacher, A. Deplagne, P. Bordachar, M. Hocini, P. Jaïs, J. Clémenty, and M. Haïssaguerre. "High efficacy of the multi-faceted strategy for persistent atrial fibrillation". *Kardiovaskuläre Medizin*, Vol. 11, No. 2, pp. 39–46, February 2008.

[Knec 08b] S. Knecht, H. Skali, M. O'Neill, M. Wright, S. Matsuo, G. M. C., C. Haffajee, I. Nault, G. Gijsbers, F. Sacher, F. Laurent, M. Montaudon, O. Corneloup, M. Hocini, M. Haïssaguerre, M. Orlov, and P. Jaïs. "Computed tomography-fluoroscopy overlay evaluation during catheter ablation of left atrial arrhythmia". *Europace*, Vol. 10, No. 8, pp. 931–938, August 2008.

[Koch 11] M. Koch, A. Langenkamp, A. Kiraly, A. Brost, N. Strobel, and J. Hornegger. "Navigation System with Contact Force Assessment to Guide Pulmonary Vein Isolation Procedures". In: *23rd Conference of the Society for Medical Innovation and Technology (SMIT 2011), Tel Aviv, Israel, September 13–16*, pp. 1–2, 2011.

[Koch 12] M. Koch, A. Brost, N. Strobel, and J. Hornegger. "Post-procedural evaluation of catheter contact force characteristics". In: B. van Ginneken and C. Novak, Eds., *Proceedings of SPIE Medical Imaging 2012: Computer-Aided Diagnosis, San Diego, CA, USA, February 4–9*, p. 83152J, 2012.

[Koll 09] M. Koller and B. Schumacher. "Cryoballoon ablation of paroxysmal atrial fibrillation: bigger is better and simpler is better". *European Heart Journal*, Vol. 30, No. 6, pp. 636–637, February 2009.

[Koth 03] U. Köthe. "Edge and Junction Detection with an Improved Structure Tensor". *Lecture Notes in Computer Science (Proceedings of 25th DAGM Symposium, Magdeburg, Germany, September 10–12)*, Vol. 2781, pp. 25–32, 2003.

[Kurz 12] T. Kurzendorfer, A. Brost, F. Bourier, M. Koch, K. Kurzidim, J. Hornegger, and N. Strobel. "Cryo-Balloon Catheter Tracking in Atrial Fibrillation Ablation Procedures". In: *Bildverarbeitung für die Medizin (BVM 2012), Berlin, Germany, March 18–20*, pp. 386–391, 2012.

[Lanc 66] P. Lancaster. *Lambda Matrices and Vibrating Systems*. Pergamon Press, Oxford, UK, 1966.

[Land 11] U. Landmesser and D. Holmes. "Left atrial appendage closure: a percutaneous transcatheter approach for stroke prevention in atrial fibrillation". *European Heart Journal*, Vol. [Epub ahead of print], October 2011.

[Liao 08] R. Liao, N. Xu, and Y. Sun. "Location Constraint Based 2D-3D Registration of Fluoroscopic Images of CT Volumes for Image-Guided EP Procedures". In: M. I. Miga and K. R. Cleary, Eds., *Proceedings of SPIE Medical Imaging 2008: Visualization, Image-guided Procedures, and Modeling, San Diego, CA, USA, February 16–21*, p. 69182T, 2008.

[Libu 06] L. Libuda, I. Grothues, and K.-F. Kraiss. "Ellipse Detection in Digital Image Data Using Geometric Features". In: *International Conference on*

Computer Vision Theory and Applications (VISAPP 2006), Setúbal, Portugal, February 25–28, February 2006.

[Lint 10] C. Linte, J. Moore, and T. Peters. "How accurate is accurate enough? A brief overview on accuracy considerations in image-guided cardiac interventions". In: I. E. in Medicine & Biology Society, Ed., *32nd Annual International Conference of the IEEE Engineering in Medicine and Biology Society (EMBC 2010), Buenos Aires, Argentina, August 31 – September 4*, pp. 2313–2316, 2010.

[Lip 95] G. Lip and R. Watson. "ABC of Atrial Fibrillation: Differential Diagnosis of Atrial Fibrillation". *BMJ*, Vol. 311, pp. 1495–1498, December 1995.

[Lotu 00] R. Lotufo, a. A. Falc and F. Zampirolli. "Fast Euclidean Distance Transform using a Graph-Search Algorithm". In: *Proceedings XIII Brazilian Symposium on Computer Graphics and Image Processing (SIBGRAPI 2000), Gramado, Brazil, October 17–20*, pp. 269–275, 2000.

[Lowe 99] D. Lowe. "Object recognition from local scale-invariant features". In: *Proceedings of the Seventh IEEE International Conference on Computer Vision (ICCV 1999), Kerkyra, Greece, September 20–27, 1999*, pp. 1150–1157, September 1999.

[Ma 06] J. Ma, K. Tang, F. s. Ma, Y. h. Jia, S. Zhang, and C. x. Huang. "Linear ablation of left atrium for the treatment of atrial fibrillation guided by double Lasso catheters and three dimensional electroanatomical mapping". *Chinese Medical Journal*, Vol. 119, No. 24, pp. 2042–2048, December 2006.

[Ma 10] Y. Ma, A. P. King, N. Gogin, C. A. Rinaldi, J. Gill, R. Razavi, and K. S. Rhode. "Real-Time Respiratory Motion Correction for Cardiac Electrophysiology Procedures Using Image-Based Coronary Sinus Catheter Tracking". *Lecture Notes in Computer Science (13th International Conference on Medical Image Computing and Computer-Assisted Intervention, MICCAI 2010), Beijing, China, September 20 – 14*, Vol. 6361, pp. 391–399, 2010.

[Ma 11] Y. Ma, A. King, N. Gogin, G. Gijsbers, C. Rinaldi, J. Gill, R. Razavi, and K. Rhode. "Comparing Image-Based Respiratory Motion Correction Methods for Anatomical Roadmap Guided Cardiac Electrophysiology Procedures". In: D. Metaxas and L. Axel, Eds., *Lecture Notes in Computer Science (Proceedings of the 6th International Conference on Functional Imaging and Modeling of the Heart, FIMH 2011), New York, NY, USA, May 25–27*, pp. 55–62, 2011.

[Ma 96] S. Ma and L. Li. "Ellipsoid Reconstruction from Three Perspective Views". *Proceedings of the 13th International Conference on Pattern Recognition (ICPR 1996), Vienna, Austria, August 25–29*, Vol. 1, p. 344, 1996.

[Mahf 03] M. Mahfouz, W. A. Hoff, R. D. Komistek, and D. A. Dennis. "A robust method for registration of three-dimensional knee implant models to two-dimensional fluoroscopy images". *IEEE Transactions on Medical Imaging*, Vol. 22, No. 12, pp. 1561–1574, December 2003.

[Mano 94a] A. Manolis, P. Wang, and N. Estes. "Radiofrequency ablation of slow pathway in patients with atrioventricular nodal reentrant tachycardia. Do arrythmia recurrences correlate with persistent slow pathway conduction or site of successful ablation?". *Circulation*, Vol. 90, No. 6, pp. 2815–2819, December 1994.

[Mano 94b] A. Manolis, P. Wang, and N. Estes. "Radiofrequency Catheter Ablation for Cardiac Tachyarrhythmias". *Annals of Internal Medicine*, Vol. 121, No. 6, pp. 452–461, September 1994.

[Mano 99] A. Manolis, V. Vassilikos, T. Maounis, H. Melita-Manolis, L. Psarros, A. Haliasos, and D. Cokkinos. "Detection of Myocardial Injury During Radiofrequency Catheter Ablation by Measuring Serum Cardiac Troponin I Levels: Procedural Correlates". *Journal of the American College of Cardiology*, Vol. 34, No. 4, pp. 1099–1105, October 1999.

[Marc 09] G. Marcus, E. Keung, and M. Scheinman. "The Year in Review of Clinical Cardiac Electrophysiology". *Journal of the American College of Cardiology*, Vol. 54, No. 9, pp. 777–787, August 2009.

[Marc 11] S. Marchandise, C. Scavée, C. Goesaert, J. Vanoverschelde, and J. Kefer. "Left atrial appendage occlusion and pulmonary vein isolation: interest of non-invasive imaging". *Acta Cardiologica*, Vol. 66, No. 5, pp. 653–656, October 2011.

[McCa 09] D. McCabe, J. Kinsella, and W. Tobin. "Left atrial appendage occlusion in non-valvular atrial fibrillation". *The Lancet*, Vol. 374, No. 9689, pp. 504–506, August 2009.

[McLe 02] K. McLeish, D. Hill, D. Atkinson, J. Blackall, and R. Razavi. "A study of the motion and deformation of the heart due to respiration". *IEEE Transactions on Medical Imaging*, Vol. 21, No. 9, pp. 1142–1150, September 2002.

[Meij 02] A. Meijster, J. Roerdink, and W. Hesselink. "A General Algorithm for Computing Distance Transforms in Linear Time". In: J. Goutsias, L. Vincent, and D. Bloomberg, Eds., *Mathematical Morphology and its Applications to Image and Signal Processing*, pp. 331–340, Springer US, 2002.

[Mill 05a] P. Miller, F. Andersson, and L. Kalra. "Are Cost Benefits of Anticoagulation for Stroke Prevention in Atrial Fibrillation Underestimated?". *Stroke*, Vol. 36, No. 2, pp. 360–366, February 2005.

[Mill 05b] P. Miller, M. Drummond, L. Langkilde, J. McMurray, and M. Ögren. "Economic factors associated with antithrombotic treatments for stroke prevention in patients with atrial fibrillation". *European Heart Journal Supplements*, Vol. 7, No. Supplement C, pp. C41–C54, May 2005.

[Miqu 03] M. Miquel, D. Hill, E. Baker, S. Qureshi, R. Simon, S.Keevil, and R. Razavi. "Three- and four-dimensional reconstruction of intracardiac anatomy from two-dimensional magnetic resonance images". *International Journal of Cardiovascular Imaging*, Vol. 19, No. 3, pp. 239–254, June 2003.

[Mont 05a] A. Montenero, N. Bruno, A. Antonelli, D. Mangiameli, L. Barbieri, P. Andrew, and F. Zumbo. "Comparison Between a 7 French 6 MM Tip Cryothermal Catheter and a 9 French 8 MM Tip Cryothermal Catheter for Cryoablation Treatment of Common Atrial Flutter". *Journal of Interventional Cardiac Electrophysiology*, Vol. 13, pp. 59–69, June 2005.

[Mont 05b] A. Montenero, N. Bruno, F. Zumbo, A. Antonelli, L. Fiocca, L. Barbieri, F. de Bernardi, P. Andrew, and V. Affinito. "Cryothermal Ablation Treatment of Atrial FlutterŮExperience with a New 9 French 8 mm Tip Catheter". *Journal of Interventional Cardiac Electrophysiology*, Vol. 12, pp. 45–54, January 2005.

[Muld 11] A. Mulder, M. Wijffels, E. Wever, and L. Boersma. "Pulmonary vein isolation and left atrial complex-fractionated atrial electrograms ablation for persistent atrial fibrillation with phased radio frequency energy and multi-electrode catheters: efficacy and safety during 12 months follow-up". *Europace*, Vol. 13, No. 12, pp. 1695–1702, December 2011.

[Murg 02] F. Murgatroyd, A. Krahn, G. Klein, R. Yee, and A. Skanes. *Handbook of Cardiac Electrophysiology*. Andrew Ward (ReMEDICA Publishing Limited), London, UK, February 2002.

[Nade 04] K. Nademanee, J. McKenzie, E. Kosar, M. Schwab, B. Sunsaneewitayakul, T. Vasavakul, C. Khunnawat, and T. Ngarmukos. "A new approach for cather ablation of atrial fibrillation: mapping of the electrophysiologic substrate". *Journal of the American College of Cardiology*, Vol. 43, No. 11, pp. 2044–2053, June 2004.

[Neum 06] T. Neumann, A. Erdogan, T. Dill, H. Greiss, A. Berkowitsch, J. Sperzel, M. Kuniss, K. Kurzidim, C. Hamm, and H.-F. Pitschner. "Asymptomatic recurrences of atrial fibrillation after pulmonary vein isolation". *Europace*, Vol. 8, No. 7, pp. 495–498, July 2006.

[Neum 08] T. Neumann, J. Vogt, B. Schumacher, A. Dorszewski, M. Kuniss, H. Neuser, K. Kurzidim, A. Berkowitsch, M. Koller, J. Heintze, U. Scholz, U. Wetzel, M. Schneider, D. Horstkotte, C. Hamm, and H.-F. Pitschner. "Circumferential Pulmonary Vein Isolation With the Cryoballoon Technique: Results From a Prospective 3-Center Study". *Journal of the American College of Cardiology*, Vol. 52, No. 4, pp. 273–278, July 2008.

[Nitt 12] T. Nitta, Y. Ishii, and S.-I. Sakamoto. "Surgery for atrial fibrillation: recent progress and future perspective". *General Thoracic and Cardiovascular Surgery*, Vol. 60, No. 1, pp. 13–20, January 2012.

[Nolk 08] G. Nölker, K. Gutleben, H. Marschang, G. Ritscher, S. Asbach, N. Marrouche, J. Brachmann, and A. Sinha. "Three-dimensional left atrial and esophagus reconstruction using cardiac C-arm computed tomography with image integration into fluoroscopic views for ablation of atrial fibrillation: Accuracy of a novel modality in comparison with multislice computed tomography". *Heart Rhythm*, Vol. 5, No. 12, pp. 1651–1657, December 2008.

[Noo 07] F. Noo, S. Hoppe, F. Dennerlein, G. Lauritsch, and J. Hornegger. "A new scheme for view-dependent data differentiation in fan-beam and cone-beam computed tomography". *Physics in Medicine and Biology*, Vol. 52, No. 17, pp. 5393–5414, September 2007.

[Oral 06] H. Oral, A. Chugh, E. Good, S. Sankaran, S. Reich, P. Igic, D. Elmouchi, D. Tschopp, T. Crawford, S. Dey, A. Wimmer, K. Lemola, K. Jongnarangsin, F. Bogun, F. P. Jr, and F. Morady. "A Tailored Approach to Catheter Ablation of Paroxysmal Atrial Fibrillation". *Circulation*, Vol. 113, No. 15, pp. 1824–1831, April 2006.

[Orlo 07] M. Orlov, P. Hoffmeister, G. Chaudhry, I. Almasry, G. Gijsbers, T. Swack, and C. Haffajee. "Three-dimensional rotational angiography of the left atrium and esophagus: a virtual computed tomography scan in the electrophysiology lab?". *Heart Rhythm*, Vol. 4, No. 1, pp. 37–43, January 2007.

[Ortm 05] T. Ortmaier, M. Groeger, D. Boehm, V. Falk, and G. Hirzinger. "Motion Estimation in Beating Heart Surgery". *IEEE Transactions on Biomedical Engineering*, Vol. 52, No. 10, pp. 1729–1740, October 2005.

[Otsu 79] N. Otsu. "A Threshold Selection Method from Gray-Level Histograms". *IEEE Transactions on Systems, Man, and Cybernetics*, Vol. 9, No. 1, pp. 62–66, January 1979.

[Palt 97] D. Palti-Wassermann, A. Brukstein, and R. Beyar. "Identifying and Tracking a Guide Wire in the Coronary Arteries During Angioplasty from X-Ray Images". *IEEE Transactions on Biomedical Engineering*, Vol. 44, No. 2, pp. 152–164, February 1997.

[Papa 10] C. Papalazarou, P. Rongen, and P. de With. "Surgical needle reconstruction using small-angle multi-view X-ray". In: *17th IEEE International Conference on Image Processing (ICIP), Hong Kong, China, September 26–29, 2010*, pp. 4193–4196, September 2010.

[Papp 00] C. Pappone, S. Rosanio, G. Oreto, M. Tocchi, F. Gugliotta, G. Vicedomini, A. Salvati, C. Dicandia, P. Mazzone, V. Santinelli, S. Gulletta, and S. Chierchia. "Circumferential radiofrequency ablation of pulmonary vein ostia: A new anatomic approach for curing atrial fibrillation". *Circulation*, Vol. 102, No. 21, pp. 2619–2628, November 2000.

[Penn 98] G. P. Penney, J. Weese, J. A. Little, P. Desmedt, D. L. G. Hill, and D. J. Hawkes. "A Comparision of Similarity Measures for Use in 2-D - 3-D Medical Image Registration". *IEEE Transactions on Medical Imaging*, Vol. 17, No. 4, pp. 586–595, August 1998.

[Penn 99] G. P. Penney. *Registration of Tomographic Images to X-ray Projections for Use in Image Guide Interventions*. PhD thesis, Computational Imaging Science Group, Division of Radiological Sciences and Medical Engineering, Guy's, King's and St. Thomas' School of Medicine, King's College London, December 1999.

[Perr 12] D. Perry, A. Morris, N. Burgon, C. McGann, R. MacLeod, and J. Cates. "Automatic classification of scar tissue in late gadolinium enhancement cardiac MRI for the assessment of left-atrial wall injury after radiofrequency ablation". In: B. van Ginneken and C. Novak, Eds., *Proceedings of SPIE Medical Imaging 2012: Computer-Aided Diagnosis, San Diego, CA, USA, Febuary 4–9*, p. 83151D, 2012.

[Plui 03] J. P. W. Pluim, J. B. A. Maintz, and M. A. Viergever. "Mutual information based registration of medical images: a survey". *IEEE Transactions on Medical Imaging*, Vol. 22, No. 8, pp. 986–1004, August 2003.

[Pori 07] F. Porikli and T. Kocak. "Fast Distance Transform Computation using Dual Scan Line Propagation". In: N. Kehtarnavaz and M. Carlsohn, Eds., *Proceedings of SPIE Real-Time Image Processing 2007, San Jose, CA, USA, January 29–30*, p. 649608, 2007.

[Prat 07] W. Pratt. *Digital Image Processing: PIKS Scientific Inside*. Wiley & Sons, Hoboken, NJ, USA, 2007.

[Prum 05] M. Prümmer, J. Han, and J. Hornegger. "2D-3D Non-rigid Registration using Iterative Reconstruction". In: G. Greiner, J. Hornegger, H. Niemann, and M. Stamminger, Eds., *10th International Fall Workshop Vision, Modeling, and Visualization (VMV 2005), Erlangen, Germany, November 16–18*, pp. 187–194, 2005.

[Prum 06a] M. Prümmer, J. Hornegger, M. Pfister, and A. Dörfler. "Multi-modal 2D-3D Non-rigid Registration". In: J. M. Reinhardt and J. P. W. Pluim, Eds., *Proceedings of SPIE Medical Imaging 2006: Image Processing, San Diego, CA, USA, February 4–9*, 2006.

[Prum 06b] M. Prümmer, L. Wigström, J. Hornegger, J. Boese, G. Lauritsch, N. Strobel, and R. Fahrig. "Cardiac C-arm CT: Efficient Motion Correction for 4D-FBP". In: *IEEE Nuclear Science Symposium Conference Record 2006, San Diego, CA, USA, October 29 – November 1*, 2006.

[Prum 07] M. Prümmer, R. Fahrig, L. Wigström, J. Boese, G. Lauritsch, N. Strobel, and J. Hornegger. "Cardiac C-arm CT: 4D Non-Model based Heart Motion Estimation and its Application". In: J. Hsieh and M. Flynn, Eds., *Proceedings of SPIE Medical Imaging 2007: Physics of Medical Imaging, San Diego, CA, USA, February 17–22*, p. 651015, 2007.

[Prum 09] M. Prümmer, J. Hornegger, G. Lauritsch, L. Wigström, E. Girard-Hughes, and R. Fahrig. "Cardiac C-arm CT: a unified framework for motion estimation and dynamic CT". *IEEE Transactions on Medical Imaging*, Vol. 28, No. 11, pp. 1836–1849, November 2009.

[Quan 96] L. Quan. "Conic Reconstruction and Correspondence From Two Views". *IEEE Transactions On Pattern Analysis And Machine Intelligence*, Vol. 18, No. 2, pp. 151–160, February 1996.

[Ramr 07] L. Ramrath, A. Schlaefer, F. Ernst, S. Dieterich, and A. Schweikard. "Prediction of Respiratory Motion with a Multi-Frequency Based Extended Kalman Filter". *Robotics*, Vol. 2, pp. 56–58, 2007.

[Rao 05] B. Rao, K. Sharada, and C. Narasimhan. "Successful-Radiofrequency Catheter Ablation of Recurrent Atrial Fibrillation due to Left Inferior Pulmonary Vein Tachycardia". *Indian Heart Journal*, Vol. 57, pp. 339–342, July 2005.

[Redd 09] V. Reddy, P. Neuzil, S. Themistoclakis, S. Danik, A. Bonso, A. Rossillo, A. Raviele, R. Schweikert, S. Ernst, K.-H. Kuck, and A. Natale. "Visually-guided balloon catheter ablation of atrial fibrillation: experimental feasibility and first-in-human multicenter clinical outcome". *Circulation*, Vol. 120, No. 1, pp. 12–20, July 2009.

[Rich 07] G. Richter, T. Engelhorn, T. Struffert, M. Doelken, O. Ganslandt, J. Hornegger, W. Kalender, and A. Doerfler. "Flat Panel Detector Angiographic CT for Stent-Assisted Coil Embolization of Bread-Based Cerebral Aneurysms". *American Journal of Neuroradiology*, Vol. 28, No. 10, pp. 1902–1908, November 2007.

[Rich 09] G. Richter, M. Pfister, T. Struffert, T. Engelhorn, M. Doelken, M. Spiegel, J. Hornegger, and A. Doerfler. "Technical feasibility of 2D-3D coregistration for visualization of self-expandable microstents to facilitate coil empolization of broad-based intracranial aneurysms: an in vitro study". *Neuroradiology*, Vol. 51, No. 12, pp. 851–854, December 2009.

[Rohk 08] C. Rohkohl. *3-D Reconstruction of dynamic high contrast objects for C-Arm CT*. Master's thesis, Lehrstuhl für Mustererkennung, Institut für Informatik, Friedrich-Alexander-Universität Erlangen-Nürnberg, September 2008.

[Rohk 09] C. Rohkohl, G. Lauritsch, M. Prümmer, and J. Hornegger. "Interventional 4-D Motion Estimation and Reconstruction of Cardiac Vasculature without Motion Periodicity Assumption". *Lecture Notes in Computer Science (12th International Conference on Medical Image Computing and Computer-Assisted Intervention, MICCAI 2009), London, UK, September 20–24*, Vol. 5761, pp. 132–139, 2009.

[Rose 01] M. Rosenthal, S. Weeks, S. Aylward, E. Bullitt, and H. Fuchs. "Intraoperative Tracking of Anatomical Structures Using Fluoroscopy and a Vascular Balloon Catheter". *Lecture Notes in Computer Science (4th International Conference on Medical Image Computing and Computer Assisted Intervention, MICCAI 2001), Utrecht, The Netherlands, October 14–17*, Vol. 2208, pp. 1253–1254, 2001.

[Ross 08] J. Ross, N. Subramanian, and S. Solomon. "Motion Correction for Augmented Fluoroscopy - Application to Liver Embolization". In: *5th IEEE International Symposium on Biomedical Imaging: From Nano to Macro (ISBI 2008), Paris, France, May 14–17*, pp. 1553–1556, May 2008.

[Rost 09] R. Rost, B. Licea-Kane, D. Ginsburg, J. Kessenich, B. Lichtenbelt, H. Malan, and M. Weiblen. *OpenGL Shading Language*. Addison-Wesley Professional, Boston, MA, USA, 3rd Ed., July 2009.

[Roug 93] A. Rougee, C. Picard, Y. Trousset, and C. Ponchut. "Geometrical calibration for 3D x-ray imaging". In: Y. Kim, Ed., *Proceedings of SPIE Medical Imaging 1993: Image Capture, Formatting, and Display, Newport Beach, CA, USA, February 14–15*, pp. 161–169, 1993.

[Sach 07] F. Sacher, P. Jaïs, K. Stephenson, M. O'Neill, M. Hocini, J. Clémenty, W. Stevenson, and M. Haïssaguerre. "Phrenic Nerve Injury After Catheter Ablation of Atrial Fibrillation". *Indian Pacing and Electrophysiology Journal*, Vol. 7, No. 1, pp. 1–6, January 2007.

[Saka 09] O. Saka, A. McGuire, and C. Wolfe. "Cost of stroke in the United Kingdom". *Age and Ageing*, Vol. 38, No. 1, pp. 27–32, January 2009.

[Sarr 01] L. Sarry and J.-Y. Boire. "Three-Dimensional Tracking of Coronary Arteries From Biplane Angiographic Sequences Using Parametrically Deformable Models". *IEEE Transactions On Medical Imaging*, Vol. 20, No. 12, pp. 1341–1351, December 2001.

[Sart 08] R. Sartini, M. Scanavacca, E. Sosa, L. Moreira, S. Lara, C. Hardy, F. Darrieux, and D. Hachul. "Radiofrequency Ablation of Paroxysmal Atrial Fibrillation: Factors Determining Long-Term Clinical Efficacy". *Arquivos Brasileiros de Cardiologia*, Vol. 90, No. 2, pp. 112–118, February 2008.

[Sato 98] Y. Sato, S. Nakajima, N. Shiraga, H. Atsumi, S. Yoshida, T. Koller, G. Gerig, and R. Kikinis. "3D Multi-Scale Line Filter for Segmentation and Visualization of Curvilinear Structures in Medical Images". *Medical Image Analysis*, Vol. 2, No. 2, pp. 143–168, June 1998.

[Scha 05] C. Scharf, J. Schläpfer, C. Sticherling, S. Osswald, J. Fuhrer, and D. Shah. "Catheter ablation for atrial fibrillation: pathophysiology, techniques, results and current indications". *Kardiovaskuläre Medizin*, Vol. 8, No. 2, pp. 53–61, February 2005.

[Sche 10a] M. Schenderlein and K. Dietmayer. "Image-based catheter tip tracking during cardiac ablation therapy". *Methods*, pp. 1–5, 2010.

[Sche 10b] M. Schenderlein, S. Stierlin, R. Manzke, V. Rasche, and K. Dietmayer. "Catheter Tracking in Asynchronous Biplane Fluoroscopy Images by 3D B-Snakes". *SPIE Medical Imaging 2010: Visualization, Image-Guided Procedures, and Modeling, San Diego, CA, USA, March 4–10*, Vol. 7625, p. 76251U, 2010.

[Sche 11] M. Schenderlein, V. Rasche, and K. Dietmayer. "Three-Dimensional Catheter Tip Tracking from Asynchronous Biplane X-Ray Image Sequences using Non-Linear State Filtering". In: H. Handels, J. Ehrhardt, T. Deserno, H.-P. Meinzer, and T. Tolxdorff, Eds., *Bildverarbeitung für die Medizin (BVM 2011), Lübeck, Germany, March 20–22*, pp. 234–238, 2011.

[Schm 05] F. Schmidt. *Catheter Localization in Coronary Biplane X-ray Imaging*. Master's thesis, Friedrich-Alexander-Universität Erlangen-Nürnberg, Germany, October 2005.

[Schm 08] B. Schmidt, K. Chun, A. Metzner, F. Ouyang, and K.-H. Kuck. "Balloon Catheters for Pulmonary Vein Isolation". *Herz*, Vol. 33, No. 8, pp. 580–584, December 2008.

[Scho 11] P. Schoenhagen, S. Kapadia, S. Halliburton, L. Svensson, and E. Tuzcu. "Computed tomography evaluation for transcatheter aortic valve implantation (TAVI): Imaging of the aortic root and iliac arteries". *Journal of Cardiovascular Computed Tomography*, Vol. 5, No. 5, pp. 293–300, September 2011.

[Schu 07] N. Schütz, M. Zimmermann, and P. Schopfer. "Radiofrequency catheter ablation of atrioventricular nodal reentrant tachycardia in a patient with dextrocardia". *Kardiovaskuläre Medizin*, Vol. 10, No. 10, pp. 334–336, October 2007.

[Shah 06] D. Shah, G. Leo, N. Aeby, E. le Royer, H. Sunthorn, H. Burri, and P. Gentil-Baron. "AB36-6: Evaluation of a new catheter sensor for real-time measurement of tissue contact". *Heart Rhythm*, Vol. 3, No. 5, pp. S75–S76, May 2006.

[Shah 10] D. Shah, H. Lambert, H. Nakagawa, A. Langenkamp, N. Aeby, and G. Leo. "Area Under the Real-Time Contact Force Curve (Force–Time Integral) Predicts Radiofrequency Lesion Size in an In Vitro Contractile Model". *Journal of Cardiovascular Electrophysiology*, Vol. 21, No. 9, pp. 1038–1043, September 2010.

[Shah 11a] D. Shah, H. Lambert, A. Langenkamp, Y. Vanenkov, G. Leo, P. Gentil-Baron, and B. Walpoth. "Catheter tip force required for mechanical perforation of porcine cardiac chambers". *Europace*, Vol. 13, No. 2, pp. 277–283, February 2011.

[Shah 11b] D. Shah, V. Reddy, J. Kautzner, N. Saoudi, C. Siklódy, P. Jaïs, G. Hindricks, A. Yulzari, H. Lambert, P. Neuzil, and K.-H. Kuck. "Contact Force During Ablation Predicts AF Recurrence at 12 Months". In: *Heart Rhythm 2011 (HRS 2011), 32th Annual Scientific Sessions, San Francisco, CA, USA, May 4–7*, Heart Rhythm Society, May 2011.

[Shec 04] G. Shechter, C. Ozturk, J. Resar, and E. McVeigh. "Respiratory motion of the heart from free breathing coronary angiograms". *IEEE Transactions on Medical Imaging*, Vol. 23, No. 8, pp. 1046–1056, August 2004.

[Shec 05] G. Shechter, B. Shechter, J. Resar, and R. Beyar. "Prospective Motion Correction of X-ray Images for Coronary Interventions". *IEEE Transactions on Medical Imaging*, Vol. 24, No. 4, pp. 441–450, April 2005.

[Shec 06] G. Shechter, J. Resar, and E. McVeigh. "Displacement and velocity of the coronary arteries: cardiac and respiratory motion". *IEEE Transactions on Medical Imaging*, Vol. 25, No. 3, pp. 369–375, March 2006.

[Shre 09] D. Shreiner. *OpenGL Programming Guide: The Official Guide to Learning OpenGL*. Addison-Wesley Professional, Boston, MA, USA, 7th Ed., July 2009.

[Sick 07] P. Sick, G. Schuler, K. Hauptmann, E. Grube, S. Yakubov, Z. Turi, G. Mishkel, S. Almany, and D. Holmes. "Initial Worldwide Experience With the WATCHMAN Left Atrial Appendage System for Stroke Prevention in Atrial Fibrillation". *Journal of the American College of Cardiology*, Vol. 49, No. 13, pp. 1490–1495, April 2007.

[Sier 03] G. Sierra, A. LeBlanc, M. Leonard, R. Nadeau, and P. Savard. "Prototype of a fluoroscopic navigation system to guide the catheter ablation of cardiac arrhythmias". In: *25th Annual International Conference of the IEEE Engineering in Medicine and Biology Society (IEMBS 2003), Cancún, Mexico, September 17–21*, pp. 138–141, September 2003.

[Silv 10] E. Silver, J. Silva, S. Ceresnak, N. Chiesa, E. Rhee, A. Dubin, K. Avasarala, G. van Hare, and K. Collins. "Cryoablation with an 8-mm Tip Catheter for Pediatric Atrioventricular Nodal Reentrant Tachycardia Is Safe and Efficacious with a Low Incidence of Recurrence". *Pacing and Clinical Electrophysiology*, Vol. 33, No. 6, pp. 681–686, June 2010.

[So 09] Y. c. So. "Atrial Fibrillation Catheter Ablation". *The Hong Kong Medical Diary*, Vol. 14, No. 1, pp. 27–29, January 2009.

[Spie 07] M. Spiegel. *Towards Realtime Catheter / Guide Wire Segmentation from Neuro-Fluoroscopy Images*. Master's thesis, Pattern Recognition Lab, Department of Computer Science, Friedrich-Alexander-University Erlangen-Nuremberg, March 2007.

[Sra 07] J. Sra, G. Narayan, D. Krum, A. Malloy, R. Cooley, A. Bhatia, A. Dhala, Z. Blanck, V. Nangia, and M. Akhtar. "Computed Tomogrpahy-Fluoroscopy Image Integration-Guided Catheter Ablation of Atrial Fibrillation". *Journal of Cardiovascular Electrophysiology*, Vol. 18, No. 4, pp. 409–414, April 2007.

[Stan 08] S. Standring, Ed. *Gray's Anatomy: The Anatomical Basis of Clinical Practice*. Churchill Livingstone, Oxford, UK, 40th Ed., 2008.

[Stro 03] N. Strobel, B. Heigl, T. Brunner, O. Schuetz, M. Mitschke, K. Wiesent, and T. Mertelmeier. "Improving 3D image quality of x-ray C-arm imaging systems by using properly designed pose determination systems for calibrating the projection geometry". In: M. Yaffe and L. Antonuk, Eds., *Proceedings of SPIE Medical Imaging 2003: Physics of Medical Imaging, San Diego, CA, USA, February 15–20*, pp. 943–954, 2003.

[Stro 09] N. Strobel, O. Meissner, J. Boese, T. Brunner, B. Heigl, M. Hoheisel, G. Lauritsch, M. Nagel, M. Pfister, E.-P. Rührnschopf, B. Scholz, B. Schreiber, M. Spahn, M. Zellerhoff, and K. Klingenbeck-Regn. "Imaging with Flat-Detector C-Arm Systems". In: M. Reiser, C. Becker, K. Nikolaou, and G. Glazer, Eds., *Multislice CT (Medical Radiology / Diagnostic Imaging)*, Chap. 3, pp. 33–51, Springer Berlin / Heidelberg, January 2009.

[Suri 12] R. Suri and N. Thalji. "Minimally Invasive Heart Valve Surgery: How and Why in 2012". *Current Cardiology Reports*, Vol. 14, No. 2, pp. 171–179, April 2012.

[Taka 06] Y. Takahashi, P. Sanders, P. Jaïs, M. Hocini, R. Dubois, M. Rotter, T. Rostock, C. Nalliah, F. Sacher, J. Clémenty, and M. Haïssaguerre. "Oranization of Frequency Spectra of Atrial Fibrillation: Relevance to Radiofrequency Catheter Ablation". *Journal of Cardiovascular Eletrophysiology*, Vol. 17, No. 4, pp. 382–388, April 2006.

[Tamu 10] H. Tamura, T. Watanabe, O. Hirono, S. Nishiyama, S. Sasaki, T. Shishido, T. Miyashita, T.Miyamoto, J. Nitobe, T. Kayama, and I. Kubota. "Low Wall Velocity of Left Atrial Appendage Measured by Trans-Thoracic Echocardiography Predicts Thrombus Formation Caused by Atrial Appendage Dysfunction". *Journal of the American Society of Echocardiography*, Vol. 23, No. 5, pp. 545–552, May 2010.

[Tayl 05] R. Taylor, A. David, D. Phillips, S. Fields, and J. Scherger, Eds. *Taylor's Cardiovascular Diseases - A Handbook*. Springer, New York, NY, USA, 1st Ed., January 2005.

[Tayl 96] T. Taylor, P. Davis, J. Torner, J. Holmes, J. Meyer, and M. Jacobson. "Lifetime Cost of Stroke in the United States". *Stroke*, Vol. 27, pp. 1459–1466, September 1996.

[Thom 11] D. Thomas, H. Katus, and F. Voss. "Asymptomatic pulmonary vein stenosis after cryoballoon catheter ablation of paroxysmal atrial fibrillation". *Journal of Electrocardiology*, Vol. 44, No. 4, pp. 473–476, July 2011.

[Tilz 07] R. Tilz, F. Ouyang, J. Chung, B. Schmidt, K. Satomi, T. Zerm, S. Ernst, B. Köktürk, I. Köster, K. Kuck, and M. Antz. "Ablation von paroxysmalem und persistierendem Vorhofflimmern mit der Doppel-Lasso-Technik". *Journal für Kardiologie - Austrian Journal of Cardiology*, Vol. 14, No. Supplementum B - Forum Rhythmologie, pp. 3–8, 2007.

[Tops 09] L. Tops and J. Bax. "The Year in Imaging Related to Electrophysiology". *Journal of the American College of Cardiology Imaging*, Vol. 2, No. 4, pp. 498–510, April 2009.

[Tu 05] Z. Tu. "Probabilistic Boosting-Tree: Learning Discriminative Models for Classification, Recognition, and Clustering". In: *Proceedings of the Tenth IEEE International Conference on Computer Vision (ICCV 2005), Beijing, China, October 17–20*, pp. 1589–1596, 2005.

[Turg 05] G.-A. Turgeon, G. Lehmann, G. Guiraudon, M. Drangova, D. Holdsworth, and T. Peters. "2D-3D registration of coronary angiograms for cardiac procedure planning and guidance". *Medical Physics*, Vol. 32, No. 12, pp. 3737–3749, December 2005.

[Viol 01] P. Viola and M. Jones. "Rapid object detection using a boosted cascade of simple features". In: *Proceedings of the 2001 IEEE Computer Society Conference on Computer Vision and Pattern Recognition (CVPR 2001), Kauai, Hawaii, USA, December 8–14*, pp. I–511 – I–518 Vol.1, 2001.

[Viol 04] P. Viola and M. Jones. "Robust Real-time Face Detection". *International Journal of Computer Vision*, Vol. 57, No. 2, pp. 137–154, May 2004.

[Voss 88] A. Vossepoel. "A note on "distance transformations in digital images"'. *Computer Vision, Graphics, and Image Processing*, Vol. 43, No. 1, pp. 88–97, July 1988.

[Wang 07] Y. Wang, P. Cuculich, P. Woodward, B. Lindsay, and Y. Rudy. "Focal Atrial Tachycardia after Pulmonary Vein Isolation: Noninvasive Mapping with Electrocardiographic Imaging (ECGI)". *Hearth Rhythm*, Vol. 4, No. 8, pp. 1081–1084, August 2007.

[Wazn 05] O. Wazni, N. Marrouche, D. Martin, A. Verma, M. Bhargava, W. Saliba, D. Bash, R. Schweikert, J. Brachmann, J. Gunther, K. Gutleben, E. Pisano, D. Potenza, R. Fanelli, A. Raviele, S. Themistoclakis, A. Rossillo, A. Bonso, and A. Natale. "Radiofrequency ablation vs antiarrhythmic drugs as first-line treatment of symptomatic atrial fibrillation: a randomized trial". *Journal of the American Medical Association*, Vol. 293, No. 21, pp. 2634–2640, January 2005.

[Welc 95] G. Welch and G. Bishop. "An Introduction to the Kalman Filter". Tech. Rep., University of North Carolina at Chapel Hill, Chapel Hill, NC, USA, 1995.

[Wije 05] S. Wijewickrema and A. Paplinski. "Principal Component Analysis for the Approximation of an Image as an Ellipse". In: *13th International Conference in Central Europe on Computer Graphics, Visualization and Computer Vision (WSCG 2005), Plzen-Bory, Czech Republic, January 31 – February 4*, pp. 69–70, 2005.

[Wije 06a] S. Wijewickrema, A. Paplinski, and C. Esson. "Reconstruction of ellipsoids on rollers from stereo images using occluding contours". In: *International Conference on Computer Vision Theory and Applications (VISAPP 2006), Setúbal, Portugal, February 25–28*, February 2006.

[Wije 06b] S. Wijewickrema, A. Paplinski, and C. Esson. "Reconstruction of Spheres using Occluding Contours from Stereo Images". In: *18th International Conference on Pattern Recognition (ICPR 2006), Hong Kong, August 20–24*, 2006.

[Will 07] J. Willerson, H. Wellens, J. Cohn, and D. Holmes, Eds. *Cardiovascular Medicine*. Springer, London, UK, 3rd Ed., 2007.

[Witt 02] F. Wittkampf, P. Loh, R. Derksen, T. Simmers, and L. Eckardt. "Real-Time, Three-Dimensional, Nonfluoroscopic Localization of the Lasso Catheter". *Journal of Cardiovascular Electrophysiology*, Vol. 13, No. 6, p. 630, June 2002.

[Witt 99] F. Wittkampf, E. Wever, R. Derksen, A. Wilde, H. Ramanna, R. Hauer, and E. de Medina. "LocaLisa - New Technique for Real-Time 3-Dimensional Localization of Regular Intracardiac Electrodes". *Circulation*, Vol. 99, No. 13, pp. 1312–1317, March 1999.

[Wolf 91] P. Wolf, R. Abbott, and W. Kannel. "Atrial fibrillation as an independent risk factor for stroke: the Framingham Study". *Stroke*, Vol. 22, No. 8, pp. 983–988, August 1991.

[Wrig 09] B. Wrigley and G. Lip. "Can the WATCHMAN device truly PROTECT from stroke in atrial fibrillation?". *The Lancet*, Vol. 8, No. 10, pp. 877–878, October 2009.

[Wrig 10] R. Wright, N. Haemel, G. Sellers, and B. Lipchak. *OpenGL SuperBible*. Addison-Wesley Professional, Boston, MA, USA, 5th Ed., August 2010.

[Wu 11] W. Wu, T. Chen, A. Barbu, P. Wang, N. Strobel, S. Zhou, and D. Comaniciu. "Learning-based hypothesis fusion for robust catheter tracking in 2D X-ray fluoroscopy". In: *24th IEEE Conference on Computer Vision and Pattern Recognition. Colorado Springs, CO, USA. June 20–25*, pp. 1097–1104, June 2011.

[Wu 12] W. Wu, T. Chen, N. Strobel, and D. Comaniciu. "Robust tracking of a virtual electrode on a coronary sinus catheter for atrial fibrillation ablation procedures". In: D. Holmes and K. Wong, Eds., *Proceedings of SPIE Medical Imaging 2012: Image-Guided Procedures, Robotic Interventions, and Modeling, San Diego, CA, USA, Febuary 4–9*, p. 83162U, 2012.

[Wyse 09] D. Wyse. "Cardioversion of Atrial Fibrillation of Maintenance of Sinus Rhythm". *Circulation*, Vol. 120, No. 14, pp. 1444–1452, October 2009.

[Xie 02] Y. Xie and Q. Ji. "A New Efficient Ellipse Detection Method". In: *16th International Conference on Pattern Recognition (ICPR 2002), Quebec, Canada, August 11–15*, pp. 957–960, 2002.

[Yao 03] J. Yao and R. Taylor. "Assessing accuracy factors in deformable 2D/3D medical image registration using a statistical pelvis model". In: *Proceedings of Ninth IEEE International Conference on Computer Vision (ICCV 2003), Nice, France, October 13–16*, pp. 1329–1334, October 2003.

[Yao 04] J. Yao, N. Kharma, and P. Grogono. "Fast Robust GA-Based Ellipse Detection". In: *17th International Conference on Pattern Recognition (ICPR 2004), Cambridge, UK, August 23–26*, pp. 859–862, 2004.

[Yao 05] J. Yao, N. Kharma, and P. Grogono. "A Multi-Population Genetic Algorithm for Robust and Fast Ellipse Detection". *Pattern Analysis & Applications*, Vol. 8, No. 1, pp. 149–162, September 2005.

[Zago 07] L. Zagorchev, R. Manzke, R. Cury, V. Y. Reddy, and R. C. Chan. "Rapid fusion of 2D x-ray fluoroscopy with 3D multislice CT for image-guided electrophysiology procedures". In: K. R. Cleary and M. I. Miga, Eds., *Proceedings of SPIE: Medical Imaging 2007: Visualization and Image-Guided Procedures, San Diego, CA, USA, February 17–22*, p. 65092B, 2007.

[Zell 05] M. Zellerhoff, B. Scholz, E.-P. Ruehrnschopf, and T. Brunner. "Low contrast 3D reconstruction from C-arm data". In: M. Flynn, Ed., *Proceedings of SPIE Medical Imaging 2005: Physics of Medical Imaging, San Diego, CA, USA, February 12–17*, pp. 646–655, 2005.

[Zhen 10] Y. Zheng, M. John, R. Liao, J. Boese, U. Kirschstein, B. Georgescu, K. Zhou, J. Kempfert, T. Walther, G. Brockmann, and D. Comaniciu. "Automatic aorta segmentation and valve landmark detection in C-Arm CT: application to aortic valve implantation". *Lecture Notes in Computer Science (13th International Conference on Medical Image Computing and Computer-Assisted Intervention, MICCAI 2010), Beijing, China, September 20 – 14*, Vol. 6361, pp. 476–483, 2010.

[Zwil 06] D. Zwillinger. *CRC Standard Mathematical Tables and Formulae*. Chapman & Hall / CRC Press, Boca Raton, FL, USA, 31st Ed., 2006.